SCUOLA DI DOTTORATO
UNIVERSITÀ DEGLI STUDI DI MILANO-BICOCCA

Department of Materials Science

PhD program in Materials Science and Nanotechnology

Cycle: XXXVII

Sustainability in TiO_2 recovery and application for environmental remediation

PhD Candidate: Viganò Lorenzo

Registration number: 811978

Supervisor: Prof. Barbara Di Credico

Tutor: Prof. Roberto Scotti

Coordinator: Prof. Francesco Montalenti

ACADEMIC YEAR 2023/2024

Abstract

Over the past decades, the rapid depletion of natural resources and the progressive environmental deterioration have highlighted the urgent need for more sustainable chemical processes. In this context, the first solution is represented by sustainable remediation, which involves removing pollutants released in the environment. Certainly, photocatalysis is an interesting and efficient process able to remove contaminants at ambient temperature and pressure and, in particular, titanium dioxide is the most appealing photocatalyst being non-toxic, chemically stable, commercially available and inexpensive. Furthermore, the use of nanoparticles (NPs) provided some benefits, such as increased surface area or high reactivity. TiO_2 NPs have proved highly effective in photodegrading a wide range of organic molecules, thanks to the oxygen radicals generated by UV irradiation, and in photoreduction processes such as CO_2 conversion into valuable products. However, a more efficient approach is to address the issue upstream, by directly improving sustainability and reducing pollutant generation in the overall process. For this reason, due to the high environmental impact of its production and the volume of its market, more sustainable practices in both the preparation and use of TiO_2 are needed.

Regarding TiO_2 preparation, the extraction from minerals and common liquid-phase synthesis are the main strategies, but they require high energy and solvent consumption. Despite the extraction of TiO_2 from wastes has been considered, this solution still has a strong environmental impact. Therefore, the direct use of Ti-rich residues or their improvement through mild chemical procedures remain more sustainable options, but these methods are poorly explored in the literature.

Concerning TiO_2 application, environmental and industrial safety is usually obtained through the immobilisation of TiO_2 NPs on adsorbent supports, to improve material recovery and NPs dispersion, reducing aggregation phenomenon. At the same time, a more innovative and efficient use of catalysts has been recently explored, with photothermo catalysis being a promising alternative because, by synergically combining photon and thermal excitations, the reactions proceed at lower temperatures, with higher yields and selectivity compared to conventional thermo- or photo-catalysis.

In this context, the present PhD thesis aims to design efficient TiO_2-based materials

with a sustainable approach to be applied for environmental remediation. The topic is developed by optimizing a TiO_2-rich waste material for its utilization as an alternative photocatalyst to commercial TiO_2, and by the application of well-dispersed TiO_2 NPs supported on spherical and bidimensional SiO_2 NPs, as well as on sepiolite and halloysite, for the methanation of CO_2 by photothermo catalysis.

First, the Ti-rich waste material, obtained by neutralisation of TiO_2 industrial production residuals, known as tionite, has been considered and thoroughly characterised to determine its composition and morphology. Its composition was improved through mild procedures to enhance its photoactivity. Specifically, the residuals neutralization step was modified by using NaOH instead of lime $Ca(OH)_2$ and silica components were removed by controlled acid or basic treatments, producing tionite samples having different physico-chemical characteristics. As part of this recovery strategy, tionites were tested for different photocatalytic applications in order to provide a new life for the Ti-rich waste. At first, samples were employed to photodegrade organic pollutants under UV irradiation in both traditional photocatalysis and photo-Fenton processes, but no significant decay was observed. Thus, these results suggested the exploration of tionite in the partial oxidation of ferulic acid to vanillin, an industrially relevant compound. All recovered materials showed a significant selectivity for vanillin, with the acidic treated sample providing the best results. Adsorption tests of vanillin and ferulic acid were also performed and the overall results were connected to the different surface features of each sample. These results are particularly relevant being ferulic acid one of the main waste compounds in many aqueous effluents downstream of several agro-food processes, while vanillin is probably the most relevant flavour compound, and its industrial green production is currently performed with low selectivity values.

In addition, peroxymonosulfate (PMS)-assisted catalysis was explored, as it can be easily activated by a wide range of metals, and all samples demonstrated remarkable efficiency in PMS activation and, consequently, in 4-chlorophenol (4-CP) degradation. In particular, the best results were achieved with the neutralized samples, without further treatments, and faster kinetics were observed by increasing the number of photons. It must be highlighted that the recovered catalysts were active also under visible light.

Regarding the sustainable application, the research activity focused on the preparation

and characterization of TiO_2 NPs immobilized on various silica-based supports. Photocatalytic tests were conducted on paracetamol (PC), with all supported catalysts proving effective in degrading the pollutant, while adsorption tests for a mixture of metal cations demonstrated the superiority of sepiolite-supported material in their removal. Successively, to explore the efficacy of these materials in photo-thermo catalysis, samples were decorated with Ru NPs and tested in the methanation reaction. Preliminary results indicate a significant synergistic effect: indeed, the same CH_4 yield obtained in the dark was achieved at lower temperatures, when irradiated with UV light.

In conclusion, the results suggest that TiO_2-based materials not only can reduce environmental pollution by degrading organic molecules or transforming CO_2 into valuable products, but the development of sustainable strategies for their production, preparation and application is possible. The key challenges remain to further implement the efficient and mindful recovery of TiO_2 from waste materials and eco-friendlier application strategies, like photothermo catalysis.

Riassunto

Negli ultimi decenni, il rapido consumo di risorse naturali e il deterioramento dell'ambiente hanno evidenziato l'urgente necessità di sviluppare processi chimici più sostenibili. In questo contesto, la prima soluzione è rappresentata dal disinquinamento sostenibile, che prevede la rimozione degli inquinanti rilasciati nell'ambiente. Certamente, la fotocatalisi è un processo interessante ed efficiente in grado di rimuovere i contaminanti a temperatura e pressione ambiente e, in particolare, il biossido di titanio è il fotocatalizzatore più attraente essendo atossico, chimicamente stabile, disponibile in commercio e poco costoso. Inoltre, l'uso di nanoparticelle (NP) ha fornito alcuni vantaggi, come l'aumento dell'area superficiale o l'elevata reattività. In realtà, le NP di TiO_2 si sono dimostrate altamente efficaci nella fotodegradazione di un'ampia gamma di inquinanti organici, grazie ai radicali ossigeno generati tramite luce UV, e in processi di fotoriduzione come la conversione della CO_2 in molecole ad alto valore aggiunto. Tuttavia, un approccio più efficiente consiste nell'affrontare il problema a monte, migliorando direttamente la sostenibilità e riducendo la generazione di inquinanti nell'intero processo. Per questo motivo, dato l'elevato impatto ambientale della sua produzione e il volume del suo mercato, sono necessarie pratiche più sostenibili sia nella preparazione che nell'uso del TiO_2.

Relativamente alla preparazione di TiO_2, l'estrazione da minerali e la sintesi in fase liquida rimangono le strategie principali, ma comportano un elevato consumo di energie e reagenti. Sebbene sia stata considerata l'estrazione di TiO_2 da materiali di scarto, questa soluzione ha ancora un forte impatto ambientale. Pertanto, l'uso diretto di scarti ricchi di Ti o la loro modifica con processi blandi rimangono le soluzioni più sostenibili, anche se poco inesplorate in letteratura.

Relativamente all'applicazione di TiO_2, la sicurezza ambientale e industriale è solitamente ottenuta tramite l'immobilizzazione delle NP su supporti adsorbente, migliorando così il recupero del materiale e la dispersione delle NP, riducendo il fenomeno di aggregazione. Allo stesso tempo, l'utilizzo di catalizzatori in processi innovativi ed efficienti è continuo oggetto di studio e la fototermo catalisi rappresenta un'alternativa promettente. Infatti, combinando sinergicamente eccitazione fotonica e termica, le reazioni procedono a temperature più basse, con rese e selettività superiori

rispetto alla termo- o foto-catalisi convenzionali.

In questo contesto, la presente tesi di dottorato mira a progettare materiali a base di TiO_2 con un approccio sostenibile e ad alta efficienza per la loro applicazioni ambientale L'argomento è stato sviluppato ottimizzando un materiale di scarto ricco di TiO_2 per il suo utilizzo come fotocatalizzatore alternativo al TiO_2 commerciale e mediante l'applicazione di NP di TiO_2 ben disperse supportate su NP di SiO_2, sferiche e bidimensionali, nonché su sepiolite e halloysite, per la metanazione di CO_2 mediante fototermocatalisi.

In primo luogo, è stato preso in considerazione e caratterizzato in modo approfondito il materiale di scarto ricco di Ti, ottenuto dalla neutralizzazione dei residui di produzione industriale di TiO_2, noto come tionite. La sua composizione è stata migliorata mediante trattamenti chimici blandi per aumentarne la fotoattività. Nello specifico, la fase di neutralizzazione dei residui è stata modificata utilizzando NaOH invece di calce $Ca(OH)_2$ e i componenti a base di silice sono stati rimossi mediante trattamenti acidi o basici controllati, producendo campioni di tionite con diverse caratteristiche fisico-chimiche.

Come parte di questa strategia di recupero, i campioni di tionite sono stati testati per diverse applicazioni fotocatalitiche, al fine di dare nuova vita a questo materiale di scarto. In un primo momento, i campioni sono stati utilizzati nella fotodegradazione di inquinanti organici sotto irradiazione UV, sia in fotocatalisi tradizionale che in processi foto-Fenton, ma non è stato osservato alcun risultato significativo. Inoltre, il contenuto di Fe della tionite è stato sfruttato per la degradazione foto-Fenton del 4-CP, con scarsi esiti. Questi risultati hanno portato ad applicare la tionite nella reazione di ossidazione parziale dell'acido ferulico a vanillina, un composto di rilevanza industriale. Tutti i materiali recuperati hanno mostrato una significativa selettività per la vanillina, con il campione trattato con acido che ha fornito i risultati migliori. Sono stati inoltre eseguiti test di adsorbimento di vanillina e acido ferulico e i risultati complessivi sono stati collegati alle diverse caratteristiche superficiali di ciascun campione. Questi risultati sono particolarmente rilevanti poiché l'acido ferulico è uno dei principali composti di scarto in molti effluenti acquosi a valle di diversi processi agroalimentari, mentre la vanillina è probabilmente il composto aromatico più rilevante e la sua produzione industriale verde viene attualmente eseguita con bassi valori di selettività.

È stata inoltre investigata la fotodegradazione mediata da perossimonosolfato (PMS), poiché la molecola può essere attivata da un'ampia gamma di metalli, e tutti i campioni si sono dimostrati efficaci nell'attivazione del PMS e, di conseguenza, nella degradazione del 4-clorofenolo (4-CP). In particolare, i migliori risultati sono stati ottenuti con i campioni neutralizzati, senza ulteriori trattamenti e si è osservato un miglioramento della velocità di reazione aumentando il numero di fotoni. È importante sottolineare che i catalizzatori recuperati sono risultati attivi anche con luce visibile.
Riguardo all'applicazione sostenibile, l'attività di ricerca si è concentrata sulla preparazione e caratterizzazione di NP di TiO_2 immobilizzate su vari supporti a base di silice. Test fotocatalitici sono stati condotti sul paracetamolo (PC) e tutti i campioni si sono dimostrati efficaci nella degradazione dell'inquinante, mentre i test di adsorbimento per una miscela di cationi metallici hanno dimostrato la superiorità del materiale supportato da sepiolite nella loro rimozione. Successivamente, per esplorare l'efficacia di questi materiali nella fototermo catalisi, sono stati decorati con NP e applicati nella reazione di metanazione della CO_2. I risultati preliminari mostrano un notevole effetto sinergico: infatti, la stessa resa in CH_4 osservata in condizioni di buio è stata ottenuta a temperature più basse quando irradiata con luce UV.

In conclusione, i risultati suggeriscono che i materiali a base di TiO_2 non solo possono ridurre l'inquinamento ambientale degradando molecole organiche o trasformando CO_2 in prodotti di valore, ma è anche possibile sviluppare strategie sostenibili per la loro produzione, preparazione e applicazione. Le sfide principali restano l'ulteriore implementazione di un recupero efficiente e consapevole di TiO_2 dai materiali di scarto e di strategie di applicazione più ecocompatibili, come la fototermo catalisi.

List of Abbreviations

4-CP	4-Chlorophenol
AOP	Advanced oxidation process
ATR	Attenuated total reflectance
BET	Brunauer-Emmet-Teller
BJH	Barret-Joyner-Halenda
BFS	Blast furnace slag
CB	Conduction band
DRS	Diffuse Reflectance Spectroscopy
EDX	Energy dispersive X-ray analysis
FTIR	Fourier transform infrared spectroscopy
Hall	Halloysite
HPLC	High-performance liquid chromatography
I	Irradiance
K	Apparent kinetic constant
LSPR	Localized surface plasmon resonance
ICP-OES	Inductively coupled plasma optical emission spectrometry
NP	Nanoparticle
PC	Paracetamol
PMS	Peroxymonosulfate
rpm	Revolutions per minute
RT	Room temperature
SCRC	Selective catalytic reduction catalyst
SEM	Scanning electron microscopy
Sep	Sepiolite
Supp@TiO_2	TiO_2 NPs immobilized on silica-based supports
TEM	Transmission electron microscopy
TGA	Thermogravimetric analysis
TOC	Total organic carbon

UV	Ultraviolet light
VB	Valence band
Vis	Visible light
VOC	Volatile organic compound
wt. %	Weight percentage
XPS	X-ray photoelectron spectroscopy
XRD	X-ray diffraction
XRF	X-ray fluorescence

Summary

Preface: introduction and aims

i) Introduction

Since the groundbreaking discovery of water splitting by Fujishima and Honda[1] in 1972 photocatalysis has garnered significant attention, being utilized in a wide range of applications, particularly related to environmental remediation, chemical synthesis and energy production. Photocatalytic materials have been mainly involved in exploiting light for oxidising or reducing substances; specifically, they find application in the production of fuels like hydrogen, in decontaminating surfaces from bacteria, in medicine for anti-cancer therapy, in self-cleaning surfaces and in the catalysis of organic reactions towards specific products. Among many photocatalysts available, TiO_2 is mostly known for its efficiency in water treatment and air decontamination, especially in the form of nanodimensional particles. The extended investigation of this material is attributed to two factors: i) the extreme efficiency in degrading and mineralising both organic pollutant and volatile organic compounds (VOC) and ii) its chemical-physical properties like chemical stability, nontoxicity, low cost, availability and transparency to visible light.[2–6]

Despite its outstanding properties, TiO_2 cannot be overlooked by the increasing attention that the scientific and governmental authorities are emphasising on better utilization of resources and sustainable production of energy. In this optic, the 2023 COP28 conference[7] further highlighted the necessity to reach the maximum greenhouse gasses emission in 2025 and to decrease their amount of 43% by 2030 and of 60% by 2035 in order to limit the global warming effect. However, the efforts cannot be directed only on CO_2 production, but on the overall sources of pollution, especially in a field such as chemistry. The green chemistry principles introduced by Paul Anastas and John Warner[8] represent a pivotal step towards the development of greener and more environment-friendly chemical processes and products. The 12 fundamental points[9] of green chemistry provide the fundamental factors to consider and optimize for a sustainable chemical process: prevent the production of pollutants, reduce hazardous chemicals and improve the efficiency of the process towards the production of the desired product. In addition, the energetical and environmental sectors have been focusing their attention on the recycling of materials, either in the form of reuse or by reprocessing them through environmentally friendly procedures.

Indeed, the increasing demand for sustainable photoactive materials in these fields over the past years led to more intense research on the topic, with even more sophisticated and refined sustainable solutions being developed or proposed.

In this context, the concept of “circular economy” is a direct application of green chemistry principles. In a typical linear economy, the main rule is “take-make-dispose: the industrially produced goods at the end of their lifetime are not valorised through their reuse, but they are mostly disposed into landfills or incinerated. Contrarily, the circular economy system, based on the slogan “reduce, reuse, recycle and recover”, aims to reduce the wastes associated with industrial products by recovering and recycling their components. This can potentially represent a smart solution to reduce the risks and environmental impact of common industrial processes.[10]

In this context, the consumption of TiO_2 keeps increasing year by year; according to the Mineral Commodity Summaries 2024,[11] the production in 2023 reached the volume of 10.2 million tons worldwide, while in 2013[12] it was 6.8 million tons, meaning a 37.3 % increase in the last 10 years. The application of green chemistry rules is therefore fundamental in order to reduce the environmental impact of TiO_2. Specifically, the focus should not be directed only on the production of TiO_2, but also on its application. Based on the green chemistry principle, the synthetic process of TiO_2, both on an industrial and laboratory scale, should be designed in terms of safety and efficiency. The utilization and generation of less hazardous chemicals are the focal points to improve the synthesis strategy, as well as the reduction of solvents and chemical additives. In addition, the atom economy is a strategic parameter to define the process efficiency: the final product should contain the maximum number of atoms introduced with the reactants. Taking atom economy into account would indeed be fundamental to improve and maximise the process yield, with indirect information about the amount of waste produced and their nature.

On the other hand, even the utilization of TiO_2 should be subjected to an accurate analysis. Focusing on the main application of TiO_2, photocatalysis and photodegradation of pollutants, the process itself adheres to the green chemistry principles. Indeed, being TiO_2 a catalyst, its role is improving the reaction efficiency and selectivity, without being consumed at the end of the process. In addition, its specific application in the degradation of pollutants or their conversion into less

dangerous products is indeed fitting the green chemistry principles. However, some limitations can be detected: i) TiO_2 can be activated only by UV light and ii) its efficiency is limited by the high charge carriers recombination rate.[13]

In this context, regarding the TiO_2 origin, the investigation of a more sustainable TiO_2 source is under investigation; especially the focus is directed towards the valorisation of waste materials. On the application hand, new methodologies to improve the efficiency, selectivity and solar exploitation of TiO_2 in environmental degradation applications are being explored.

ii) Aim of the thesis

In this scenario, the research activity reported in this PhD thesis is directed towards the sustainability implementation in both the origin and application in environmental decontamination by TiO_2.

In order to improve the sustainability in TiO_2 production, a not well-known Ti-rich material obtained as a by-product of the TiO_2 industrial process was investigated. Due to a lack of precise information about his composition and morphology, its characterization was a focal point for understanding both its properties and its potential applications. The results confirmed the presence of TiO_2 in the waste material and this directed the investigation towards a photocatalytic application. For this purpose, the investigation followed this logical path:

- Preliminary photodegradation tests were utilised to define the waste material efficiency
- According to the results, mild chemical processes were applied to improve tionite composition and enhance the photocatalytic efficiency
- Raw and modified tionites were then applied as catalysts in different photodegradation strategies

Simultaneously, the research has been devoted to the development of TiO_2 catalyst supported onto SiO_2 with different morphologies or SiO_2-based clays. The homogeneous dispersion of the catalysts is aimed to improve the exposed surface, by avoiding aggregation, and increase the catalyst accessibility to the target molecule thanks to the adsorbent properties of the support.

These hybrid materials were then tested in a traditional photocatalytic test, but also in the photothermo catalytic methanation of CO_2. Photothermo catalysis is a new and developing catalytic strategy, which synergically combines the photon and thermal excitation, to carry out reactions with higher efficiency and selectivity and at a lower temperature, compared to classical thermo catalysis.

iii) Thesis structure

The present work is structured on two main topics: i) characterization of tionite waste material, its composition improvement and utilization in photocatalytic applications and ii) the design of immobilized TiO_2 samples and their application in photothermo catalysis.

Chapter 1 is a general introduction to the systems and contest in which this thesis was developed. In detail, the state of the art on the TiO_2 photocatalyst has been described, focusing on the electronic structure of the material, the limits of its application for photocatalytic purposes and the solution to overcome some drawbacks. The common synthetic technique for TiO_2 nanoparticles (NPs) at both industrial and laboratory scales will be described. Successively, the available strategies to extract TiO_2 from different Ti-rich waste materials as a potential sustainable option will be presented along with an examination of the literature examples related to the direct use of such wastes in photocatalytic applications. Finally, starting from the limitations of heterogeneous photocatalysis and thermocatalysis, the basic principles of photothermo catalysis will be reported.

Chapter 2 reports the extensive characterization of raw tionite to define its composition and morphology. Three different chemical treatments are proposed to improve the material composition and, for each, a characterization aiming to define the changes in its properties is performed.

Chapter 3 is dedicated to the photocatalytic application of all the tionite samples produced. At first, the photocatalytic degradation of paracetamol was used to preliminary define the efficiency of each sample. Then the performance of tionite samples was tested for the partial selective oxidation of ferulic acid to the high-added value vanillin, along with adsorption test on both organic molecules to link the catalytic

efficiency to the structure and composition of the materials. Following, the application of all samples in the photo-Fenton degradation of 4-chlorophenol is reported. Finally, the peroxymonosulfate-assisted degradation of the same pollutant is tested, with an in-depth investigation of the influence of irradiance and different light sources to define the mechanism involved.

Chapter 4 described the synthetic procedure of TiO_2 NPs on two SiO_2 supports with different morphologies and two clays, sepiolite and halloysite. All the samples were characterized to define the effective functionalization with the semiconductor and the morphology of its particles. Preliminary photocatalytic information was provided by testing their efficiency in degrading paracetamol. Successively, all the samples were functionalized with Ru NPs by impregnation and photo-assisted deposition procedure, and they were tested in the photothermal methanation of CO_2.

iv) Bibliography

[1] K. Honda, A. Fujishima, *Nature* **1972**, *238*, 37–38.

[2] I. Ali, M. Suhail, Z. A. Alothman, A. Alwarthan, *RSC Adv.* **2018**, *8*, 30125–30147.

[3] J. Roy, *J. Ind. Eng. Chem.* **2022**, *106*, 1–19.

[4] C. Ayappan, R. Xing, X. Zhang, D. Luo, S. Liu, A. Fujishima, *Coord. Chem. Rev.* **2024**, *515*, 215960.

[5] N. Ahmadpour, M. Nowrouzi, V. Madadi Avargani, M. H. Sayadi, S. Zendehboudi, *J. Water Process Eng.* **2024**, *57*, 104597.

[6] C. H. Kirk, P. Wang, C. Y. D. Chong, Q. Zhao, J. Sun, J. Wang, *J. Mater. Sci. Technol.* **2024**, *183*, 152–164.

[7] COP28 - Global Stocktake decision, **2023**.

[8] P. T. Anastas, J. C. Warner, *Green Chemistry: Theory and Practice*, Oxford University Press, **2000**.

[9] P. Anastas, N. Eghbali, *Chem. Soc. Rev.* **2010**, *39*, 301–312.

[10] T. Keijer, V. Bakker, J. C. Slootweg, *Nat. Chem.* **2019**, *11*, 190–195.

[11] *Mineral Commodity Summaries 2024*, **2024**.

[12] *Minerals Commodity Summaries 2014*, **2014**.

[13] H. Dong, G. Zeng, L. Tang, C. Fan, C. Zhang, X. He, Y. He, *Water Res.* **2015**, *79*, 128–146.

Chapter 1: Sustainability in TiO_2 origin and application

Chapter 1 reports the state-of-the-art in the application of the sustainability concept to the production and application of TiO_2. In detail, starting from the fundamental aspects of sustainability, the problem of environmental pollution and the necessity for more sustainable processes are presented. The properties of TiO_2 are illustrated, with a focus on the photocatalytic properties of the material. The common strategies for TiO_2 synthesis will be illustrated, focusing on both a large-scale production of the material and the strategies that guarantee more control over the morphology. An evaluation of the available procedure for recovering TiO_2 from industrial waste is reported, along with the recent attention to the direct utilization of waste materials. Regarding the sustainability in the application of TiO_2, the attention will be directed towards the advantages of immobilizing TiO_2 on adsorbent supports and in a novel photocatalytic application, known as photothermo catalysis.

1.1 Fundamental aspects of sustainability

The rising awareness towards resource depletion, environmental degradation and the necessity to develop sustainable and circular practices have been modifying the way of producing chemicals and managing waste. Indeed, in the last decades, the keyword in chemistry research, both at the academic and industrial levels, has become “sustainability”. According to the report “Our Common Future” published by the World Commission on Environment and Development in 1989[1], the concept of sustainability was defined as a contribution to development without compromising, but instead improving or at least maintaining the ability for future generations to access available resources.

In this context, great interest is gained by sustainable remediation, which defines all the strategies developed to contrast the pollution crisis caused by not-so-green processes with the aim of restoring contaminated environments.[2] Over the last decades, water and air contamination due to inorganic species, namely heavy metal ions (Fe^{3+}, Cu^{2+}, Mn^{2+}, Ni^{2+}), organic molecules such as pesticides or volatile organic compounds (VOCs) and especially carbon dioxide, due to its climatic effect as a greenhouse gas, has become a primary problem, that needs to be solved.

The development of cheaper, effective and novel methods for decontamination is currently an active research field and several purification treatments have been considered, such as chemical oxidation, solvent extractions or thermal decomposition, but these strategies show some limits. In addition, among the various treatments for water and air pollutants, only a few are commonly used by the industrial sector for economic and technological reasons due to their cost, efficiency, environmental impact and the formation of toxic by-products.[3] Certainly, decontamination technologies based on advanced oxidation processes (AOPs) present the highest potential. The generation of reactive radical species, such as hydroxyl radicals, through photochemical or thermal activation mechanisms proved extremely efficient in mineralizing a wide range of pollutants. In this context, the combination of H_2O_2 with Fe-based catalyst (Fenton or photo-Fenton), O_3, photocatalysis, irradiation and sonolysis are all well-established strategies to degrade pollutants.[4–6] However, photocatalysis is an interesting process that in the last decades has proven to be a highly efficient strategy: it does not require any chemicals for its process, it can be

applied on a large scale, it has high efficiency in a short time and the catalyst can be recovered and recycled.[7]

Despite sustainable remediation represent an efficient strategy to reduce the environmental impact of everyday processes, it operates at the end of the problematic chain. Indeed, it is more efficient to tackle the problem upstream, by directly improving sustainability and reducing pollutant generation in the process.

To effectively reach this goal the necessity is to reduce the continuous and incessant consumption of fresh raw materials, whose availability is limited, and the improvement of the resources utilization in the overall production system. However, this must go along with the development of new technologies or the optimization of the already available ones to reduce the environmental impact of the process. In both cases, the main objective is the reduction of waste and energy, to reduce fossil fuel consumption and the consequential greenhouse gasses emission, but also the potential pollutants released in the environment.

The implementation in the sustainability of a process (Figure 1.1) starts directly in the designing step of the products with the selection of materials, namely the substitution of current materials with those with less environmental impact, but also in the reduction of the complexity and efficiency of materials to reduce the amount involved and facilitate their separation at the end of their life.[8] Once optimized this aspect, the following step is the preparation process of the material where operating in milder conditions and with fewer chemicals is the goal. In this optic, reducing the temperature, the utilization of organic solvents or strong acids and bases and decreasing the waste generated from the process are the main goals.[9] In addition, extending the lifetime of the product by improving its durability and maintenance is effective in reducing the demand and consequentially the amount of material and waste.

However, once the product is disposed, its recovery and recycling are a consequential step.[10] The main advantage is that materials and components, recovered from non-primary resources, require fewer modifications for their reuse, but often several materials are mixed, making this step more difficult and less sustainable. In this context, resource depletion and environmental sustainability have boosted the research on the recycling aspect towards waste material, not only on end-life products.

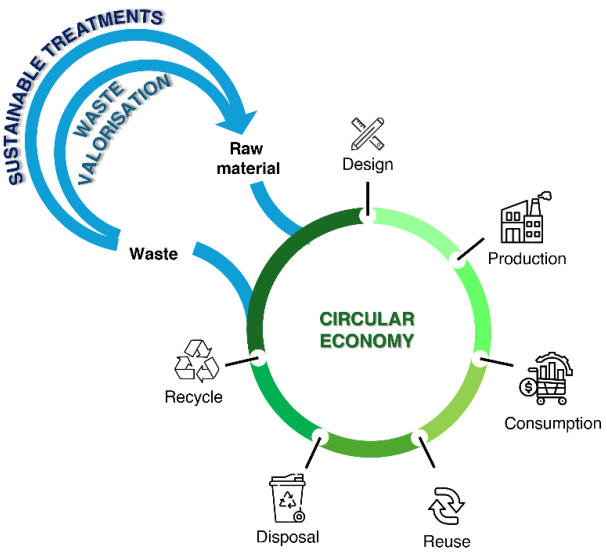

Figure 1.1: schematic representation of circular economy step considered in the implementation of sustainability, with a highlight on the reusability of waste materials.

Those waste materials often contain valuable components that could be useful for other applications, therefore giving them new life as high-added value products is a potential solution.[11] On the other hand, their complex composition, contaminations and low quality can require intense chemical and physical steps to make them economically and commercially attractive.[12] To make this strategy feasible, the investigation and development of more sustainable and less impacting processes for the valorisation of waste materials is of primary importance.

1.2 TiO_2: properties, photocatalytic applications and challenges

Titanium dioxide (TiO_2), an inorganic compound composed of titanium and oxygen, is considered very close to an ideal semiconductor for its high chemical stability, non-toxicity, opacity, low cost and safety for both humans and the environment, making it a vital material in industries such as paints, coatings and cosmetics.

TiO_2 has three common polyforms: anatase (tetragonal), brookite (orthorhombic) and rutile (tetragonal) (Figure 1.2). In this Thesis, only the crystal structures and properties of the rutile and anatase polymorphs will be considered. Specifically, both anatase and rutile crystal structures are composed of chains of TiO_6 octahedra with different connectivity: in anatase each octahedra shares four edges, while in rutile only two edges connect the octahedra with their nearest neighbours.[13] Due to the repulsion

forces between positive polyhedral cores, increasing the number of shared edges or faces causes a destabilization in the structure; therefore TiO_2 is a large band semiconductor, with band gaps of 3.2, and 3.02 eV for the anatase, and rutile phases, respectively. As any semiconductor, TiO_2 photocatalytic action is related to the redox processes induced by light irradiation. A semiconductor has an energy band structure composed of a low-energy valence band (VB) and a high-energy conduction band (CB), and the band gap between a conduction band and a valence band is called a forbidden band.[14]

a)

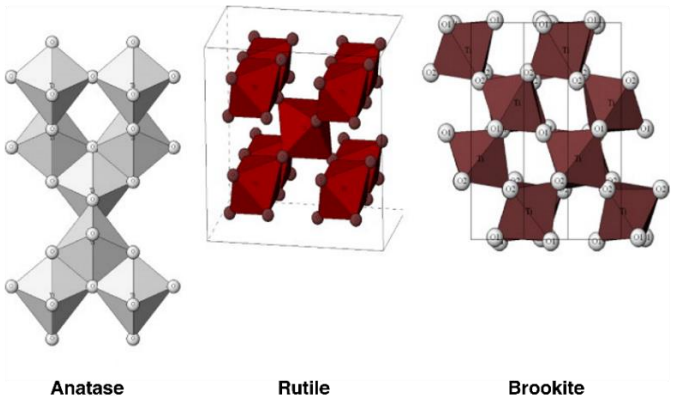

b)

	Rutile	Anatase	Brookite
Crystal structure	tetragonal	tetragonal	Orthorhombic
Lattice constant (Å)	a= 4.5936 c=2.9587	a=3.784 c=9.515	a= 9.184 b=5.447 c=6.145
Space group	$P4_2/mnm$	$I4_1/amd$	$Pbca$
Molecule/cell	2	4	8
Volume/molecule ($Å^3$)	31.2160	34.061	32.172
Density (g/cm_3)	4.14	3.79	3.99
Ti-O bond length (Å)	1.949-1.980	1.937-1.965	1.87-2.04
O-Ti-O bond angle	81.2° 90.0°	77.7° 92.6°	77.0°-105°

Figure 1.2: a) crystalline structure and b) crystal structure data of TiO_2 anatase, rutile and brookite. Adapted from[15] and[16].

When the energy of the incident light is larger than the band gap of the semiconductor, the electrons in the VB of the semiconductor are excited to the CB by photons and an electron-hole (e^-/h^+) pair is generated in the semiconductor electronic structure. Charge carriers can undergo recombination, neutralizing each other, or they can move (charge carriers mass transfer) to the surface of semiconductor particles, where they can act as strong oxidizers or reductants, respectively, for substances adsorbed on the surface or in the surrounding environment. The photocatalytic mechanism generally consists in a first adsorption of reactants in the liquid/gas phase to the surface, their reaction in the adsorbed phase and, finally, the products desorption and their removal from the interface region.[17]

The presence of oxygen facilitates the degradation of pollutants since they start a reaction mechanism involving a radical pathway. The radical chain reaction is normally initiated by the reduction of surface Ti(IV) to Ti(III) by the electrons and the following

generation of superoxide radical anions($O_2^{\cdot -}$) from surface-adsorbed O_2. At the same time, holes contribute to the radical chain by forming hydroxyl radicals from adsorbed water molecules. Photogenerated holes can also be directly involved in the complete mineralization of organic compounds to CO_2 and H_2O, mainly at low water content or high surface pollutant adsorption. Figure 1.3 shows the main phenomena involved in TiO_2 photoexcitation.

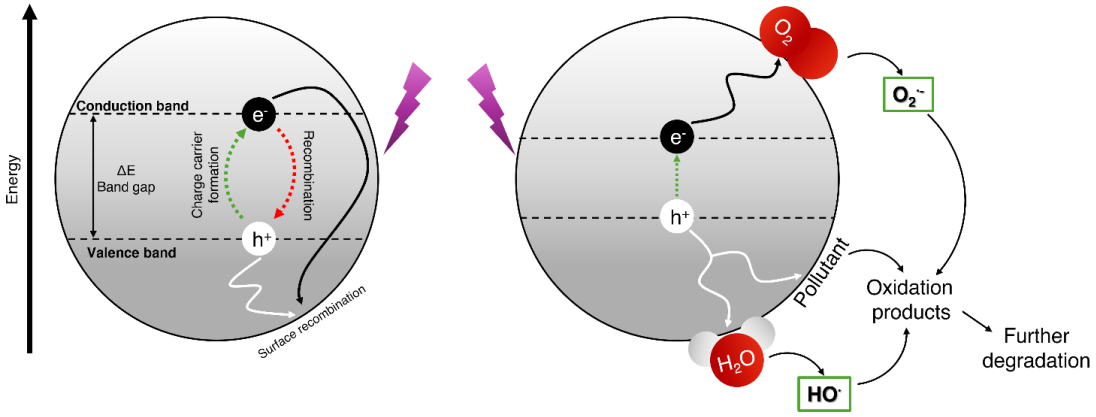

Figure 1.3: schematic representation of electronic process involved in a semiconductor for the degradation of pollutants

Throughout the propagation phase, various other reactive oxygen species are formed: reaction between superoxide and H^+ leads to hydroperoxyl radical, H_2O_2 and OH radicals as final active species, while singlet oxygen can be formed through the photo-oxidation of superoxide by TiO_2.[18]

The overall mechanism can be summarized by Eq. 1.1- 1.8.

$$TiO_2 + hv \rightarrow e_{cb}^- + h_{vb}^+ \quad 1.1$$

$$e_{cb}^- + Ti(IV) \rightarrow Ti(III) \quad 1.2$$

$$Ti\ (III) + O_2 \rightarrow Ti(IV) + O_2^{\cdot -} \quad 1.3$$

$$h_{vb}^+ + H_2O \rightarrow OH^{\cdot} + H^+ \quad 1.4$$

$$O_2^{\cdot -} + H^+ \rightarrow HOO^{\cdot} \quad 1.5$$

$$2\,HOO^{\cdot} \rightarrow H_2O_2 + O_2 \quad 1.6$$

$$H_2O_2 + e_{cb}^- \rightarrow OH^{\cdot} + OH^- \quad 1.7$$

$$OH^{\cdot} \setminus O_2^{\cdot -} \setminus h_{vb}^+ + pollutant \rightarrow\rightarrow\rightarrow oxidation \quad 1.8$$

Anatase TiO_2 is considered to be the more active photocatalytic component based on charge carrier dynamics, chemical properties and the photoactivity towards the degradation of organic compounds. This is due to the surface band bending of anatase that forms spontaneously in a deeper region with a steeper potential with respect to the rutile phase (Figure 1.4). Thus, surface hole trapping rules because spatial charge separation is achieved by the transfer of photogenerated holes towards the surface of the particle by means of strong upward band bending. On the other hand, in the rutile, the bulk recombination of electrons and holes occurs, and only holes very close to the surface are trapped and transferred to the surface.[19]

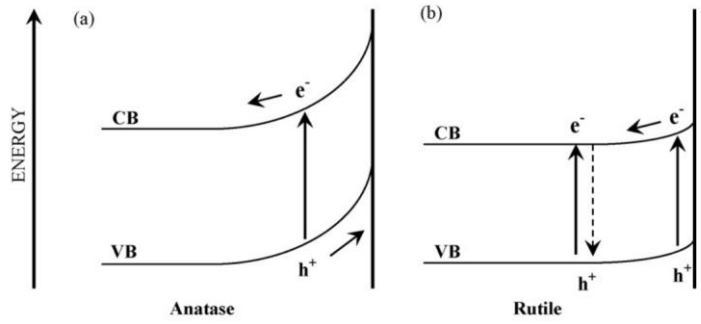

Figure 1.4: surface band bending for a) anatase ad b) rutile. Reprinted from [19]

However, a combination of the rutile and anatase phases proved to be extremely efficient in increasing TiO_2 photoactivity, for this reason the commercial Degussa P25 TiO_2, consisting of 75% anatase and 25% rutile is considered the gold standard in photocatalysis.[20]

It is worth considering that a variety of studies have demonstrated that TiO_2 in the form of nanoparticles (NPs) is much more efficient as a photocatalyst than in bulk powder. In fact, each charge carrier appears to behave quantum mechanically as a simple particle in a box (Figure 1.5), when a semiconductor particle possesses the diameter of the crystallites below a critical radius of about 10 nm. This confinement produces the band gap increase and the shift of the band edges to yield larger redox potentials.[21]

On the other hand, the nanometric dimension of TiO_2 gives rise to critical issues from the application point of view: i) NPs undergo aggregation during the photocatalytic process due to their dimensional-induced instability, lowering the surface area available for adsorption and irradiated by light, ii) higher light scattering is observed

for nanometric particles and iii) when operating in a liquid system, TiO_2 particles recovery is challenging, with repercussions on both economical and safety level. A solution to these problems is to anchor TiO_2 NPs on supports like clays, zeolite and others which prevent their aggregation and make them more easily recoverable (more details in Paragraph 1.4.1).

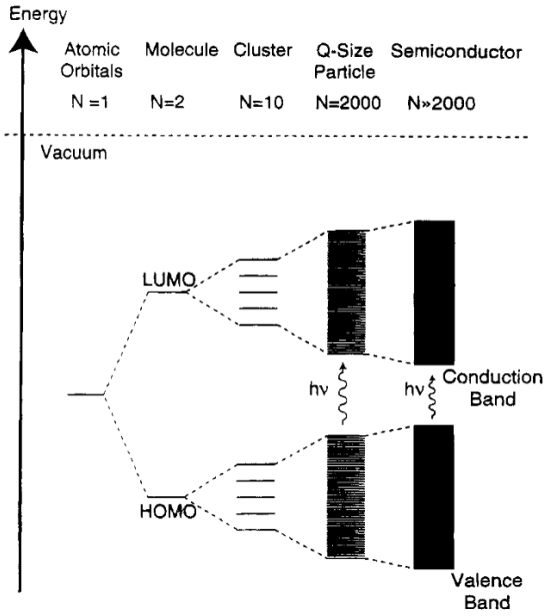

Figure 1.5: molecular orbital model for particle growth at increasing monomeric unit (N). Reprinted from [22]

The efficiency of TiO_2-based photocatalysts also depends on (i) the pollutant concentration, (ii) the amount of penetrating light on the surface of TiO_2 and (iii) the duration of light irradiation. However, limitations in the application of TiO_2 for photocatalytic purposes are mainly related to the limitations in the mass transfer on the catalyst surface. Indeed, photoactivity and photodegradation are strictly limited to the material surface, where the oxygen species or pollutants need to be adsorbed in order to be degraded. The limited TiO_2 surface area and its polar nature limit its efficiency due to the reduction in the adsorption rate of organic pollutants, especially hydrophobic molecules, slowing down the degradation rate. Therefore, controlling TiO_2 NPs synthetic steps allows to tailor the surface properties and the morphology to obtain nanotubes, hollow, flower-like and highly porous structures.[23] In this context, Harris *et al.*[24] synthesised TiO_2 nanoflowers through a hydrothermal procedure involving Ti-butoxide and acetic acid as solvent. Through a calcination at 400 °C for 1 h, the obtained isotropic particle provided a surface area of 107 $m^2\ g^{-1}$. On the other hand, Ko *et al*.[25] prepared mesoporous TiO_2 NPs using a sol-gel strategy. Starting

from Ti-isopropoxide and isopropyl alcohol, sol was formed through the addition of water; the collected particles were then dried at 200 °C for 5 h providing a mesoporous structure with a surface area of 196.2 m^2 g^{-1} and an average pore diameter of 8.34 nm. Finally, Shayegan *et al.*[26] demonstrated that the fluorination of P25 through a treatment with ammonium fluoride increases the hydrophobicity of the material, improving its adsorption capacity towards toluene, methylethylketone and isobutanol, at different humidity levels.

As TiO_2 photocatalyst is only active under UV light, artificial UV light sources usually have to be provided for almost all the photocatalytic applications. To make the photocatalytic technology cost-competitive for practical applications, significant recent research interest has been devoted to utilizing the naturally available sunlight as a possible “free” light source for photocatalytic reactions, and several modification strategies have been developed, for example by doping TiO_2 with precious metals, metal oxides, or inorganic components such as nitrogen (N) or carbon (C), surface dye photosensitization, surface metal deposition, constructing heterojunctions and others.[27,28] Commonly, almost all of these studies involved at least a high temperature treatment process in the preparation method (often >300−400 °C). In this context, Kwak *et al.*[29] proposed a synthesis for C-doped TiO_2 NPs consisting in mixing polyvinylalcohol with a solution of Ti-isopropoxide in isopropanol followed by the addition of H_2O and a calcination at 400 °C for 4 h, demonstrating the decreasing of the band gap to 2.82 eV, corresponding to 440 nm light. Alternatively, Kaviyarasan *et al.*[30] prepared a heterojunction nanocomposite combining Cu_2O and TiO_2 through a sonochemical procedure involving P25 and $CuSO_4 \cdot 5H_2O$, ascorbic acid as reducing agent, and poly(vinylpyrrolidone), obtaining a band gap value of 2.9 eV, with an adsorption between 400 and 600 nm. Instead, Moradi *et al.*[30] proposed a sonochemical synthesis of Fe-doped TiO_2 using Ti-tetrabutoxide and $FeCl_3 \cdot 6H_2O$ as precursors followed by a calcination at 600 °C for 1 h. By introducing 10% of Fe, the band gap decreased to 2.1 eV.

From a practical perspective, all these adjustments further increase the number of synthetic steps and the amount of both material and chemicals required to provide TiO_2 with the proper characteristics for a photocatalytic application. Consequentially, all these elements make more evident the necessity of tailoring the synthetic procedure to further improve the sustainability of the overall process.

1.3 Sustainability in the TiO_2 synthesis

1.3.1 Traditional large-scale synthesis strategies

On an industrial scale, TiO_2 production relies on the extraction from Ti-rich ores. A wide range of minerals fit into this classification, however only ilmenite and rutile ores are suitable for TiO_2 production. The two minerals show profound differences in their chemical compositions: ilmenite chemical formula is $FeTiO_3$ or $FeO{\cdot}TiO_2$, since the material includes a significant amount of both titanium dioxide and iron oxide, while rutile primarily consists of TiO_2. As a consequence of their composition, ilmenite contains between 40 and 60 % of TiO_2, while rutile is richer in the metal oxide, with a percentage of > 90%.[31] Being more abundant and less expensive, ilmenite is preferred to rutile as raw material for TiO_2 production; indeed, it accounts for 90% of global TiO_2 production.[32] In this context, two main methods are nowadays exploited for producing TiO_2 from mineral ores: sulfate and chloride processes.

In the sulfate process,[33–35] ilmenite raw mineral is digested with an excess of concentrated sulphuric acid (80-98 %) generally in the temperature range between 100 and 200 °C (Figure 1.6). Thanks to the high temperature, titanium is dissolved in the form of titanium sulfate (Eq. 1.9). The solid residue, known as ilmenite mud, is separated and the liquid phase, containing both Ti and Fe salts, is added with metallic iron to reduce Fe(III) to Fe(II), impeding its oxidation in the following steps. Thermal hydrolysis of the titanium precursor is carried out by heating the digestion mixture above 100 °C, which causes the formation of a gelatinous precipitate, consisting of hydrated titanium oxide $TiO_2{\cdot}H_2O$ and a significant amount of diluted H_2SO_4 (Eq. 1.10). To eliminate any residual acid, the precipitate is washed multiple times during the purification process. The hydrolysis product is then calcinated (Eq. 1.11): around 200–300 °C the dehydration of the hydrolysed material occurs until, at approximately 480°C, crystalline TiO_2 starts forming. The calcination temperature plays a crucial role in determining the final crystal phase: heating up to 750–850 °C favours the production of the anatase phase, while rutile phase is obtained at temperatures above 900 °C.

$$2H_2SO_4\,(aq) + FeTiO_3\,(s) \rightarrow TiOSO_4\,(aq) + H_2O\,(l) + FeSO_4\,(aq) \qquad 1.9$$

$$TiOSO_4\,(aq) + (n+1)\,H_2O\,(l) \rightarrow H_2SO_4\,(aq) + TiO_2 \cdot n\,H_2O\,(s) \qquad 1.10$$

$$TiO_2 \cdot n\,H_2O\,(s) \xrightarrow{\Delta} TiO_2\,(s) + n\,H_2O\,(l) \qquad 1.11$$

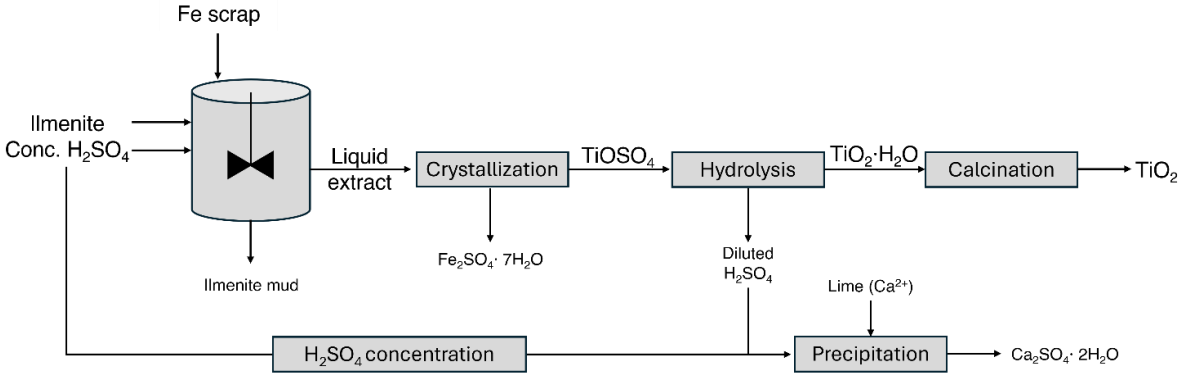

Figure 1.6: Scheme of the sulfate process extraction of TiO_2 from ilmenite ore

The chloride process represents the main alternative procedure, but it is less used since its efficiency is limited to higher-grade rutile ore (Figure 1.7). The chloride process[36,37] requires that the dry titanium ore material is heated to a temperature of 950 °C under a gaseous Cl_2 flux. The exothermic reaction is assisted by coke to favour the $TiCl_4$ production, consequentially forming carbon oxides and other chlorinated impurities as by-products (Eq. 1.12). Since the whole process takes place in the gaseous phase, volatile chloride impurities with higher molecular masses are removed through a condensation step, by cooling down the mixture. The final step requires the combustion of $TiCl_4$ with molecular oxygen, generally at temperatures around 1000 °C in order to maximise the oxidation yield (Eq. 1.13). Due to the high temperatures, the chloride process only produces TiO_2 in its rutile phase, while anatase is not formed.

$$2\,Cl_2\,(g) + TiO_2\,(s) + C\,(s) \rightarrow CO_x(g) + TiCl_4\,(g) \qquad 1.12$$

$$TiCl_4\,(g) + O_2\,(g) \rightarrow 2\,Cl_2(g) + TiO_2\,(s) \qquad 1.13$$

By comparing the two procedures, it is clear that the main advantage of the sulfate process is the possibility of obtaining TiO_2 in the anatase or rutile phase, depending on the calcination temperature. On the other hand, the chloride process guarantees the production of rutile TiO_2, but with a higher purity. Regarding the starting material and the process, the chloride strategy is more selective since requires TiO_2-rich ores, which are more expensive and rarely available.

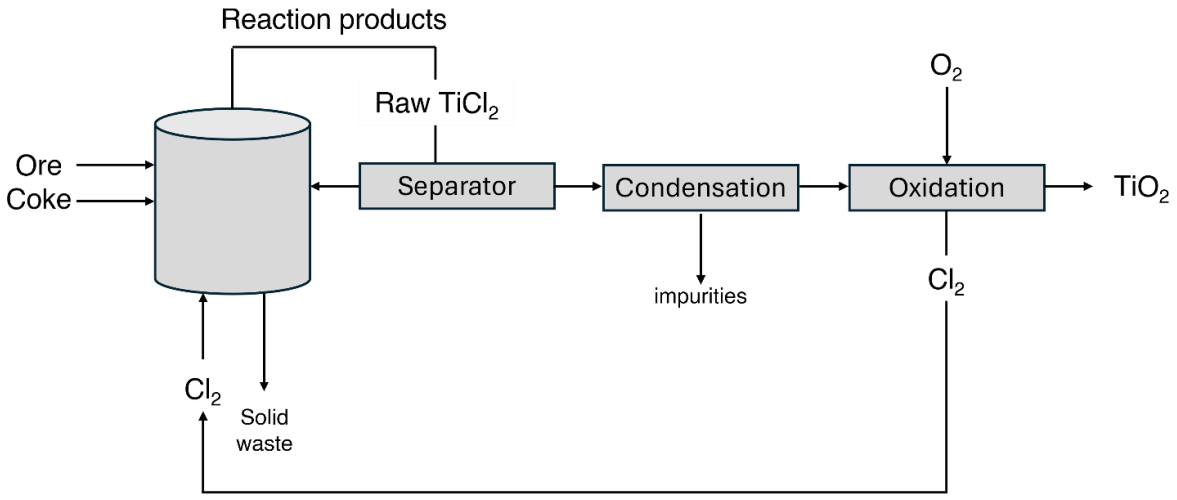

Figure 1.7: Scheme of the chloride process extraction of TiO_2 from rutile ores

Due to the high temperature and involvement of Cl_2 and $TiCl_4$, more complex and investment-requiring equipment is needed: the gasses involved are highly toxic and corrosive, meaning that a corrosion-resistant reactor and particular attention to safety measurements are needed. On the other hand, the sulfate process does not require an initial source with a high TiO_2 content, and the equipment required for the process is less expensive due to the lower temperatures and cheaper reactants involved; however, the concentrated H_2SO_4 causes the quick corrosion of the reactor that, indeed, requires frequently maintenance and replacements.

The main difference is related to the waste generated during the process. In the sulfate method, the hydrolysis step produces a huge volume of diluted sulphuric acid 20-22% contaminated with $FeSO_4$, $TiOSO_4$ and other sulfates. One option involves its concentration and reuse in the process, with additional energy expense, or it can be neutralized with limestone to produce gypsum $CaSO_4 \cdot 2H_2O$ and generally disposed into landfills.[38] On the other hand, the chloride gas by-products can be reused in the initial step of the chloride process, meaning that the waste generated is lower.[39] On the other hand, the production of one ton of titania using sulfate process generates approximately 8 tons of acidic water (around 20 wt. %) is produced.[38]

Several other strategies are known and applied on an industrial scale; however, they represent only secondary methods. An example is provided by the hydrochloride process where Ti is dissolved with concentrated HCl in the form of $TiOCl_2$, which is separated and hydrolysed at a mild temperature (100-180 °C).[40] Even basic

processes have been developed: the alkaline roasting process requires a treatment of titania with a molten strong base, like NaOH or KOH, at 500 °C for 1h to form titanate salt. These salts are dissolved in an acidic solution to form $TiO_2 \cdot nH_2O$ that is calcinated to obtain TiO_2.[41]

It is worth noticing that even P25, the gold standard for photocatalysis, is produced on an industrial scale, but no information about its synthesis is reported in literature. It is commonly accepted that it is produced through a flame spray pyrolysis, meaning that high temperature and consequently aggregation of the newly formed particles are involved.[20]

As demonstrated by all the processes proposed, the extraction of TiO_2 from ores requires the consumption of a high volume of chemicals, either acids or bases, and/or high energy consumption. All the procedures available are related to the production of wastes that require further treatment for safety and disposal reasons, which further increases the amount of chemicals involved. From a sustainability point of view, the industrial production of TiO_2 has a strong environmental impact and, by comparing the processes, the chloride is less impactful but the transition toward more efficient or greener procedures is always limited by their higher cost.

1.3.2 Controlled nanodimensional TiO_2 synthesis strategies

Once presented the classical strategies applied for TiO_2 synthesis on a large scale, the direct consequence is to investigate its production on a nanodimensional scale, with higher control over the final dimensions and properties. Figure 1.8 represents the main strategies for controlled TiO_2 NPs synthesis.

Commonly for several inorganic oxides, the most widely applied synthetic strategy is the sol-gel technique. This strategy is based on an inorganic polymerization reaction that proceeds through the hydrolysis and condensation of a Ti precursor.[42] The thermal precursor is generally a Ti alkoxides, with Ti-isopropoxide and Ti-tetrabutoxide being the most used, or halide. like $TiCl_4$. When in an aqueous or alcoholic solvent, the hydrolysis takes place by the nucleophilic substitution of the alkoxide or chloride groups with hydroxyl functionalities (Eq. 1.14).

$$Ti(OR)_4 + 4\,H_2O \rightarrow Ti(OH)_4 + 4\,ROH \qquad 1.14$$

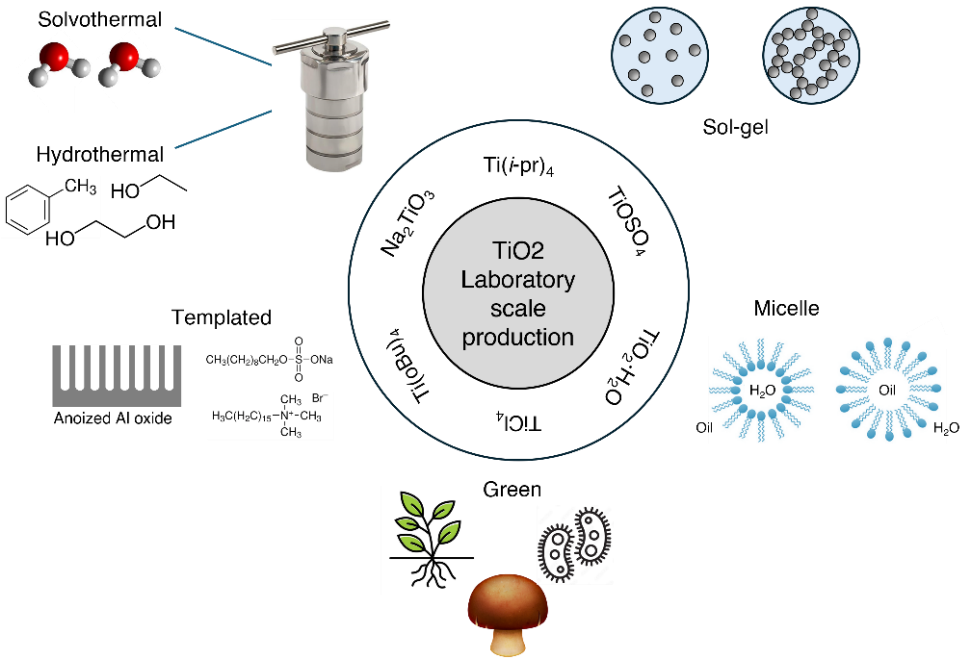

Figure 1.8: representation of the main laboratory-scale strategies for TiO_2 production in the liquid phase

Normally, an acid or a base is added to the solution to catalyse the reaction. At the same time as the hydrolysis reaction, the condensation step takes place (Eq. 1.15): the partially hydrolysed precursor interacts with another -OH bearing species or with an alkoxy group to form oxo-bridges between Ti nucleus with the removal of water or alcohol molecules, respectively.

$$Ti(OH)_4 + Ti(OH)_4 \rightarrow (OH)_3Ti - O - Ti(OH)_3 + H_2O \qquad 1.15$$

The sol-gel synthesis is the most versatile because, by controlling the experimental parameters like the concentration and nature of precursor, the nature of the solvent, pH of the solution, nature and concentration of additives (catalysts, surfactants, structure directing agents), pre- and post- treatment of the materials and ageing time, the morphology of the final product can be finely modulated.[43] Indeed, sol-gel synthesis allows the production of NPs with controlled dimensions and complex shapes like nanorods, nanobelts, nanowires or specific porosity.

The sol–gel process has the advantages of high purity, high uniformity, low synthesis temperature, and easy control of the reaction conditions. The preparation process of the sol–gel process is relatively simple and does not require special or expensive equipment. The problems of the sol–gel method are related to the large amount of

organic solvents required, the involvement of some toxic chemical compounds like NH_3, HCl or HNO_3, and the highly-cost, low stability in water and environmental impact of precursors. Despite the advantage of this strategy, to the extent of our knowledge, this is the only synthesis procedure that does not find application only on a laboratory-scale, but also industrially. However, TiO_2 NPs sol-gel synthesis is estimated to cover only 0.25 % of the global market and consumption.[44]

An alternative to the classic sol-gel technique is the microemulsion, which employs a thermodynamically stable solution of two immiscible liquids, generally stabilized by an interfacial surfactant. Two different strategies can be applied: oil-in-water[45] and water-in-oil[46] emulsions, which correspond to an aqueous and non-aqueous medium, respectively. In both cases, the procedure requires the preparation of two different emulsions containing, respectively, the Ti precursor and the precipitating agent. By mixing the two solutions, the coalescence of micelle put in contact the two reagents, inducing the formation of TiO_2. The micelles generated by the surfactant act as nano-dimensional reactors, limiting particle nucleation and growth. As a consequence, the particle size depends on the microcavities generated in the emulsion, which are affected by the surfactant and water relative concentration. The microemulsion approach is indeed effective for obtaining monodisperse NPs, with tailored size and shape, and the low temperature required reduces energy consumption. However, the NPs recovery and their separation from the reaction mixture still represent a crucial step, as well as the recovery and recycling of the organic solvent and surfactant.[47]

Another strategy is the hydrothermal[48] or solvothermal[49] treatment. In both cases, the reaction is carried out in autoclaves equipped with Teflon liners with temperatures generally lower than 200 °C and pressures below 100 bars. The main difference relies in the solvent: for hydrothermal the reaction proceeds in water, while for solvothermal organic solvents like methanol, 1,4-butanol and toluene. This technique allows mono-disperse and highly homogeneous NPs. By controlling the reaction parameters, like temperature, experimental duration, pressure, solvent, pH and starting precursor concentration the properties of the final product can be controlled. The main drawbacks involve the higher temperature required and, in the case of solvothermal, the organic solvent employed, which can be easily recovered.[50]

Particular attention has been also given to the synthesis of the anisotropic TiO_2 NPs.

A possible strategy is the hard templating method where rigid materials with specific shapes are used to define the properties of the final product. Mesoporous silica, anodized aluminium oxides, colloidal crystals or biotemplates has been widely used as supports for the synthesis of TiO_2 with different shapes and porosity. However, the main problem associated with this strategy is the recovery of TiO_2 from the template, making the procedure time-consuming and expensive. To overcome these problems, the soft-templating method involves block copolymers or surfactant molecules, generally in a classic sol-gel procedure. Thanks to their functional groups, organic molecules can interact with the progressively forming particles, directing their growth towards mesoporous or anisotropic particles. The final recovery is also facilitated by the fact that the templating agent can be thermally degraded, which represents also the main drawback: surfactants and polymers are continuously consumed. The hydrothermal procedure in acidic or basic conditions is also suitable for the synthesis of various types of TiO_2 shapes, but with longer reaction time and low size uniformity.[51–53]

Some recent advances have been made towards the sustainability of these processes. A widely explored topic is the utilization of natural plant extracts for the formation of TiO_2 NPs. Different parts of the plants can be used for this process like leaves, roots or bark, that thanks to their origin are safe, easily available, cost-effective and sustainable.[54] In addition, the extraction process is an easy procedure because it consists in the extraction of metabolites like alkaloids, proteins, polyphenols, flavonoids, terpenoids, carbohydrates and enzymes in water or ethanol, at temperatures not exceeding 100 °C due to their thermal instability. Various studies demonstrated that these extracted substances can then act as both reductants or capping agents to avoid aggregation and agglomeration during the formation of TiO_2 NPs. The properties of the final product strictly depend on the reaction conditions, namely the precursor nature and concentration, the precursor/extract ratio, temperature and pH. Commonly, the TiO_2 particles obtained have a spherical shape; however, due to the adsorption of the metabolites on the growing seed, they can also direct the synthesis towards the formation of anisotropic structures.[54–56] An alternative is represented by the biogenic synthesis of TiO_2. The utilization of microorganisms like bacteria, fungi, algae and yeast can be related to the extraction of metabolites, like the plant-based strategy. However, for all these organisms, synthesis can occur through

extra or intercellular processes. Normally the intercellular is more time-consuming because the product must be collected from the microorganism, while extracellular is faster and more efficient. Similarly to the plant-based strategy, the metal is first captured by microorganisms and confined inside or on the surface of the cells, where the high concentration of metabolites and enzymes are involved in their reduction and the consequent TiO_2 NP formation and growth. Once the material is formed, other microbial substances can anchor on its surface, acting as capping agents.[57–59] Both strategies guarantee an environmentally friendly procedure due to the green origin of the extracts/microorganisms, their low cost and low dangerousness; however, TiO_2 NPs produced have a broad size distribution and the procedure still requires Ti precursor for their synthesis.

To sum up, the laboratory scale strategies for TiO_2 NPs production guarantee a more sustainable alternative, compared to the industrial extraction from ores. The procedures commonly applied require lower temperatures and the use of fewer chemicals but, at the same time, some methods still involve moderately high temperatures or organic solvents.

1.3.3 TiO_2 from green resources

As depicted in the previous Paragraph, the strategies for nano-TiO_2 production certainly provide a more sustainable alternative, compared to the high energy and chemical-consuming industrial procedures. However, even these solutions require toxic and expensive precursors and, in some techniques, also the consumption of organic solvents or higher temperatures. An important alternative is represented by the utilization of waste materials as sources for TiO_2. In this optic, the TiO_2 production and application would rely in the circular economy framework, significantly reducing the environmental impact associated with the material.

1.3.3.1 TiO_2 extraction from Ti-rich waste materials

The direct extraction of TiO_2 from industrial waste material represents an interesting green solution, due to their high availability and low cost. Indeed, the environment

would also benefit from this strategy since the less amount of waste disposal would reduce the emission of toxic metals and substances. In this context, the focus of academic and industrial research has been directed towards this topic in the last few years.

Several studies have focused on the recovery of Ti from blast furnace slag (BFS), a by-product of the iron production industry. Briefly, iron is produced by the reduction of iron oxide-rich ores in a blast furnace, in the presence of a flux of limestone or dolomite and with coke as reducing agent; the reaction requires high temperature, normally between 1400-1600 °C. In these conditions, while the melted iron remains on the bottom, the slag stays on the surface and is progressively removed from the reactor.[60] Being a by-product of industrial production, its composition can significantly vary depending on the operative condition and the initial iron ore properties, while the crystalline features are strictly defined by the colling process.[61] Commonly, Ti-rich BFS contains around 20 % of TiO_2, mixed with common natural elements like CaO, Al_2O_3, MgO, SiO_2 and Fe_2O_3 in different proportions. Thanks to the high SiO_2 and CaO content, the most available route for its utilization without any further treatment is in the production of cementitious materials; however, an excessive amount of TiO_2 limits its application and efficiency in such field. For this reason, the material is directly disposed into landfills, with serious risks for the environment and the loss of a potential Ti source. It must be considered that just in China, 5 million tons of BFS is produced annually and only 3 % is actually reutilized[62]; therefore, the effective recovery of TiO_2 represents the perfect solution.

Currently, several procedures have been developed for an efficient TiO_2 extraction from BFS (Figure 1.9). A common extraction strategy is represented by acid leaching, mainly by H_2SO_4 or HCl treatments, followed by a separation of the desired product by exploiting solubility differences. In the sulfuric acid leaching, all the components are solubilized in their sulfate salts, such as $TiOSO_4$, $Al_2(SO_4)_3$, $MgSO_4$, $FeSO_4$ and $Fe_2(SO_4)_3$, except for $CaSO_4$, which is insoluble in water. In the hydrochloride leaching, the formation of the respective chloride salts is involved. In both cases, the following step consists of a hydrolysis to collect $TiO_2 \cdot H_2O$ or TiO_2, respectively.[63] Similar to the sulfuric acid leaching, the sulfate intermediates are obtained through a thermal treatment of BFS with the $(NH_4)_2SO_4$ process. TiO_2 in the form of $TiOSO_4$ is converted into $TiO_2 \cdot H_2O$ with ammonia and then calcinated to TiO_2.[64] The alkali roasting

resembles the previous method; it consists in the calcination of BFS with NaOH or Na_2CO_3 to produce the metal oxide sodium salt of each constituent element. Al and Si elements are converted into the soluble $NaAlO_3$ and Na_2SiO_3, which can be eliminated, while the newly formed Na_2TiO_3 intermediate can be extracted by acidic solubilization, separating it from the other solid impurities.[65]

In addition to the procedure presented, some more chemically refined procedures are available. An example is represented by the carbonization-chlorination TiO_2 extraction process: Ti is thermally treated in the presence of a carbon compound to produce TiC. Generally, the temperature range is 1400-1650 °C in order to avoid the reaction of the other oxides with carbon. The following chlorination step, carried out in the presence of Cl_2, provides $TiCl_4$ as the final product.[66] An alternative is represented by the recrystallization-enrichment strategy that consists in the concentration of dispersed titanium into a designated crystalline phase, mainly perovskite and anosovite, which are already included in the waste material, but also rutile. The procedure requires the melting of the waste slag, followed by the cooling down in a specific temperature range in order to favour the formation of the desired phase.[67,68] In this step, temperature and the atmosphere composition must be finely controlled to obtain the selected product. The addition of specific reagents in the initial slag further favours the formation of a specific crystalline phase: Cr(III), Ca, Mn(II) or Fe(III) oxides promote perovskite formation, Zr(II), Al(III) or P(V) oxides are optimal for rutile, while B(III) oxide is favourable for both rutile and anosovite.[63]

In the literature, BFS is the most investigated waste material when it comes to the extraction of TiO_2; however, the content of TiO_2 is extremely low. Consequentially, in the last decade, the focus shifted to more Ti-rich waste materials: selective catalytic reduction catalysts (SCRC). This type of catalyst is involved in the reduction of NO_x species into harmless N_2 in all processes involving the combustion of fossil fuels, especially in carbon-fired machines. NO_x species are known for being an air pollutant, dangerous for both the environment and human health, so its removal is fundamental.[69]In industrial applications, SCRC are commonly made up of TiO_2 anatase as support, V_2O_5 is the active component and WO_3 is the catalytic promoter. Other components can be included like SiO_2 and Al_2O_3 along with other doping elements to further increase the efficiency.[70] However, at the high temperature requested by the process (300-400 °C), this type of catalyst is easily deactivated both

by physical factors, due to the deposition of fly ash, ammonium and sulfate salts, and chemical factors, namely poisoning by H_2O, HCl, SO_2, alkali/alkaline-heart and heavy metals poisoning (As and Pb) or by the catalyst sintering.[71]

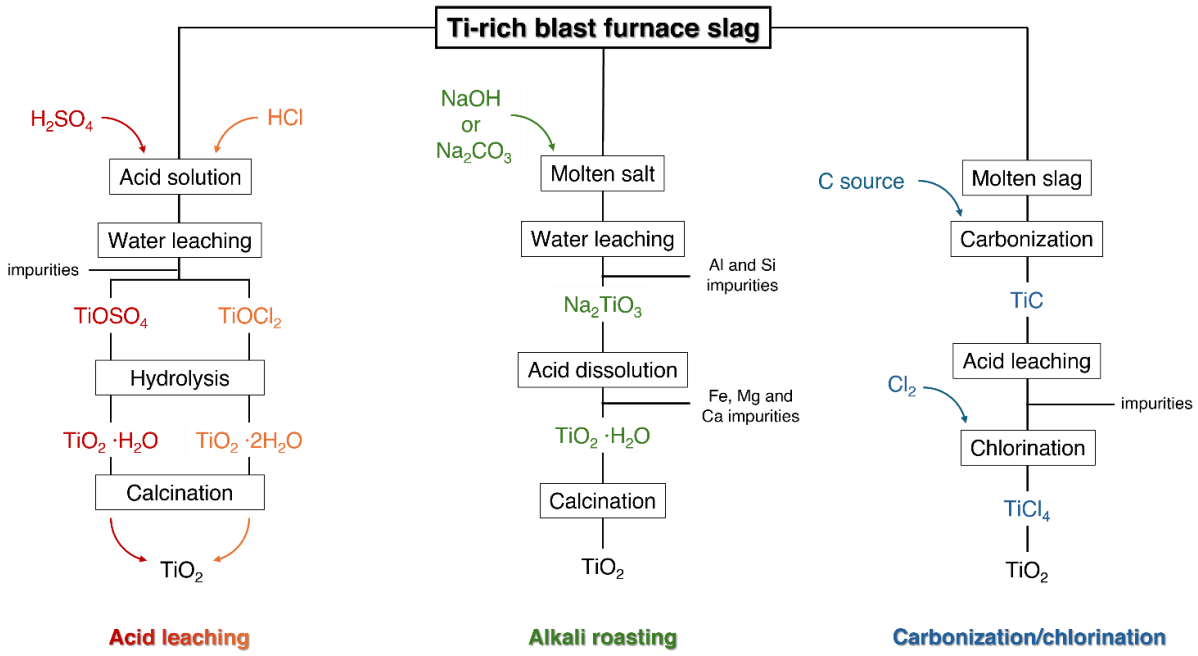

Figure 1.9: Process flow for the acid leaching, alkali roasting and carbonization/chlorination extraction of TiO_2 from BFS

As a consequence, the accumulation of exhausted SCRC is an increasing problem, mainly due to the inclusion of huge amounts of metals that make the spent catalyst extremely toxic and dangerous for both soil and water bodies. On the other hand, this same problem is actually the reason for the main interest towards this type of waste: all the elements listed could be potentially extracted and reutilized, as requested by a circular economy. In addition, the higher volume production of spent SRCRs, equal to 300000 million tons per year in China,[72] and the higher TiO_2 content of the waste, between 65-85% of its composition, makes the material more interesting than BFS, where the recoverable TiO_2 is only 20%.

In this frame, the procedures applied are similar to the one described for BFS; however, some corrections have to be made considering the profound difference in the composition and, hence, in the impurities to remove. Indeed, often the procedure applied is not directed towards the extraction of TiO_2, but to the recovery of more valuable W and V; however, even in this case, the by-product is a material extremely rich in TiO_2 and with low impurities.

Up to now, the main recovery methods for spent SCRC are the acid or basic leaching or the roasting procedure. For TiO_2 production, alkaline leaching[73] or roasting[74] involving NaOH or Na_2CO_3 are the most efficient procedure. The basic treatment converts both V and W into their respective sodium compound, $NaVO_3$ and Na_2WO_4, which are soluble and can be easily separated from the insoluble Na_2TiO_3.[75] On the other side, acid leaching is more efficient in dissolving and extracting V_2O_5 as VO^{2+} from the waste material, since TiO_2 and WO_3 have a low solubility in the acid.[76] An alternative is represented by the use of oxalic acid, which combines the acidic properties with the ability of oxalate anion to complex metal cations. The strategy is suitable for removing Fe, but most of all V from the spent catalyst.[77]

The strategies available highlight that a single treatment is generally not enough for extracting TiO_2 due to two reasons: i) some of the procedures are directed towards the extraction of a specific component, e.g. V, and ii) the efficiency of the others does not allow to obtain high purity TiO_2. For these reasons, most of the actual extraction processes consist of a combination of the aforementioned procedures, with particular attention to the alkali roasting procedure due to its efficiency in removing TiO_2.

For example, Zhang *et al.*[78] proposed a process consisting of a first NaOH roasting to convert TiO_2 to Na_2TiO_3 at the optimised condition of 550 °C for 10 min, obtaining a Ti extraction > 98%. After being separating filtration from insoluble impurities, sodium metatitanate was subjected to an acidic extraction, to complete the removal of impurities, followed by a hydrothermal treatment at 180°C for 1 h to produce high purity TiO_2, with a metal oxide content > 99%. In addition, by using HCl 1 M for the acid leaching, the final product consists of rod-shaped rutile particles. A schematic representation of the extraction process, along with the photocatalytic results provided by the extracted TiO_2 are reported in Figure 1.10.

A similar procedure was proposed by Ma et al[79]: involving a first Na_2CO_3 roasting step to dissolve TiO_2 in the spent SCRC as $Na_2Ti_3O_7$, which was extracted by an acidic leaching with an efficiency of 97.5%. After adjusting the pH of the acidic purified solution to a neutral value, the solid component was separated and calcinated at 600 °C for 3h to obtain high-purity crystalline TiO_2.

The procedure proposed shows that the combination of multiple strategies is efficient in increasing the extraction yield and final product purity, but the impact on

sustainability is significant. However, an added value of SCRC compared to BFS, is the high content of valuable elements like W, which have a potential application in photocatalysis; therefore, tailoring the extraction procedure could have some benefits. This is demonstrated by Zhang *et al.*[80]: spent SCRC was first treated with H_2SO_4 and Na_2SO_3, to selectively remove V, and then dissolved through an HF digestion to solubilize the remaining components. The solution, rich in Ti and W, underwent a hydrothermal treatment obtaining WO_3-TiO_2 as the final product, in the form of squared-shaped bidimensional NPs. Photocatalytic test on the material showed a methyl orange degradation efficiency comparable to P25, under UV irradiation.

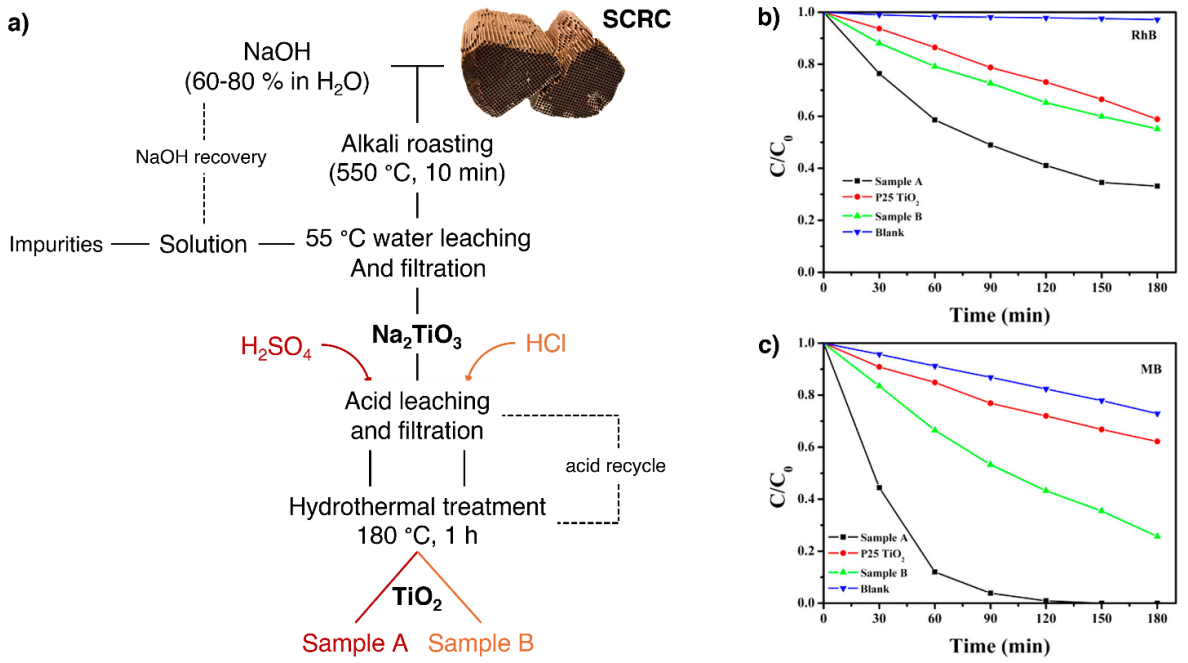

Figure 1.10: a) extraction process of TiO_2 from SCRC and b) photocatalytic results for rhodamine-B (RhB) and methylene blue (MB) obtained with the extracted TiO_2. Adapted from [78].

Finally, the extraction of TiO_2 from red mud was investigated. Red mud is a solid waste generated during the extraction process of Al from bauxite ores. Due to the high metal content and strong alkaline pH, the material is difficult to transport and its disposal is extremely expensive due to the neutralization required. Some attempts to recover TiO_2 have been made in the last decade, mainly by acid leaching[81] or reductive roasting.[82] However, despite this type of waste is produced in large quantities, approximately 90 million tons per year worldwide, the TiO_2 content is less than 15% and the high content of other components, like Fe (30-45%) and alumina (15-20%) make the extraction more chemical demanding.[83]

Here, several strategies to recover TiO_2 from waste materials have been presented. It is clear that all these processes do not utilize raw chemicals, like Ti alkoxides or chloride, to produce TiO_2 and their role in giving a higher value to waste materials is pivotal. Indeed, reducing the amount of waste disposed in landfills as well as the hazards related to them is of inestimable value. However, a critical analysis of all the processes must be done. All the strategies proposed in the literature have some non-negligible drawbacks: in some cases, high treatment temperatures are required with consequential high energy consumption. Procedures requiring concentrated acid or basic treatment demand additional chemicals and, moreover, they can involve strong changes in the solution pH, which is responsible for a large amount of acid and alkali consumption. In addition, such strong conditions cause the corrosion of the equipment, especially if the treatment is conducted under high temperatures.

Considering the above-mentioned, a careful evaluation of the actual sustainability of the TiO_2 extraction from wastes is fundamental. Particular attention should be directed towards the actual advantage of recovering TiO_2 in terms of chemicals and energy consumption, compared to the direct synthesis with procedures presented in the previous paragraph. The problem is even more significant considering the low amount of TiO_2 content of some wastes, such as BFS with a 20% TiO_2 content.

To sum up, the question arising from this overview is: is it actually worth it to extract TiO_2 from waste materials?

1.3.3.2 Direct application of Ti-rich waste materials

Due to the limitations of the extraction of TiO_2 from waste material, a potential alternative could be represented by the direct utilization of TiO_2-rich waste materials for photocatalytic applications.[84]

Focusing on SCRCs, direct reutilization is not a focal topic for both academic and industrial research since the waste composition makes it suitable for photocatalytic applications. In addition, the catalyst is considered “deactivated” with a 30-40% decrease in its activity, meaning that 60-70% of the catalyst activity is retained.[85] The effective reuse of spent SCRCs for photocatalytic application is indeed demonstrated by Ma *et al.*[86]: after a grinding and ball-milling procedure, the waste material proved

effective in degrading rhodamine B, methyl orange and tetracycline under UV irradiation, with a degradation efficiency for rhodamine B comparable to P25.

Contrarily, BFS composition and origin do not ensure an effective photocatalytic applicability of the material, which therefore has been investigated. A virtuous example of this strategy was provided by Zhang *et al*.[87] by using BFS with a 19.5% TiO_2 content for the conversion of NO into NH_3 under a 500 W Xe lamp irradiation. Unfortunately, the results show a completely null photoactivity of the titanium slag towards the selected reaction. For this reason, the authors proposed a modification procedure involving a MnO_2 doping at 1500°C for 1 h, a treatment with Na_2CO_3 in the same conditions and, finally, a leaching step with concentrated HCl. The photocatalytic activity has a net increase in efficiency, at the expense of a higher energy and chemical consumption.

A similar approach was applied by Lü *et al.*[88] on a BFS with an analogous composition and loaded with a 0.6 wt. % Pt co-catalyst by photodeposition. By evaluating the activity for the production of H_2 from an aqueous methanol solution under a 300 W Xe lamp, they obtained a negligible efficiency, with a H_2 evolution rate of 1.54 μmol h^{-1} g^{-1}. Even in this case, a $NaNO_3$ roasting at 1250 °C for 2 h followed by an HCl leaching increased the TiO_2 content in the slag, with a rise of almost 10 times in the H_2 evolution rate.

All these approaches suggest that the application of BFS in photocatalytic applications is not feasible without further treatments. However, promising results are provided by Song *et al.*[89] that utilized a BFS with 21.5 wt. % of TiO_2 for the degradation of tetracycline under visible light irradiation (400 W Xe lamp with a 420 nm cut-off filter). Indeed, the samples demonstrated a significant activity, with around 30 % of pollutant degraded in 60 min. Even in this work, the material was further modified through a thermal treatment with $(NH_4)_2SO_4$ at 450 °C for 1 h, followed by a basic leaching to improve the catalyst composition and photocatalytic efficiency.

According to the procedures reported in literature, the application of TiO_2-rich waste materials does not provide a sufficient photocatalytic yield to substitute the currently available technologies. However, when dealing with waste materials, it is common to find several procedures to improve the material composition, especially in terms of TiO_2 content, to consequentially enhance the photocatalytic activity. Most of these

procedures resemble the ones described for the TiO_2 extraction, since they combine roasting processes, thermal treatments and acidic or alkaline leaching treatments.[90–92] Therefore, the sustainability of the waste material is to a certain extent deteriorated due to the high chemical and energy consumption. However, some recent studies on the reusability of BFS shed light on some more bland chemical treatments, useful to improve the applicability of the material.

Song *et al.*[93] proposed a mild acidic treatment of BFS with HCl at 100 °C for 24 h, followed by testing its photocatalytic degradation of a 50 ppm tetracycline solution under UV irradiation. While the pristine slag provided a 60 % degradation and 30 % mineralization, after the chemical treatment, the removal yield for tetracycline and the total organic carbon were 90 % and 72 % respectively. Similarly, Ma *et al.*[94] treated BFS initially with a 0.5 mol L^{-1} HCl solution at 55 °C for 1h and secondly with a 0.5 mol L^{-1} NaOH solution in the same conditions (Figure 1.11). All the materials were tested in the degradation of volatile toluene under visible light irradiation (300 W Xe lamp with 420 nm cut-off filter). By comparing the three different samples, the best performances were observed for the acidic treated sample, with a gaseous toluene removal efficiency of 85 % in 3 h, guaranteeing almost three times increase in the yield compared to the raw slag.

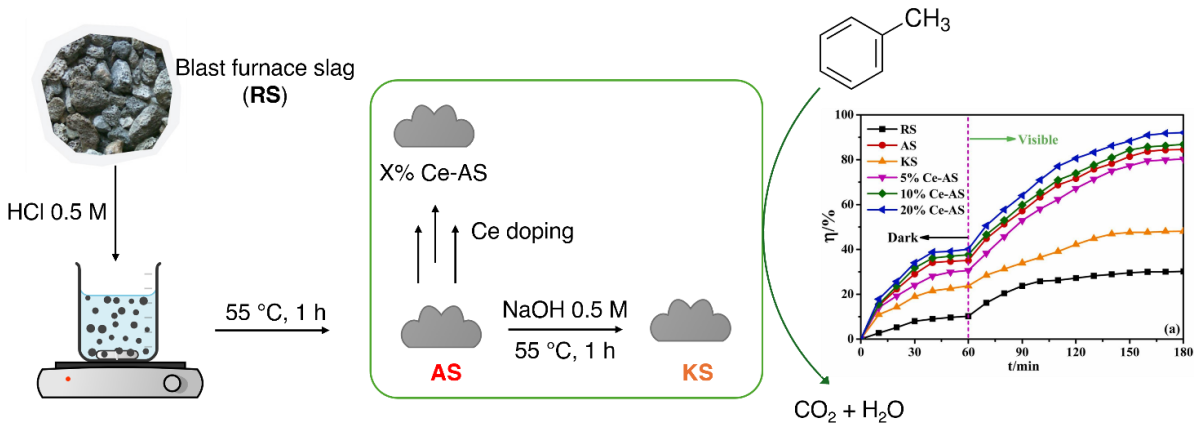

Figure 1.11: modification of BFS with mild chemical processes and photocatalytic results of the obtained products in the degradation of gaseous toluene. Adapted from [94]

These examples support the possibility of exploiting waste materials for photocatalytic applications by using mild conditions. By reducing the chemical and energetic impact of the post-production treatments, the sustainability of the material can be efficiently valorised and their introduction in a circular economy system is confirmed.

Unfortunately, the application of such strategy is really limited, and few literature examples are available on this topic. For this reason, further efforts should be directed towards the development of methodologies for adding practical value to wastes. Extending the class of materials involved in the investigation is also a crucial point. Since TiO_2 is widely used in everyday life, several waste materials could be directly used in more valuable applications. For example, rising interest is directed towards the exploitation of a new TiO_2-rich waste material obtained from TiO_2 industrial production, sometimes known as tionite (more details in Chapter 2).[95–97] For example, tionite has been re-used in the production of cementitious material[98]. However, scarce information is available on its potential photocatalytic application.

1.4 Sustainability in TiO_2 applications

The necessity to improve the sustainability in the synthesis and production of TiO_2 to reduce the environmental impact and the consumption of chemicals and energy is a critical issue, as demonstrated in Paragraph 1.1.3. However, the same attention should be also paid to the application of the material for catalytic purposes. In this frame, photocatalysis represents a greener alternative in synthesis or degradation reactions due to several aspects: i) the definition of catalyst is itself a certification of sustainability, mainly for their reusability and reduced energy consumption and ii) the procedure does not require additional chemicals. On the other hand, the material application has some limitations, like the rapid charge carrier recombination and the low adsorption of organic pollutants on TiO_2 surface that limit and slow down its photoactivity.[99] Therefore, these examples demonstrate that improving the material from the manufacturing point of view is not enough to solve the sustainability problem, but even increasing at maximum the efficiency and eco-sustainability of its application is required. In this context, the exploration of new materials, architectures and hybrid assemblies, as well as advancements in the nano-scale morphology have raised considerably the potentiality and efficiency achievable with photocatalysis.[100,101] Among the solutions investigated, the immobilization of TiO_2 NPs and the newly developed photothermo catalysis represent two solutions with great potential in overcoming the efficiency and sustainability drawbacks related to TiO_2.

1.4.1 Immobilization of Nano-TiO_2

The photodegradation of pollutants is frequently performed by operating in an aqueous system, where the catalyst NPs are well dispersed. Due to the NPs stability in water and their limited dimensions, their recovery from the slurry can be very difficult and can require expensive separation procedures with long recovery time and potential loss of material. In addition, TiO_2 NPs dispersion in the environment may be dangerous for human and animal health due to the potential inflammatory and cytotoxic effects caused by its accumulation in the organism, through oral exposure or inhalation.[102]

It's also important to consider that the high surface energy of nanodimensional particles leads to their aggregation with a consequential decrease in the exposed surface area. As a result, the amount of target molecule adsorbed on the surface and the efficient exploitation of light for the photocatalytic process are hindered by this phenomenon.[103] Both the problems observed are significantly detrimental to the sustainability of the process. In the first place, the advantage of using a catalyst is that it is not consumed during the reaction, and it can potentially be reused for several cycles, but the difficulties in its recovery lead to a use and disposal pathway. On the other hand, the sustainability of the catalytic process is also favoured by a higher efficiency of the catalyst.

A strategy to overcome these problems is to immobilize TiO_2 NPs on a support. The advantages of this solution are hindering NPs aggregation and making them more easily recoverable, with a consequential reduction in the procedure cost and time, especially for large-scale applications, and minimization of catalyst loss. Choosing a proper support is the key point because it has to provide a strong affinity with the photocatalyst for stable anchoring and avoid leaching effects, it must have a high surface area and be resistant to long-term operations and to the reactive oxygen species generated during the process.[104]

The utilisation of adsorbent supports is a strategic choice. Firstly, the application of the adsorption technique in wastewater treatment is of increasing interest because it provides an efficient, inexpensive and safe option for the removal of heavy metal cations.[105] The combination of a photocatalyst and an adsorbent, known as integrated photocatalyst adsorbent, has the advantage of combining an adsorbent material capable of also degrading toxic organic molecules when irradiated with light.[105]

Moreover, a synergic combination is beneficial for catalytic performances: adsorbent centres bring organic pollutants close to TiO_2 photoactive sites, improving the degradation efficiency and capacity of the system.[106,107] Supports consisting in polymers have been investigated due to their low cost, availability and for being chemically inert and mechanically stable. Despite the sustainability lacking can be overcome by using biodegradable or naturally occurring polymers, their poor thermal resistance and instability under irradiation, make their application problematic.[108] An interesting class of supports are carbon-based materials, namely activated carbon, graphene, graphene oxide and carbon nanotubes, which are particularly appreciated for their high surface area and porosity. In this context, the work of Sanches *et al.*[109] highlighted the benefits of combining TiO_2 NPs with different amounts of activated carbon in the photocatalytic degradation of paracetamol. The pollutant removal efficiency benefits from the increasing amount of adsorbent materials included in the sample, demonstrating that an increased concentration of pollutant adsorbed close to the photocatalyst is beneficial for its removal. In addition, they also assessed that the improved photocatalytic properties can be associated to the reduction in the charge carriers recombination rate. Indeed, It is reported in literature that photogenerated electrons are trapped by carbon-based material when TiO_2 is immobilized on them, resulting in an increased electron-hole pair separation, which significantly improves the photocatalytic efficiency.[110] The utilization of this type of support has some drawbacks, mainly related to their dark colour and the consequential interferences with the adsorption of light.[111]

On the other hand, ceramic materials, like oxides, have gained increasing relevance due to their low cost, high stability to both chemicals and high temperature and especially for their porosity.[112] A remarkable example is provided by Crippa *et al.*[113] who reported an innovative sol–gel synthesis to produce photoactive anatase TiO_2 nanocrystals, with tailored structural and morphological features, anchored onto a macroporous silica support. The material showed efficiency similar to those of the unsupported oxide in the photodegradation of selected pharmaceuticals. The authors related the interesting performance of the material to the porosity of silica support: being the structure highly accessible to the pollutant molecules, the enrichment of their density at the catalytic active sites can occur. Moreover, the peculiar porous structure of silica or silica-based materials, such as clays, enables the formation of minicages

where the catalyst is confined and operates, preserving from annihilation the short-living radical intermediates involved in the photodegradation mechanism.[114]

This benefit is not only observed in the aqueous phase; indeed similar results were also observed in the gas phase.[115–117] For example, Mo *et al.*[118] studied the degradation of toluene in the gas phase using P25 supported on different supports. The authors highlighted that using SiO_2 or Mordenite, a zeolite, as a matrix for TiO_2 better photocatalytic efficiencies are observed compared to bare P25. The reason for this behaviour was attributed to the adsorption of the pollutant by the support and its higher concentration around the photocatalyst, as reported in previous examples, but also for gas applications.

1.4.2 Photothermo catalysis

Up to now, thermal- and photo- excitations represent the two main approaches to overcome the activation energy barrier. The role of photocatalyst relies on creating a new reaction pathway that leads to the same reaction products through a new and less energetic transition state, while temperature increases molecules kinetic energy, leading to more frequent and energetic collisions able to surpass the activation energy barrier. However, both strategies have their limitation. While for photocatalysis the disadvantages have been extensively described in the chapter, thermo-catalysis problems are: i) the extreme temperature and pressure required, ii) catalyst deactivation due to coking, inhibitor poisons and changes in its physic and chemical properties and iii) the low selectivity in the reaction that generates dangerous by-products.[119–122]

The necessity of decreasing the environmental and energetic impact makes the development of new strategies a pivotal step towards more efficient and sustainable catalytic processes. The objective is to achieve comparable production yields at lower temperatures and pressures or, ideally, under less impactful conditions. Due to the application of milder and less favourable conditions, accelerating the reaction rates to increase the production yield and shorten the processing time is fundamental. Furthermore, enhancing the reaction selectivity while minimizing by-product formation is another vital request for a more environmentally friendly approach. These

improvements not only contribute to sustainability, but also extend the lifetime of the catalyst and drastically reduce its potential deactivation.

An ideal solution involves coupling both catalytic processes by simultaneously photonic and thermal stimulation in a light-assisted thermocatalytic reaction, to exploit the potential benefits of this synergic system in several catalytic applications.[123][124] It is indeed possible to distinguish several synergistic effects under dual excitation[125]: i) photons facilitate the reaction by allowing it to proceed through a lower-energy transition state, while thermal excitation affects the rate-determining step of the dark type, leading to an activation energy reduction; ii) photon-excitation alters the surface interaction with reagents and intermediates, increasing the rate due to a higher influx of reactants on the catalyst surface; iii) synergic effect, the most investigated in literature, involves a non-radiative relaxation: some materials can convert photons into thermal energy via non-radiative recombination of the charge carriers. The additional localized heating generated by the photothermal effect, exposes the catalyst to a higher temperature than the bulk temperature, allowing to reduce the external energy supply.

Photothermal effect can be activated by irradiating the surface plasmon resonance adsorption band of metal NPs particles. According to the theories of Gustav Mie[126] and Drude-Maxwel[127], inside metal NPs conducting free metal electrons can oscillate when subjected to the electromagnetic field of an external photon flux.[128] This collective oscillation of electrons is known as surface plasmon and its frequency is typically described by Eq. 1.16.

$$\omega_P = \sqrt{\frac{Ne^2}{\varepsilon_0 m^*}} \tag{1.16}$$

where N and m* are the density and effective mass of the charge carriers, respectively, *e* is the electron charge and ε_0 is the electric permittivity. Due to spatial confinement, the incident wavelength is larger than the NP size and all electrons are subjected to the same electromagnetic field. When the incident electromagnetic field and the electron cloud oscillate at the same frequency, strong electric fields are generated on the surface of plasmonic NPs, known as hot-spots (Figure 1.12).[129] The energy stored in surface plasmons can be released through a radiative decay, in the form of photons

with the resonance wavelength. Alternatively, non-radiative decay can occur through electron-electron collisions or the adsorption of plasmon energy by the metal NP generating hot electron-hole pairs.[130] Hot carriers can be transferred from the metal NP to another species or they can recombine, dissipating the plasmon energy in the form of lattice phonons.[131,132]

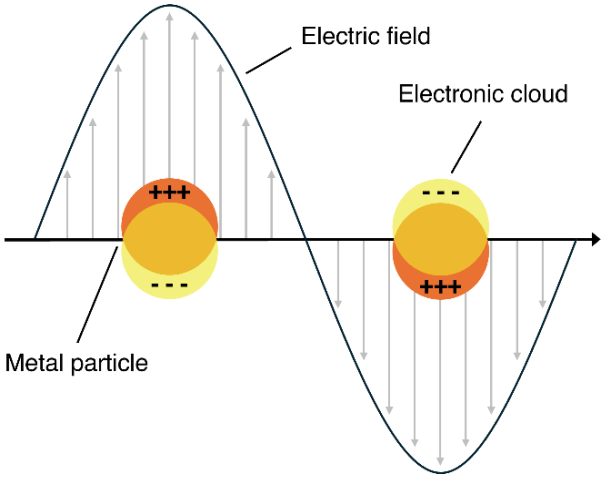

Figure 1.12: coherent localized oscillation of the electron density under the influence of an external electric field on plasmonic metal NP

The localized surface plasmon resonance (LSPR) phenomena can be observed in conductive materials, like Au, Ag, Cu and the adsorption wavelength can be easily tuned in the visible and near-IR (NIR) region by tailoring their size,[133] shape[134] and composition.[135] In addition, for a single spherical metal NPs, the local photothermal temperature increase (ΔT) can be enhanced by modulating the NP size (R_{NP}),[136] according to Eq. 1.17

$$\Delta T \propto R_{NP}^2 \qquad (1.17)$$

As already mentioned, the hot charge carriers generated by plasmonic resonance can recombine in a non-radiative process (Figure 1.13a), but they can also be transferred to other species with electron-accepting orbitals, such as adsorbate and semiconductors.[137,138]

Reactants can be adsorbed on the metallic surface and the electron transfer from the metal to the lowest-unoccupied molecular orbital (LUMO) can occur via a direct or indirect electron transfer (Figure 1.13b). The direct mechanism is a two-step process:

first, the hot electrons are promoted in the metal NP and then they are transferred to the LUMO of the adsorbate. On the other hand, when a hybridization between the excited surface plasmons and the unoccupied adsorbate states occurs, hot electrons are directly generated into the LUMO of the adsorbed molecules. The single-step transfer is more efficient and less energy is lost in the process; however, the orbital hybridization requires a strong interaction between the two components, which is not that common. In both cases, the electron transfer to antibonding orbitals of adsorbed molecules results in the weakening or breakage of molecular bonds, inducing their chemical transformation. In addition, hot electrons in the adsorbate electronic state can undergo also a thermalization process.[139–141]

Plasmonic materials are generally not used on their own; indeed, inorganic oxide semiconductors are commonly involved in catalyst formulations with a supporting role. Materials like TiO_2, ZnO or CeO_2 are known for being activated by UV light for photocatalytic application, but they can also act as supports and stabilizers of noble metal NPs like Ag, Pt and Au, as well as less noble metals like Ni, Co, Cu and Fe. The formation of a metal-semiconductor junction causes the alignment of their Fermi level, distorting both valence and conduction bands. The metal-semiconductor interface forms a Schottky barrier, whose energy (φ_S) is equal to the difference in the work functions of metal and semiconductor.[142]

In this context, the electron transfer can occur only when its energy content is higher than φ_S. Under this condition, the photo-excited hot electron is transferred from the metal to the conduction band of the semiconductor through a direct or indirect mechanism (Figure 1.13c).[143] The φ_S assumes a pivotal role in defining the electron transfer efficiency: a lower value guarantees the transfer of a larger number of hot electrons, but its value must be high enough to hinder the back-transfer of electrons to the metal NPs and their recombination. Since the Schottky barrier is defined by the intrinsic electronic structure of both metal and semiconductor, its value can be easily tailored by choosing the right combination.[129,144] The metal-semiconductor electron transfer has several advantages: i) the promotion of the electron to the semiconductor promotes the charge carriers spatial separation, preventing their recombination and increasing the electron lifetime and availability for chemical reactions and ii) metal NPs generally require Vis or IR light to form hot carries, therefore the semiconductor activity is not strictly related to UV light.[132]

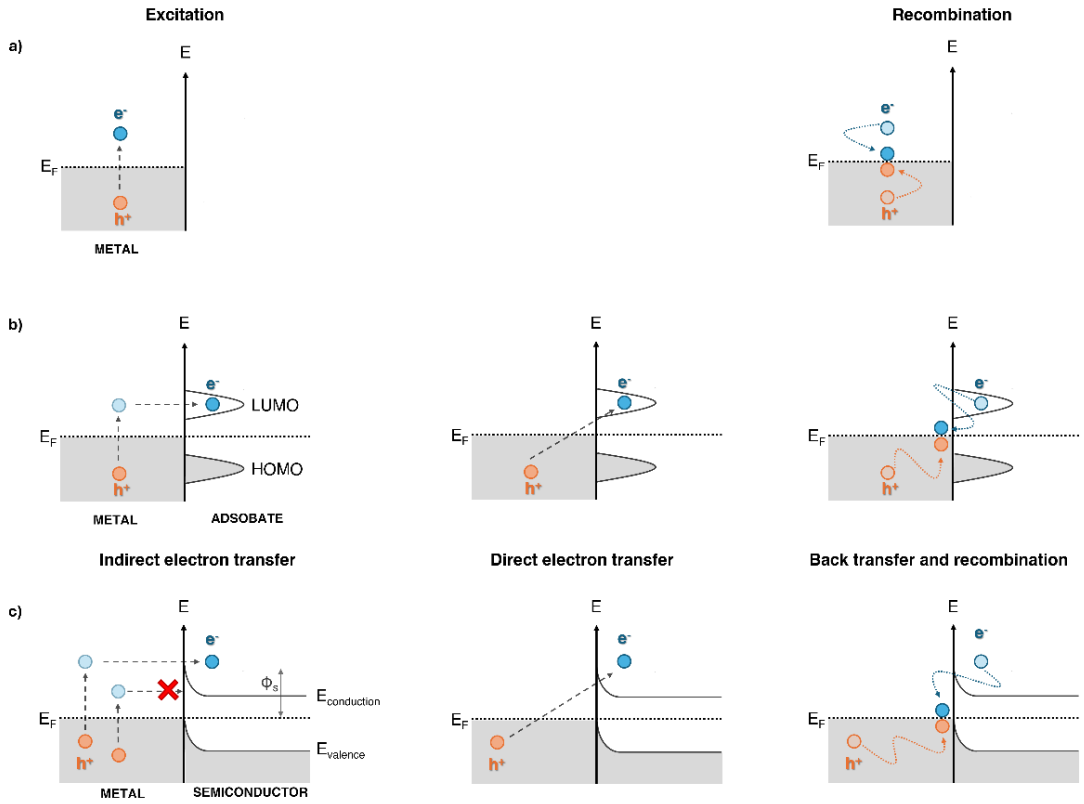

Figure 1.13: hot carrier generation via plasmon-induced process and transfer/thermalization of hot electron in a) clean metal, b) metal/adsorbate and c) metal/semiconductor. For each scheme, the left side represents the Fermi level (Ef) for plasmonic metal NP; the right side depicts the HOMO/LUMO molecular orbitals of the adsorbate (b) or the valence and conduction band of the semiconductor. Grey areas indicate the population of electronic states, Figures based on [129]

More recently, further investigation on the LSPR showed that other materials can exploit this phenomenon. Metal chalcogenides and nitride show plasmonic properties induced by high levels of structural defects in their structure[145] Alternatively, the plasmonic effect in WO_{3-x} and MoO_{3-x} metal oxides is due to the high number of oxygen vacancies in their lattice.[146] Similarly, highly doped semiconductors, like Sn-doped In_2O_3, show a strong LSPR due to the charge carriers introduced by the doping procedure.[147]

It must be noted that photothermal effect is not strictly related to LSPR and metal NPs; indeed materials like bidimensional MXenes[148] and metal-organic frameworks[149] showed this property. In addition, Sarina *et al.*[150] demonstrated that non-plasmonic metal NPs, namely Pd, Pt, Rh and Ir, provide a photothermo enhancement by transferring hot electrons from the metal to the LUMO of the adsorbed molecules.
Metal oxide non-plasmonic semiconductors can be involved in photothermal heating generation. Once reached the charge separation, photo-excited electron in the

conduction band can relax to the lower energy state through a non-radiative process, specifically through Auger and Schockley-Read-Hall recombination mechanisms[151], producing heat.

Finally, thermal vibrations in molecules are also responsible for local heating through a non-radiative relaxation of photoexcited electrons from the highest occupied molecular orbital (HOMO) to the LUMO belonging to the molecule. This phenomenon is observed for carbon-based materials, e.g. graphene or carbon nanotubes, and some polymers, thanks to the abundance of conjugated π bonds.[152,153]

The mechanism and materials presented, thanks to the photothermal synergy find several applications in environmental remediation processes. A brief sum-up of the main field of application is reported in Figure 1.14).

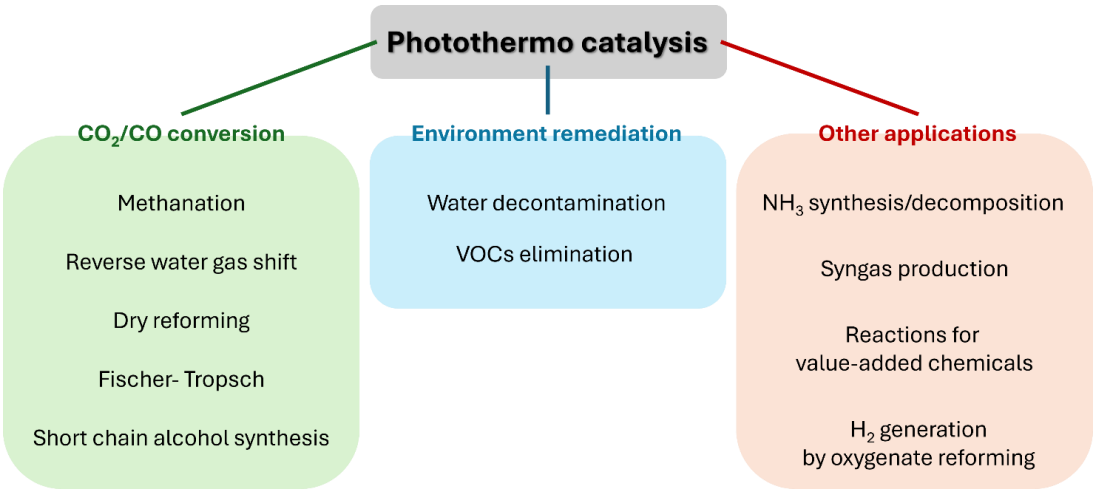

Figure 1.14: schematic sum of the wide variety of applications for photothermo catalysis

For instance, the removal of VOC is of fundamental interest since they are common indoor gaseous pollutants with detrimental effects on air quality and human health. In this context, Li *et al.*[154] applied photothermo catalysis in the degradation of toluene by loading Pt NPs on Mn-TiO_2. Or else, Wang *et al.*[155] demonstrated the improved photo-thermal degradation of acetone with $Ce_{0.25}Mn_{0.75}O_x$.

The application of photothermo synergistic effect is not only limited to the gaseous state. Indeed, Wang *et al.*[156] proposed the application of $Mn_3O_4/MnCO_3$ heterojunctions for the degradation of methylene blue and formaldehyde in aqueous solution, while Yuan *et al.*[157] successfully synthetised flower spherical-like S-scheme $Bi_7O_9I_3$/AgI which proved efficient in degrading phenol.

The environmental application of photothermo catalysis is not limited to the degradation of pollutants; indeed, the production of chemical fuels is one of the most promising and fast pacing developing application. The photothermal effect can indeed be applied in the reforming of oxygenated molecules, like methanol[158] or ethanol[159], for H_2 production or also in organic reactions for producing high-added value compounds as substrates for fine chemicals production.[160] Similarly, the synthesis of aromatic aldehydes, which have a central role in several chemical and pharmaceutical processes, normally requires toxic and corrosive oxidants like $KMnO_4$, Cr^{3+}, ClO^- or Cl_2. Photothermal synergic effect proved efficient in this field, for example in a more sustainable conversion of benzyl alcohol to benzaldehyde.[161] Also ammonia synthesis and degradation can benefit from photothermo catalysis, since both processes need high temperatures and pressures.[162,163] Particular interest has been devoted to CO_2 and CO conversion, especially considering the central role played by CO_2 in global warming and environmental damage. Reactions like methanation, reverse water gas-shift, hydrogenation into short-chain alcohol, dry reforming or Fischer-Tropsch have been all investigated in a photothermo application.[164,165]

It is worth noticing that the application of photothermo catalysis in the up-conversion of biomasses is an under-developing topic. Some promising results were provided by Zhong et al.[166] in the conversion of cellulose in lactic acid using Cu_2O/Cu-palygorskite. In a similar attempt, Zhang *et al.*[167] obtained a high-yield conversion of glycerol, a by-product of biodiesel production, to hydrogen with Au NPs-decorated TiO_2. A promising material for the photothermo application is lignin, a major by-product of biorefineries and paper industry, as well as a renewable natural source rich in aromatic functionalities. Interesting photothermo catalytic results are obtained on model compounds, while lignin conversion is still unexplored due to the complexity and inconstant composition of the molecule. [168,169]

1.5 Bibliography

[1] J. Butlin, *J. Int. Dev.* **1989**, *1*, 284–287.

[2] P. Bardos, *Remediation* **2014**, *25*, 23–32.

[3] D. Negrete-Bolagay, C. Zamora-Ledezma, C. Chuya-Sumba, F. B. De Sousa, D. Whitehead, F. Alexis, V. H. Guerrero, *J. Environ. Manage.* **2021**, *300*, DOI 10.1016/j.jenvman.2021.113737.

[4] D. Kanakaraju, B. D. Glass, M. Oelgemöller, *J. Environ. Manage.* **2018**, *219*, 189–207.

[5] M. Priyadarshini, I. Das, M. M. Ghangrekar, L. Blaney, *J. Environ. Manage.* **2022**, *316*, 115295.

[6] Y. Deng, R. Zhao, *Curr. Pollut. Reports* **2015**, *1*, 167–176.

[7] S. Mishra, B. Sundaram, *Mater. Today Proc.* **2023**, DOI 10.1016/j.matpr.2023.07.147.

[8] E. Delaney, W. Liu, Z. Zhu, Y. Xu, J. S. Dai, *Des. Sci.* **2022**, *8*, DOI 10.1017/dsj.2022.11.

[9] V. G. Zuin, I. Eilks, M. Elschami, K. Kümmerer, *Green Chem.* **2021**, *23*, 1594–1608.

[10] E. A. Olivetti, J. M. Cullen, *Science (80-.).* **2018**, *360*, 1396–1398.

[11] Z. Yu, S. A. R. Khan, P. Ponce, H. M. Zia-ul-haq, K. Ponce, *J. Clean. Prod.* **2022**, *350*, DOI 10.1016/j.jclepro.2022.131305.

[12] M. Arun, D. Barik, S. S. R. Chandran, *Chem. Eng. J. Adv.* **2024**, *18*, DOI 10.1016/j.ceja.2024.100589.

[13] M. Landmann, E. Rauls, W. G. Schmidt, *J. Phys. Condens. Matter* **2012**, *24*, DOI 10.1088/0953-8984/24/19/195503.

[14] S. W. Verbruggen, *J. Photochem. Photobiol. C Photochem. Rev.* **2015**, *24*, 64–82.

[15] S. Wang, Z. Ding, X. Chang, J. Xu, **2020**, 1–38.

[16] S. D. Mo, W. Y. Ching, *Phys. Rev. B* **1995**, *51*, 1–23.

[17] H. Kisch, *Angew. Chemie - Int. Ed.* **2013**, *52*, 812–847.

[18] J. Schneider, M. Matsuoka, M. Takeuchi, J. Zhang, Y. Horiuchi, M. Anpo, D. W. Bahnemann, *Chem. Rev.* **2014**, *114*, 9919−9986.

[19] C. I. N. Morgade, N. J. Castellani, G. F. Cabeza, *J. Comput. Electron.* **2018**, *17*, 1505–1514.

[20] B. Ohtani, O. O. Prieto-Mahaney, D. Li, R. Abe, *J. Photochem. Photobiol. A Chem.* **2010**, *216*, 179–182.

[21] R. A. Marcus, *J. Phys. Chem.* **1990**, *94*, 1050–1055.

[22] M. R. Hoffmann, S. T. Martin, W. Choi, D. W. Bahnemann, *Chem. Rev.* **1995**, *95*, 69–96.

[23] C. B. Anucha, I. Altin, E. Bacaksiz, V. N. Stathopoulos, *Chem. Eng. J. Adv.* **2022**, *10*, DOI 10.1016/j.ceja.2022.100262.

[24] J. Harris, R. Silk, M. Smith, Y. Dong, W. T. Chen, G. I. N. Waterhouse, *ACS Omega* **2020**, *5*, 18919–18934.

[25] W. Ko, S. Zhao, K. Kim, Y. D. Kim, H. O. Seo, *Mater. Chem. Phys.* **2023**, *299*, DOI 10.1016/j.matchemphys.2023.127519.

[26] Z. Shayegan, F. Haghighat, C. S. Lee, A. Bahloul, M. Huard, *Chem. Eng. J.* **2018**, *346*, 578–589.

[27] M. Pelaez, N. T. Nolan, S. C. Pillai, M. K. Seery, P. Falaras, A. G. Kontos, P. S. M. Dunlop, J. W. J. Hamilton, J. A. Byrne, K. O'Shea, M. H. Entezari, D. D. Dionysiou, *Appl. Catal. B Environ.* **2012**, *125*, 331–349.

[28] H. N. C. Dharma, J. Jaafar, N. Widiastuti, H. Matsuyama, S. Rajabsadeh, M. H. D. Othman, M. A. Rahman, N. N. M. Jafri, N. S. Suhaimin, A. M. Nasir, N. H. Alias, *Membranes (Basel).* **2022**, *12*, DOI 10.3390/membranes12030345.

[29] C. H. Kwak, U. S. Im, S. W. Seo, M. Il Kim, Y. S. Huh, J. S. Im, *Mater. Lett.* **2021**, *288*, 2–5.

[30] K. Kaviyarasan, V. Vinoth, T. Sivasankar, A. M. Asiri, J. J. Wu, S. Anandan, *Ultrason. Sonochem.* **2019**, *51*, 223–229.

[31] N. C. Kothari, *Int. J. Miner. Process.* **1974**, *1*, 287–305.

[32] *Mineral Commodity Summaries 2024*, **2024**.

[33] C. Thambiliyagodage, R. Wijesekera, M. G. Bakker, *Discov. Mater.* **2021**, *1*.

[34] S. Tahooni Bonab, H. Abdollahi, A. Abbaspour, *Miner. Process. Extr. Metall. Rev.* **2024**, *00*, 1–17.

[35] T. H. Nguyen, M. S. Lee, *Miner. Process. Extr. Metall. Rev.* **2019**, *40*, 231–247.

[36] A. H. J. Sampath, N. D. Wickramasinghe, K. M. N. de Silva, R. M. de Silva, *Minerals* **2023**, *13*.

[37] F. Yang, V. Hlavacek, *AIChE J.* **2000**, *46*, 355–360.

[38] M. H. Sadeghi, M. Nasr Esfahany, *Ind. Eng. Chem. Res.* **2022**, *61*, 1786–1796.

[39] W. Zhang, Z. Zhu, C. Y. Cheng, *Hydrometallurgy* **2011**, *108*, 177–188.

[40] M. H. H. Mahmoud, A. A. I. Afifi, I. A. Ibrahim, *Hydrometallurgy* **2004**, *73*, 99–109.

[41] E. Foley, P. Mackinnon, *J. Solid State Chem.* **1970**, *1*, 566–575.

[42] M. Parashar, V. K. Shukla, R. Singh, *J. Mater. Sci. Mater. Electron.* **2020**, *31*, 3729–3749.

[43] S. M. Gupta, M. Tripathi, *Cent. Eur. J. Chem.* **2012**, *10*, 279–294.

[44] U.S. Environmental Protection Agency, *State of the Science Literature Review : Nano Titanium Dioxide Environmental Matters*, **2010**.

[45] M. Sanchez-Dominguez, G. Morales-Mendoza, M. J. Rodriguez-Vargas, C. C. Ibarra-Malo, A. A. Rodriguez-Rodriguez, A. V. Vela-Gonzalez, S. A. Perez-Garcia, R. Gomez, *J. Environ. Chem. Eng.* **2015**, *3*, 3037–3047.

[46] R. K. Keswani, H. Ghodke, D. Sarkar, K. C. Khilar, R. S. Srinivasa, *Colloids Surfaces A Physicochem. Eng. Asp.* **2010**, *369*, 75–81.

[47] M. Sanchez-Dominguez, K. Pemartin, M. Boutonnet, *Curr. Opin. Colloid Interface Sci.* **2012**, *17*, 297–305.

[48] J. K. Oh, J. K. Lee, S. J. Kim, K. W. Park, *J. Ind. Eng. Chem.* **2009**, *15*, 270–274.

[49] C. S. Kim, B. K. Moon, J. H. Park, S. T. Chung, S. M. Son, *J. Cryst. Growth* **2003**, *254*, 405–410.

[50] A. H. Mamaghani, F. Haghighat, C. S. Lee, *Chemosphere* **2019**, *219*, 804–825.

[51] L. Zhang, L. Jin, B. Liu, J. He, *Front. Chem.* **2019**, *7*, 1–13.

[52] W. Zhang, Y. Tian, H. He, L. Xu, W. Li, D. Zhao, *Natl. Sci. Rev.* **2020**, *7*, 1702–1725.

[53] H. Li, W. Zhang, D. Liu, W. Li, *Emergent Mater.* **2020**, *3*, 315–329.

[54] N. E. Sunny, S. S. Mathew, N. Chandel, P. Saravanan, R. Rajeshkannan, M. Rajasimman, Y. Vasseghian, N. Rajamohan, S. V. Kumar, *Chemosphere* **2022**, *300*, DOI 10.1016/j.chemosphere.2022.134612.

[55] V. Verma, M. Al-Dossari, J. Singh, M. Rawat, M. G. M. Kordy, M. Shaban, *Polymers (Basel).* **2022**, *14*, DOI 10.3390/polym14071444.

[56] S. Shiva Samhitha, G. Raghavendra, C. Quezada, P. Hima Bindu, *Mater. Today Proc.* **2022**, *54*, 765–770.

[57] O. A. Qamar, F. Jamil, M. Hussain, S. Bae, A. Inayat, N. S. Shah, A. Waris, P. Akhter, E. E. Kwon, Y. K. Park, *Chem. Eng. J.* **2023**, *460*, DOI 10.1016/j.cej.2023.141734.

[58] M. S. Samuel, M. Ravikumar, A. John, E. Selvarajan, H. Patel, P. S. Chander, J. Soundarya, S. Vuppala, R. Balaji, N. Chandrasekar, *Catalysts* **2022**, *12*, 44–63.

[59] C. Langa, N. C. Hintsho-Mbita, *Chem. Phys. Impact* **2023**, *7*, DOI 10.1016/j.chphi.2023.100293.

[60] E. Özbay, M. Erdemir, H. İ. Durmuş, *Constr. Build. Mater.* **2016**, *105*, 423–434.

[61] G. Wang, *The Utilization of Slag in Civil Infrastructure Construction*, **2016**.

[62] G. Fan, M. Wang, J. Dang, R. Zhang, Z. Lv, W. He, X. Lv, *Waste Manag.* **2021**, *120*, 626–634.

[63] J. Shi, Y. Qiu, B. Yu, X. Xie, J. Dong, C. Hou, J. Li, C. Liu, *Jom* **2022**, *74*, 654–667.

[64] Z. zhong BIAN, Y. li FENG, H. ran LI, *Trans. Nonferrous Met. Soc. China (English Ed.* **2020**, *30*, 2836–2847.

[65] S. He, H. Sun, D. g Tan, T. Peng, *Procedia Environ. Sci.* **2016**, *31*, 977–984.

[66] Y. Cai, N. Song, Y. Yang, L. Sun, P. Hu, J. Wang, *Int. J. Miner. Metall. Mater.* **2022**, *29*, 22–31.

[67] J. Li, Z. Guo, J. Gao, *ISIJ Int.* **2014**, *54*, 743–749.

[68] M. Hu, R. Wei, F. Yin, L. Liu, Q. Deng, *Jom* **2016**, *68*, 2502–2510.

[69] X. Qian, W. Ao, H. Ding, X. Wang, S. Sun, *Materials (Basel).* **2022**, *15*, DOI 10.3390/ma15227984.

[70] B. Ye, B. Jeong, M. jin Lee, T. H. Kim, S. S. Park, J. Jung, S. Lee, H. D. Kim, *Nano Converg.* **2022**, *9*, DOI 10.1186/s40580-022-00341-7.

[71] A. Szymaszek, B. Samojeden, M. Motak, *Energies* **2020**, *13*, 15–18.

[72] T. Niu, J. Wang, H. Chu, C. Qian, N. Duan, G. Michael Gadd, W. Shi, B. Xin, *Chem. Eng. J.* **2021**, *420*, DOI 10.1016/j.cej.2020.127722.

[73] Q. Su, J. Miao, H. Li, Y. Chen, J. Chen, J. Wang, *Hydrometallurgy* **2018**, *181*, 230–239.

[74] Q. Zhang, Y. Wu, T. Zuo, *Metall. Mater. Trans. B Process Metall. Mater. Process. Sci.* **2019**, *50*, 471–479.

[75] Y. Wei, D. Li, J. Qiao, X. Guo, *J. Environ. Chem. Eng.* **2023**, *11*, DOI 10.1016/j.jece.2023.110104.

[76] C. Zhao, C. Wang, X. Wang, H. Li, Y. Chen, W. Wu, *Waste Manag.* **2023**, *155*, 338–347.

[77] W. Wu, C. Wang, W. Bao, H. Li, *Hydrometallurgy* **2018**, *179*, 52–59.

[78] Q. Zhang, Y. Wu, T. Zuo, *ACS Sustain. Chem. Eng.* **2018**, *6*, 3091–3101.

[79] B. Ma, Z. Qiu, J. Yang, C. Qin, J. Fan, A. Wei, Y. Li, *Waste and Biomass Valorization* **2019**, *10*, 3037–3044.

[80] Q. Zhang, Y. Wu, L. Li, T. Zuo, *ACS Sustain. Chem. Eng.* **2018**, *6*, 12502–12510.

[81] X. B. Zhu, W. Li, X. M. Guan, *Trans. Nonferrous Met. Soc. China (English Ed.* **2015**, *25*, 3139–3145.

[82] S. Li, J. Pan, D. Zhu, Z. Guo, Y. Shi, T. Dong, S. Lu, H. Tian, *Resour. Conserv. Recycl.* **2021**, *168*, DOI 10.1016/j.resconrec.2020.105314.

[83] J. Liu, H. Li, J. Liang, L. Wang, *Multipurp. Util. Miner. Resour.* **2022**, *43*, 107–112.

[84] J. Zou, Z. Liu, Q. Guo, *Can. Metall. Q.* **2024**, *63*, 927–934.

[85] J. Zhao, X. Zhang, F. Yang, Y. Ai, Y. Chen, D. Pan, *ACS Omega* **2024**, *9*, 6036–6058.

[86] J. Ma, S. Xu, H. Ding, Y. Li, H. Zhang, *Chem. Phys. Lett.* **2024**, *840*, DOI 10.1016/j.cplett.2024.141158.

[87] Z. Zhang, H. Lü, X. Li, X. Li, S. Ran, Z. Chen, Y. Yang, X. Wu, L. Li, *ACS Sustain. Chem. Eng.* **2019**, *7*, 10299–10309.

[88] H. Lü, N. Li, X. Wu, L. Li, Z. Gao, X. Shen, *Metall. Mater. Trans. B Process Metall. Mater. Process. Sci.* **2013**, *44*, 1317–1320.

[89] N. Song, Y. Cai, L. Sun, P. Hu, Q. Zhou, J. Wu, J. Wang, *Materials (Basel).* **2022**, *15*, DOI 10.3390/ma15041514.

[90] X. F. Lei, X. X. Xue, *Trans. Nonferrous Met. Soc. China (English Ed.* **2010**, *20*, 2294–2298.

[91] H. Liu, T. Xia, H. K. Shon, S. Vigneswaran, *J. Ind. Eng. Chem.* **2011**, *17*, 461–467.

[92] X. F. Lei, X. X. Xue, H. Yang, *Trans. Nonferrous Met. Soc. China (English Ed.* **2012**, *22*, 1771–1777.

[93] Z. Song, H. Gao, W. Zhang, D. Wang, *J. Water Process Eng.* **2020**, *36*, DOI 10.1016/j.jwpe.2020.101399.

[94] H. Ma, Z. Wang, P. Yuan, B. Shen, J. Xu, *J. Environ. Chem. Eng.* **2023**, *11*, 109945.

[95] W. Hajjaji, G. Costa, C. Zanelli, M. J. Ribeiro, M. P. Seabra, M. Dondi, J. A. Labrincha, *J. Eur. Ceram. Soc.* **2012**, *32*, 753–764.

[96] J. A. Labrincha, J. I. Marques, W. Hajjaji, L. Senff, C. Zanelli, M. Dondi, F. Rocha, *Waste and Biomass Valorization* **2014**, *5*, 385–392.

[97] D. C. Paz-Gómez, I. S. Vilarinho, J. Carvalheiras, S. M. Pérez-Moreno, M. P. Seabra, J. A. Labrincha, J. P. Bolívar, *Waste and Biomass Valorization* **2024**, DOI 10.1007/s12649-024-02629-7.

[98] F. Chylinski, J. Bobrowicz, F. Chyli, *Material* **2020**, *13*, 3555.

[99] H. Dong, G. Zeng, L. Tang, C. Fan, C. Zhang, X. He, Y. He, *Water Res.* **2015**, *79*, 128–146.

[100] A. Kubacka, M. Fernández-García, G. Colón, *Chem. Rev.* **2012**, *112*, 1555–1614.

[101] C. Xu, P. Ravi Anusuyadevi, C. Aymonier, R. Luque, S. Marre, *Chem. Soc. Rev.* **2019**, *48*, 3868–3902.

[102] S. Shabbir, M. F. e. A. Kulyar, Z. A. Bhutta, P. Boruah, M. Asif, *Bionanoscience* **2021**, *11*, 621–632.

[103] C. Li, N. Zhu, S. Yang, X. He, S. Zheng, Z. Sun, D. D. Dionysiou, *Chemosphere* **2021**, *273*, DOI 10.1016/j.chemosphere.2021.129723.

[104] H. M. Ali, F. Arabpour Roghabadi, V. Ahmadi, *Sol. Energy* **2023**, *255*, 99–125.

[105] N. Yahya, F. Aziz, N. A. Jamaludin, M. A. Mutalib, A. F. Ismail, W. N. Salleh, J. Jaafar, N. Yusof, N. A. Ludin, *J. Environ. Chem. Eng.* **2018**, *6*, 7411–7425.

[106] E. Jimenez-Relinque, S. F. Lee, L. Plaza, M. Castellote, *Environ. Sci. Pollut. Res.* **2022**, *29*, 39712–39722.

[107] S. S. Alias, Z. Harun, F. H. Azhar, S. A. Ibrahim, B. Johar, *J. Clean. Prod.* **2020**, *251*, DOI 10.1016/j.jclepro.2019.119448.

[108] S. Singh, H. Mahalingam, P. K. Singh, *Appl. Catal. A Gen.* **2013**, *462–463*, 178–195.

[109] D. C. S. Gloria, C. H. V. Brito, T. A. P. Mendonça, T. R. Brazil, R. A. Domingues, N. C. S. Vieira, E. B. Santos, M. Gonçalves, *Mater. Chem. Phys.* **2023**, *305*, DOI 10.1016/j.matchemphys.2023.127947.

[110] A. Ahmad, M. Ali, A. G. Al-Sehemi, A. A. Al-Ghamdi, J. W. Park, H. Algarni, H. Anwer, *Chem. Eng. J.* **2023**, *452*, DOI 10.1016/j.cej.2022.139436.

[111] C. Thambiliyagodage, *Environ. Nanotechnology, Monit. Manag.* **2022**, *18*, DOI 10.1016/j.enmm.2022.100737.

[112] S. Danfá, R. C. Martins, M. J. Quina, J. Gomes, *Molecules* **2021**, *26*, DOI 10.3390/molecules26175363.

[113] M. Crippa, E. Callone, M. D'Arienzo, K. Müller, S. Polizzi, L. Wahba, F. Morazzoni, R. Scotti, *Appl. Catal. B Environ.* **2011**, *104*, 282–290.

[114] B. Di Credico, I. R. Bellobono, M. D'Arienzo, D. Fumagalli, M. Redaelli, R. Scotti, F. Morazzoni, *Int. J. Photoenergy* **2015**, *2015*, DOI 10.1155/2015/919217.

[115] N. Todorova, T. Giannakopoulou, S. Karapati, D. Petridis, T. Vaimakis, C. Trapalis, *Appl. Surf. Sci.* **2014**, *319*, 113–120.

[116] L. Zou, Y. Luo, M. Hooper, E. Hu, *Chem. Eng. Process. Process Intensif.* **2006**, *45*, 959–964.

[117] M. Li, B. Lu, Q. F. Ke, Y. J. Guo, Y. P. Guo, *J. Hazard. Mater.* **2017**, *333*, 88–98.

[118] J. Mo, Y. Zhang, Q. Xu, R. Yang, *J. Hazard. Mater.* **2009**, *168*, 276–281.

[119] H. F. Abbas, W. M. A. Wan Daud, *Int. J. Hydrogen Energy* **2010**, *35*, 1160–1190.

[120] A. Galadima, O. Muraza, *Renew. Sustain. Energy Rev.* **2019**, *115*, DOI 10.1016/j.rser.2019.109333.

[121] M. D. Argyle, C. H. Bartholomew, *Catalysts* **2015**, *5*, 145–269.

[122] C. H. Bartholomew, *Appl. Catal. A Gen.* **2001**, *212*, 17–60.

[123] V. Nair, M. J. Muñoz-Batista, M. Fernández-García, R. Luque, J. C. Colmenares, *ChemSusChem* **2019**, *12*, 2098–2116.

[124] Z. jun Wang, H. Song, H. Liu, J. Ye, *Angew. Chemie - Int. Ed.* **2020**, *59*, 8016–8035.

[125] N. Keller, J. Ivanez, J. Highfield, A. M. Ruppert, *Appl. Catal. B Environ.* **2021**, *296*, DOI 10.1016/j.apcatb.2021.120320.

[126] G. Mie, *Ann. Phys.* **1908**, *330*, 377–445.

[127] P. Drude, *Ann. Phys.* **1900**, *306*, 566–613.

[128] H. Yu, Y. Peng, Y. Yang, Z. Li, **2019**, 1–14.

[129] Y. Zhang, S. He, W. Guo, Y. Hu, J. Huang, J. R. Mulcahy, W. D. Wei, *Chem. Rev.* **2018**, *118*, 2927–2954.

[130] M. L. Brongersma, N. J. Halas, P. Nordlander, *Nat. Nanotechnol.* **2015**, *10*, 25–34.

[131] A. M. Brown, R. Sundararaman, P. Narang, W. A. Goddard, H. A. Atwater, *ACS Nano* **2016**, *10*, 957–966.

[132] D. Mateo, J. L. Cerrillo, S. Durini, J. Gascon, *Chem. Soc. Rev.* **2021**, *50*, 2173–2210.

[133] S. Link, M. A. El-Sayed, *J. Phys. Chem. B* **1999**, *103*, 4212–4217.

[134] C. L. Nehl, J. H. Hafner, *J. Mater. Chem.* **2008**, *18*, 2415–2419.

[135] N. E. Motl, A. F. Smith, C. J. Desantis, S. E. Skrabalak, *Chem. Soc. Rev.* **2014**, *43*, 3823–3834.

[136] A. O. Govorov, H. H. Richardson, *Nano Today* **2007**, *2*, 30–38.

[137] P. Christopher, H. Xin, S. Linic, *Nat. Chem.* **2011**, *3*, 467–472.

[138] M. J. Kale, T. Avanesian, P. Christopher, *ACS Catal.* **2014**, *4*, 116–128.

[139] P. Christopher, M. Moskovits, *Annu. Rev. Phys. Chem.* **2017**, *68*, 379–398.

[140] C. Boerigter, R. Campana, M. Morabito, S. Linic, *Nat. Commun.* **2016**, *7*, DOI 10.1038/ncomms10545.

[141] S. Sarina, E. Jaatinen, Q. Xiao, Y. M. Huang, P. Christopher, J. C. Zhao, H. Y. Zhu, *J. Phys. Chem. Lett.* **2017**, *8*, 2526–2534.

[142] R. T. Tung, *Mater. Sci. Eng. R Reports* **2001**, *35*, 1–138.

[143] G. V. Hartland, L. V. Besteiro, P. Johns, A. O. Govorov, *ACS Energy Lett.* **2017**, *2*, 1641–1653.

[144] Y. K. Lee, C. H. Jung, J. Park, H. Seo, G. A. Somorjai, J. Y. Park, *Nano Lett.* **2011**, *11*, 4251–4255.

[145] A. Agrawal, S. H. Cho, O. Zandi, S. Ghosh, R. W. Johns, D. J. Milliron, *Chem. Rev.* **2018**, *118*, 3121–3207.

[146] J. Li, Z. Lou, B. Li, *Chinese Chem. Lett.* **2022**, *33*, 1154–1168.

[147] X. Liu, M. T. Swihart, *Chem. Soc. Rev.* **2014**, *43*, 3908–3920.

[148] H. Lu, J. Wang, H. Li, W. Zhou, Q. Yuan, S. Liu, *Mater. Chem. Front.* **2023**, *7*, 4372–4399.

[149] X. Yin, F. Ai, L. Han, *Front. Chem.* **2022**, *10*, 1–15.

[150] S. Sarina, H.-Y. Zhu, Q. Xiao, E. Jaatinen, J. Jia, Y. Huang, Z. Zheng, H. Wu, *Angew. Chemie Int. Ed.* **2014**, *53*, 2935–2940.

[151] M. Ghoussoub, M. Xia, P. N. Duchesne, D. Segal, G. Ozin, *Energy Environ. Sci.* **2019**, *12*, 1122–1142.

[152] L. Xiao, X. Chen, X. Yang, J. Sun, J. Geng, *ACS Appl. Polym. Mater.* **2020**, *2*, 4273–4288.

[153] J. Zhu, L. Huang, F. Bao, G. Chen, K. Song, Z. Wang, H. Xia, J. Gao, Y. Song, C. Zhu, F. Lu, T. Zheng, M. Ji, *Mater. Reports Energy* **2024**, *4*, 100245.

[154] G. Li, M. Zhang, J. Chen, Q. Li, H. Jia, *J. Hazard. Mater.* **2023**, *449*, 131041.

[155] X. Wang, B. Zhao, F. Chen, *J. Phys. Chem. Solids* **2023**, *172*, 111058.

[156] G. Wang, B. Huang, Z. Lou, Z. Wang, X. Qin, X. Zhang, Y. Dai, *Appl. Catal. B Environ.* **2016**, *180*, 6–12.

[157] Y. Yuan, W. Pan, R. Guo, L. Hong, Z. Lin, X. Ji, *Sep. Purif. Technol.* **2022**, *297*, 121538.

[158] W. Lin, J. Li, Z. Zengcai, B. Zhang, X. Wu, Y. Pi, T. Wang, *Fuel* **2024**, *357*, 129990.

[159] S. Luo, H. Song, D. Philo, M. Oshikiri, T. Kako, J. Ye, *Appl. Catal. B Environ.* **2020**, *272*, 118965.

[160] Q. Yang, Q. Xu, S.-H. Yu, H.-L. Jiang, *Angew. Chemie Int. Ed.* **2016**, *55*, 3685–3689.

[161] Q. Wei, K. G. Guzman, X. Dai, N. H. Attanayake, D. R. Strongin, Y. Sun, *Nano-Micro Lett.* **2020**, *12*, 1–10.

[162] P. Liu, L. Sun, Z. Zhang, X. Wang, Y. Zhang, X. Yang, *Mol. Catal.* **2023**, *543*, DOI 10.1016/j.mcat.2023.113160.

[163] X. Li, X. Zhang, H. O. Everitt, J. Liu, *Nano Lett.* **2019**, *19*, 1706–1711.

[164] F. Zhang, Y.-H. Li, M.-Y. Qi, Y. M. A. Yamada, M. Anpo, Z.-R. Tang, Y.-J. Xu, *Chem Catal.* **2021**, *1*, 272–297.

[165] Y. Li, R. Li, Z. Li, Y. Xu, H. Yuan, S. Ouyang, T. Zhang, *Sol. RRL* **2022**, *6*, 2200493.

[166] M. Zhong, X. Li, X. Chu, H. Gui, S. Zuo, C. Yao, Z. Li, Y. Chen, *Appl. Catal. B Environ.* **2022**, *317*, DOI 10.1016/j.apcatb.2022.121718.

[167] J. Zhang, D. Wang, R. Chen, X. Zhu, D. Ye, Y. Yang, Q. Liao, *Energy Convers. Manag.* **2023**,

277, 116626.

[168] H. Wang, X. Cheng, Z. Li, L. Jing, J. Hu, *Chem. Eng. J.* **2024**, *496*, DOI 10.1016/j.cej.2024.153772.

[169] Q. Y. Liu, C. Ma, Y. Chen, Z. Y. Wang, F. G. Zhang, J. P. Tang, Y. J. Yuan, *ACS Appl. Mater. Interfaces* **2023**, *15*, 50206–50215.

Chapter 2: Tionite characterization and compositional improvement

With the aim of investigating the application of a new waste material for a photocatalytic application, tionite, a by-product of TiO_2 industrial manufacture, is characterized and modified to optimize its composition and applicability.

This chapter presents the current state-of-the-art in the origin and composition of tionite, the procedure available to extract TiO_2 or to increase its content in the material and the current large-scale application of tionite.

Starting from these concepts, an in-depth characterization of the classic lime-neutralized tionite sample is performed to define its composition and morphology. According to the results, specific procedures are tested with the aim of simplifying the material composition. At first, a neutralization strategy based on NaOH is evaluated, followed by the application of mild chemical treatments involving acid/base reactions to further improve TiO_2 content and accessibility. All the samples prepared are characterized with a multi-technique approach to evaluate the efficiency of the treatments and the changes induced in the samples.

2.1 Introduction to tionite and its recovery

The industrial TiO_2 production through the sulfate process (described in Paragraphs 1.2.1) provides, as main products, TiO_2 and $FeSO_4 \cdot 7H_2O$. The main by-products of the process are diluted H_2SO_4 and a solid waste, generally known as ilmenite mud or tionite. Tionite mainly consists of all the insoluble impurities included in ilmenite ore mixed with residues of sulfuric acid. This material is considered hazardous according to the European classification[1] due to its low pH, and therefore it is commonly disposed into landfills with significant cost and difficulties.[2] In some cases, the mud is mixed with other waste materials to reduce its acidity and avoid the release of heavy metals in the environment. However, in order to reduce the environmental impact and all the problems related to material disposal, its valorisation could represent a valuable and beneficial solution.

To establish an effective re-use of tionite, knowing its composition is fundamental; however, it is extremely variable since it depends on the characteristics of the initial ilmenite mineral and the extraction efficiency of the industrial process. For this reason, the TiO_2 content in tionite can vary in the range of 30-55 wt. % and it is generally mixed with a significant amount of SiO_2 and Al_2O_3, along with several alkali and alkaline-heart metals like Ca, Mg, Na, and finally Fe_2O_3 and sulphur compounds.

Starting from its composition, the extraction of TiO_2 from tionite has been rarely investigated and only a few attempts are reported in literature. Meng et al.[3,4] proposed a procedure based on a hydrothermal alkaline extraction with 50 % NaOH at 240 °C for 1 h, the solid residue is then recovered and washed with 55 °C water. The solid underwent an acid leaching with 40 % H_2SO_4 at 55 °C for 1 h to obtain titanyl sulfate that, upon neutralization, provides TiO_2 with a Ti recovery of 96.7%. On the other hand, a purification process was developed, based on a first step to remove sulphur compounds at 1000 °C for 5 h, followed by a second thermal treatment with graphite at 1700 °C for 60 min and a magnetic separation step to remove iron alloys. Thanks to this process, the TiO_2 content in the materials passed from 32.3 % to 52.4 %.[5] Despite the results, these extraction procedures are high energy and solvent demanding: this led to investigate the direct application of tionite for practical applications (Figure 2.1).

In any case, tionite has to be neutralized with lime, which increases the Ca content of

the material. Consequentially, the enrichment in Ca along with its natural Si and Al compounds make tionite composition potentially suitable for an application in the construction materials industry. In this optic, Dondi et al.[6] tested the applicability of tionite as a colouring agent in clay bricks, by adding the waste material till up to 9 wt. %. He noticed that with inclusions of up to 3 wt. % no variation in the process and product quality was observed, but above 5 wt. % problems related to mechanical strength arose. Contreras et al.[7] demonstrated that adding between 3 and 10 wt. % of tionite in the manufacture of red stoneware ceramic tiles improved the bending strength up to 15 % and reduced porosity and water adsorption, providing a product with better performance compared to commercial products. In addition, the same group also proved the beneficial effect of a 20 wt. % tionite addition in the preparation of sulphur polymer cement in increasing the material strength and reducing water adsorption.[8] Similarly, Bobrowicz et al.[9] assesses that a replacement of up to 20% with tionite in the Portland cement production does not significantly alter the material properties. Perez-Moreno et al.[10] observed an improvement in the fire-insulating properties of a material consisting of red gypsum and 25 % of tionite, while Chylinski et al.[11] improved the frost resistance of cement by adding 10.8 % of the waste material.

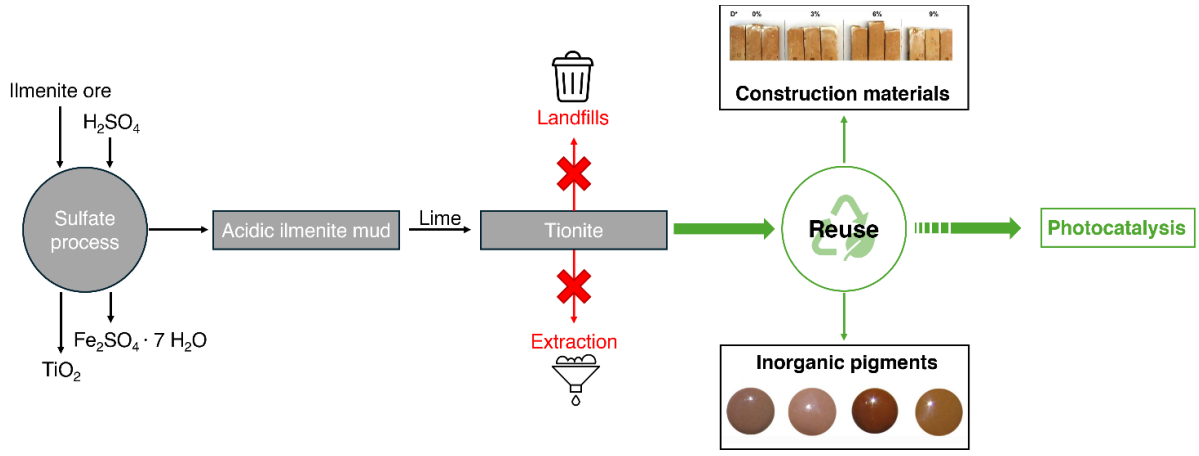

Figure 2.1: schematic representation of tionite production and applications. Adapted from [6] *and* [13]

The application of tionite in the preparation of inorganic pigment was also investigated. Brown coloured compounds were obtained by thermal treating the waste material at the temperature range of 1000-1200 °C and additioning transition metals like Cr or Co.[12–14]

It is clear that the current applications of tionite are suitable strategies to recover tionite

and to valorise it, reducing its environmental impact. However, the amount of tionite adsorbed by this industry is not enough to cover the worldwide production of this by-product. The investigation of new potential applications is therefore mandatory and an interesting starting point is provided by the work of Latorrata et al.[15]. Considering the TiO_2 content of tionite, they tested its application for the photocatalytic degradation of a pollutant, showing optimistic results. However, being the only example in literature, more in-depth research on the application of this waste material as a photocatalyst seems a promising path. For this reason, the composition and morphology of lime-neutralized tionite will be investigated and, considering the potential photocatalytic application, procedures aimed to improve its composition will be developed always keeping sustainability in mind. Particular attention will be given to the compositional and morphological characterization, especially to the surface properties of the different tionite samples.

2.2 Materials and methods

Specifications on the characterization conditions employed and the related sample preparation are reported in Appendix - 2.

2.2.1 Materials

Sodium hydroxide ≥98 % and H_2O HPLC grade were purchased from VWR. Hydrofluoric acid 38-40 % and $Ca(NO_3)_2 \cdot xH_2O$ 99.997 % were purchased from Sigma-Aldrich.

An undissolved residue known as “tionite”, hereby labelled as St-Tionite (starting tionite), was generated during the digestion of titanium-rich minerals in the sulfate process of TiO_2 production [6] performed by the Venator TiO_2 plant in Scarlino (Italy). Tionite was provided in two forms, either lime neutralized which is the usual industrial processing route to prepare the material for landfilling, or as a raw acidic material. The neutralized samples were labelled nCa_Tionite.

2.2.2 Preparation of nNa_Tionite

The raw acidic tionite was neutralised with NaOH to pH = 7 (pHmeter Mettler Toledo),

by adding an aqueous solution of NaOH 0.77 mol L^{-1} dropwise to a slurry of tionite 1:5 by weight in water, under magnetic stirring. The neutralised slurry was then washed three times with distilled H_2O (dH_2O) and centrifuged at 9000 revolutions per minute (rpm) for 15 min. Then, the sample was dried in an oven at 80 °C overnight. To confirm the removal of sulfate anions, the supernatant separated at each washing was added with $Ca(NO_3)_2 \cdot xH_2O$, to induce the precipitation of water-insoluble $CaSO_4$. A white solid formed into the solution, which was recovered by centrifugation at 9000 rpm for 10 min and washed three times with dH_2O. The solid was dried in an oven at 60 °C overnight. The new form of tionite was labelled as nNa_Tionite and used as it is or treated as following described. The solid collected by precipitation is hereby named nNa_Tionite_prec.

2.2.3 Acid and basic treatments of nNa_Tionite

The acid treatment of nNa_Tionite was carried out by dispersing 200 mg of the powder in 50 mL of a 5 % HF aqueous solution, at room temperature (RT) and under magnetic stirring for 24 h. The precipitate was separated by centrifugation at 9000 rpm for 10 min, washed once with HF 5 % and then three times with dH_2O, and finally dried overnight at 80 °C. The sample was labelled nNa_Tionite_A. To identify the dissolved elements, the supernatant collected during the washings was separated and neutralised with NaOH 1 mol L^{-1}. The formed precipitate was recovered and washed three times with dH_2O and centrifuged at 9000 rpm for 10 min. The sample was dried in an oven at 80 °C overnight and labelled Precipitate_A.

The basic treatment of nNa_Tionite was carried out by dispersing 200 mg of nNa_Tionite in 50 mL of NaOH 1 mol L^{-1} aqueous solution at 100 °C under magnetic stirring for 24 h. The suspension was then centrifuged at 9000 rpm for 10 min and the solid residue was washed with NaOH 1 mol L^{-1} and then three times with dH_2O, followed by centrifugation. In the end, the sample was dried overnight at 80 °C. The sample was labelled nNa_Tionite_B. The supernatant of each washing was collected and neutralised with HCl 37 %. The formed precipitate was recovered and washed three times with dH_2O and centrifuged at 9000 rpm for 10 min. The sample was dried in an oven at 80 °C overnight and labelled Precipitate_B.

Figure 2.2 summarizes the treatments and samples described.

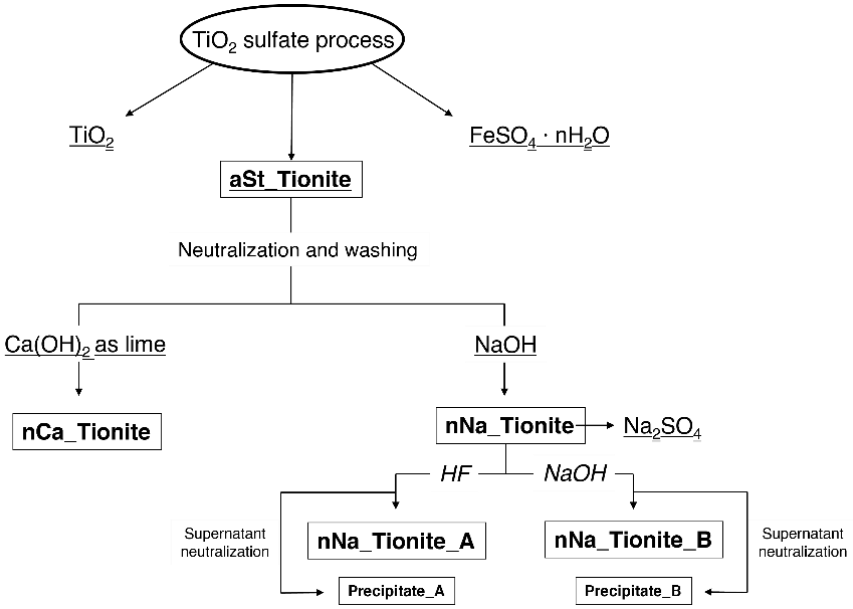

Figure 2.2: flow sheet of the recovering process of St-Tionite with the chemical treatments applied

2.3 Results and Discussion

2.3.1 Structural and morphological characterization of nCa_Tionite

To re-use and recycle the titanium dioxide-based waste material for catalytic applications, a thorough characterisation of the as-received neutralised tionite sample was carried out thus implementing the datasheet information on the elemental composition provided by the company.

At first, the composition of nCa_Tionite was investigated by XRF analysis, in order to define the main constituent elements.

According to spectra shown in Figure 2.3a, the most intense peaks at 4.51 and 4.93 keV correspond to the Kα1 and Kβ1 signals of Ti, respectively. In addition, the intense emissions at 3.69 and 4.10 keV and at 6.40 and 7.06 keV represent both Kα1 and Kβ1 signals of Fe and Ca. The presence of both elements is easily explained: Fe is included in ilmenite whereas Ca is a common element in nature and it could also be introduced by the neutralization procedure with $Ca(OH)_2$. In the magnification of Figure 2.3b, peaks with lower intensity are observed and, according to their position, they are attributed to the presence of Si, S and K. The peak at 5.90 keV cannot be uniquely attributed because it corresponds to both the Kα1 of Mn and the Kβ1 of Cr; in addition, the second XRF signal for both elements is overlapped with others. The Si content

observed for nCa_Tionite is limited, but it is worth noticing that XRF analysis is ineffective in detecting low Z number elements. Consequentially, the presence of Si in the sample can be confirmed, but quantitative considerations are not reliable.

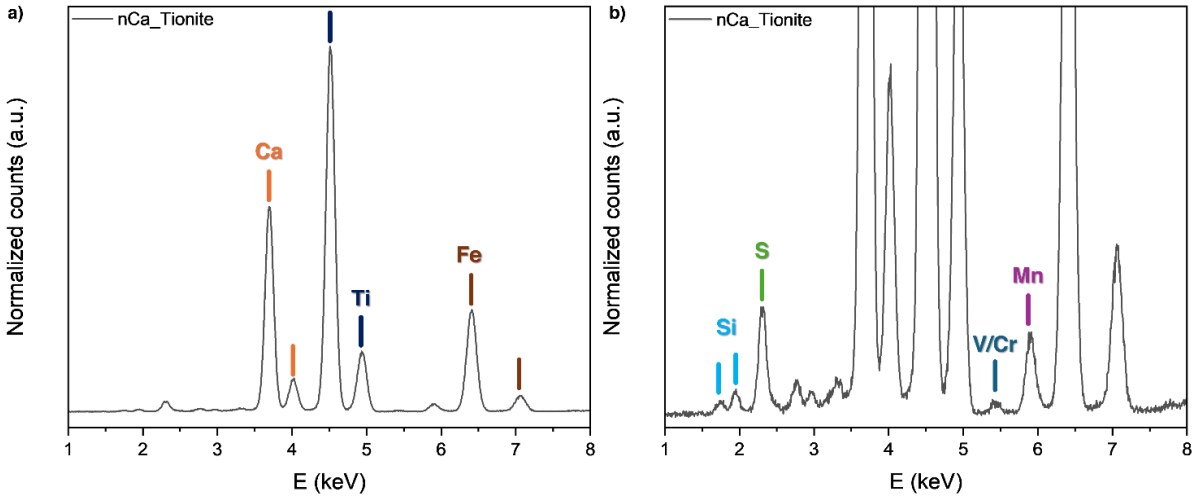

Figure 2.3: a) XRF spectra for nCa_Tionite and b) magnification to highlight low intensity peaks. The element attributed to each signal is reported

Anyway, quantitative information about the sample composition is reported in the datasheet provided by the producing industry. Specifically, TiO_2 is the most abundant component of the material, accounting for almost 30 % of the sample. In addition, nCa_Tionite contains a non-negligible amount of Si (16 % as SiO_2) and Ca (12.7 % as CaO), with small traces of Fe, Al and Mn (2.48 % as Fe_2O_3, 2.99 % as Al_2O_3 and 0.34 % as MnO). In addition, by the CHNS elemental analysis, the non-metallic components of nCa_Tionite were quantified (Table 2.1). The results show that nitrogen is virtually absent, while a considerable weight percentage of sulfur was detected, attributable to traces of sulfuric acid or its by-products still included in the samples. It must be highlighted the high content in carbon, whose nature is not clear.

Table 2.1: CHNS elemental analysis results for nCa_Tionite

C (%)	H (%)	N (%)	S (%)
4.38	1.37	0.12	4.40
4.89	1.54	0.09	5.15
3.83	1.71	0.32	4.08
4.4 (±0.5)	1.5 (±0.2)	0.2 (±0.1)	4.5 (±0.5)

In order to understand how these elements are combined in nCa_Tionite, XRD analysis was performed. The XRD pattern (Figure 1.4) shows a large number of peaks, indicating the presence of several crystalline phases. The main phases are attributed to TiO_2 in both anatase and rutile form. In addition, gypsum ($CaSO_4 \cdot 2H_2O$) is also included in the samples, which explains the high quantities of Ca and S detected in the previous analysis. Calcite ($CaCO_3$) is clearly identified by its signals and that could explain the carbon detected by CHNS analysis. At first sight, the presence of $CaCO_3$ is suspicious because the material went through an acidic treatment, which should eliminate this type of inorganic species in the form of CO_2 and H_2O. However, the neutralization process involved lime that, contrarily to commercial $Ca(OH)_2$, includes several impurities, such as $CaCO_3$. Finally, other components identified by the diffractogram are pseudobrookite ($FeTiO_3$) and an amorphous phase, that provides the wide peak centered at low 2θ values.

A crucial aspect for the photocatalytic application relies on the rutile content in the sample compared to the anatase one, and the nCa_Tionite sample exhibits a very high rutile/anatase ratio of 82:18.

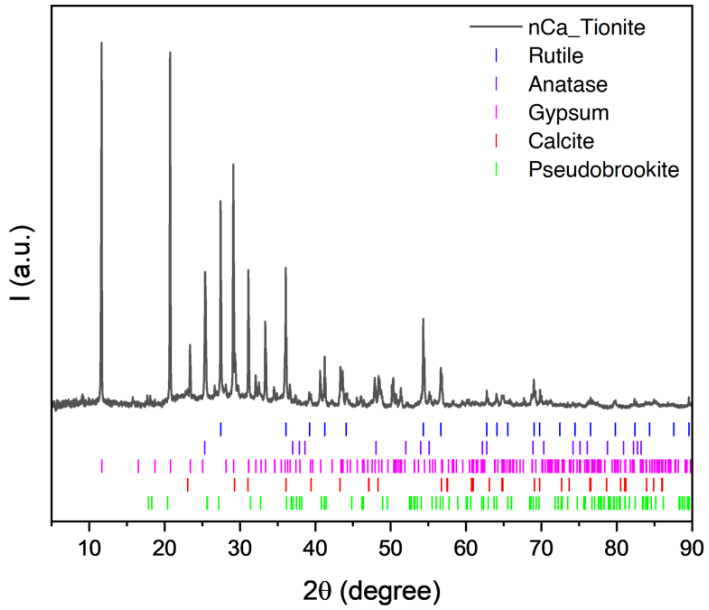

Figure 2.4: XRD pattern of nCa_Tionite. At the bottom, reference diffractograms of rutile (blue), anatase (purple), gypsum (pink), calcite (red) and pseudobrookite (green) are reported.

The Raman spectrum of nCa_Tionite (Figure 2.5) corroborates the XRD results. Indeed, the signals attributed to both anatase and rutile TiO_2 phases, [17] calcite,[18] and gypsum [19] could be detected, according to the attributions reported in Table 2.2.

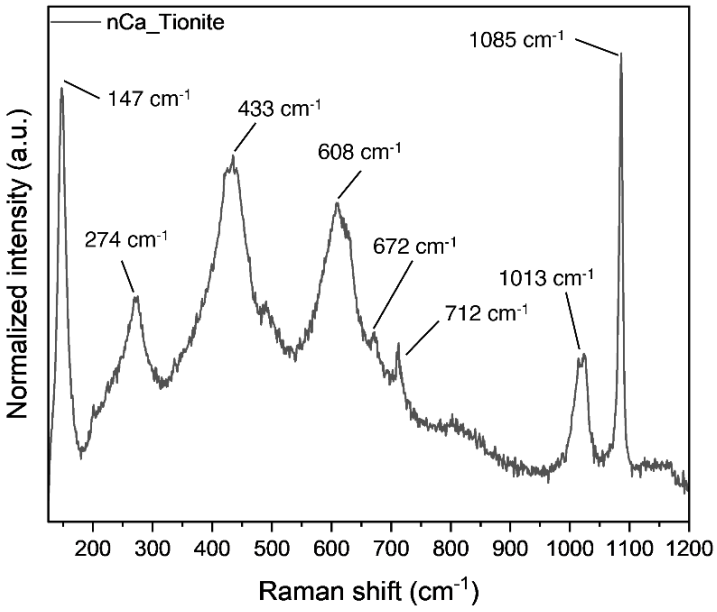

Figure 2.5: Raman spectrum of nCa_Tionite. Positions of peaks are indicated

Table 2.2: attributions of Raman peaks for nCa_Tionite

Raman shift (cm^{-1})	Spatial group	Attribution
147	E_g (Anatase), B_{1g} (Rutile)	Anatase and rutile
274	E_g	Lattice modes of calcite
433	E_g	Rutile
608	A_{1g}	Rutile
672	B_g	Asymm. bending SO_4^{2-}
712	E_g	In-plane bending CO_3^{2-}
1013	A_g	Symm. stretching SO_4^{2-}
1085	A_{1g}	Symm. stretching CO_3^{2-}

The FTIR spectrum of the nCa_Tionite sample (Figure 2.6) confirms the presence of the $CaSO_4$ gypsum phase.[20] In fact, the bands of OH stretching and bending, at 3532, 3399 cm^{-1} and at 1619, 1683 cm^{-1}, respectively, in combination with the signal at 668 and 600 cm^{-1}, attributed to sulfate bending, can be observed. Moreover, the signals at 1125 and 1004 cm^{-1} confirm the presence of silica[21] or silicate[22], supporting the composition analysis results. The signals at 709, 872 and 1418 cm^{-1} can be attributed to different CO_3^{2-} stretching vibrations of calcite [23]. Finally, the band in the region

between 900 and 500 cm^{-1} is associable with several metal-O signals, including Ti-O stretching.[24] More details on attributions are listed in Table 2.3.

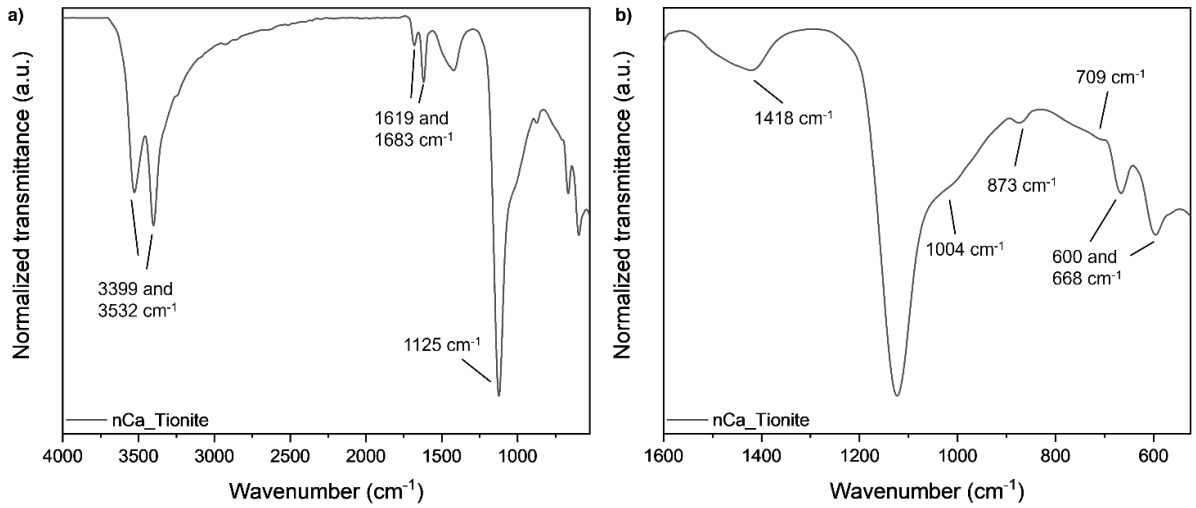

Figure 2.6: a) ATR-FTIR spectra for nCa_Tionite and b) magnification of the lower wavenumber region. The position of each peak is indicated

Table 2.3: attributions of ATR-FTIR peaks for nCa_Tionite

Wavenumber (cm^{-1})	Assignment
3532 and 3399	O-H stretching of gypsum water
1683 and 1619	O-H bending of gypsum water
1418	CO_3^{2-} asymm. stretching
1125	Si-O-Si and SO_4^2 asymm. stretching
1004	Si-O in-plane stretching
873	CO_3^{2-} asymm. stretching
709	CO_3^{2-} symm. stretching
668 and 600	SO_4^{2-} asymm. bending of gypsum

TGA analysis provided information on thermal phenomena of nCa_Tionite (Figure 2.7a). Due to the complex and not completely defined composition of the material, it's not possible to attribute each weight loss to a specific phenomenon, however some hypotheses can be formulated. Specifically, part of the weight loss up to 150 °C could be related to adsorbed water molecules and gypsum dehydration steps: at a temperature above 95 °C bassanite ($CaSO_4 \cdot 0.5\ H_2O$) is the more stable phase,

whereas above 120 °C anhydrite is obtained ($CaSO_4$).[25] The weight loss between 650 and 750 °C can be associated to the calcite decomposition to CaO.[26] The attribution of the thermal phenomena occurring between 300 and 400 °C is not straightforward, due to the lack of exhaustive comprehension of the material composition. However, the analysis coupling TGA with FTIR spectroscopy (Figure 2.7b,c) revealed that the most relevant signal detected between 300 and 400 °C corresponds to CO_2 release. Considering the temperature range, the phenomena can be associated with the decomposition of organic compounds or inorganic oxalate[27,28] and carbonates. Both organic molecules and oxalates can be excluded because they are easily detected by ATR-FTIR spectroscopy. Among the carbonate compounds, $MgCO_3$ is the only one that decomposes at such low temperatures[29], but this result is inconsistent with both composition and XRD results. The last option is that CO_2 could tentatively derive from the thermal decomposition of an amorphous carbon phase.

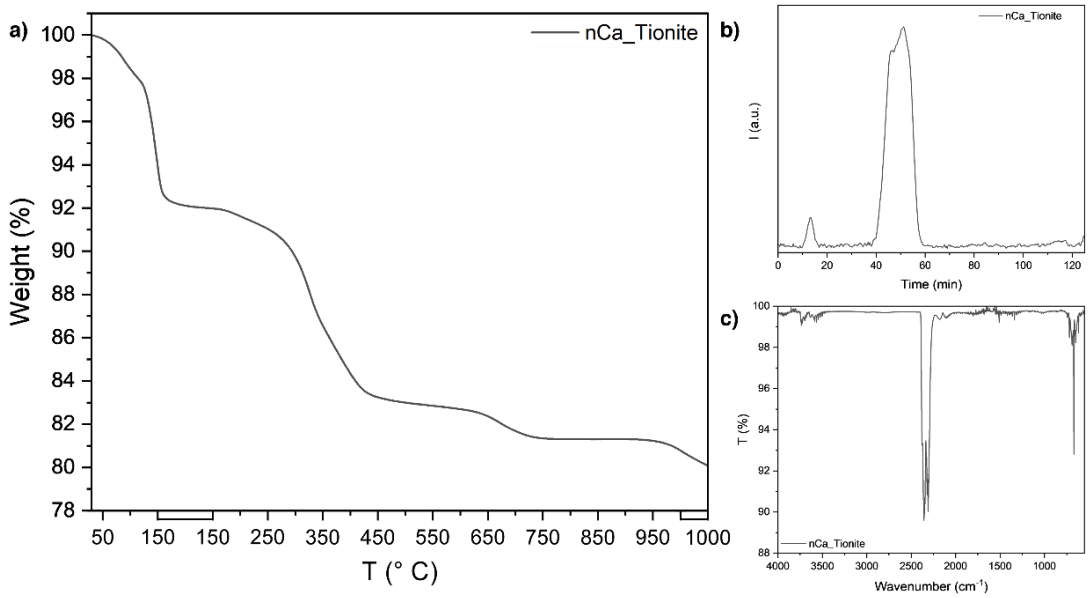

Figure 2.7: a) TGA thermogram, b) IR intensity signal and c) IR spectra at 45 min obtained by TGA-FTIR for nCa_Tionite.

Preliminary information regarding tionite particles' dimensions was obtained by the granulometric analysis. The particle size distribution of tionite is shown in Figure 2.8. The plot indicates the presence of primary particles with an average diameter of 0.55 µm, so in the nanometric range, which form aggregates of two different dimensions, equal to about 6 µm and 50 µm. The overall particles' size distribution is described by D_{10} = 1.25 µm, D_{50} = 22.4 µm and D_{90} = 62.4 µm, meaning that 90 % of analyzed

particles have a diameter below 62.4 µm.

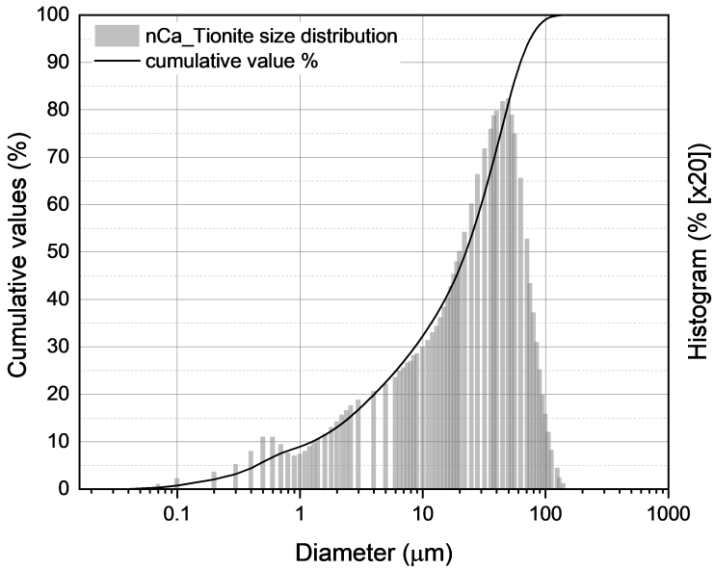

Figure 2.8: granulometry results for nCa_Tionite

From the morphological point of view, SEM images (Figure 2.9a) of nCa_Tionite show a complex material with no defined or uniform morphology, even if the characteristic rod-shaped crystals[30] (red arrows in figure) confirm the presence of gypsum. More detailed morphological information was provided by TEM microscopy. The micrographs evidence the different morphology of nCa_Tionite with nanometric aggregated particles (Figure 2.9b) and bigger lamellar structures showing small particles distributed on their surface.

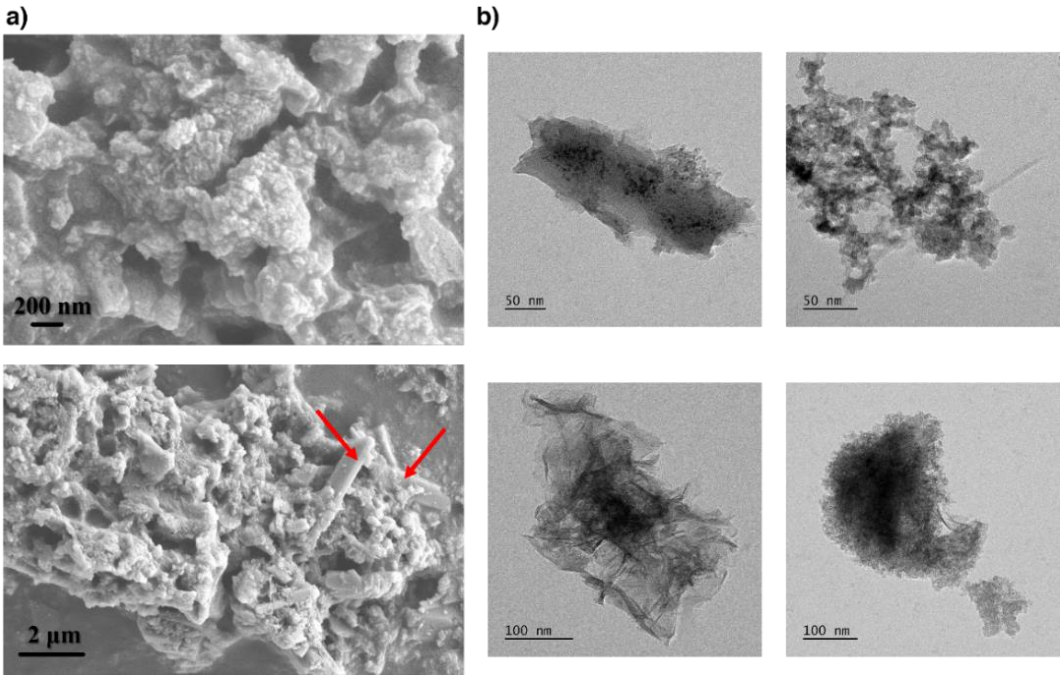

Figure 2.9: a) SEM and b) TEM images of Tionite_Ca. Red arrows indicate the rod-shaped crystals of $CaSO_4$

By combining SEM and EDX analysis, further information about the composition and combination of the constitutive elements of nCa_Tionite was collected.

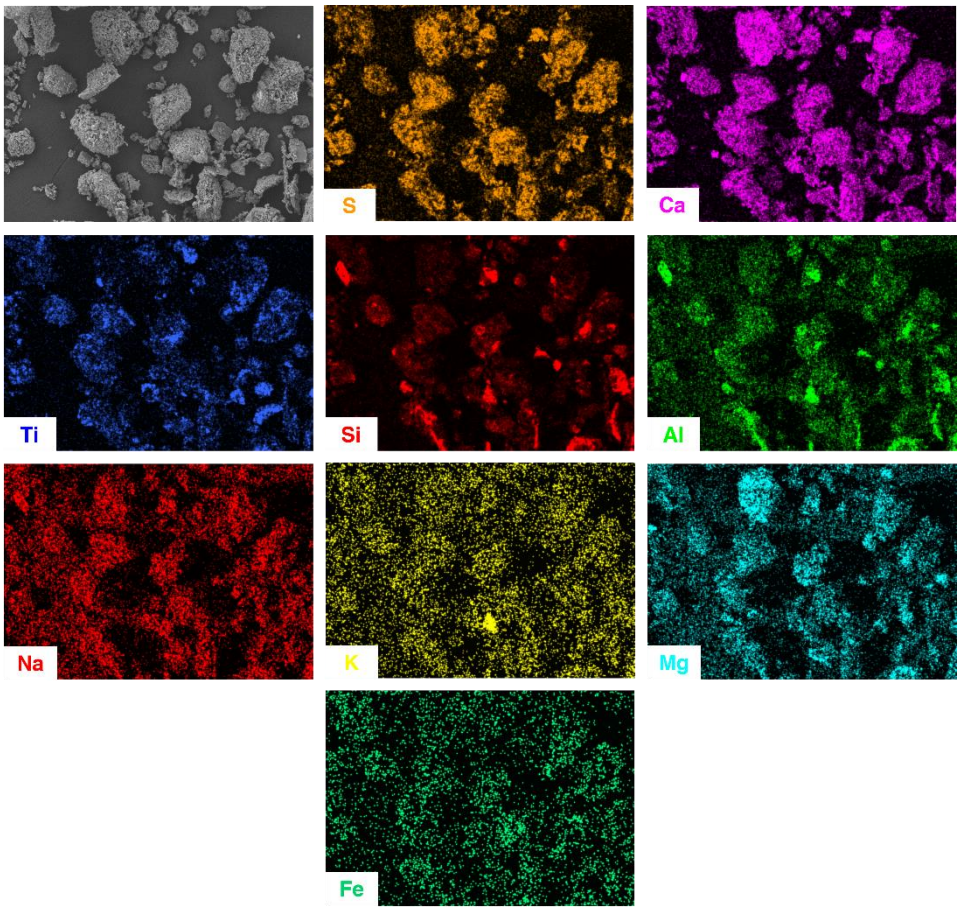

Figure 2.10: SEM-EDX maps for nCa_Tionite (1000x magnification)

EDX maps (Figure 2.10) show the colocalization of Ca and S, further confirming the presence of $CaSO_4$ in the material. Ti forms isolated TiO_2 structures uniformly distributed. Si, Al, Mg, Na and K species are distributed randomly and their colocalization suggests the presence of Mg-rich aluminosilicates with Na and K acting as counterions. Fe was also detected in a limited quantity and randomly distributed in the whole sample.

Finally, DRS was performed to study the electronic structure of nCa_Tionite. The spectrum (Figure 2.11) shows a reflectance decrease corresponding to the bad gap of P25; however, the variation is too low to allow a proper estimation of the nCa_Tionite band gap. In addition, although the absorbance value is not directly known, the sample has a dark gray colour; therefore, the lower reflectance observed in the visible range can be reasonably associated to an adsorption of light.

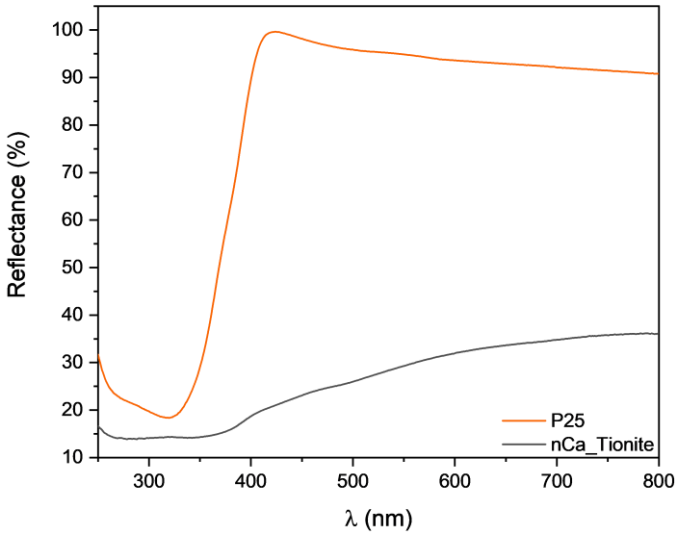

Figure 2.11: DRS spectrum for nCa_Tionite. P25 is used as reference

2.3.2 Structural and morphological characterization of nNa_Tionite and nNa_Tionite_prec

According to the results reported in Paragraph 2.3.1, the high amount of $CaSO_4 \cdot 2H_2O$ detected in nCa_Tionite originated from the neutralization reaction between $Ca(OH)_2$, in the form of lime, and residual traces of H_2SO_4. For this reason, the utilization of NaOH as neutralizing agent was tested with the aim of eliminating the sulfate anions in the form of water-soluble Na_2SO_4 and, consequentially, simplifying tionite composition. The formation of a white precipitate after the addition of $Ca(NO_3)_2$ to the supernatant suggests the correctness of our hypothesis. The chemical composition of nNa_Tionite_prec was investigated by ATR-FTIR spectroscopy.

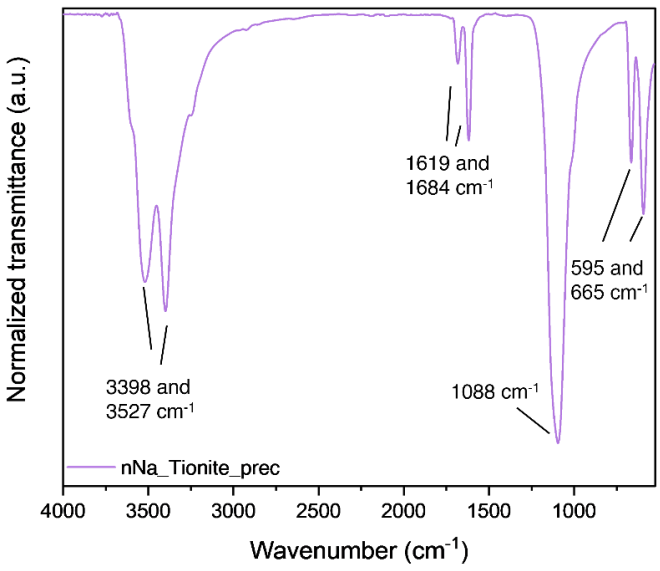

Figure 2.12: ATR-FTIR spectra of nNa_Tionite_prec. Signals position is indicated

The spectrum reported in Figure 2.12 provides signals perfectly matching the results obtained for nCa_Tionite and described in Figure 2.6 and Table 2.3. Specifically, the precipitate consists of $CaSO_4 \cdot 2H_2O$ and this is made possible because the different hydration grades of calcium sulfate provide deeply different IR signals.[20] This represents a small pass towards a more sustainable approach which allows to recovery not only tionite, but also sulfate anions in the form gypsum, which is commonly applied in everyday life.

Focusing on nNa_Tionite, the XRF spectrum (red spectrum in Figure 2.13a) indicates a composition similar to nCa_Tionite, with Ti and Fe providing the strongest signal. A net decrease in the Ca content and the disappearance of the sulfur signal at 2.31 keV suggest the effective removal of the inorganic sulfate from the sample. The absence of $CaSO_4$ was also confirmed by CHNS analysis (Figure 2.13b) as the sulfur wt. % is virtually null, especially when compared to nCa_Tionite. However, the remarkable carbon content of tionite remains unaltered.

a)

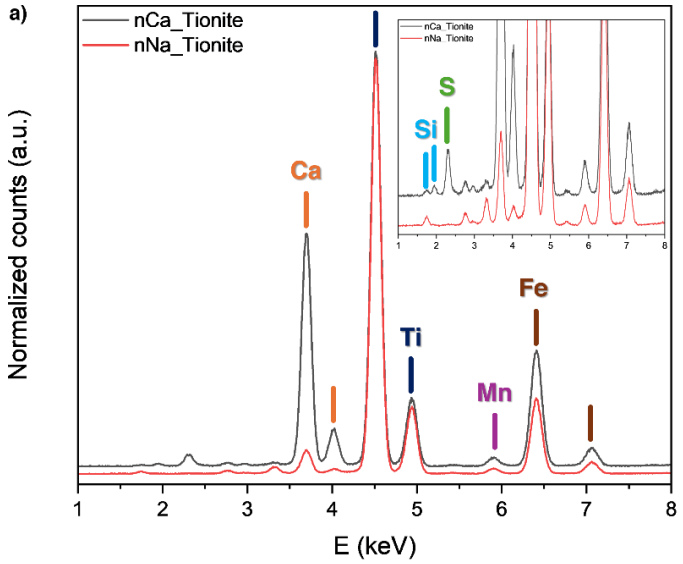

b)

C (%)	H (%)	N (%)	S (%)
5.17	1.07	0.23	0.241
4.78	1.13	0.30	0.311
5.28	1.12	0.31	0.278
5.1 (±0.3)	1.11 (±0.03)	0.28(±0.04)	0.28 (±0.04)

Figure 2.13: a) XRF spectra and b) CHNS analysis for nNa_Tionite. The XRF spectra for nCa_Tionite (black) is shown for comparison

From the XRD diffractogram it is noticed that the main signals of nNa_Tionite are attributable to the rutile and anatase phase of TiO_2. The rutile/anatase weight ratio (86:14) did not change significantly with respect to nCa_Tionite. In addition, the patterns related to both calcite and gypsum are absent in the nNa_Tionite diffractogram (Figure 2.14a). It is worth noticing that the XRD diffractograms of both nCa_Tionite and nNa_Tionite samples show a broad halo in the 2θ range between 20

and 40° that, according to previous observations, can be ascribed to the presence of amorphous phases. The carbonaceous nature of this phase can be inferred, by considering that the amount of carbon in the two samples is similar, even though the calcite component is absent in the nNa_Tionite one. Moreover, the contribution of an amorphous siliceous component is also probable. The Raman spectrum of the nNa_Tionite sample (Figure 2.14b) shows the main signals of rutile and anatase TiO_2; the residual peak at 260 cm^{-1} is attributed to a multi-phonon process typical of rutile.[31] At the same time, the signals above 650 cm^{-1} detected for nCa_Tionite and attributed to the two inorganic species containing Ca (gypsum and calcite) are absent (see attribution in Table 2.2).

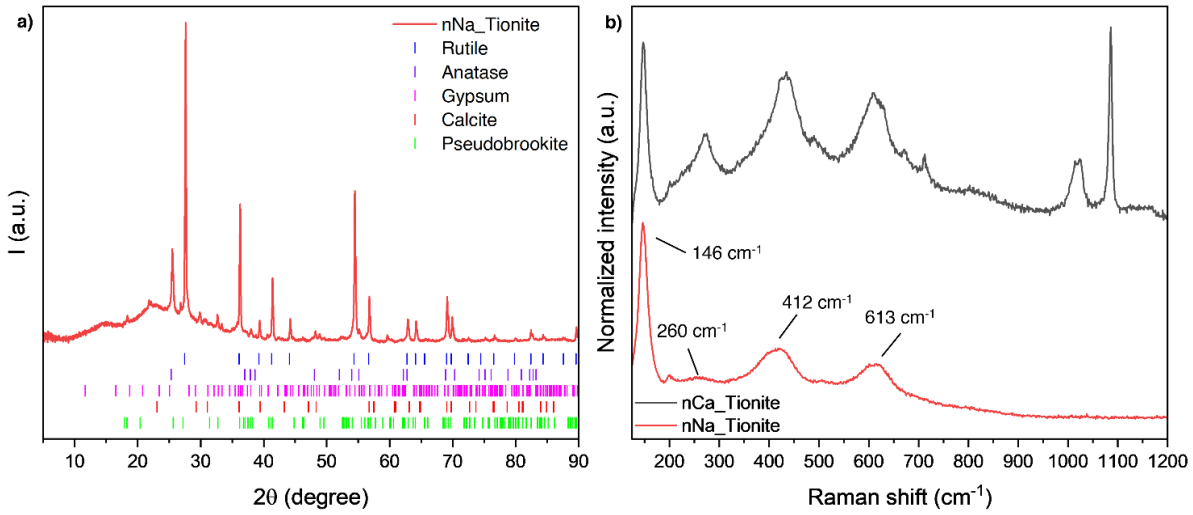

Figure 2.14: a) XRD spectra of nNa_Tionite; at the bottom, reference diffractograms of rutile (blue), anatase (purple), gypsum (pink), calcite (red) and pseudobrookite (green) are reported. b) Raman spectra comparison between nCa_Tionite (black) and nNa_Tionite (red); signals Raman shift is indicated.

The ATR-FTIR spectrum of nNa_Tionite (Figure 2.15a) exhibits some of the bands already observed for nCa_Tionite: specifically, the band between 500 and 800 cm^{-1} attributed to metal-O bonds stretching, including Ti-O bond, and the signal at 1057 cm^{-1} due to Si-O-Si bond stretching. However, the spectrum did not show the signals attributed to inorganic sulfate and carbonate, further confirming the efficiency of the new neutralization process.

nNa_Tionite thermogram in Figure 2.15b exhibits only one major weight loss between 250 and 450 °C, associated to CO_2 loss (TGA-FTIR Figure 2.15c,d), which was also observed for nCa_Tionite. The water release at temperature below 150 °C is of lower extent with respect to the nCa_Tionite sample. On the other hand, the weight loss

between 650 and 750 °C, observed for nCa_Tionite, is absent, further confirming the absence of calcite in the sample.

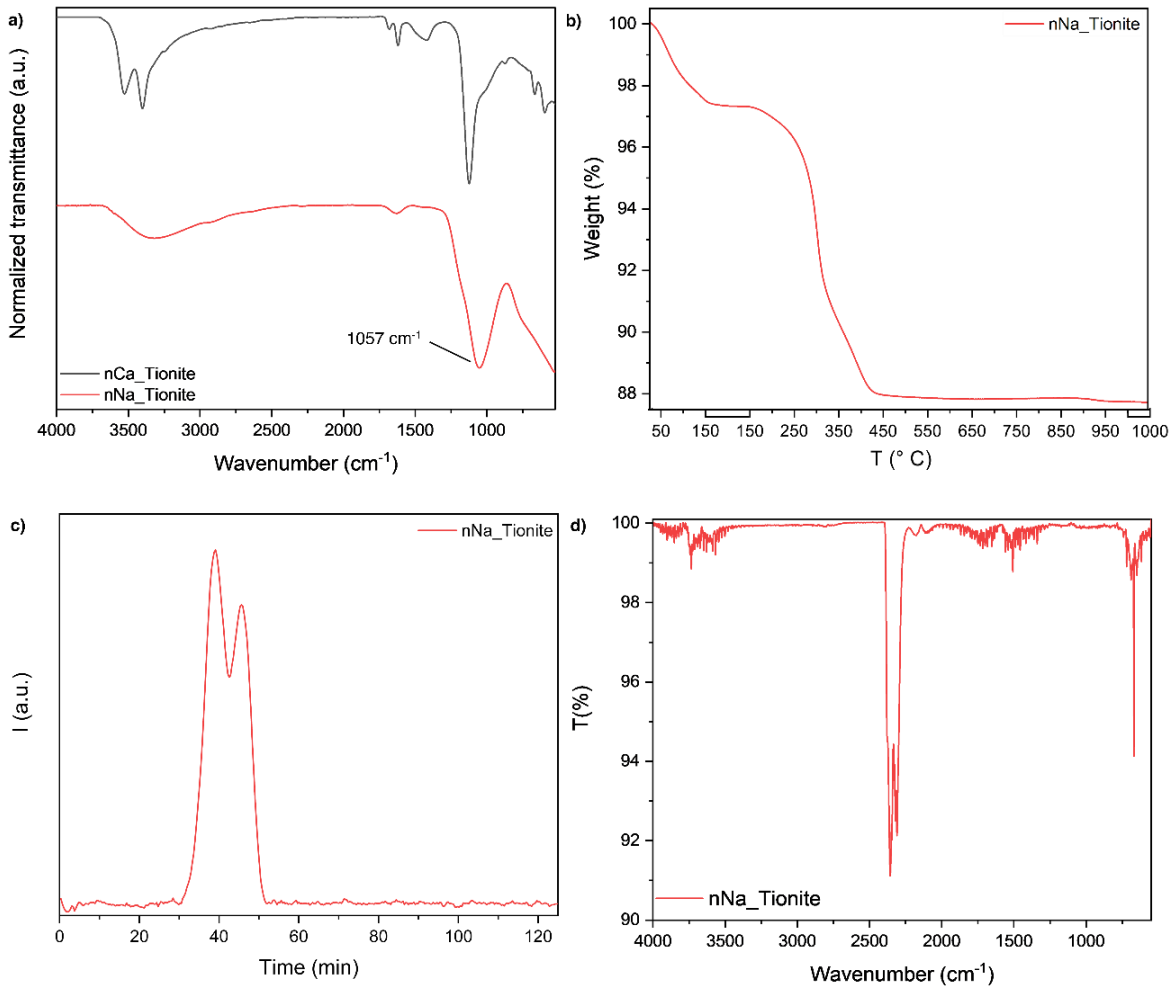

Figure 2.15: a) ATR-FTIR spectrum of nNa_Tionite (red) compared to nCa_Tionite (black), b) TGA thermogram , c) IR overall intensity signal and d) IR spectra at 45 min obtained by TGA-FTIR analysis for nNa_Tionite

Morphological information was provided by SEM images (Figure 2.16a) which suggest that nNa_Tionite consists of particles of different morphologies with inhomogeneous dimensions, ranging from fraction of μm to more than 10 μm. However, bidimensional sheet-like particles can be observed throughout the sample, as also confirmed by TEM micrographs (Figure 2.16b), showing nNa_Tionite as aggregated nanometric particles and sheets-structured elements which, at a higher magnification, result decorated by smaller NPs.

SEM analysis with EDX mapping (Figure 2.17) was performed in order to highlight the elemental distribution within nNa_Tionite samples.

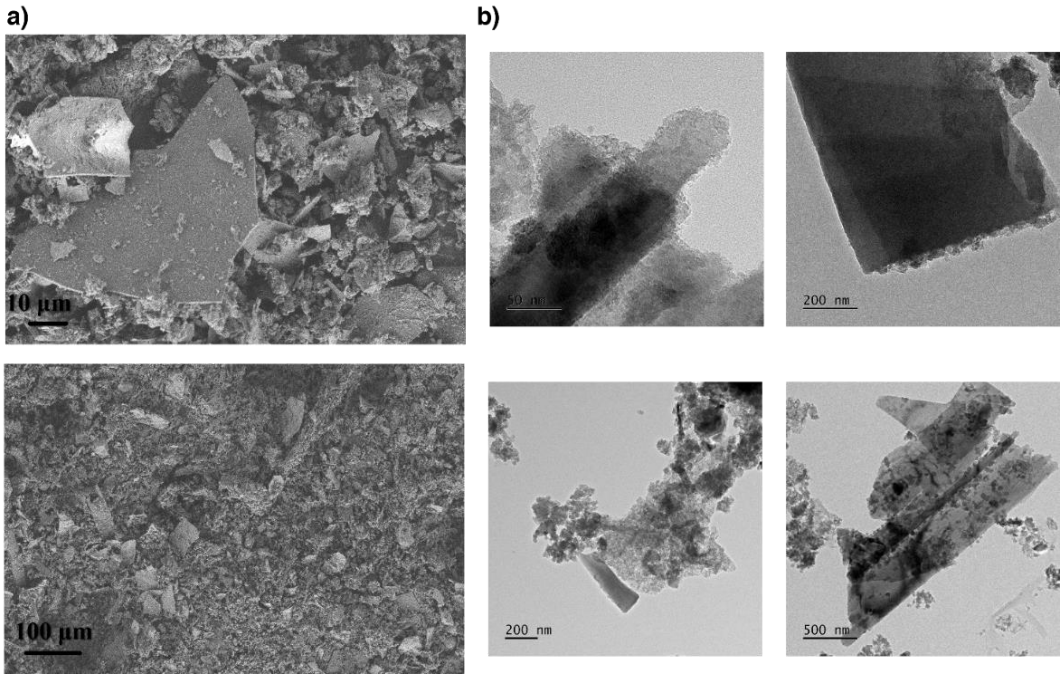

Figure 2.16: a) SEM images and b) TEM micrographs of nNa_Tionite

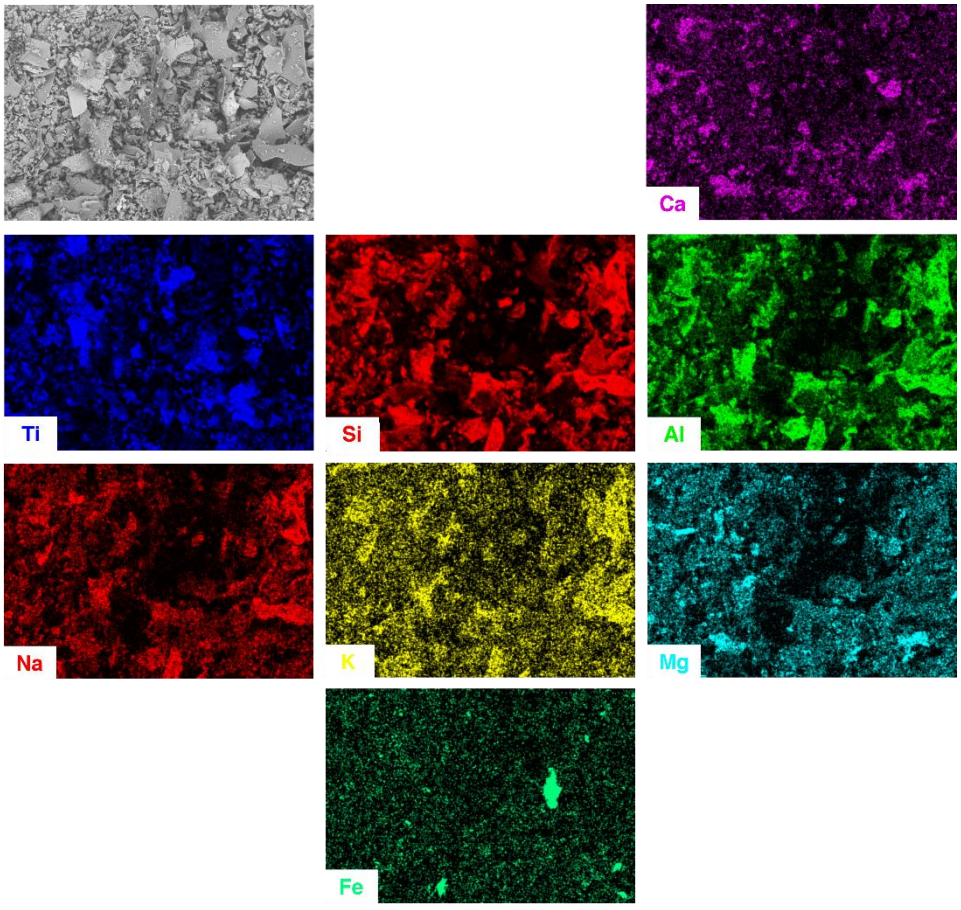

Figure 2.17: SEM-EDX maps for nNa_Tionite (1000x magnification)

In the nNa_Tionite sample, titanium is distributed uniformly, even if the silicon amount in the sample is remarkable when compared with the nCa_Tionite sample. Notably, Si atoms are co-localized on sheet-like particles with Al, Mg, Na, K, and Ca species present in lower quantities, suggesting that the bidimensional elements of nNa_Tionite are essentially aluminosilicate with Na, Mg, K and Ca acting as counterions. Finally, iron species are low in extent and inhomogeneously distributed in the nNa_Tionite sample, whereas sulfur is absent. TEM-EDX analysis (Figure 2.18) further confirms the colocalization of Si, Al, Na and Mg on sheet-like particles; in addition, a small part of Ti is localized on these bidimensional particles, which could suggest that the small decorating particles could be made of TiO_2.

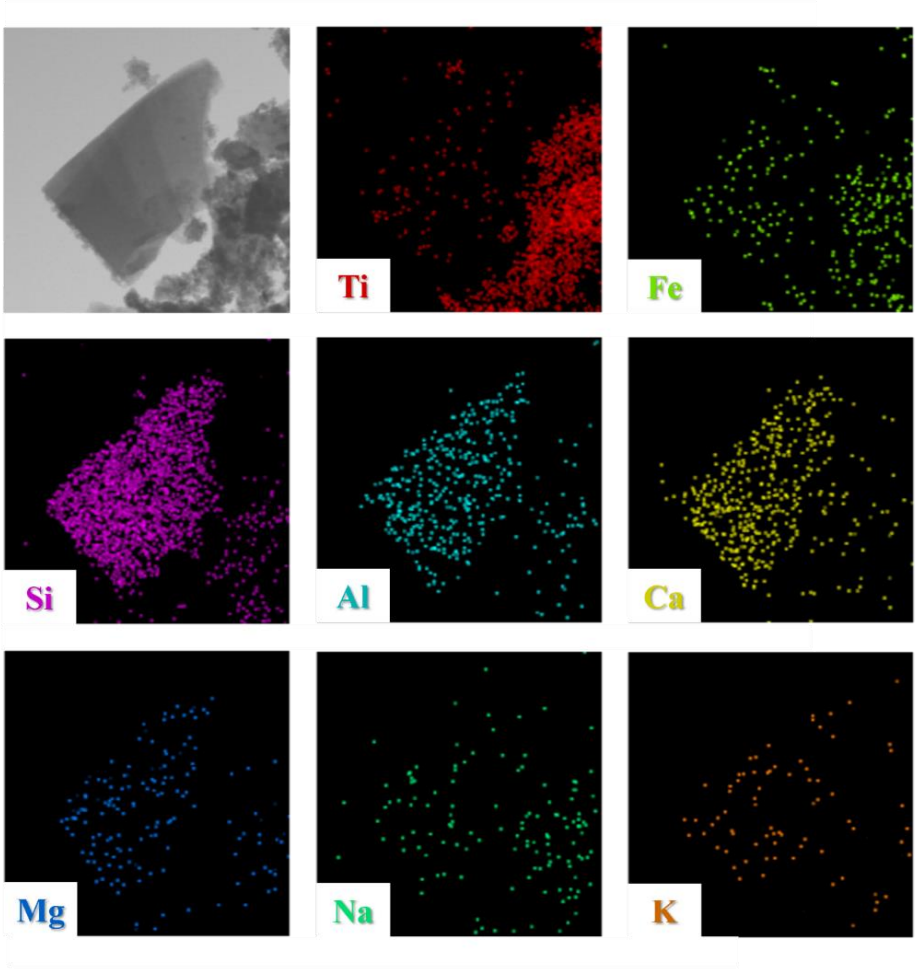

Figure 2.18: TEM-EDX maps for nNa_Tionite

Finally, DRS was performed on nNa_Tionite and the spectrum shows a more evident TiO_2 band gap compared to nCa_Tionite, probably thanks to the higher concentration of the oxide due to the removal of impurities (Figure 2.19).

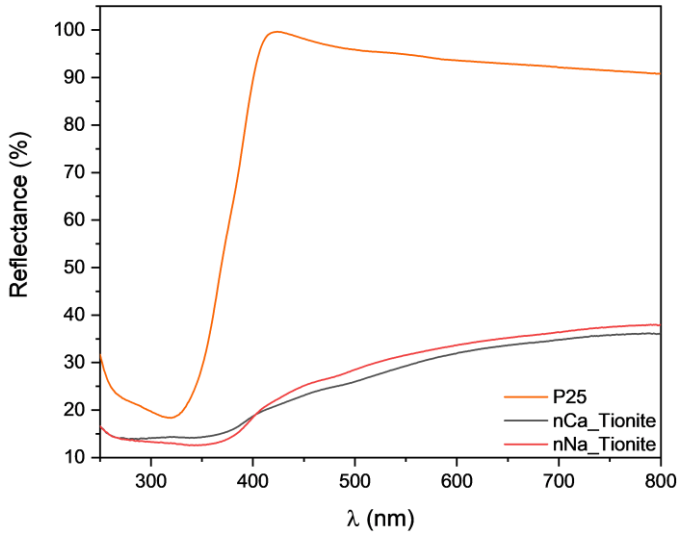

Figure 2.19: DRS spectrum of nNa_Tionite (red). P25 (orange) and nCa_Tionite (black) spectra are reported as references.

2.3.3 Structural and morphological characterization of nNa_Tionite_A and nNa_Tionite_B

Further purification steps were carried out only on the nNa_Tionite sample, due to its simpler chemical composition compared to the nCa_Tionite one. To further enhance the relative amount and the accessibility of the titanium dioxide component for photocatalytic applications, a basic and an acidic treatment were performed in order to remove the photocatalytically inert aluminosilicate counterpart and the traces of metal ions, which could act as recombination centres for the photogenerated charges, thus possibly reducing the photocatalytic activity.

The changes in the composition of nNa_Tionite after the treatment with NaOH (nNa_Tionite_B) can be highlighted by means of XRF and ATR-FTIR spectroscopies, as reported in Figure 2.20. The XRF spectra (Figure 2.20a) show that the basic treatment only slightly reduced the intensity of the iron signals, while, more interestingly, it completely removed the K and Si signals. These results are confirmed by ATR-FTIR spectroscopy (Figure 2.20b) as the spectrum of nNa_Tionite_B shows the dramatic reduction of the Si-O-Si bond stretching band at 1057 cm^{-1}, also supported by the decrease of the amorphous phase in the XRD spectrum (Figure 2.22a). The analysis of precipitate_B confirms the presence of Si XRF signals along with traces of Ti, while the ATR-FTIR spectrum clearly shows the presence of the Si-O-Si stretching signal at 1057 cm^{-1}. Consequentially, Si is the main element dissolved during the basic treatment, confirming its removal.

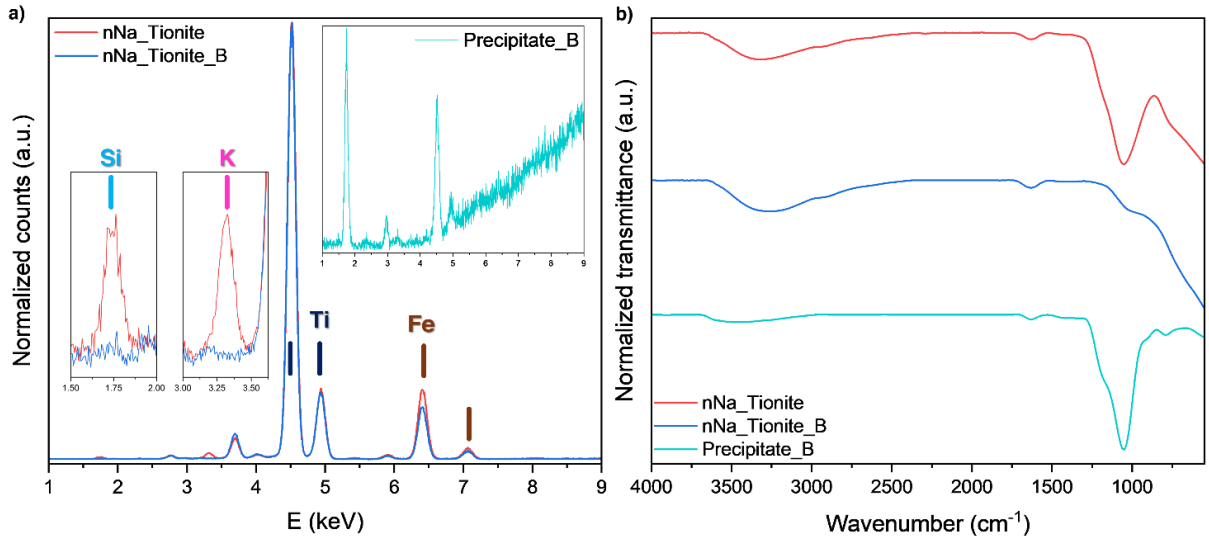

Figure 2.20: a) XRF and b) ATR-FTIR spectra for nNa_Tionite_B (blue) and precipitate_B (light blue). nNa_Tionite (red) is reported as reference. In the XRF spectrum, two insets highlight the changes in the Si and K signals.

Regarding the acidic treatment, the complete removal of the silicate component from the sample was obtained as suggested by XRF and FTIR (Figure 2.21a,b) and XRD (Figure 2.22a) spectra, even if with a more remarkable decrease in the concentration of Fe, Ca and Mn, compared to nNa_Tionite_B. Indeed, the XRF spectrum of precipitate_A clearly shows the presence of both Ti and Fe while ATR-FTIR analysis shows, alongside with the typical Si-O-Si stretching signal at 1057 cm^{-1}, a band between 525 and 750 cm^{-1} due to Me-O bond stretching. The higher dissolving power of HF, compared to NaOH, easily explains the removal of several metals; however, thanks to the normalization of XRF spectra on Ti signal, nNa_Tionite_A shows a more simplified composition than the basic treated version.

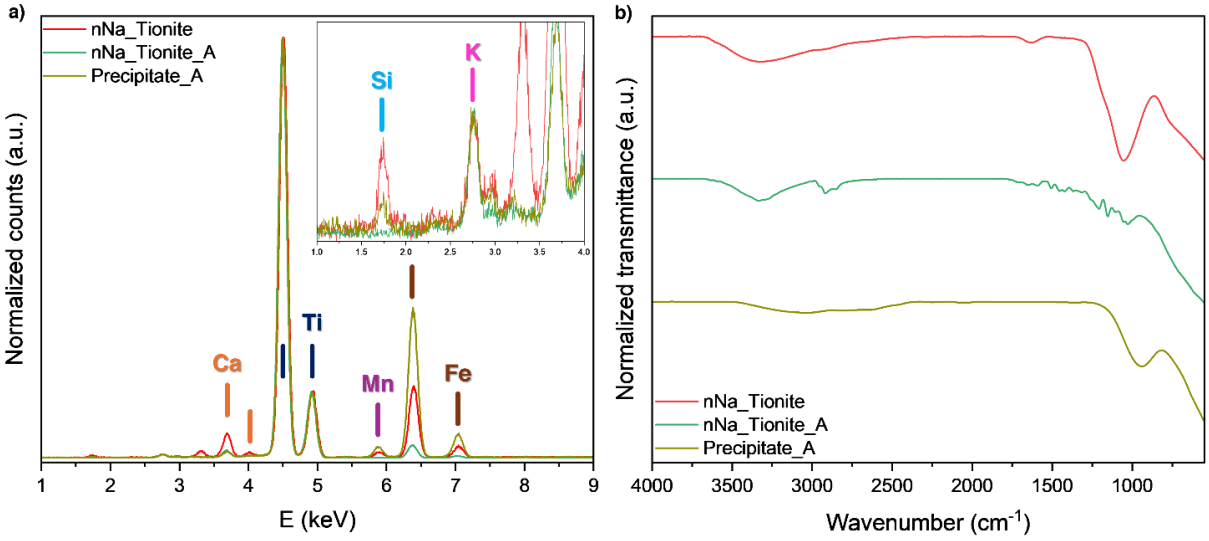

Figure 2.21: a) XRF and b) ATR-FITR spectra for nNa_Tionite_A (green) and precipitate_B (military green). nNa_Tionite (red) is reported as reference. In the XRF spectrum, the inset highlights the change in Si and K signals.

Interesting results are shown by the TGA analysis of different samples. In fact, the thermograms (Figure 2.22b) show a higher weight loss for the HF-treated sample, compared to the other samples. Specifically, the difference is observed in the temperature range 250 - 450 °C: all samples provide a weight loss between 9-9.5 wt. %, while for nNa_Tionite_A it is equal to 20 wt. %. Considering the combined TGA-FTIR results, the acidic treated sample has a two-fold increase in the amorphous carbon compounds, due to the stronger simplification in its composition.

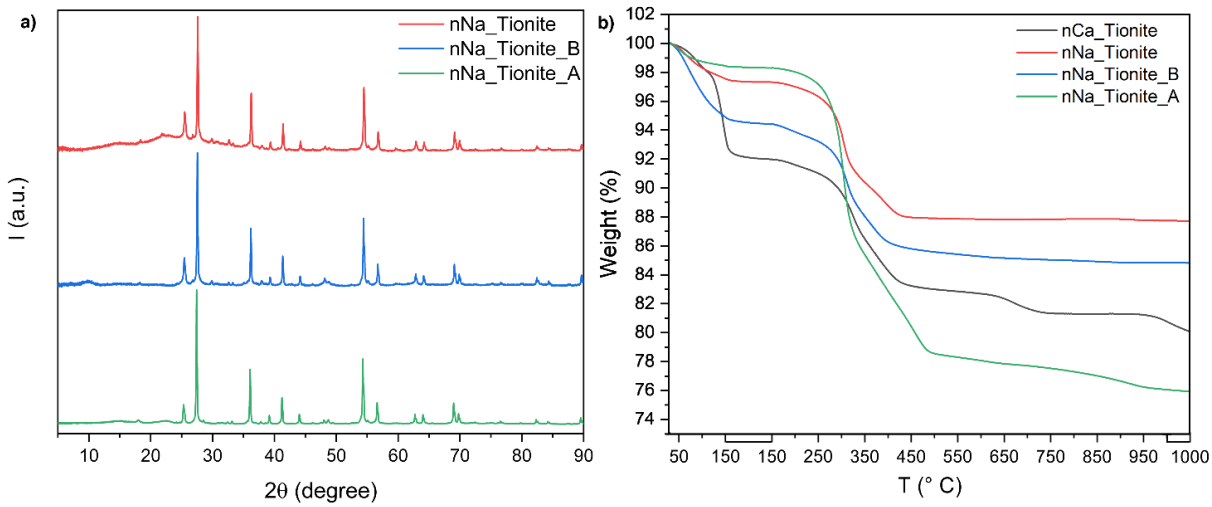

Figure 2.22: a) XRD spectra and b) TGA thermograms comparison for nNa_Tionite (red), nNa_Tionite_B (blue) and nNa_Tionite_A (green). For TGA, the result for nCa_Tionite (black) is shown for comparisons

To further assess the variation in composition taking place upon acidic or basic treatment, SEM-EDX analysis was performed (Figure 2.23). SEM images show that the basic treatment only slightly affects the morphology of the sample, while the acidic treatment produces major changes in terms of particles size and shape. The net decrease in the amount of both Si and Al, as indicated by XRF and FTIR analyses for both samples, is therefore evident from the EDX images of the nNa_Tionite_B sample, while it could be masked by the morphological changes in the nNa_Tionite_A sample. Similar conclusions can be drawn for other elements, like Mg and Ca.

Finally, the electronic structure of both treated tionite samples was investigated by DRS spectroscopy. The samples, reported in Figure 2.24, present a significant adsorption in the visible range. In addition, changes in the shape of the spectrum can be detected, but the drop in the reflectance value in the region of the TiO_2 band gap is still observable.

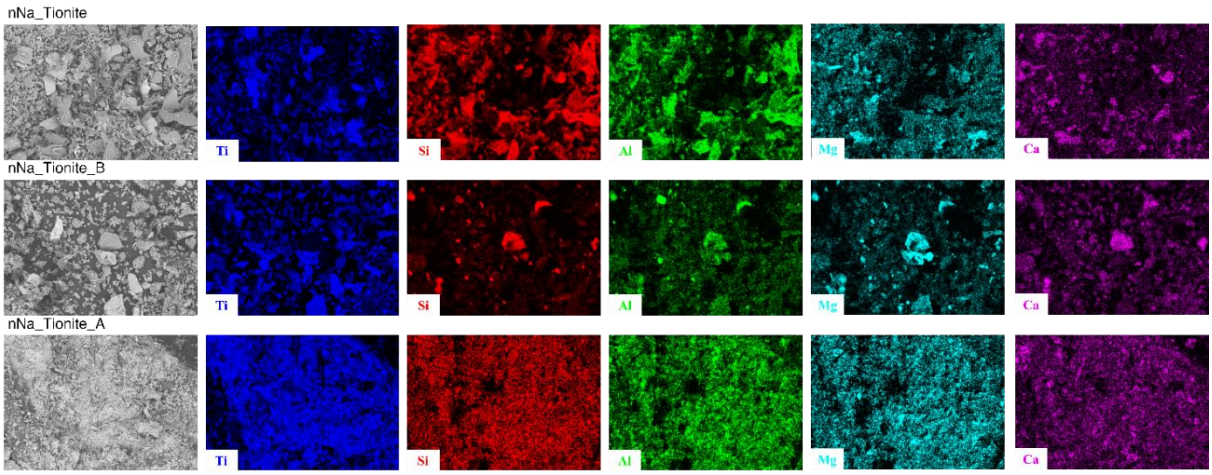

Figure 2.23: SEM images with the associated EDX mapping analysis of nNa_Tionite and nNa_Tionite_B in comparison to nNa_Tionite_A (1000x magnification).

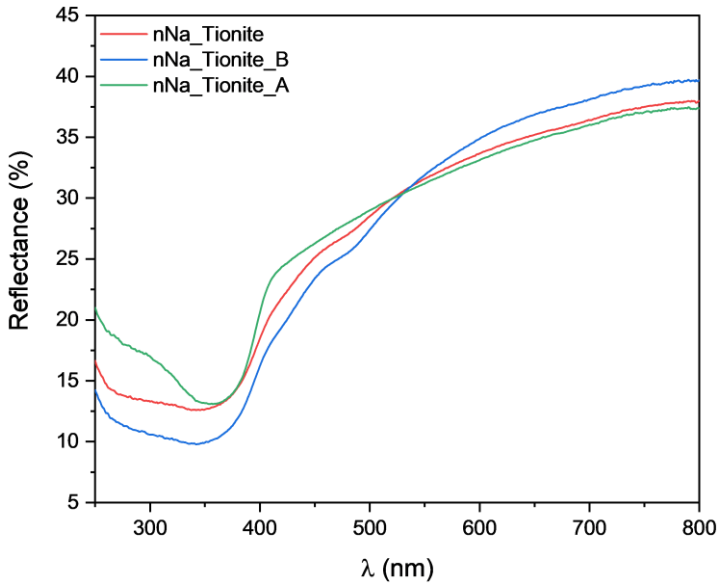

Figure 2.24: DRS spectra for nNa_Tionite_B (blue) and nNa_TIonite_A (green). nNa_Tionite spectrum (red) is shown as reference

2.3.4 Surface characterization of pristine and modified tionite materials

XPS characterization was performed on all samples. Due to the extremely complex composition, the analysis cannot be used to investigate variations in the chemical state of each element; however, it can be useful to highlight variations in the surface composition of the samples. The calculations to define the composition, explained in Appendix – 2, provided the results presented in Table 2.4.

By comparing the untreated nCa_Tionite and nNa_Tionite samples, the XPS analysis

supports that both $CaCO_3$ and $CaSO_4$ are totally exposed on the surface since the neutralization process with NaOH completely removes both Ca and S species. By removing these two components, the surface composition is significantly changed, revealing new elements like Na and Fe. The basic treatment of nNa_Tionite provided a net decrease in the Si content, in accordance with the previous results. This results in a specific increase in the surface Ca concentration and in the appearance of Mg.
nNa_Tionite_A sample provided the most interesting results: its composition in the simplest of all samples. Specifically, the absence of signals attributed to Si, Al and their counterions Na and Mg suggests the complete removal of silica/aluminosilicate; however, Ca is not significantly affected by HF treatment.

Table 2.4: surface composition calculated by XPS

Element %	Ti	O	Si	Al	Ca	Fe	Mg	Na	S	F
nCa_Tionite	10.2	60.4	8.6	1.2	13.0	0.8	2.5	-	3.3	-
nNa_Tionite	16.8	63.7	13.2	0.3	0.7	2.0	-	3.4	-	-
nNa_Tionite_B	18.3	54.9	4.9	1.4	9.5	2.4	5.5	3.1	-	-
nNa_Tionite_A	14.9	29.9	-	-	15.9	-	-	-	-	39.3

A significant result is the appearance of fluoride on the nNa_Tionite_A sample surface. In fact, the surface of TiO_2 is reported to undergo a ligand exchange of the hydroxyl functinalities with the fluoride groups, promoted by their similar ionic radius. The efficiency of this displacement is strongly dependent on both the pH and fluoride concentration in the solution.[32] In particular, the process is favoured under acidic pH (approximately 3) and at high fluoride concentrations. Since the acidic treatment was performed by using a 5 % HF aqueous solution, both conditions were fulfilled. Indeed, the XPS composition shows a net decrease in the surface oxygen content in favour of fluorine.

The surface fluorination of nNa_Tionite_A was also confirmed by SEM-EDX mapping (Figure 2.25), highlighting a significant amount of fluorine in the sample, while the same element was completely absent in the other tionite samples.

Contact angle measurements were carried out to highlight the surface hydrophilicity

of the samples, which can be roughly correlated with the surface hydroxylation degree. The pictures recorded during the sessile drop procedure provided the contact angle values listed in Figure 2.26.

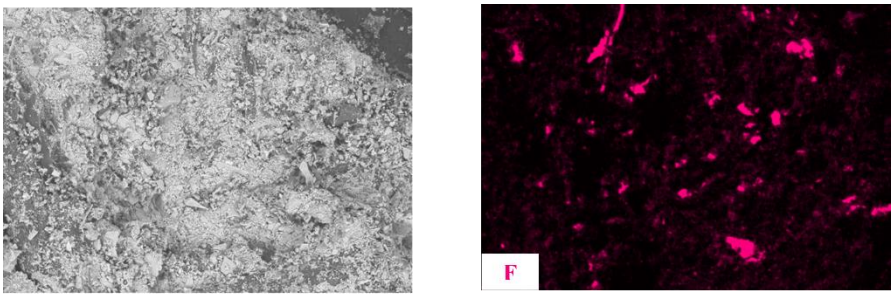

Figure 2.25: SEM image and Fluorine EDX mapping for nNa_Tionite_A. No fluorine was detected in other samples

Both nCa_Tionite and nNa_Tionite samples show a contact angle value lower than 90°, indicating their hydrophilicity. In detail, the presence of gypsum and calcite in nCa_Tionite could be responsible for the relatively higher contact angle value. The basic treatment with NaOH does not significantly alter the surface properties of the nNa_Tionite material, as the contact angle of the nNa_Tionite_B only slightly increased. Contrarily, the HF treatment leads to a net increase in the contact angle, indicating a less hydrophilic surface. This result is in agreement with the relevant literature on the fluorination of metal oxides such as TiO_2 [32–35], which is reported to confer surface hydrophobicity.

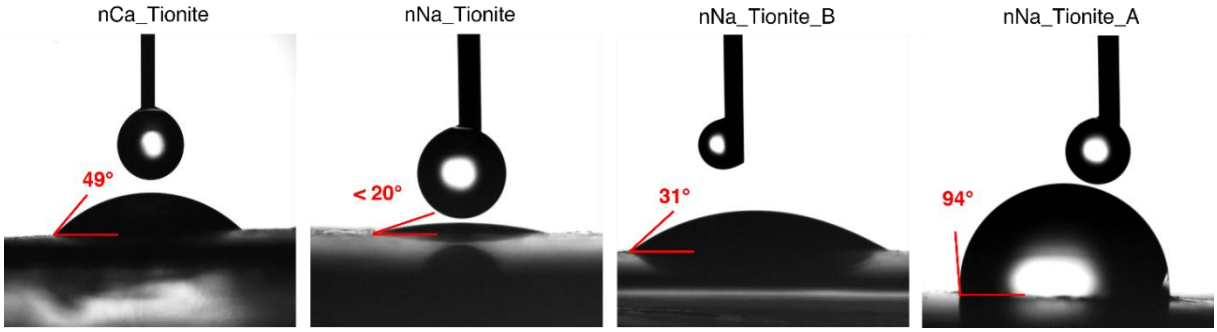

Figure 2.26: contact angle results for all samples. The measured angle is reported

N_2 isotherm adsorption analysis on each sample allowed to quantify specific surface area (SSA) and porosity. The isotherms of all samples (in Figure 2.27a) can be ascribed to type IV, according to the IUPAC classification,[36] which is typical for mesoporous materials. The hysteresis can be categorized as H3, which indicates the

presence of slit-shaped pores. Notably, the nNa_Tionite_B sample shows a significant hysteresis, with a step in the desorption branch between 0.4 and 0.5 P/P^0, with a higher surface area and pore volume compared to the others.[37] From the values listed in Figure 2.27c, it is apparent that performing the neutralization step with $Ca(OH)_2$ produces a sample with slightly lower SSA value (56 $m^2\ g^{-1}$) compared to the NaOH process (68 $m^2\ g^{-1}$). Moreover, the subsequent basic treatment of the nNa_Tionite sample produces a relatively low increase of the surface area (from 68 to 85 $m^2\ g^{-1}$), possibly due to the dissolution of the aluminosilicate component. Contrarily, the HF treatment caused a strong reduction of the SSA of the nNa_Tionite_A sample (*ca.* 7 $m^2\ g^{-1}$), below the instrumental limit). These observations are in good agreement with the porosity results reported in Figure 2.27b,c. The nNa_Tionite sample shows higher mesoporosity than the nCa_Tionite one, in agreement with the higher surface area. The subsequent basic treatment of nNa_Tionite sample strongly increased the mesoporosity, possibly due to the opening of new pores or the exposure of already existing ones, which were closed by silica-like phases. On the contrary, the reduced SSA of the nNa_Tionite_A sample is well reflected in the low porosity of the sample. Considering the higher dissolving efficiency of HF, the structure might be corroded to the point of losing porosity to a certain extent, or alternatively, the fluorine surface substitution could block or narrow mesopores as elsewhere reported.[38,39]

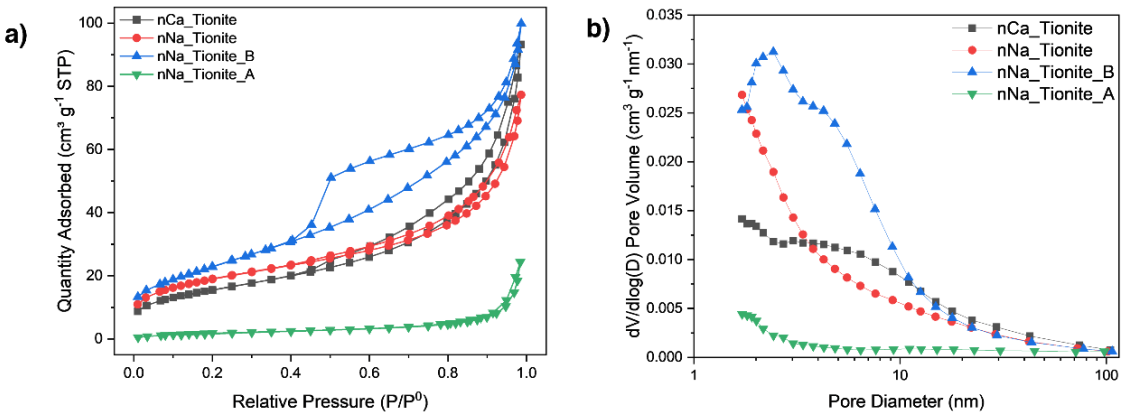

c)

	SSA ($m^2\ g^{-1}$)	V pore ($cm^3\ g^{-1}$)
nCa_Tionite	56	0.142
nNa_Tionite	67	0.112
nNa_Tionite_B	85	0.155
nNa_Tionite_A	7	0.0386

Figure 2.27: a) N_2 adsorption-desorption isotherms at 77 K, b) pore size distribution curves by BJH method and c) table with SSA and pore volume values for nCa_Tionite (black), nNa_Tionite (red), nNa_Tionite_B (blue) and nNa_Tionite_A (green)

2.4 Final considerations

The growing attention to circular economy and sustainability led us to investigate a TiO_2 manufacture by-product called tionite. Tionite is obtained by treating ilmenite ($FeTiO_3$) with concentrated H_2SO_4 at 100 °C, followed by the recovery and neutralization of the residual mud. nCa_Tionite, obtained by neutralization with lime, exhibits NPs with various shapes made of a combination of TiO_2, mainly in the rutile phase, aluminosilicates, $CaCO_3$ and a significant amount of $CaSO_4 \cdot 2H_2O$. The high level of TiO_2 included in the sample suggests its application for photocatalytic purposes; however, tionite composition could be further improved.

In a first attempt, a new neutralization method involving NaOH was applied in order to remove the insoluble $CaSO_4$ originated by the neutralization reaction between residual H_2SO_4 and $Ca(OH)_2$. According to the characterization results, the new procedure proved efficient in removing not only calcium sulfate, but also its carbonate. The compositional and morphological characterization highlighted the concentration increase of aluminosilicate, which assumes a particular bidimensional sheet-like shape. These results suggested the idea to further treat the sample to remove this silica/aluminosilicate component, in order to further improve the concentration and accessibility of TiO_2.

Two new strategies were investigated: a basic treatment with NaOH and an acidic one with HF. Both procedures proved effective in removing the target impurity, with HF being more effective in dissolving also other elements. However, the two samples showed profoundly different surface properties: nNa_Tionite_B provided a hydrophilic sample with a SSA and pore volume consistent with the pristine nNa_Tionite; on the other hand, nNa_Tionite_A showed a fluorinated surface that gives the material hydrophobic properties and a net decrease in its surface area and porosity.

Thanks to the described treatments, four different versions of tionite are originated.

The TiO_2 content, the remarkable differences in their composition and surface properties make their photocatalytic application extremely interesting.

2.5 Bibliography

[1] European Parliament, *Directive 2008/98/EC of the European Parliament and of the Council of 19 November 2008 on Waste and Repealing Certain Directives*, **2008**.

[2] F. Chyliński, K. Kuczyński, P. Lukowski, *Materials (Basel).* **2020**, *13*, 1–16.

[3] F. cheng Meng, T. yan Xue, Y. hui Liu, G. zhi Zhang, T. Qi, *Trans. Nonferrous Met. Soc. China (English Ed.* **2016**, *26*, 1696–1705.

[4] F. Meng, T. Xue, Y. Liu, W. Wang, T. Qi, *Hydrometallurgy* **2016**, *161*, 112–116.

[5] K. Choi, J. G. Ahn, H. Park, *Jom* **2023**, *75*, 549–556.

[6] M. Dondi, G. Guarini, M. Raimondo, C. Zanelli, D. D. Fabbriche, A. Agostini, *Ceram. Int.* **2010**, *36*, 2461–2467.

[7] M. Contreras, M. I. Martín, M. J. Gázquez, M. Romero, J. P. Bolívar, *Constr. Build. Mater.* **2014**, *72*, 31–40.

[8] M. Contreras, M. J. Gázquez, I. García-Díaz, F. J. Alguacil, F. A. López, J. P. Bolívar, *J. Environ. Manage.* **2013**, *128*, 625–630.

[9] J. Bobrowicz, F. Chyliński, *J. Therm. Anal. Calorim.* **2016**, *126*, 493–498.

[10] S. M. Pérez-Moreno, M. J. Gázquez, A. G. Barneto, J. P. Bolívar, *Thermochim. Acta* **2013**, *552*, 114–122.

[11] F. Chyliński, K. Kuczyński, *Materials (Basel).* **2020**, *13*, DOI 10.3390/ma13132904.

[12] D. C. Paz-Gómez, I. S. Vilarinho, J. Carvalheiras, S. M. Pérez-Moreno, M. P. Seabra, J. A. Labrincha, J. P. Bolívar, *Waste and Biomass Valorization* **2024**, DOI 10.1007/s12649-024-02629-7.

[13] W. Hajjaji, G. Costa, C. Zanelli, M. J. Ribeiro, M. P. Seabra, M. Dondi, J. A. Labrincha, *J. Eur. Ceram. Soc.* **2012**, *32*, 753–764.

[14] W. Hajjaji, C. Zanelli, M. P. Seabra, M. Dondi, J. A. Labrincha, *Chem. Eng. J.* **2011**, *171*, 1178–1184.

[15] A. Basso Peressut, C. Cristiani, G. Dotelli, A. Dotti, S. Latorrata, A. Bahamonde, A. Gascó, D. Hermosilla, R. Balzarotti, *Nanomaterials* **2023**, *13*, DOI 10.3390/nano13061043.

[16] D. Mahon, G. Claudio, P. Eames, *Energies* **2021**, *14*, DOI 10.3390/en14051316.

[17] S. Challagulla, K. Tarafder, R. Ganesan, S. Roy, *Sci. Rep.* **2017**, *7*, 1–11.

[18] F. C. Donnelly, F. Purcell-Milton, V. Framont, O. Cleary, P. W. Dunne, Y. K. Gun'ko, *Chem. Commun.* **2017**, *53*, 6657–6660.

[19] N. Krishnamurthy, V. Soots, *Can. J. Phys.* **1971**, *49*, 885–896.

[20] Y. Liu, A. Wang, J. J. Freeman, *40th Lunar Planet. Sci. Conf.* **2009**.

[21] R. Poliah, S. Sreekantan, *J. Nanomater.* **2011**, *2011*, DOI 10.1155/2011/239289.

[22] J. Madejová, W. P. Gates, S. Petit, *IR Spectra of Clay Minerals*, **2017**.

[23] Y. Ennaciri, H. El Alaoui-Belghiti, M. Bettach, *J. Mater. Res. Technol.* **2019**, *8*, 2586–2596.

[24] P. Praveen, G. Viruthagiri, S. Mugundan, N. Shanmugam, *Spectrochim. Acta - Part A Mol. Biomol. Spectrosc.* **2014**, *117*, 622–629.

[25] F. Paulik, J. Paulik, M. Arnold, *Thermochim. Acta* **1992**, *200*, 195–204.

[26] T. Siva, S. Muralidharan, S. Sathiyanarayanan, E. Manikandan, M. Jayachandran, *J. Inorg. Organomet. Polym. Mater.* **2017**, *27*, 770–778.

[27] D. Dollimore, *Thermochim. Acta* **1987**, *117*, 331–363.

[28] J. M. Adams, V. Ramdas, G. G. T. Guarini, C. J. Adams, *J. Chem. Soc. Dalt. Trans.* **1980**, 269–275.

[29] N. Khan, D. Dollimore, K. Alexander, F. W. Wilburn, *Thermochim. Acta* **2001**, *367–368*, 321–333.

[30] M. H. H. Mahmoud, M. M. Rashad, I. A. Ibrahim, E. A. Abdel-Aal, *J. Colloid Interface Sci.* **2004**, *270*, 99–105.

[31] C. M. Mbulanga, R. M. Erasmus, Z. N. Urgessa, S. R. T. Djiokap, E. J. Olivier, W. E. Goosen, J. R. Botha, R. Betz, *Appl. Phys. A Mater. Sci. Process.* **2019**, *125*, DOI 10.1007/s00339-019-2688-4.

[32] S. Liu, J. Yu, B. Cheng, M. Jaroniec, *Adv. Colloid Interface Sci.* **2012**, *173*, 35–53.

[33] Z. Shayegan, F. Haghighat, C. S. Lee, A. Bahloul, M. Huard, *Chem. Eng. J.* **2018**, *346*, 578–589.

[34] N. Fessi, M. F. Nsib, Y. Chevalier, C. Guillard, F. Dappozze, A. Houas, L. Palmisano, F. Parrino, *Langmuir* **2020**, *36*, 13545–13554.

[35] N. Fessi, M. F. Nsib, L. Cardenas, C. Guillard, F. Dappozze, A. Houas, F. Parrino, L. Palmisano, G. Ledoux, D. Amans, Y. Chevalier, *J. Phys. Chem. C* **2020**, *124*, 11456–11468.

[36] M. Thommes, K. Kaneko, A. V. Neimark, J. P. Olivier, F. Rodriguez-Reinoso, J. Rouquerol, K. S. W. Sing, *Pure Appl. Chem.* **2015**, *87*, 1051–1069.

[37] M. Thommes, B. Smarsly, M. Groenewolt, P. I. Ravikovitch, A. V. Neimark, *Langmuir* **2006**, *22*, 756–764.

[38] J. Yu, W. Wang, B. Cheng, B. L. Su, *J. Phys. Chem. C* **2009**, *113*, 6743–6750.

[39] Y. S. Lee, Y. H. Kim, J. S. Hong, J. K. Suh, G. J. Cho, *Catal. Today* **2007**, *120*, 420–425.

Chapter 3: Photocatalytic application of tionite samples

Chapter 3 reports the photocatalytic investigations for the tionite samples in order to demonstrate that an industrial waste can be valorised by proposing a tailored regeneration strategy.

To find a new and more valuable application, four different advanced oxidation process strategies were evaluated for both environmental remediation and organic synthesis.

To help the reader through the chapter, the current state-of-the-art in these different strategies will be presented.

3.1 Tionite application in the partial oxidation of ferulic acid

In this Paragraph, tionite samples were tested in photocatalytic applications. At first, preliminary information was obtained by the photodegradation test of paracetamol (PC), a common antipyretic and analgesic, as well as a persistent water pollutant. The results helped to understand the sample criticalities and design the modification processes described in Chapter 2. Starting from the poor photocatalytic results, the application of the material in a milder oxidation processs was tested: the partial oxidation of ferulic acid to vanillin.

3.1.1 Introduction to ferulic acid and its conversion to vanillin

Vanillin (4-hydroxy-3-methoxybenzaldehyde) is an aromatic aldehyde whose main application is in the aroma of vanilla, which is one of the most important and widespread flavour in the world. Due to its chemical properties, it is also used in the cosmetic industry, chemical industry, agriculture and medicine. In nature, vanillin can be extracted from vanilla pods, from the plant "*Vanilla planifolia*", through a long and expensive procedure.[1] The annual production of vanillin from plant extraction is about 50 tons; corresponding to 1 % of the total vanillin production.[2] Since natural extraction is not sufficient to satisfy the growing market, vanillin is therefore produced through chemical procedures, starting from oil-derived phenol. In the classical industrial route, phenol is methoxylated to guaiacol, which reacts with glyoxylic acid in a two-step process involving a base-promoted condensation and an oxidative decarboxylation of vanillymandelic acid to vanillin, catalysed by Cu(II) in alkaline medium at 80-130 °C.[3,4] Lignin also represents a valuable source of vanillin on an industrial scale, accounting for 15 % of total global vanillin production[5]. The process consists in a treatment in an alkaline aqueous solution with oxidants, at high temperature and pressure, to depolymerize lignin. The final product consists of a mixture of vanillin with structurally similar compounds, difficult to separate.[4,6]

The high energy and chemical consumption or the scarce selectivity of the process make the development of more sustainable process a priority. In this optic, the utilization of renewable or natural substrate is a first step towards a greener process; among the numerous potential precursors, ferulic acid has captured the attention. Ferulic acid can be found in several plants like rice, wheat, oats and pineapple, but

also grasses, grains, vegetables, flowers and others and its extraction can proceed through acidic or alkaline processes. Alternatively, the enzymatic extraction has been investigated, but the process is complicated by the combination of ferulic acid with lignin and other biopolymers.[7] However, being a potential component of lignin, it can be obtained as a by-product in the depolymerization process of vanillin production. Regarding the conversion of ferulic acid to vanillin, several studies have been dedicated to the biotransformation process, involving enzyme or microbial –mediated conversion. However, they show some limitations due to the high cost, long production times, complex separation processes and the necessity to isolate selected and hazardous microorganisms.[8–10] On the other hand, the application of photocatalytic process takes place in relatively short time and in mild conditions, especially because only a suspension of the photocatalyst and ferulic acid as the only chemical is required.

In this context, TiO_2 was investigated in the ferulic acid conversion to vanillin at first by Augugliaro *et al.*[11], considering commercial P25 and Merck Anatase, in comparison with different polymorphs of synthetic titanium dioxide in the partial oxidation of ferulic acid to vanillin under UV irradiation (365 nm), demonstrating the importance of crystallinity in the process. Specifically, the Authors observed better selectivity results for well-crystalized samples like Merck anatase (12 %) and P25 (3 %), compared to the two synthesised samples, consisting of a badly crystalized rutile and a combination of amorphous TiO_2 with anatase and rutile (75:25), which provided a selectivity ≤ 2 %. By studying the intermediates, the Authors proposed a mechanism (Figure 3.1) for the photo-oxidation of ferulic acid consisting in three different parallel pathways: i) the mineralization of ferulic acid through intermediates that do not desorb in the bulk solution, ii) partial oxidation to vanillin with the formation of intermediates that desorb, and iii) the complete oxidation of these intermediated through progressive adsorption and desorption steps.

Successively, Parrino *et al.*[12] demonstrated a second strategy for the ferulic acid conversion to vanillin under visible light (λ > 400 nm) obtaining, with P25, a selectivity of 2 %. They demonstrated the formation of a charge transfer complex between ferulic acid and TiO_2 with a broad adsorption up to 600 nm, which is involved in the conversion of ferulic acid to vanillin.

Similarly, Di Paola *et al.*[13] tested commercial Merck anatase TiO_2 loaded with different

amounts of WO_3, demonstrating an increase in the selectivity compared to bare TiO_2, obtaining 18 % selectivity with a 1 % loading of WO_3. Being WO_3 inactive in the photo-oxidation of vanillin, they suggest that its partial covering of TiO_2 protects the molecule from further oxidation.

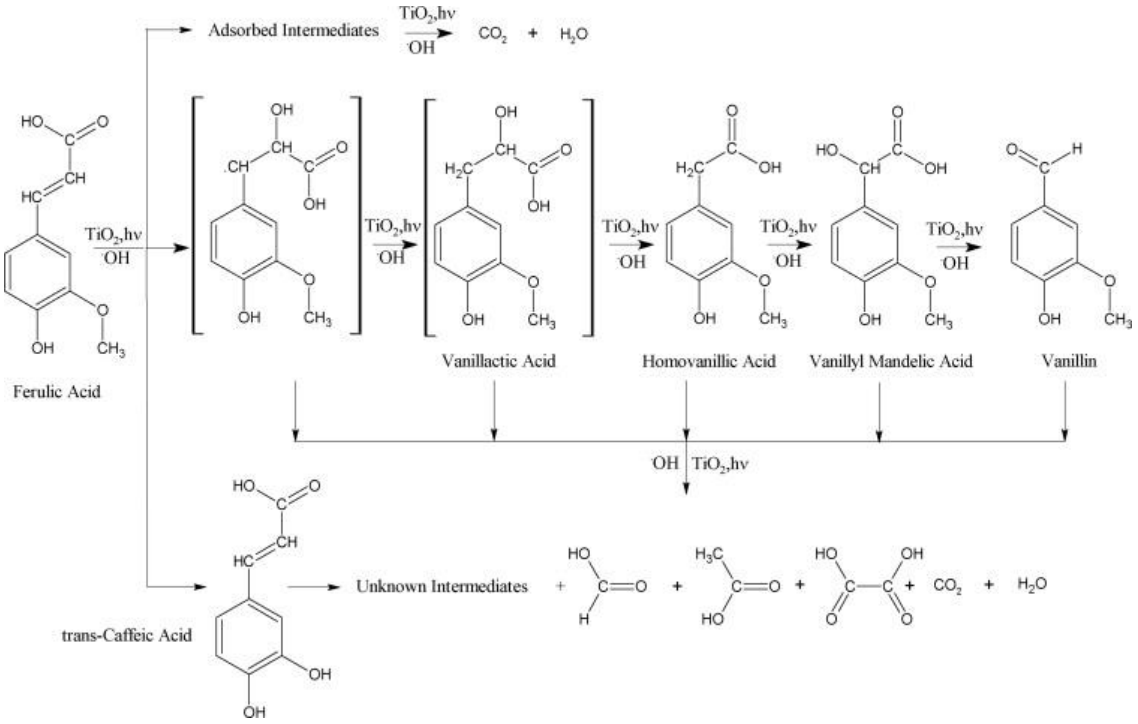

Figure 3.1: proposed photo-oxidation mechanism for ferulic acid. Adapted from [11]

TiO_2 is not the only photocatalyst investigated. Indeed, even bare and Eu-doped ZnO[14] and Bi_2WO_6[15] were also proved efficient in the partial photo-oxidation of ferulic acid, providing a selectivity to vanillin of 2-2.5 % under UV light and 4.9 % under simulated solar irradiation, respectively.

It is worth noticing that several articles[12,14] highlighted a strict relationship between surface hydrophilicity and the selectivity towards vanillin. The surface hydrophilicity, defined by the amount of hydroxyl groups, enhances the surface interaction with ferulic acid, promoting its mineralization instead of the partial oxidation to vanillin.

The application of photocatalysis for vanillin production through the partial oxidation of ferulic acid is an emerging but promising topic. Despite the strategy needing some further investigation and improvement, the application of a waste material like tionite seems a promising path to follow, since the combination of TiO_2 with other components could be efficient in protecting vanillin from over-oxidation.

3.1.2 Materials and methods

This Paragraph reports the procedures applied for the photocatalytic application of tionite samples in degrading PC and in the partial oxidation of ferulic acid are reported. The adsorption properties towards ferulic acid and vanillin are also investigated to assess the mechanism involved.

3.1.2.1 Materials

Paracetamol (PC) 98 % was purchased from Thermo Scientific and used as received. Sodium hydroxide ≥98 % and H_2O HPLC grade were purchased from VWR. Acetonitrile HPLC grade ≥99.9 %, glacial acetic acid ≥99 %, vanillin ≥99 %, and ferulic acid ≥99 % were purchased from Sigma-Aldrich. Milli-Q water with a resistivity ρ > 18.2 MΩ cm was used. nCa_Tionite, nNa_Tionite, nNa_Tionite_B and nNa_Tionite_A were obtained as described in Paragraph 2.2.

3.1.2.2 Photocatalytic tests procedure for PC

The photocatalytic experiments with PC were performed in a 0.5 L cylindrical Pyrex batch photoreactor. A 125 W medium-pressure Hg lamp (Helios Italquartz, Italy), with a maximum emission at 365 nm, was axially immersed within the photoreactor. The suspension was kept in the dark for 30 min to reach the adsorption-desorption equilibrium, with O_2 bubbling at a flow rate of 50 mL min^{-1}. The solution temperature during the experiment was controlled by water circulation through a jacket surrounding the reactor. A magnetic stirrer was used to guarantee the homogeneity of the reaction mixture. The catalyst amount was 0.4 g L^{-1}, and the initial PC concentration was 30 mg L^{-1}. Samples were withdrawn at fixed times; the supernatant was filtered through a 0.22 μm hydrophilic PTFE syringe filter (VWR). The quantitative determination of PC was performed with an HPLC Agilent 1100 series equipped with a ZORBAX Eclipse XBD-C18, 5 μm, 150 x 4.6 mm column and a UV-Vis detector set at 243 nm. The eluent, consisting of 90% v/v of water and 10% v/v acetonitrile, had a flow rate of 0.8 mL min^{-1} and the injection volume was 20 μ L.
Photocatalytic runs have been performed in triplicate and the standard deviation was within ±5 %.

3.1.2.3 Photocatalytic tests procedure for partial oxidation of ferulic acid

Photocatalytic partial oxidation of ferulic acid to vanillin was performed in a cylindrical Pyrex reactor (internal diameter 3 cm) containing 30 mg of the photocatalyst dispersed in 50 mL of a 0.5 mmol L^{-1} ferulic acid aqueous solution. The mixture was sonicated for 5 min at RT and stirred for 30 min under dark conditions. The obtained suspension was irradiated by UV-A light under a constant O_2 flux by means of six actinic lamps (15 W each, λ_{max} = 365 nm, total radiant flux 40.15 W m^{-2}) hexagonally arranged at the same distance from the reactor placed in the center. The photonic flux impinging the photocatalytic suspension was measured by using a Delta Ohm photo quantum meter (model HD9021, Selvazzano Dentro, Italy) equipped with a LP 9021 UVA sensor probe. The amount of photocatalyst dispersed corresponded to reaction conditions at which the photonic flux exiting from the reaction medium was *ca.* 10% of the impinging one. This ensures a safe comparison of the results obtained in the presence of different photocatalysts. Samples of the reaction mixture were withdrawn at fixed times and filtered (hydrophilic PTFE syringe filter, 0.22 μm, VWR). The quantitative determination of ferulic acid and vanillin was performed with a Shimadzu HPLC Prominence equipped with a Shimpack GWS C18, 5 μm, 150 x 4.6 mm column and a diode-array UV-vis detector. The HPLC chromatograms were obtained at 322 nm, with a flow rate of 0.7 mL min^{-1}, and an injection volume of 20 μ L. The eluent consisted of a solution containing 80% v/v of a 1% v/v CH_3COOH aqueous solution and 20% v/v acetonitrile.

The vanillin selectivity values were calculated during irradiation according to Eq. 3.1:

$$S\%\ [\text{Vanillin}]_t = \frac{[\text{Vanillin}]_t}{\Delta[\text{Ferulic acid}]} \cdot 100 \qquad 3.1$$

where $[\text{Vanillin}]_t$ is the vanillin concentration at the sampling time t and Δ[Ferulic acid] is the variation of the ferulic acid concentration between the sampling time t and the initial concentration (t= 0 min).

Selected photocatalytic runs have been performed in triplicate and standard deviation was within ±5 %.

3.1.2.4 Ferulic acid photo-adsorption tests

The ferulic acid photo-adsorption behavior of all samples was investigated by performing photocatalytic runs under the same experimental conditions described above, but under N_2 flux before and during the irradiation to remove O_2 and avoid ferulic acid degradation.

3.1.2.5 Ferulic acid and vanillin adsorption test procedure

nNa_Tionite, nNa_Tionite_B and nNa_Tionite_A samples were tested for the adsorption of vanillin and ferulic acid. Four different concentrations were used for both molecules (0.25, 0.1, 0.05 and 0.01 mmol L^{-1}) in the presence of a constant amount of photocatalyst. The amount of sample used was calculated to keep constant the amount of the TiO_2 component in the two tests. EDX analysis revealed a 45 % content of TiO_2 for the nNa_Tionite sample, while the amount of TiO_2 in the nNa_Tionite_B sample was calculated by considering the mass lost during the chemical treatment. The suspensions were left under magnetic stirring overnight to reach the adsorption-desorption equilibrium and then the photocatalyst was separated by filtration (hydrophilic PTFE syringe filter, 0.22 µm, VWR). The quantification of vanillin and ferulic acid in the solution was carried out by HPLC, as described above. The experimental data were fitted by using the Langmuir isotherm model (Eq. 3.2):[16]

$$Q_e = \frac{q_0 K C_e}{K C_e + 1} \qquad 3.2$$

where Q_e is the amount of vanillin adsorbed at the equilibrium, q_0 is the maximum amount of vanillin adsorbed per adsorbent mass, C_e is the vanillin concentration in solution at the equilibrium, and K is the thermodynamic adsorption constant.

3.1.3 Results and discussion

In this paragraph the results of preliminary photodegradation test, partial oxidation of ferulic acid to vanillin and adsorption test of vanillin and ferulic acid are illustrated.

3.1.3.1 Photocatalytic degradation of PC with tionite samples

Pristine and treated tionite materials were initially tested for the degradation of PC in water to get information on the viability of the tionite purification strategy and at the same time to check the feasibility of environmental applications. In fact, PC is a widely used antipyretic and analgesic drug, which is excreted unchanged or after being transformed into toxic metabolites. In this way, it reaches natural aqueous effluents where it enters the food chain and affects the growth and reproduction of aquatic organisms, especially upon long-term exposure.[17] Robust and cheap TiO_2-based photocatalysts efficiently mineralize PC even under simulated solar light irradiation.[18] However, as shown in Figure 3.2, the preliminary results on both nCa_Tionite and nNa_Tionite samples showed poor photocatalytic activity under UVA irradiation, maybe related to the low accessibility of light and/or reactant for titanium dioxide, which led to subsequent acid and basic treatments. Unfortunately, even if better efficiency was obtained, the most active sample (nNa_Tionite_A) provided only 43% degradation of PC after 6 h irradiation, while the figures obtained in the presence of the other samples ranged between 17 and 28 %.

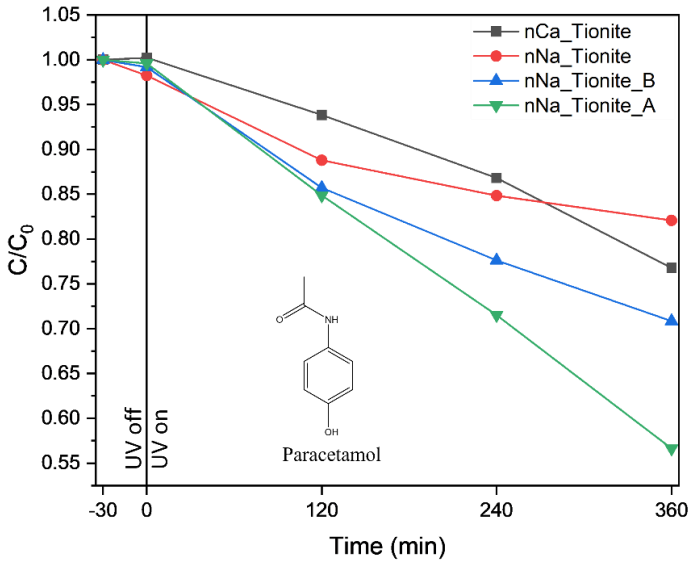

Figure 3.2: variation of PC concentration by photo-degradation with nCa_Tionite (black), nNa_Tionite (red), nNa_Tionite_B (blue) and nNa_Tionite_A (grey).

3.1.3.2 Partial photo oxidation of ferulic acid with tionite samples

The rather low oxidizing power of tionite discouraged us from proposing traditional environmental applications for this waste material. Instead, this feature could be

remarkably useful in the field of photocatalytic partial oxidations, where the formation of high added value intermediate compounds could be maximized in the presence of suitable photocatalysts, which limit the overoxidation of the desired products. Therefore, the partial oxidation of ferulic acid to vanillin (Figure 3.3) was studied using tionite as the photocatalyst.

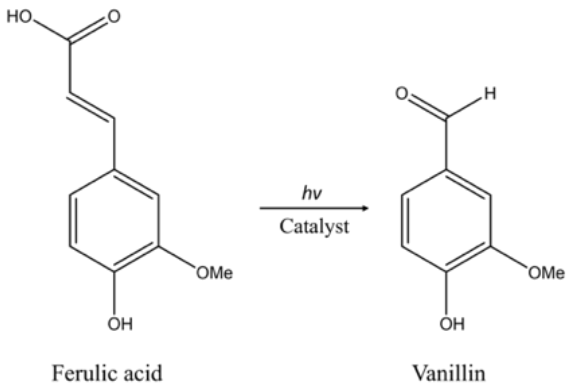

Figure 3.3: Ferulic acid partial oxidation to vanillin

The photocatalytic production of vanillin was reported with selectivity values of ca. 2 % in the presence of the benchmark photocatalyst TiO_2 P25 under UVA light irradiation.[11] Therefore, exceeding these values is relevant, due to the high commercial value of vanillin. Moreover, the use of a waste material such as tionite as a photocatalyst is a remarkable added value for this reaction. It is worth noticing that the selectivity to vanillin obtained through photocatalysis can be significantly increased by coupling the photocatalytic reactor with membrane separation units. The features and the synergistic effects of this virtuous example of process intensification have been widely discussed in previous reports.[19]

Figure 3.4a reports the concentration variation of ferulic acid in irradiated aqueous suspension of the different tionite samples. A steep decrease in ferulic acid concentration could be observed within the first hour of irradiation while, thereafter, the concentration decreased more slowly. In particular, after the first hour of irradiation, the concentration decreased with a similar slope in the presence of the two untreated (raw) samples and nNa_Tionite_B. On the other hand, faster ferulic acid degradation is apparent in the presence of nNa_Tionite_A sample, in agreement with what observed for the degradation of PC. The similar photoactivity of the nCa_Tionite, nNa_Tionite and nNa_Tionite_B samples can be related to the similar surface

properties of their photoactive TiO_2 component. On the other hand, the presence of fluoride groups at the surface of the nNa_Tionite_A sample increases the photocatalytic activity due to the often-reported beneficial effect of fluorination in terms of hydroxyl radicals generation.[20] In fact, surface fluorine groups, unlike hydroxyl ones, cannot act as surface hole traps being too high the oxidation potential of the $F^{\bullet}/F^{-}$ couple (3.6 V *vs* NHE), thus resulting in enhanced availability of holes for the direct water oxidation, which in turn results in higher production of hydroxyl radicals.[20]

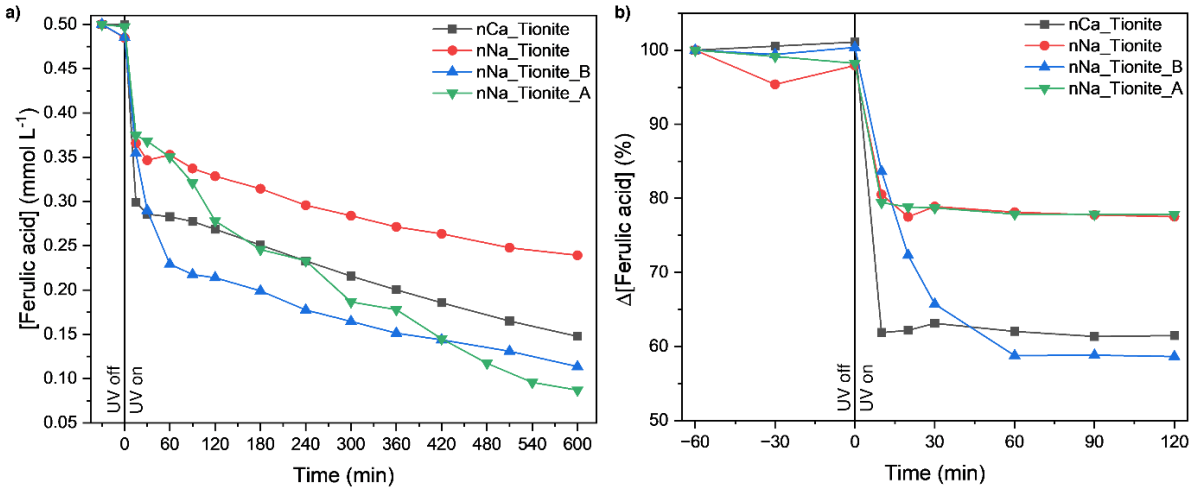

Figure 3.4: variation of the ferulic acid concentration in oxygenated (a) or deaerated (b) suspensions of nCa_Tionite (black), nNa_Tionite (red), nNa_Tionite_B (blue) and nNa_Tionite_A (green), under UVA light irradiation. Photocatalytic runs have been performed in triplicate and standard deviation was within ±5 %.

In order to correctly interpret the steep decrease in the ferulic acid concentration observed in the first hour of irradiation, we performed the same reaction under continuous nitrogen bubbling, by keeping constant all of the other experimental conditions. Results are shown in Figure 3.4b. In the absence of oxygen, the ferulic acid concentration decreases at the beginning of the test similarly to what is observed in the oxygenated suspension but, thereafter, it remains constant. This result indicates that ferulic acid strongly adsorbs under irradiation onto all of the tionite samples, especially for nCa_Tionite and nNa_Tionite_B, whose surface, therefore, undergoes the most relevant changes when irradiated.[21] After reaching photo-stationary equilibrium (after the first hour), the ferulic acid concentration remained constant due to the prevailing recombination of the photogenerated charges, which occurs preferentially in the absence of suitable electron acceptor species. On the other hand, under dark conditions, the adsorption of ferulic acid onto all the samples was negligible, as suggested by the concentration values measured prior to irradiation and

as confirmed by systematic dark-adsorption experiments carried out independently (data not reported).

Concomitant vanillin production under irradiation in the oxygenated suspensions of all tionite samples was observed. Figure 3.5 reports the vanillin selectivity values calculated during irradiation according to Eq. 3.1.

According to Figure 3.5, all samples show a gradual increase in the S% values but two different trends can be highlighted: both nNa_Tionite and nNa_Tionite_A photocatalysts produced a similar and more rapid increase in the vanillin selectivity compared to nCa_Tionite and nNa_Tionite_B samples. Notably, under the same experimental conditions, P25 provided a maximum selectivity of only 2%.[11]

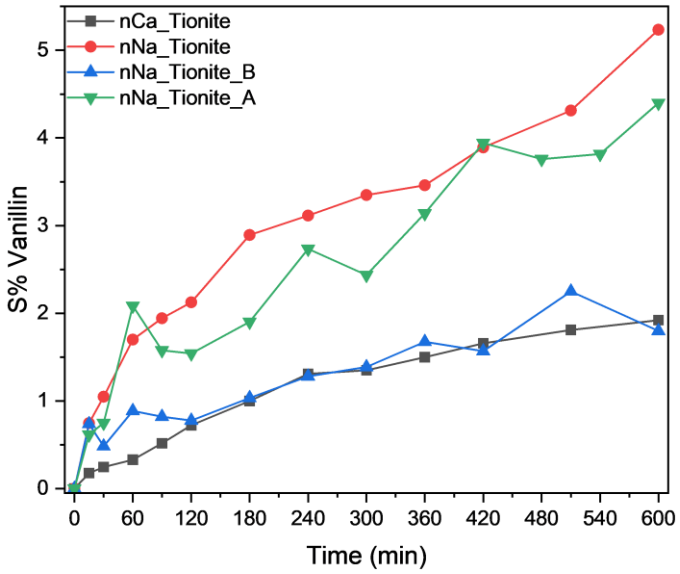

Figure 3.5: Selectivity towards vanillin as a function of the irradiation time in the presence of nCa_Tionite (black), nNa_Tionite (red), nNa_Tionite_B (blue) and nNa_Tionite_A (grey) samples.

Comparing the results in Figure 3.4 and Figure 3.5, it is evident a strong correlation between the photoadsorption behavior of the tionite samples and the selectivity towards vanillin obtained in the corresponding photocatalytic runs. In fact, the selectivity values towards vanillin obtained under irradiation follow almost linearly the photo-induced capability of the photocatalysts to adsorb organic species. This behavior confirms the hypothesis that the selectivity towards partial oxidation products is strictly related to their affinity with the surface.[22] In other words, the higher the affinity with the surface of the photocatalyst, the higher the probability that the intermediate compound of interest is overoxidized, thus dramatically reducing the selectivity of the reaction. However, this effect has been previously correlated with the

adsorption behavior under dark conditions. Hereby, for the first time, the importance of surface phenomena in determining the selectivity of partial oxidation reactions can be assessed, when irradiation dramatically changes the surface features of the photocatalyst, as in the case of tionite samples.

A relevant question, however, arises by considering that both nNa_Tionite and nNa_Tionite_B samples show dramatically different behavior under irradiation in terms of photo-adsorption and selectivity to vanillin, even though they possess quite similar morphological and surface features, as highlighted by the characterization results. It is worth remembering here that the only relevant difference between the two samples relies on their composition. In fact, besides a photo-active TiO_2 portion of comparable features in the two photocatalysts, the nNa_Tionite sample is also composed of *ca.* 55 % of an aluminosilicate component, which is not photoactive. In addition, XPS results (Paragraph 2.3.4) confirm the same trend in the surface composition of both materials, by calculating the Ti/Si and Ti/Al ratios. The basic treatment of nNa_Tionite causes an increase in the Ti/Si ratio from 1.27 to 3.73 and a decrease in Ti/Al from 56 to 13.1. Despite the Ti/Al values being extremely affected by the low Al surface %, the Ti/Si ratio clearly shows an increase in the Ti surface content at the expense of a lower Si exposure. The effects of “inert” components in tailored photocatalysts were reported to be beneficial in addressing the selectivity of photocatalytic partial oxidation reactions, producing a specific product distribution deriving from different reactive oxygen species thereby generated.[23] However, unlike the mentioned literature studies, no different product distribution is observed in the present case.

In order to highlight the reasons underlying the different behavior of nNa_Tionite and nNa_Tionite B samples we investigated the adsorption behavior of vanillin under dark in the presence of opportune amounts of the catalysts to keep constant the amount of the TiO_2 component (0.45 mg mL^{-1}). Therefore, results in Figure 3.6a express the absolute amount of vanillin adsorbed in the dark at equilibrium. For the sake of completeness, the corresponding plot obtained by considering the adsorption values per mass of the catalyst is reported in Figure 3.6b, along with the calculated thermodynamic parameters in Table 3.1.

The maximum amount of vanillin adsorbed at equilibrium in the dark is higher for the nNa_Tionite sample. By considering comparable the surface features of the TiO_2

component in the two samples, according to the characterization results, and considering that the amount of TiO_2 in the two samples is the same, this difference can be ascribed to the vanillin adsorption behaviour of the aluminosilicate component present in the nNa_Tionite sample, which thus adsorbs similar amounts of vanillin in the dark. In fact, the maximum amount of vanillin adsorbed by the nNa_Tionite sample (0.0187 mmol) is ca. 55% higher than the one adsorbed by the nNa_Tionite_B sample (0.0106 mmol), which corresponds to the amount of aluminosilicate component (55 %) present in the nNa_Tionite sample.

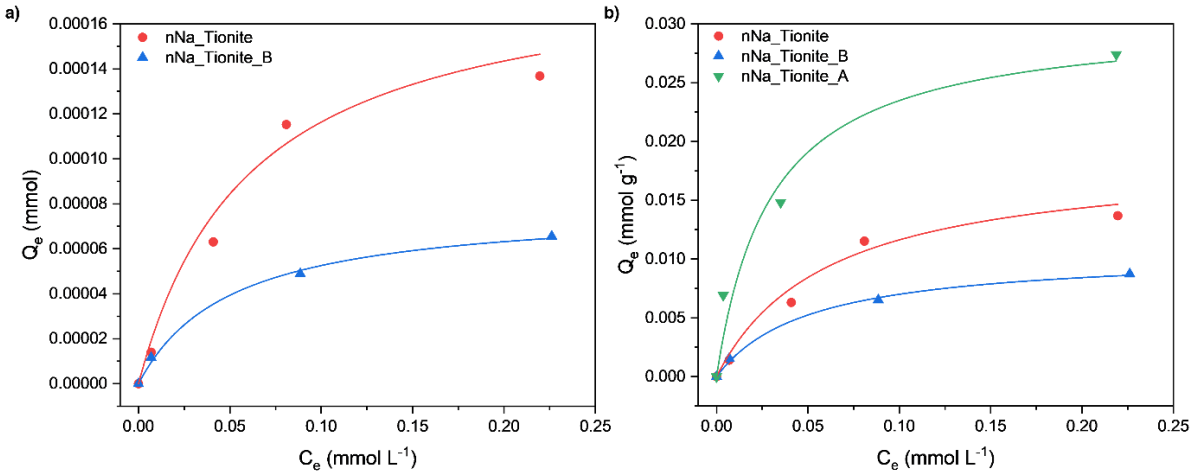

Figure 3.6: Langmuir fitting (solid lines) of the vanillin adsorption results obtained by (a) keeping constant the amount of TiO_2 component and (b) normalized for the amount of catalyst employed for nNa_Tionite (red squares) and nNa_Tionite_B (blue circles) and nNa_Tionite_A(green).

Table 3.1: q_0, K and R-square values extrapolated from the Langmuir equation by fitting vanillin adsorption results normalized for the amount of catalyst

	q_0	K	R-square
nCa_Tionite	-	-	-
nNa_Tionite	0.0187	16.4	0.921
nNa_Tionite_B	0.0106	19.8	0.997
nNa_Tionite_A	0.0305	33.5	0.961

The ability of the aluminosilicate component to adsorb vanillin could justify the different selectivities obtained in the presence of irradiated nNa_Tionite and nNa_Tionite_B samples as schematically depicted in Figure 3.7. Considering, instead, only the adsorption of vanillin on the two samples, a greater adsorption should correspond to a lower selectivity, with the vanillin remaining on the catalyst surface.[24]

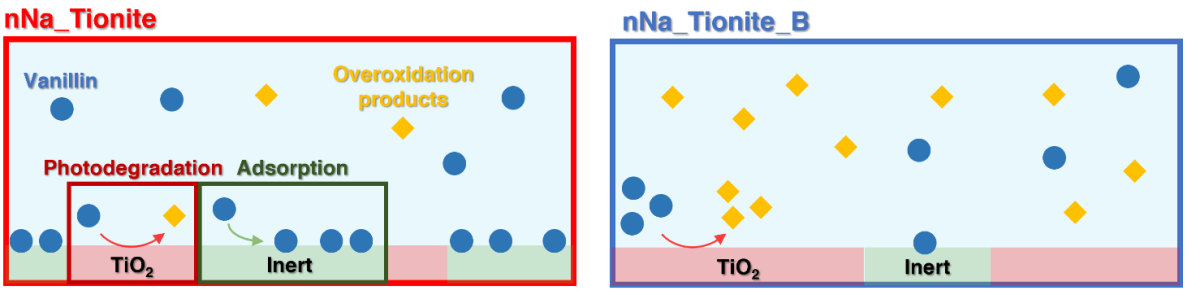

Figure 3.7: Scheme of the photo-induced overoxidation reactions of vanillin at the surface of nNa_Tionite and nNa_Tionite_B samples

In fact, the vanillin photocatalytically produced onto the TiO_2 component of the samples could easily undergo further oxidation in the nNa_Tionite_B sample, while the non-photo-active aluminosilicate component of the nNa_Tionite sample can adsorb vanillin and consequently preventing its photocatalytic decomposition. Similar hypothesis was invoked by Tsukamoto et al.[25] for the partial oxidation of alcohols to aldehydes in the presence of TiO_2/WO_3 composites synthesized on purpose. The WO_3 component that is partially covering TiO_2, was not able to over-oxidize the aldehyde products, thus resulting in higher selectivity values. The peculiar interaction between photoactive and non-photoactive components intrinsically present in the waste material tionite, is a useful feature for photocatalytic partial oxidations and could be used for further similar applications.

3.1.4 Final considerations

Tionite samples were employed in photocatalytic tests to evaluate their application in the photodegradation of organic molecules and the effect of the treatments on their performance. Preliminary results on the photodegradation of PC showed a general low activity for all samples, despite both basic and acidic treatments leading to a slight increase in the efficiency, with 40 % of PC degraded in 6 h with nNa_Tionite_A.

The low photoactivity of all materials encouraged us to explore their application in the partial oxidation reactions. The photocatalytic conversion of ferulic acid to vanillin was chosen as a model reaction, considering the remarkable features of this process in terms of sustainability and economic impact. All of the tionite-based catalysts have shown a gradual increase of the vanillin selectivity under irradiation, with the best performances were obtained in the presence of nNa_Tionite and nNa_Tionite_A

samples. Compared to P25, which provides a maximum selectivity to vanillin of 2 %, these two samples reach a value of 4-5 % in 6 h. While the performance of nNa_Tionite_A is difficult to compare with the other samples, due to the fluorinated surface and its effect on the photocatalytic process, both nNa_Tionite and nNa_Tiontie_B efficiency in the process can be strictly related to the surface properties and composition.

Vanillin adsorption studies on the two samples showed a higher affinity to vanillin for the nNa_Tionite samples which, on the other hand, provides the best selectivity. This behaviour was ascribed to the sample composition, since a remarkable amount of aluminosilicate is mixed with TiO_2. This suggests that the adsorption of vanillin on the aluminosilicate components protects the molecule from over-oxidation. On the contrary, nNa_Tionite_B, with its lower selectivity and lower adsorption of vanillin, degrades more easily the molecule cause of the lower amount of aluminosilicate.

The results provided by tionite samples in the partial oxidation of ferulic acid to vanillin show that the low efficiency of a photocatalyst can exploited for processes that do not require the complete degradation of an organic pollutant, but its transformation into an intermediate. Since tionite samples proved more efficient than P25 in the partial oxidation process, it is worth to further investigate the application of such material in other AOPs strategies.

3.2 Application of tionite in the photodegradation of 4-chlorophenol

3.2.1 Introduction to PMS-assisted photodegradation processes

In the last decade, advanced oxidation processes (AOPs) have been widely investigated and developed for their application in environmental remediation. Along with the direct application of photocatalysts, like TiO_2, and their photogenerated electron-hole pairs, an increasing number of papers on photo-Fenton processes have been proposed. In this strategy, the hydroxyl radicals are generated by a redox reaction between Fe^{2+} and H_2O_2, followed by the photochemical reduction of newly generated Fe^{3+} to the bivalent state to start the process again.

However, new AOPs are progressively emerging and the attention has been captured

by sulfate radicals-mediated water decontamination due to its versatility and sustainability. Sulfate radicals ($SO_4^{\cdot-}$) are particularly appreciated for their higher redox potential, ranging between 2.5 - 3.1 eV depending on the activation mechanism, and longer life-time compared to hydroxyl radicals ($OH^{\cdot}$), making them extremely efficient in degrading emerging contaminants.[26] Among the compounds employed for sulfate radical generation, peroxymonosulfate (PMS) has gained more attention due to its higher reactivity.

The main advantage of PMS is the possibility of being activated by several methods. The easiest way to activate PMS is thermally: by heating at temperature > 40 °C, the O-O bond can easily break providing sulfate radicals (Eq. 3.3).[27] Due to the high temperature, a side reaction (Eq. 3,4) between sulfate radicals and water, forming hydroxyl radicals, is also accelerated, making hydroxyl the main radicals involved in the degradation process through thermal activation.[28]

$$HSO_5^- \rightarrow SO_4^{\cdot-} + OH^{\cdot} \quad 3.3$$

$$SO_4^{\cdot-} + H_2O \rightarrow SO_4^{2-} + OH^{\cdot} + H^+ \quad 3.4$$

Alternatively, PMS can be activated in alkaline conditions, when pH > 11.[29] Under this condition, PMS can be considered fully deprotonated and is hydrolysed to form hydroperoxyl anion, the conjugated base of hydrogen peroxide (Eqs. 3.5 and 3.6) . This new anion can efficiently interact with PMS leading to the formation of sulfate and superoxide radicals; however, at high pH values, the sulfate radicals are quickly converted to hydroxyl radicals (Eqs 3.7 and 3.8)[30]

$$HSO_5^- + OH^- \rightarrow SO_5^{2-} + H_2O \quad 3.5$$

$$SO_5^{2-} + H_2O \rightarrow HO_2^- + SO_4^{2-} + H^+ \quad 3.6$$

$$HSO_5^- + HO_2^- \rightarrow SO_4^{\cdot-} + O_2^{\cdot-} + H_2O \quad 3.7$$

$$SO_4^{\cdot-} + OH^- \rightarrow SO_4^{2-} + OH^{\cdot} \quad 3.8$$

Indeed, the pH has a strong influence on the radicals involved in the overall reaction mediated by PMS: starting from acid conditions where sulfate radicals are favoured, at neutral or slightly basic pH both radicals contribute but by further increasing the

alkalinity, hydroxyl radicals are predominant.

In addition, UV light can also be efficient in activating PMS, with 254 nm being the preferred wavelength employed.[31] Also gamma rays[32] and ultrasounds[33] have proved efficient in breaking the O-O persulfate bond. The utilization of a light source, especially UV, is the most appreciated because while the thermal activation is energy demanding, the alkaline strategy requires the pH adjustment of the treated solution.

However, most commonly the activation of PMS is mediated by transition metals or metal oxide, both in the homogeneous and heterogeneous phases. Despite dissolved metal ions like Ag, Co, Fe or Mn[34] being more efficient because independent from the mass transfer, they cannot be easily recovered from the water stream, high amounts are required, their stability is strictly dependent on the pH (since precipitation can occur) or by water composition (due to the complexation efficiency of several organic molecules).[35] For these reasons, heterogeneous activation based on metal oxides is preferred: i) with Co_3O_4[36] and Mn_2O_3,[37] being the most efficient and investigated material, ii) iron oxides, iii) the most efficient ferrites that can be recovered easily from the solution thanks to their magnetic properties[38] or iv) CuO[39]. In both metal- and metal oxide- mediated PMS activation, the mechanism involves a redox cycle reaction of transition metal, as described by Eq. 3.9:

$$HSO_5^- + M^n \rightarrow M^{n+1} + SO_4^{\cdot-} + OH^{\cdot} \qquad 3.9$$

A similar mechanism can be activated in more complex metal oxides. Bi-metallic[40] or multi-metallic oxides[41] can involve an electron transfer between the different metals included in their structure in a synergic activation of PMS, making them more efficient than mono-metallic oxides. A wide investigation of the application of transition metal demonstrated that other compounds like, layered double hydroxides and oxides,[42] perovskite,[43] supported noble or non-noble metal NPs,[44] metal organic frameworks,[45] and metal-doped carbon catalysts,[46] proved efficient in activating PMS.

Alternatively, PMS can be involved to further accelerate photocatalytic process mediated by semiconductors.[47] This phenomenon, also observed for TiO_2,[48] is promoted by the possibility for PMS to act as a conduction band electron acceptor forming either sulfate or hydroxyl radicals (Eq. 3.10) or to react with photogenerated

holes (Eq. 3.11), forming peroxymonosulfate radical ($SO_5^{\cdot-}$), obtaining as final product reactive radicals (Eq. 3.12).

$$HSO_5^- + e_{CB}^- \rightarrow OH^- + SO_4^{\cdot-} \quad or \quad SO_4^{2-} + OH^{\cdot} \qquad 3.10$$

$$HSO_5^- + h_{VB}^+ \rightarrow H^+ + SO_5^{\cdot-} \qquad 3.11$$

$$2SO_5^{\cdot-} \rightarrow SO_4^{\cdot-} + O_2 \qquad 3.12$$

An interesting class of materials involved in PMS activation are also carbon-based catalysts that, thanks to their electron-rich functional groups and extended π network, can act as electron donor. In this context, graphene oxide, activated carbon and carbon nanotubes, with their electronic density and high surface area proved effectively activated PMS.[49]

The traditional radical pathway for the activation of PMS involving the formation of sulfate and hydroxyl radicals is the most investigated and exploited. However, some recently discovered non-radical pathways are attracting the attention, namely singlet oxygen ($^1O_2$),[50] mediated electron transfer,[51] and activated high-valent metal.[40]

It is clear that compared to photo-Fenton process, which can be activated only by Fe^{2+}, the activation of PMS can be easily obtained by a wider range of metals and materials, as summarized in Figure 3.8.

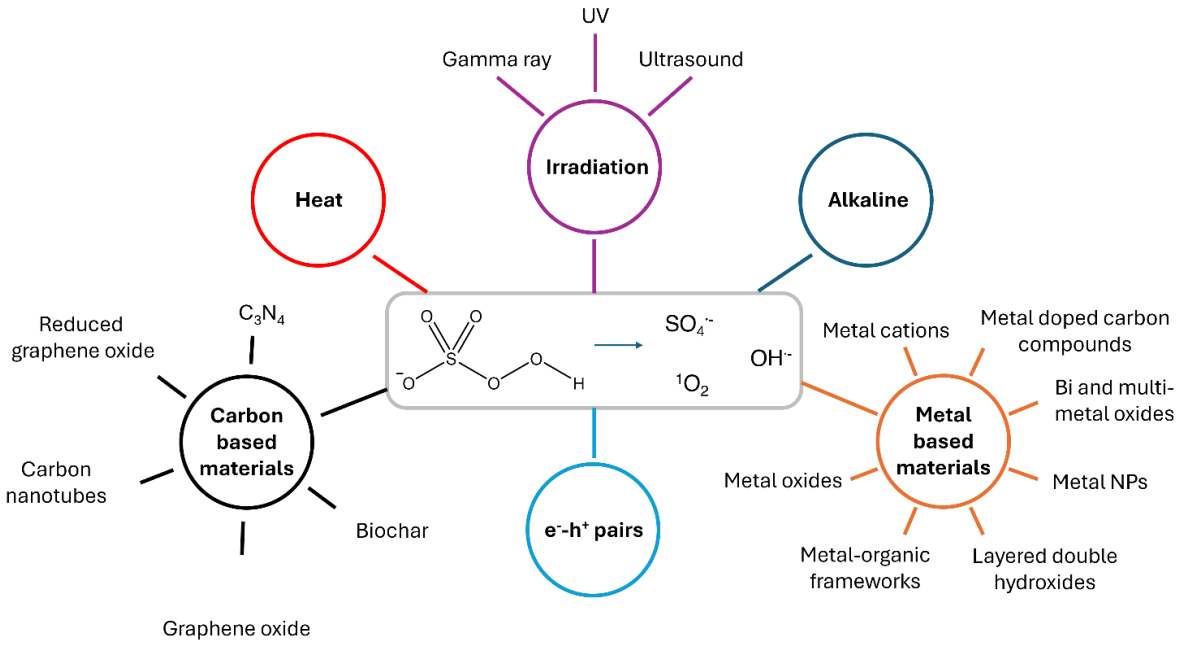

Figure 3.8: schematic representation of the different mechanisms for PMS activation

For this reason, the application of such type of AOP seems to be promising for a class of materials, like waste material, that has a very complex and not completely known composition and morphology. As an example, Chen et al.[52] demonstrated the efficiency of steel slag in activating PMS for the degradation of phenol. Furthermore, literature provided several examples of the application of biochar, a well-known waste material, in the PMS activation[53–55], further corroborating the potentiality of the application of waste materials in sulfate radicals-based AOPs.

3.2.2 Materials and methods

In this Paragraph, the procedure followed for the catalytic evaluation of tionite samples in the photodegradation of 4-CP in water is reported. Three different strategies were evaluated: photocatalysis, photo-Fenton catalysis and PMS-assisted (photo)degradation.

3.2.2.1 Materials

4-chlorophenol ≥99 % (4-CP), hydroxylamine hydrochloride 99.995% trace metal basis, Titanium (IV) oxysulfate ~ 15 % in dilute sulfuric acid, H_2O_2 30 wt. %, ortho-phenanthroline ≥99 %, PMS ($KHSO_5 \cdot ½\ KHSO_4 \cdot ½\ K_2SO_4$) and hydrochloric acid 37% were all purchased from Sigma-Aldrich. Potassium iodide 99% was purchased from Thermoscientific. Sodium hydroxide ≥98 % was purchased from VWR. Milli-Q water with a resistivity ρ >18.2 MΩ cm was used.

3.2.2.2 Photocatalytic degradation tests

The 4-CP degradation experiments were carried out in a beaker-type reactor at atmospheric pressure and RT. In a representative run, the proper amount of catalyst was dispersed by sonication and stirring at 500 rpm in 100 mL of a 25 mg mL aqueous solution of 4-CP, corresponding to a TOC value of 14.8 ppm. After the addition of the catalyst, the suspension pH was adjusted to 5.5 (pHmeter Mettler Toledo), corresponding to the natural pH of the 4-CP solution, using HCl or NaOH 0.1 M aqueous solution. At first, the catalyst suspension was stirred for 30 min in the dark to ensure to reach of the adsorption-desorption equilibrium. Irradiation was then

performed in an irradiation chamber equipped with up to 8 UV lamps (λ_{max} = 365 nm, Philips 24 W/10/4P), allowing to tune the incident irradiance (*I*) from 8.5 to 67.9 W m^{-2}. Unless otherwise stated, the number of lamps used for each catalytic test was 2, corresponding to an irradiance of 14.8 W m^{-2}. At selected time intervals, 2 mL of the photocatalytic suspension were withdrawn and filtered through a 0.20 μ m porosity filter (Aireka Cells) to remove the catalyst. The reaction was monitored by UV-Vis spectroscopy by using a UV-3100PC spectrometer (VWR) by following the disappearance of the 4-CP main absorption peak at λ = 224 nm (quartz cuvette, 1 cm optical path).

3.2.2.3 Photo-Fenton catalytic degradation tests

The photo-Fenton runs were performed under UV-A light in the same conditions previously described for the photocatalytic reactions, by adding stoichiometric amounts of H_2O_2, calculated with respect to the initial TOC concentration, e.g. 38 μ L of a 30 % H_2O_2 solution. Irradiation was performed at an irradiance of 14.8 W m^{-2} and H_2O_2 was added after the adsorption/desorption period in the dark. The evolution of the H_2O_2 concentration was measured by colorimetric titration by using the $TiOSO_4$ method.[56] Briefly, 0.5 mL of the filtered sample were added to a mixture of 4.5 mL of milli-Q H_2O and 0.5 mL of $TiOSO_4$ 15 % solution and then analysed by means of UV-Vis spectroscopy, by monitoring the signal at λ = 410 nm. The amount of Fe released during the experiment was quantified by the ortho-phenanthroline method.[57] Briefly, 2.0 mL of sample were treated with 0.25 mL of a 3 mol L^{-1} hydroxylamine aqueous solution and 0.25 mL of a 1,10-phenanthroline solution (0.125 g 1,10-phenanthroline, 50 mL milli-Q H_2O and 414 μ L of HCl 36 %). The amount of released iron was quantified by monitoring the signal at λ = 510 nm.

3.2.2.4 PMS-assisted photocatalytic degradation tests

The photocatalytic degradation of 4-CP was performed under UV light in the presence of PMS, in the condition previously described for the photocatalytic reactions. Representative runs, if not otherwise stated, were carried out in the presence of a catalyst concentration of 0.50 g L^{-1}, a PMS concentration of 0.30 g L^{-1} and an irradiance of 14.8 W m^{-2}. TOC measurements were performed to quantify the organic

carbon decrease and evaluate the 4-CP mineralization. PMS consumption during the reaction was monitored by iodometry (Eq. 3.13), followed by the reaction of iodine with iodide anion to form I_3^-.[58] Briefly, a proper volume of sample was added to 2.1 mL of milli-Q H_2O and 1.5 mL of a 0.6 mol L^{-1} KI aqueous solution. For experiments with 0.30 g L^{-1} PMS concentration, 0.20 mL of sample were used for the iodometry test; when the PMS concentration changed, the amount of sample used for the iodometry test was adjusted to keep the initial absorbance value constant. The consumption of PMS during the photocatalytic tests was monitored by UV-Vis spectroscopy using a UV-3100PC spectrometer (VWR) by following the absorption peak at λ = 350 nm.

$$HSO_5^- + 2\,I^- \rightarrow SO_4^{2-} + I_2 + OH^- \qquad 3.13$$

Photocatalytic experiments with PMS were conducted under simulated solar light irradiation by a Suntest XLS+ reaction chamber (Atlas Material Testing Technology BV), equipped with a 1700 W Xenon arc lamp providing an irradiance up to 500 W m^{-2}. The same solar simulator was used for visible light tests by using a Schott GG420 (cut-off) long-pass filter (λ > 420 nm). The emission spectra of the light source, with and without the filter, are reported in Figure 3.9. The reaction was carried out in a beaker-type glass reactor at a constant temperature of 20 ± 5 °C, controlled by a chiller, and at an irradiance of 500 and 250 W m^{-2}.

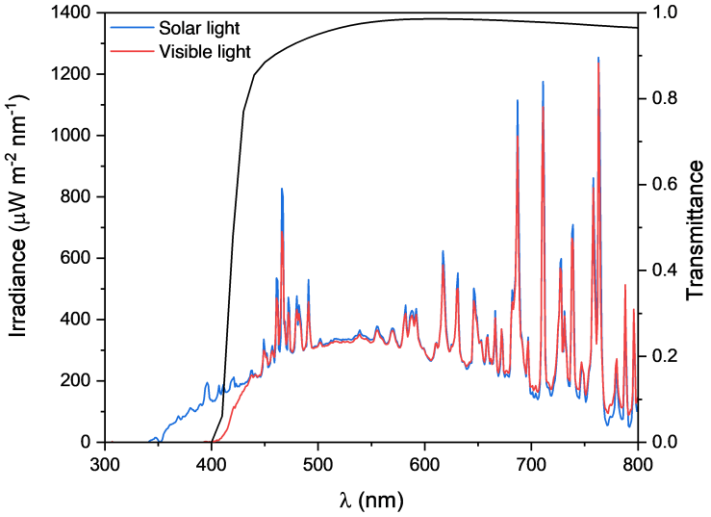

Figure 3.9: spectral distribution of the simulate solar light (blue) and of the visible light irradiation (red) obtained through a 420 nm cut-off filter. The cut off filter transmittance curve is reported. Measurements were performed by using a wideband RPS900-W rapid portable spectroradiometer (International Light Technology)

3.2.3 Results and discussion

This Paragraph describes the results of 4-CP degradation obtained with nCa_Tonite,

nNa_Tionite, nNa_Tionite_B and nNa_Tionite_A through the three different strategies. A particular focus is oriented on the PMS-driven catalytic degradation of the organic pollutant and on a preliminary investigation of the mechanism involved in the process.

3.2.3.1 Photocatalysis in the presence of tionite samples

In the first place, the photocatalytic efficiency of all tionite samples was investigated in a standard photodegradation test. According to the results in Figure 3.10, none of the samples apparently exhibits a decrease in the 4-CP concentration; actually, an increase in the C/C_0 parameter for all samples over the experiments duration was observed. However, this is a characteristics of samples showing ultra-low photocatalytic activity. Furthermore, after 6 h of irradiation, the TOC analysis for all samples (Figure 3.10b) shows an increase in the value of the total organic carbon content. This phenomenon can be related to the carbon residues detected in tionite materials by TGA and CHNS analyses, which probably are released during the experiment. Indeed, desorption experiments in Milli-Q water for all the samples revealed, after 6 h, the presence of organic carbon in the range of 4-6 ppm. By examining the UV-Vis spectra (Figure 3.10c), it is evident that the shape changes throughout the experiments. This variation can be therefore attributed to both the release of carbon compound, detected by TOC analysis, or to the appearance of the very first intermediates of 4-CP degradation, that adsorb in the same spectral region.

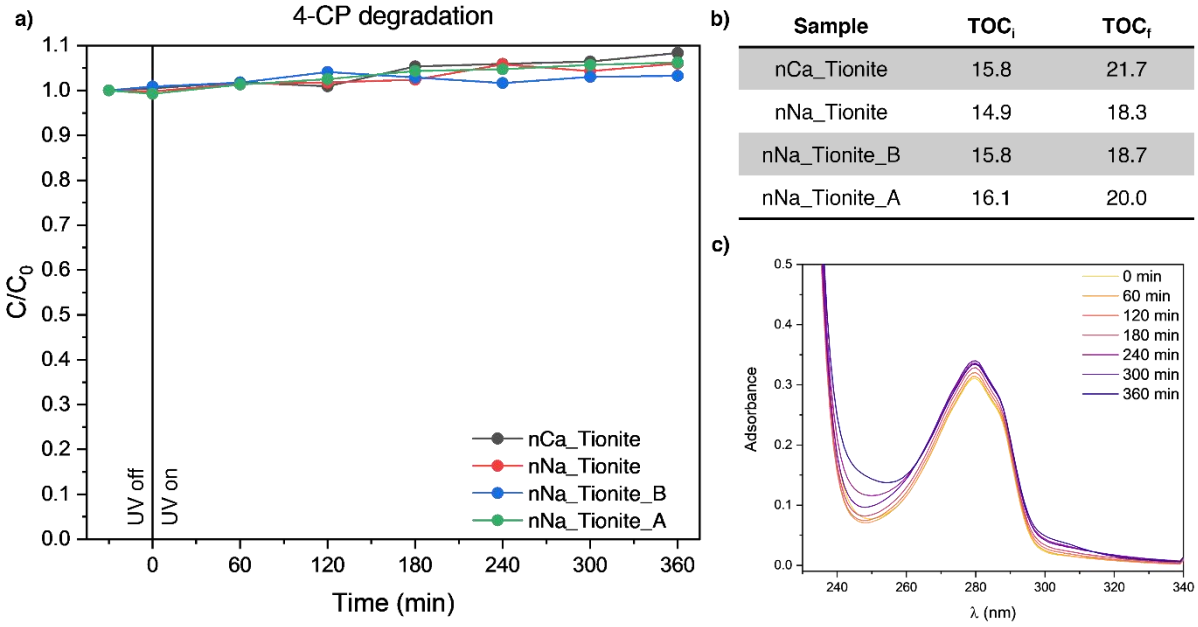

Sample	TOC_i	TOC_f
nCa_Tionite	15.8	21.7
nNa_Tionite	14.9	18.3
nNa_Tionite_B	15.8	18.7
nNa_Tionite_A	16.1	20.0

Figure 3.10: a) 4-CP degradation for nCa_Tionite (black), nNa_Tionite (red), nNa_Tionite_B (blue) and nNa_Tionite_A (green), b) TOC at -30 min (TOC_i) and at 6h (TOC_f) and c) UV-vis spectra recorder for nNa_Tionite.

3.2.3.2 *Photo-Fenton application of tionite*

Since tionite proved ineffective in the photocatalytic degradation of 4-CP, the following strategy was to exploit its iron content, as demonstrated by XRF and XPS analyses (see Paragraph 2.3) to check the possibility of performing photo-Fenton processes. Unfortunately, as shown in Figure 3.11, no significant degradation of 4-CP was observed for all samples, except for nNa_Tionite_A, which enables only 20% of 4-CP conversion after 6 h. This result can be tentatively attributed to the enhanced availability of photogenerated holes in the presence of the fluorinated tionite,[59] and to synergistic effects of photocatalysis and H_2O_2[60,61] rather than to a photo-Fenton mechanism. In fact, tionite treatment with HF completely removes iron from the surface, as demonstrated by XPS analysis. The corresponding lower consumption of H_2O_2 in the presence of the fluorinated TiO_2 sample is in agreement with the relevant literature.[62]

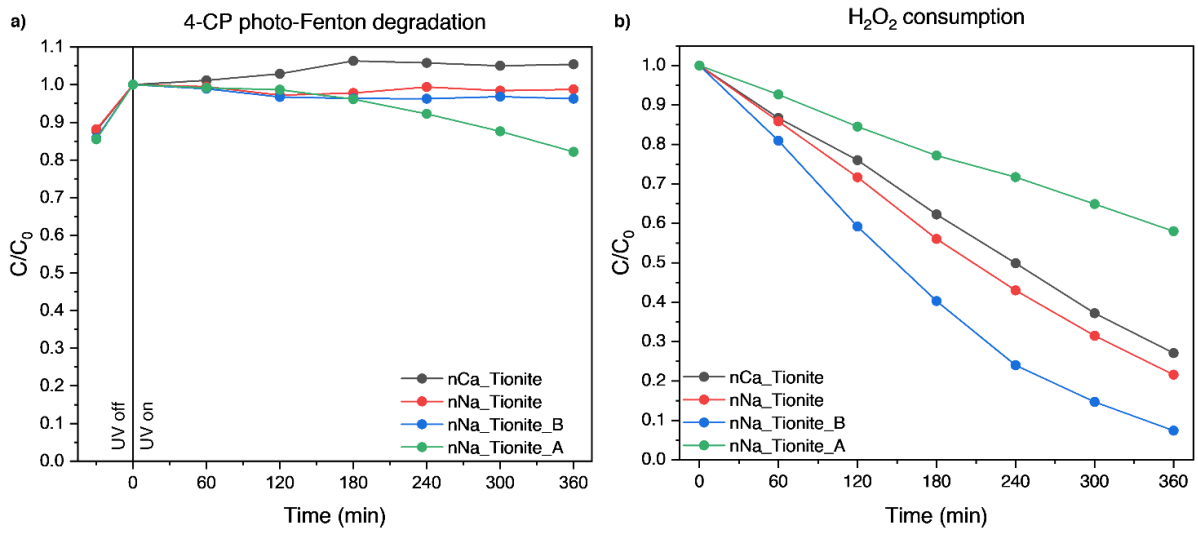

Figure 3.11: a) photodegradation of 4-CP and b) H_2O_2 consumption in the photo-Fenton process for nCa_Tionite (black), nNa_Tionite (red), nNa_Tionite_B (blue) and nNa_Tionite_A (green).

It must be noted that the titration test by the ortho-phenanthroline method did not provide any evidence of iron presence in the solution, confirming the null contribution of catalysis in the homogeneous phase. Since the contribution in the homogeneous phase is null, the photo-Fenton process could only occur *via* the iron located at the surface of the sample. According to the XPS results (Paragraph 2.3.4), the surface iron content is equal to 0.8 %, 2.0 % and 2.4 % for nCa_Tionite, nNa_Tionite and nNa_Tionite_B. The complete inactivity of the tionite samples demonstrates that the

surface iron content detected is too low to provide a sensible degradation of 4-CP or not in the proper oxidation state.

3.2.3.3 PMS-driven photodegradation on tionite under UV light

Considering tionite's inefficiency in activating H_2O_2, its potential application in sulfate radical-based AOPs was explored. PMS is a more easily activated oxidizing agent compared to hydrogen peroxide, as it can be activated by a wider range of metals and metal oxides, including Fe, Ag, Co, Mn and their mono- and bi- metallic oxides.[35]

Preliminary parametric study. Reference experiments were conducted to assess the effective role of the catalyst in the photodegradation of 4-CP and in the activation of PMS, namely involving:

- 4-CP and PMS in the dark
- 4-CP and PMS under light
- 4-CP, PMS and catalyst in the dark

Among the different reference experiments, the test conducted with 4-CP and PMS under UV irradiation was the only one showing a significant decrease in the concentration of both 4-CP and PMS. For this reason, only the results of this reference experiment will be reported for comparison in purple colour.

The determination of the efficiency of tionite samples in a PMS-driven photodegradation process towards 4-CP and the complexity of such a process required the implementation of a preliminary parametric study. At first, the effects of both the catalyst and PMS concentrations were investigated. nNa_Tionite was used as reference sample since its composition can be considered intermediate compared to the more complex nCa_Tionite or to the purified treated samples. In addition, Figure 3.12 illustrates the reduction in 4-CP and PMS concentrations at different concentrations of nNa_Tionite, namely 0.25, 0.50 and 1.00 g L^{-1}.

An increase in both PMS consumption and 4-CP degradation was observed when the concentration of nNa_Tionite was increased from 0.25 to 0.50 g L^{-1}, which is commonly attributed to a higher number of active sites available for PMS activation, resulting in a higher production of radicals.[63] On the other hand, further increasing the catalyst concentration to 1.00 g L^{-1} provided a slight decrease in the removal efficiency of both

the pollutant and PMS.

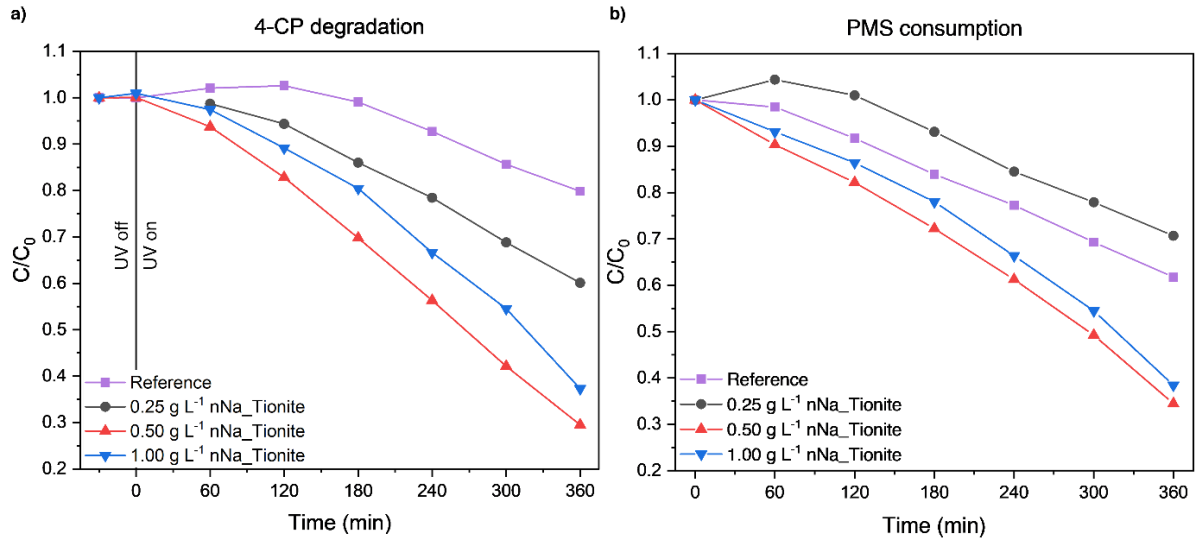

Figure 3.12: influence of nNa_Tionite concentration on a) 4-CP degradation and b) PMS consumption. Reference experiment (4-CP + PMS) is reported in purple for comparison.

Considering the shape of the degradation/consumption curves, the apparent kinetic constant (k) was calculated according to the zero-order kinetic model. This kinetic model can be observed when the catalyst surface is saturated by pollutant molecules.[64,65] For nNa_tionite, the low degradation efficiency observed suggest that the number of active sites is limited and, consequentially, it operates under saturation condition. The hypothesis is further supported by the retention of linearity even after the long duration of the experiments. The apparent k values ($R^2 > 0.98$) retrieved by the calculations are reported in Table 3.2.

Table 3.2: influence of nNa_Tionite concentration on the apparent k values for both 4-CP degradation and PMS consumption

[nNa_Tionite] (g L^{-1})	k 4-CP ($\cdot 10^{-2}$ ppm min^{-1})	k PMS ($\cdot 10^{-2}$ ppm min^{-1})
Reference	2.8	3.0
0.25	3.5	3.0
0.50	5.4	4.5
1.00	5.0	4.2

Despite the results show a similarity in the apparent k value of the reference performed with 0.15 g L^{-1} and in the absence of the catalyst, an increase from 3.5 $\cdot 10^{-2}$ to 5.4 $\cdot 10^{-2}$ ppm min^{-1} for 4-CP degradation, and from 3.0 $\cdot 10^{-2}$ to 4.5 $\cdot 10^{-2}$ ppm min^{-1} for PMS

consumption, was observed when nNa_Tionite concentration increased from 0.25 to 0.50 g L^{-1}. By operating at 1.00 g L^{-1}, the apparent k values are equal to 5.0 $\cdot 10^{-2}$ and 4.2 $\cdot 10^{-2}$ ppm min^{-1}, which are comparable to the results obtained with 0.50 g L^{-1} of Tionite_Na.

Based on these results, a catalyst concentration of 0.50 g L^{-1} has been considered the optimum and has therefore been employed in subsequent experiments.

The effect of varying PMS concentration on both 4-CP degradation and PMS consumption is shown in Figure 3.13. For this purpose, PMS concentrations equal to 0.05, 0.15, 0.30 and 0.45 g L^{-1} were tested.

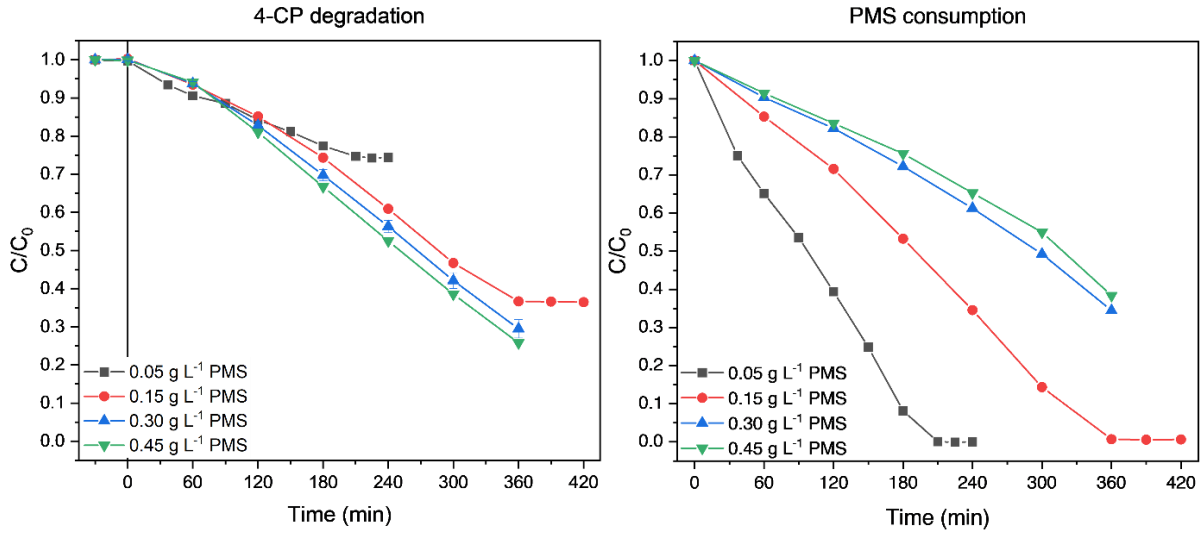

Figure 3.13: influence of PMS concentration on a) 4-CP degradation and b) PMS consumption

According to the apparent k values in Table 3.3 (R^2 > 0.98), an increase in the 4-CP degradation rate from 2.9 $\cdot 10^{-2}$ to 4.1 $\cdot 10^{-2}$ ppm min^{-1} was observed when the PMS concentration increased from 0.05 to 0.15 g L^{-1}, likely due to a more efficient PMS activation. By further increasing PMS, no variation in the pollutant degradation was observed. It is indeed reported in literature that an excessive PMS concentration does not improve the degradation yield since the radicals can be involved in scavenging reactions (Eqs. 3.14 - 3.17), rather than oxidizing the target molecule.[66–68]

$$HSO_5^- + SO_4^{\cdot -} \rightarrow SO_4^{2-} + SO_5^{\cdot -} + H^+ \quad 3.14$$

$$SO_4^{\cdot -} + SO_4^{\cdot -} \rightarrow 2SO_4^{2-} \quad 3.15$$

$$SO_4^{\cdot-} + HO^{\cdot} \rightarrow SO_4^{2-} + OH^{-} \quad 3.16$$

$$SO_4^{\cdot-} + O_2^{\cdot-} \rightarrow SO_4^{2-} + O_2 \quad 3.17$$

On the other hand, by increasing PMS concentration, the apparent k value shows a progressive decrease, due to the larger amount of molecules that need to be activated, reaching a plateau value at 0.30 g L^{-1}. It is important to note that once PMS was completely consumed by the reaction, no further degradation of 4-CP was detected; consequentially, further addition of PMS would allow to increase the final degradation level.

Table 3.3: influence of PMS concentration on the apparent k values for both 4-CP degradation and PMS consumption

[PMS] (g L^{-1})	k 4-CP (·10^{-2} ppm min^{-1})	k PMS (·10^{-2} ppm min^{-1})
0.05	2.9	12
0.15	4.1	6.8
0.30	5.4	4.5
0.45	5.8	4.3

According to the results shown, considering that the gain in performances remains minor for a PMS concentration higher than 0.30 g L^{-1}, the optimal experimental conditions have been set at a PMS concentration of 0.30 g L^{-1}. Operating at this concentration, the kinetic constant for PMS degradation is less affected by small variations in PMS quantity between experiments, since we are working in the plateau range.

In conclusion, the best experimental conditions require a catalyst concentration of 0.50 g L^{-1} and a PMS concentration of 0.30 g L^{-1}. The concentration of catalyst and PMS were employed in all the experiments described from this point forward, unless otherwise stated.

Influence of the tionite-based samples. Once the experimental conditions had been established, the investigation proceeded to examine the different tionite samples. Figure 3.14 reports the photodegradation results for all four samples of tionite. For the sake of comparison, the reference experiments is also shown.

As previously described, the experiment with 4-CP and PMS under UV irradiation is

the only reference experiment providing a decrease in both 4-CP and PMS curves. This means that PMS activation does not occur in the dark, neither by adsorption on tionite catalyst nor in the homogeneous phase. Contrarily, the activation occurs under UV irradiation in the bulk of the reactor (homogeneous system), as reported in the relevant literature,[69,70] leading to an apparent rate constant for 4-CP degradation of $2.8 \cdot 10^{-2}$ ppm min^{-1}. In addition, an increase in the C/C_0 parameter can be observed in the initial 120 min and, since the catalyst was absent, it can be attributed to the interference in the UV-vis spectra of 4-CP degradation by-products.

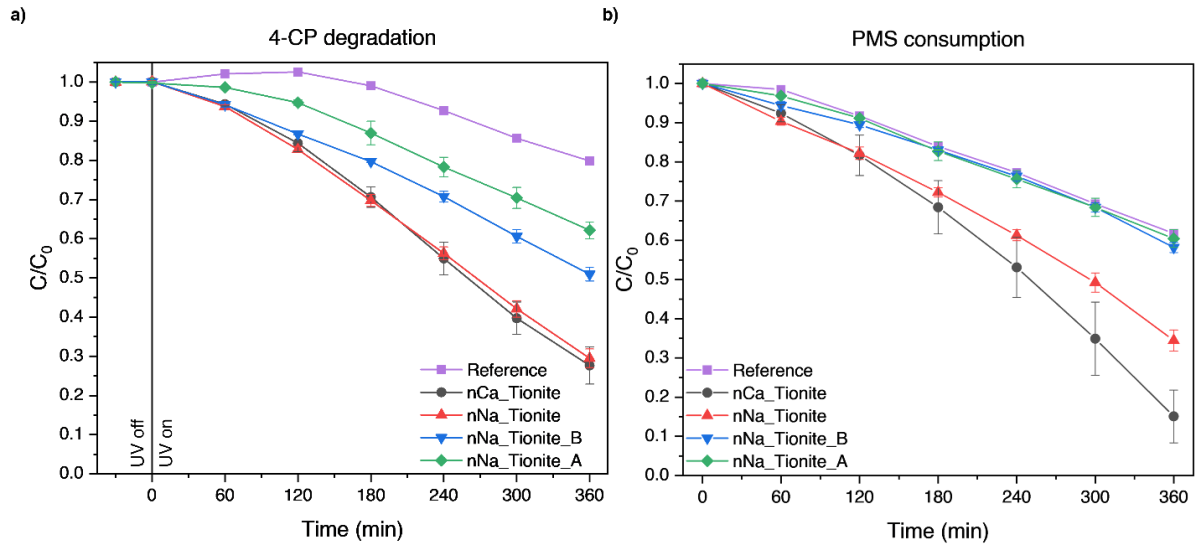

Figure 3.14: a) 4-CP degradation and b) PMS consumption results for reference (4-CP + PMS, purple) nCa_Tionite (black), nNa_Tionite (red), nNa_Tionite_B (blue) and nNa_Tionite_A (green)

When tionite samples were involved in the degradation test, no adsorption of 4-CP during the dark period was detected. Regarding both 4-CP degradation and PMS consumption, they exhibited two different behaviours. nNa_Tionite and nCa_Tionite provided a two-fold increase in both 4-CP and PMS degradation rates (Table 3.4, $R^2 >$ 0.99) compared to the reference experiment in the homogeneous phase. In contrast, the acidic and basic treated tionite samples provided k values comparable to the reaction in pure homogeneous phase.

The k values similarity between nNa_Tionite_A and _B with the reference experiment can be possibly attributed to a null sample contribution in activating PMS, meaning that the activation occurs only in the homogeneous phase. Alternatively, the activation promoted by the two tionite samples compensates a lower homogeneous phase contribution due to the scattering effect of dispersed particles that reduces the

irradiance.

To get more information, further investigations on the catalytic performances were performed by TOC analysis, shown in Figure 3.15.

Table 3.4: apparent k values calculated in both 4-CP degradation and PMS consumption curves for nCa_Tionite, nNa_Tionite, nNa_Tionite_B and nNa_Tionite_A Apparent k values for the reference are reported for comparison

Sample	k 4-CP ($\cdot 10^{-2}$ ppm min^{-1})	k PMS ($\cdot 10^{-2}$ ppm min^{-1})
Reference	2.8	3.0
nCa_Tionite	5.7	6.4
nNa_Tionite	5.5	4.5
nNa_Tionite_B	3.6	2.6
nNa_Tionite_A	3.1	3.0

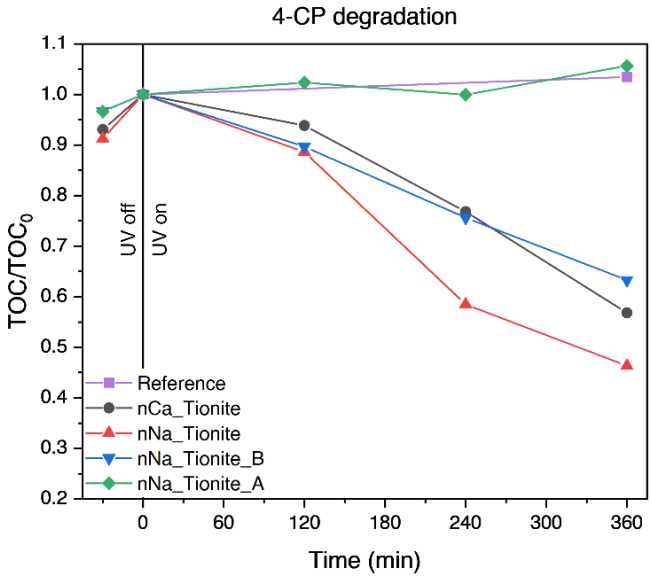

Figure 3.15: TOC results for the 4-CP degradation for the reference (4-CP + PMS, purple), nCa_Tionite (black), nNa_Tionite (red), nNa_Tionite_B (blue) and nNa_Tionite_A (green)

For all samples, the TOC value slightly increased during the dark period, further confirming the release of the carbon compounds detected in the TGA analysis and discussed previously in the paragraph devoted to photocatalytic results. However, the decrease in the TOC value observed for several samples confirms their ability to mineralize the target molecule. In this scenario, the mineralization of 4-CP by nNa_Tionite_B is significantly higher than in the reference experiment, confirming that

this sample is effectively involved in PMS activation. In contrast, nNa_Tionite_A does not provide a decrease in the carbon content of the solution; instead, the TOC value increases during the experiment. This observation can be attributed to the higher carbon compound content of nNa_Tionite_A, equal to 20 wt. %, compared to the other samples (9-9.5 wt. %) detected by TGA analysis in Paragraph 2.3.

Effect of irradiance on the tionite activation of PMS. To further confirm the catalytic activity of NaOH- and HF-treated tionites, photocatalytic tests were carried out at different irradiances. The previous part revealed the contribution of both homogeneous and heterogeneous reactions in the PMS-assisted photodegradation of 4-CP, so the effect of irradiance was assessed in pure homogeneous phase, in the absence of the catalyst. Figure 3.16 illustrates the evolution curves for the 4-CP degradation and the PMS consumption under irradiances of 8.50, 14.8, 34.2, 47.6 and 67.9 W m^{-2}, corresponding to the use of 1, 2, 4, 6 and 8 lamps, respectively.

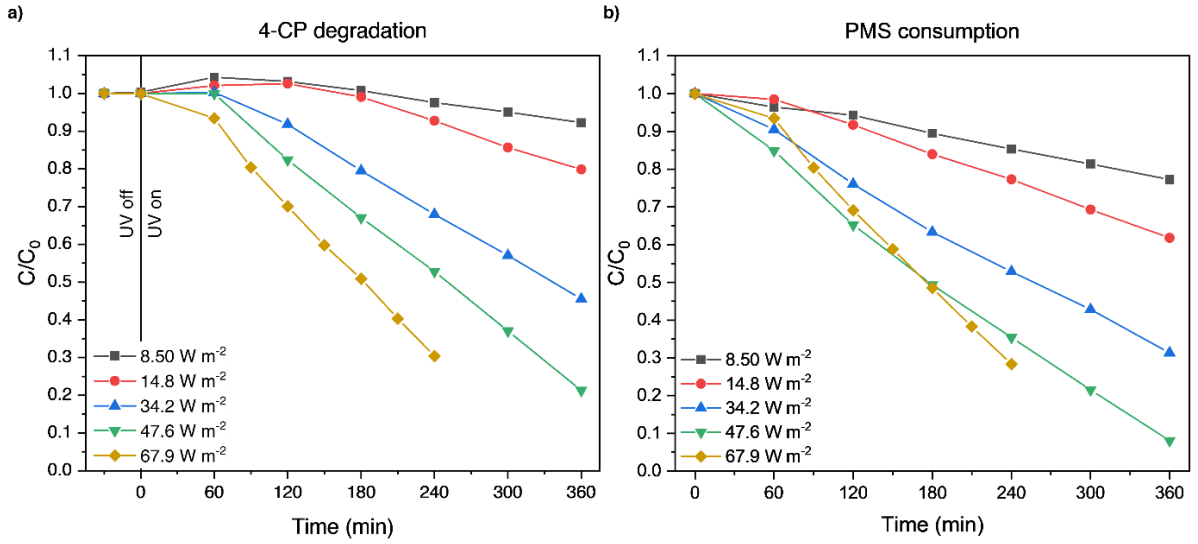

Figure 3.16: a) 4-CP degradation and b) PMS consumption results for reference experiments (4-CP + PMS) conducted at I = 8.5 W m^{-2} (black), 14.8 W m^{-2}(red), 34.2 W m^{-2}(blue), 47.6 W m^{-2}(green) and 67.9 W m^{-2}(brown).

Increasing the photon flux leads to a noticeable increase in both 4-CP degradation and PMS consumption apparent rates (R^2 > 0.99). This trend, depicted in Figure 3.17 in colour purple, shows a clear linear relationship between the irradiance and the apparent k values, indicating that both 4-CP degradation and PMS consumption – and more globally the overall photochemical process – operate according to a photon-limited regime.

Thereby the experiments were subsequently conducted with all four tionite catalysts. The graphs for 4-CP degradation and PMS consumption curve at different irradiances for all samples are reported in Figure S1 in Appendix – 1. For the sake of simplicity, in Figure 3.17, only the relationship between apparent k values and irradiance is depicted ($R^2 > 0.97$).

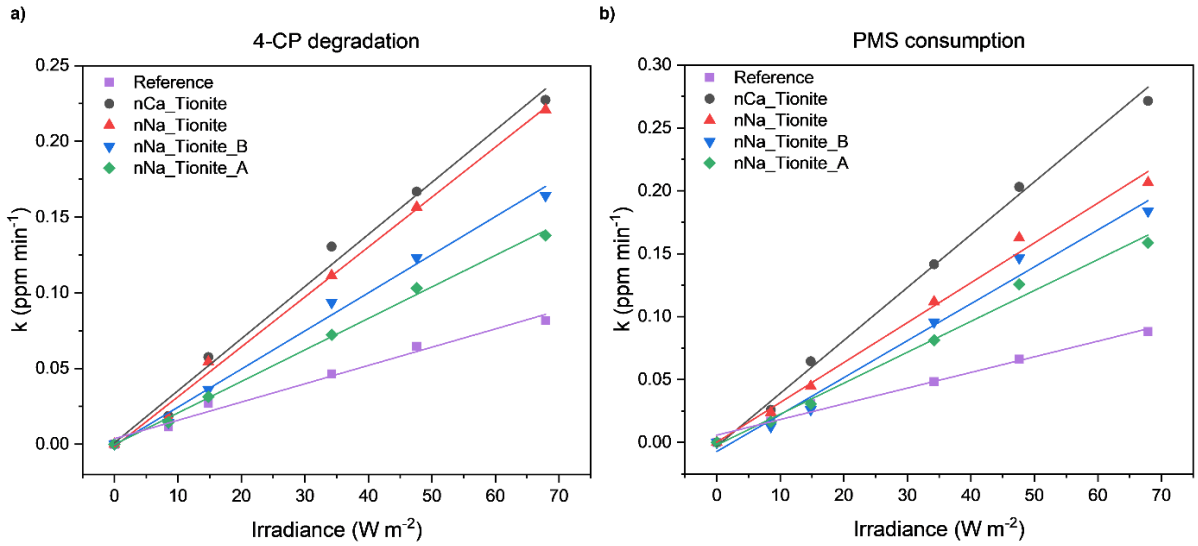

Figure 3.17: k values vs I and linear fitting for a) 4-CP degradation and b) PMS consumption for the reference experiments (4-CP + PMS, purple), nCa_Tionite (black), nNa_Tionite (red), nNa_Tionite_B (blue) and nNa_Tionite_A (green).

In the presence of the heterogeneous catalyst, a linear relationship between the apparent k constant and the irradiance is also observed regardless of the nature of the catalyst ($R^2 > 0.99$). In particular, at higher irradiance values, the two treated samples, nNa_Tionite_B and nNa_Tionite_A, exhibited a clear increase in the k value, which further supports their effectiveness in activating PMS. However, the overall results prove that the untreated samples are more efficient in activating PMS and, consequently, in photodegrading the target molecule. On the other hand, it is important to consider that the mechanism involved in PMS activation is significantly different from a standard UV photocatalysis on TiO_2. The extremely complex composition of tionite samples complicates the identification of the precise causes of this behaviour, especially because the activation mechanism of PMS activation might involve multiple metal elements, as previously stated.

In one possible mechanism, it occurs the formation of a surface charge-transfer complex between PMS and TiO_2. In fact, through its hydroxyl functionality, PMS can chelate titanol groups on the TiO_2 surface, forming a complex, active in the visible light

range, with an adsorption tail up to 500 nm. Upon irradiation, the electron transfer from the visible-responsive complex to the TiO_2 conduction band induces the PMS activation, leading to the formation of active radicals.[71–73] It is realist to hypothesize this route in the presence of tionite samples because the lamps utilized for the tests, despite working with UV light, have an emission at 405 and 435 nm that could activate the complex.[74]

Another proposed mechanism suggests a weakening in the HSO_5^- bond as a consequence of its electrostatic adsorption on the catalyst surface, which facilitates the photoactivation with UV light.[66] This strategy is commonly associated with a side activation mechanism of PMS, involving a change in the oxidation state of surface metal atoms, such as Co[75–77] or Mn.[78–80]

Despite different activation mechanisms could be involved, they share a common initial step: the adsorption of PMS onto the catalyst surface. The experimental results, reported in Figure 3.17, further confirm this aspect. It is well-known that for classic photocatalysts, such as TiO_2, the number of involved photons and the reaction rate have a linear relationship at low light intensities. At higher irradiances, however, this relationship shifts to a half-order type till the final step of the zero order, where the photodegradation rate reaches a plateau value due to the higher probability of electron-hole recombination.[81,82] In the case of tionite samples, the linearity persists up to the irradiance value of 67.9 W m^{-2}, suggesting that the main role of light is not directly related to the heterogeneous semiconductor catalyst.

Taking all the results into account, it is therefore reasonable to conclude that PMS activation is not primarily induced by the interaction between the light and the catalyst. Instead, the evidence strongly suggest that light alone plays a direct and pivotal role in the activation of PMS and tionite improves the activation efficiency. This phenomenon is advantageous for the application of tionite in the photodegradation of organic pollutants: even though the material does not exhibit outstanding photocatalytic performances, the same 4-CP degradation yield can be achieved in a shorter time by increasing (concentrating) the photon flux.

To highlight the role played by tionite in the activation of PMS and to quantify the synergistic effect provided by the heterogeneous semiconductor catalyst, the synergic k_{syn}(PMS) parameter was defined and calculated according to Eq. 3.18.

$$k_{syn}(PMS) = \frac{k_{PMS+cat}}{k_{PMS}} \quad 3.18$$

where $k_{PMS+cat}$ is the apparent kinetic constant for the PMS consumption calculated for the experiment involving both PMS and the catalyst, k_{PMS} is the apparent kinetic constant for the PMS consumption calculated in the homogeneous phase experiment with only PMS.

In a similar manner, the synergic constant k_{syn}(4-CP) was calculated for the degradation of 4-CP, according to Eq. 3.19.

$$k_{syn}(4\text{-CP}) = \frac{k_{PMS+cat}}{k_{PMS} + k_{cat}} \quad 3.19$$

where $k_{PMS+cat}$ and k_{PMS} have the same definition of Eq. 6, but referred to the 4-CP degradation curve, while k_{cat} is the apparent kinetic constant for the classic photocatalytic test with only the catalyst, which was found to be null in our test conditions, as noted earlier in the paragraph

Based on the Eqs. 6 and 7, k_{syn}(4-CP) and k_{syn}(PMS) define how faster 4-CP is degraded and PMS is consumed in the presence of the heterogeneous semiconductor catalyst compared to the homogeneous phase degradation experiment. In other words, the parameter indicates the sole contribution of the tionite samples to the reaction, without considering the PMS activation by UV light.

Figure 3.18 depicts the k synergic values at different irradiances for all samples.

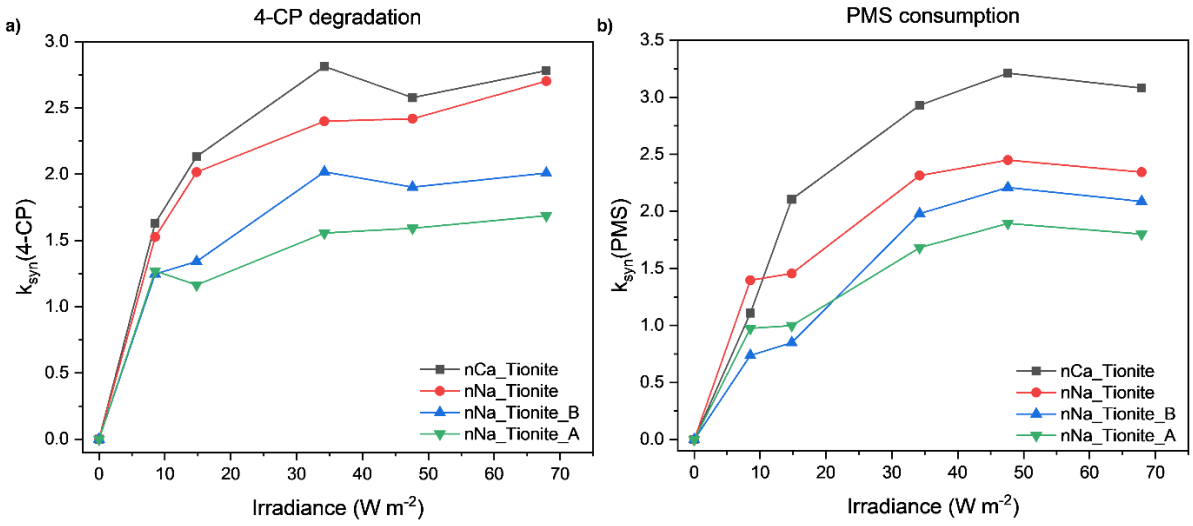

Figure 3.18: influence of I on k_{syn} values for a) 4-CP degradation and b) PMS consumption for nCa_Tionite (black), nNa_Tionite (red), nNa_Tionite_B (blue) and nNa_Tionite_A (green).

For both 4-CP and PMS graphs, the k_{syn} values show a progressive increase when the irradiance passes from value 0 up to 34.2 W m^{-2}. Beyond this point, as the number of photons increases, the parameter reaches a plateau. At low irradiances, the reactor could be not uniformly irradiated and scattering effect cause by the dispersed particles are more considerable while, by increasing the photon-flux, the effect provided by the catalyst is maximized. On the other hand, being k_{syn} constant at higher irradiance values, the effect of increasing the photon flux must be equal on both the reference and the catalytic experiments. If the effect of the light would depend on the catalyst, a continuous increase in the k_{syn} should be seen, because the photocatalyst would better exploit UV light. As a result, the species that effectively adsorbs UV light is not the catalyst, but PMS and/or, depending on the mechanism, the complex between PMS and TiO_2.

Considering the plateau value reached, the different efficiency between the treated and untreated tionite samples is even more clear. Indeed, while nNa_Tionite and nCa_Tionite provide an average increase in the 4-CP degradation of 2.5 times, nNa_Tionite_B and nNa_Tionite_A contribute only to a two-fold rate increase. In this scenario, the removal of SiO_2/aluminosilicate due to the basic treatment (nNa_Tionite_B) proved detrimental to the activation of PMS. Although SiO_2 on its own is not efficient in activating PMS[83], kaolinite proved efficient in activating the molecule for the degradation of atrazine thanks to the formation of a complex between PMS and kaolinite through the surface hydroxyl groups.[84] For this reason, a mechanism involving aluminosilicate cannot be excluded. Similar considerations could be also applied to the HF-treated sample; however, as previously described, the fluorination of its surface alters both the catalytic and adsorption properties of the material, further complicating the identification of the underlying mechanism.

3.2.3.4 PMS-driven photocatalysis of tionite under solar irradiation

The catalytic activity of nNa_Tionite in activating PMS was tested under both simulated solar light and visible light, in order to determine to which extent the visible fraction of the solar spectrum contributes to the overall activity. Figure 3.19 shows the 4-CP degradation and PMS consumption for both types of light and at two different irradiances: 500 and 250 W m^{-2}. Notably, the experiments labelled as “reference” were

conducted in the presence of PMS and 4-CP only, in the absence of the catalyst. In the absence of PMS, hence in a pure photocatalysis test, no variation in the 4-CP absorbance was detected, in agreement with results observed in Paragraph 3.2.3.1.

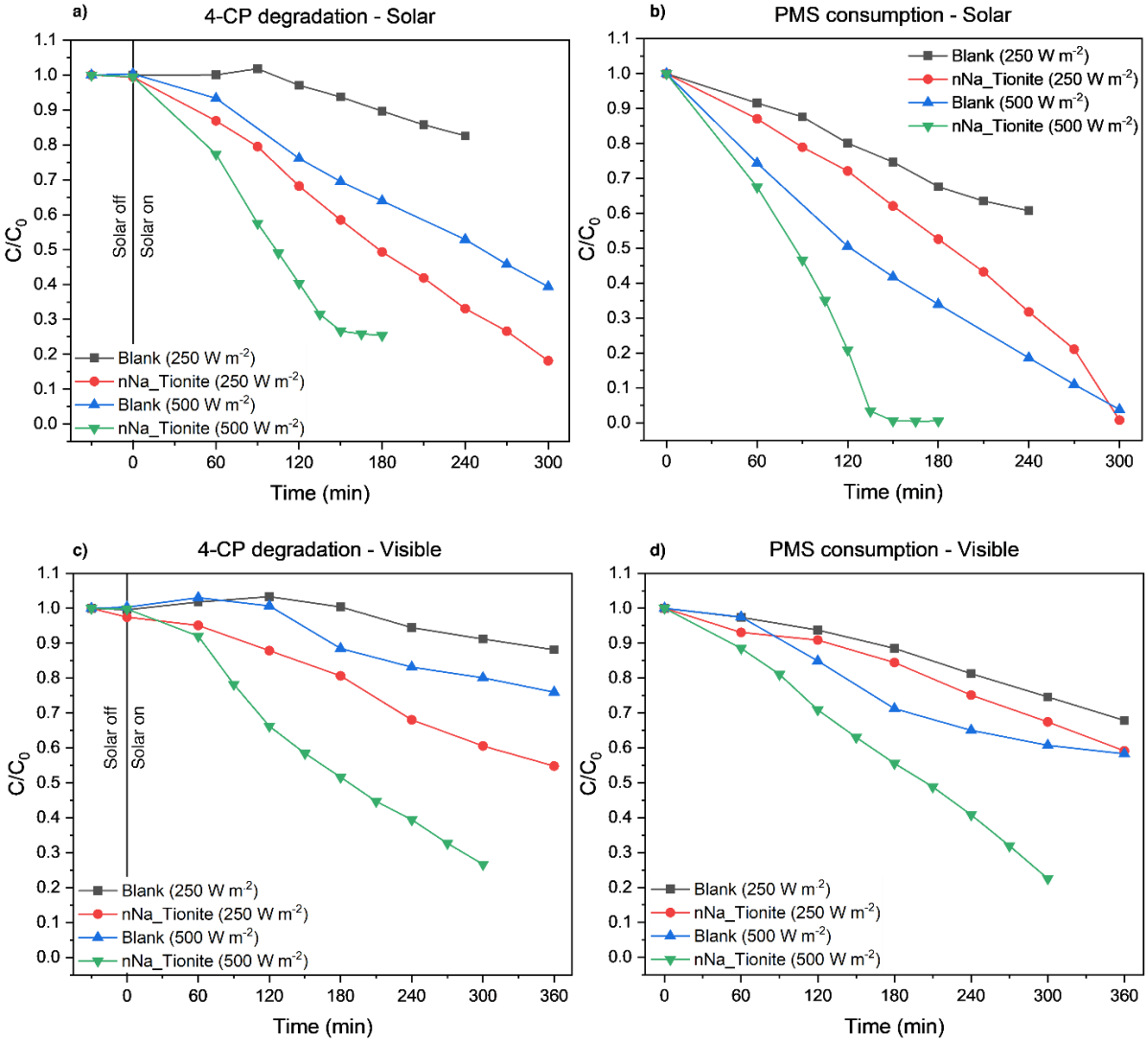

Figure 3.19: 4-CP degradation and PMS consumption for nNa_Tionite at 500 and 250 W m^{-2} under solar (a,b) and visible (c,d) irradiation

For both degradation tests performed under solar light and visible light, the apparent kinetic constants (Table 3.5, R^2 > 0.97) are clearly directly proportional to the irradiance. As consequence, by doubling the photon flux employed in the reaction, the apparent k values increase two-fold. This result is better depicted in Figure 3.20, where the relationship between apparent k and irradiance is fitted with a linear function with a R^2 values always > 0.99.

Table 3.5: apparent k values calculated in the first order trait of both 4-CP and PMS degradation curves for the reference and nNa_Tionite experiments, at 500 and 250 W m^{-2}

Irradiance (W m^{-2})	Sample	k 4-CP degradation (·10^{-2} ppm min^{-1})		k PMS consumption (·10^{-2} ppm min^{-1})	
		Solar	*Visible*	*Solar*	*Visible*
250	Reference	3.2	1.6	4.2	1.6
250	nNa_Tionite	7.2	3.5	7.4	2.8
500	Reference	5.4	3.0	7.8	2.8
500	nNa_Tionite	14	6.5	16	7.7

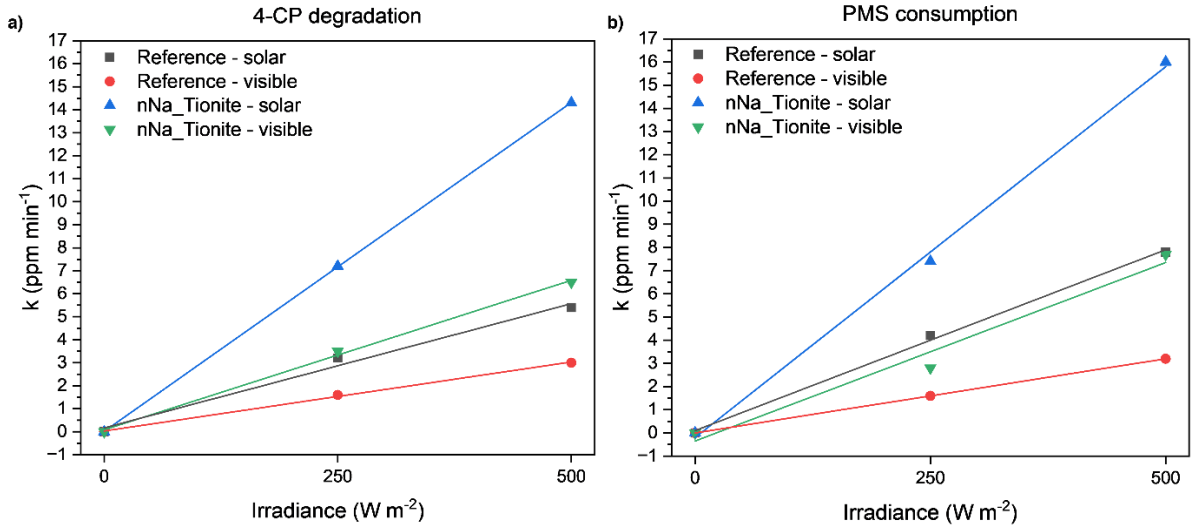

Figure 3.20: influence of irradiance value on the apparent k values of (a) 4-CP degradation and (b) and PMS consumption

Table 3.6: k_{syn} valued calculated for 4-CP degradation and PMS consumption under solar or visible irradiation, at 500 or 250 W m^{-2}

Irradiance (W m^{-2})	k_{syn} (4-CP)		k_{syn} (PMS)	
	Solar	*Visible*	*Solar*	*Visible*
250	2.26	2.13	1.75	1.78
500	2.65	2.15	2.07	2.07

By comparing the results, it is possible to notice that the experiments performed with the full solar spectrum show a higher rate constant for all the experiments performed. The reason for this phenomenon can be associated to the role played by UV light in activating PMS, as demonstrated in the previous paragraph. In addition, in all

experimental conditions, the presence of the catalyst induces an increase in the rate of both 4-CP degradation and PMS consumption. The calculation of k_{syn} according to Eq 3.18 and 3.19, based on these values, provides the results reported in Table 3.6, which show an interesting phenomenon.

Despite the different contributions of UV light, the k_{syn} values for both solar and visible experiments are identical. These results suggest that visible light is sufficient to promote the tionite role in the activation of PMS. As consequence, the mechanism involving the formation of a charge-transfer complex between TiO_2 and PMS which is active in the visible range cannot be excluded.

3.2.4 Final considerations

With the aim of exploring the potentiality of tionite in the photocatalytic degradation of a representative organic pollutant, 4-CP, various catalytic processes were investigated. Initially a standard photocatalytic application was tested, considering the TiO_2 content in tionite. However, no significant degradation was observed. Another trial was conducted by applying a photo-Fenton strategy, leveraging the iron content in tionite. Unfortunately, this method also proved ineffective in degrading the target molecule and the low efficiency observed for nNa_Tionite_A was tentatively attributed to the reported synergy between fluorinated TiO_2 and H_2O_2.

As a final approach, the mediation of PMS in degrading 4-CP was examined. These tests showed promising results, with tionite samples demonstrating a high efficiency in activating PMS and in achieving the minerlization of 4-CP, as confirmed by TOC measurements. A comparison of the efficency across different tionite samples revealed that the best performances were obtained with the untreated samples, specifically nCa_Tionite and nNa_Tionite.

From a sustainability perspective, these findings are ideal, as they show that the best degradation yield of the organic pollutant was achieved using the least processed and more sustainable samples. Moreover, the lack of need to treat tionite with chemicals, such as HF and NaOH, further enhances its sustainability, especially considering that tionite itself is a waste material.

These considerations prompted a deeper investigation of the PMS-driven process. By

studying the reaction at various light intensities, a perfectly linear relationship was observed between the apparent kinetic constant and the photonic flux for both 4-CP degradation and PMS consumption, up to an irradiance value of 67.9 W m^{-2}. These findings led to two key conclusions: i) the same 4-CP degradation yield can be obtained in a shorter time by increasing the number of photon flux and ii) the mechanism does not involve a photocatalytic stimulation of tionite, which instead, acts as a conventional catalyst.

Additional Insights into the mechanism were obtained by studying the same reaction under simulated solar and visible light. Calculation of the k_{syn} factor indicated that the increase in the degradation rate induced by nNa_Tionite was identical under both under solar and visible irradiation. This suggested that the activation of PMS through the formation of a visible-light active charge transfer complex between TiO_2 and PMS cannot be excluded.

Starting from these observations, a more in-depth investigation of the mechanism involved in the PMS activation is required. In particular, the attention should be focused on the formation of the charge transfer complex, whose involvement can be easily demonstrated by modifying the sample surface with phosphate anions, which block PMS adsorption. In addition, radical scavengers would provide information about the effective chemical species involved in the process.

Overall, the results highlight the potentiality of tionite application in the photodegradation of organic pollutants. Finding a potential application for a waste material, without requiring additional chemical or mechanical treatments, is a pivotal step forward in both circular economy practices and a more sustainable water decontamination.

3.3 Bibliography

[1] D. Jadhav, R. B.N., P. R. Gogate, V. K. Rathod, *J. Food Eng.* **2009**, *93*, 421–426.

[2] P. D'Arrigo, L. A. M. Rossato, A. Strini, S. Serra, *Molecules* **2024**, *29*, 1–32.

[3] W. Bin Huang, C. Y. Du, J. A. Jiang, Y. F. Ji, *Res. Chem. Intermed.* **2013**, *39*, 2849–2856.

[4] M. Fache, B. Boutevin, S. Caillol, *ACS Sustain. Chem. Eng.* **2016**, *4*, 35–46.

[5] J. Nayak, A. Basu, P. Dey, R. Kumar, A. Upadhaya, S. Ghosh, *Biomass Convers. Biorefinery* **2023**, *13*, 14317–14340.

[6] E. I. Evstigneyev, S. M. Shevchenko, *Wood Sci. Technol.* **2020**, *54*, 787–820.

[7] N. Kumar, V. Pruthi, *Biotechnol. Reports* **2014**, *4*, 86–93.

[8] S.-C. Liu, X. Xin, Z.-J. He, Z.-H. Xie, Z.-X. Xie, Z.-H. Liu, B.-Z. Li, Y.-J. Yuan, *Int. J. Biol. Macromol.* **2024**, *281*, 136406.

[9] A. Sharma, J. Singh, P. Sharma, G. S. Tomar, S. Singh, M. Grover, L. Nain, *3 Biotech* **2021**, *11*, 1–10.

[10] P. Upadhyay, N. K. Singh, R. Tupe, A. Odenath, A. Lali, *Prep. Biochem. Biotechnol.* **2020**, *50*, 341–348.

[11] V. Augugliaro, G. Camera-Roda, V. Loddo, G. Palmisano, L. Palmisano, F. Parrino, M. A. Puma, *Appl. Catal. B Environ.* **2012**, *111–112*, 555–561.

[12] F. Parrino, V. Augugliaro, G. Camera-Roda, V. Loddo, M. J. López-Muñoz, C. Márquez-Álvarez, G. Palmisano, L. Palmisano, M. A. Puma, *J. Catal.* **2012**, *295*, 254–260.

[13] A. Di Paola, M. Bellardita, B. Megna, F. Parrino, L. Palmisano, *Catal. Today* **2015**, *252*, 195–200.

[14] O. Sacco, P. Franco, I. De Marco, V. Vaiano, E. Callone, R. Ceccato, F. Parrino, *J. Mater. Sci. Technol.* **2022**, *112*, 49–58.

[15] R. Ciriminna, R. Delisi, F. Parrino, L. Palmisano, M. Pagliaro, *Chem. Commun.* **2017**, *53*, 7521–7524.

[16] I. Langmuir, *J. Am. Chem. Soc.* **1918**, *40*, 1361–1403.

[17] W. Koagouw, N. A. Stewart, C. Ciocan, *Environ. Sci. Pollut. Res.* **2021**, *28*, 48823–48836.

[18] N. Blangetti, F. S. Freyria, M. C. Calviello, N. Ditaranto, S. Guastella, B. Bonelli, *Catalysts* **2023**, *13*.

[19] M. Bellardita, G. Camera-Roda, V. Loddo, F. Parrino, L. Palmisano, *Catal. Today* **2020**, *340*, 128–144.

[20] M. Mrowetz, E. Selli, *Phys. Chem. Chem. Phys.* **2005**, *7*, 1100–1102.

[21] F. Parrino, V. Loddo, V. Augugliaro, G. Camera-Roda, G. Palmisano, L. Palmisano, S. Yurdakal, *Catal. Rev. - Sci. Eng.* **2019**, *61*, 163–213.

[22] F. Parrino, C. De Pasquale, L. Palmisano, *ChemSusChem* **2019**, *12*, 589–602.

[23] A. Gottuso, A. Köckritz, M. L. Saladino, F. Armetta, C. De Pasquale, G. Nasillo, F. Parrino, *J. Catal.* **2020**, *391*, 202–211.

[24] M. Bellardita, G. Escolano-Casado, L. Palmisano, L. Mino, *Catal. Today* **2023**, *413–415*, 113983.

[25] D. Tsukamoto, M. Ikeda, Y. Shiraishi, T. Hara, N. Ichikuni, S. Tanaka, T. Hirai, *Chem. – A Eur. J.* **2011**, *17*, 9816–9824.

[26] A. B. Ross, P. Neta, *Natl. Bur. Stand. Natl. Stand. Ref. Data Ser.* **1982**, *1027*.

[27] H. Milh, D. Cabooter, R. Dewil, *Chem. Eng. J.* **2021**, *422*, 1–11.

[28] S. Yang, P. Wang, X. Yang, L. Shan, W. Zhang, X. Shao, R. Niu, *J. Hazard. Mater.* **2010**, *179*, 552–558.

[29] S. Wacławek, H. V. Lutze, V. K. Sharma, R. Xiao, D. D. Dionysiou, *Curr. Opin. Chem. Eng.* **2022**, *37*, DOI 10.1016/j.coche.2022.100854.

[30] C. Liang, H. W. Su, *Ind. Eng. Chem. Res.* **2009**, *48*, 5558–5562.

[31] M. Mahdi-Ahmed, S. Chiron, *J. Hazard. Mater.* **2014**, *265*, 41–46.

[32] S. Wang, J. Wang, *Chem. Eng. J.* **2018**, *336*, 595–601.

[33] Y. Lee, S. Lee, M. Cui, Y. Ren, B. Park, J. Ma, Z. Han, J. Khim, *Chem. Eng. J.* **2021**, *413*, DOI 10.1016/j.cej.2020.127487.

[34] G. P. Anipsitakis, D. D. Dionysiou, *Environ. Sci. Technol.* **2004**, *38*, 3705–3712.

[35] J. Wang, S. Wang, *Chem. Eng. J.* **2018**, *334*, 1502–1517.

[36] X. Chen, J. Chen, X. Qiao, D. Wang, X. Cai, *Appl. Catal. B Environ.* **2008**, *80*, 116–121.

[37] H. Li, N. Yuan, J. Qian, B. Pan, *Environ. Sci. Technol.* **2022**, *56*, 4498–4506.

[38] B. Kakavandi, M. Z. Salmasi, P. Bashardoust, S. Giannakis, R. R. Kalantary, *Process Saf. Environ. Prot.* **2024**, *182*, 426–442.

[39] F. Ji, C. Li, L. Deng, *Chem. Eng. J.* **2011**, *178*, 239–243.

[40] A. Gu, K. Chen, X. Zhou, C. Gong, P. Wang, Y. Jiao, P. Mao, K. Chen, J. Lu, Y. Yang, *Chem. Eng. J.* **2023**, *468*, DOI 10.1016/j.cej.2023.143444.

[41] W. Li, P. Wu, Y. Zhu, Z. Huang, Y. Lu, Y. Li, Z. Dang, N. Zhu, *Chem. Eng. J.* **2015**, *279*, 93–102.

[42] M. Jin, B. Xu, J. Zhang, Z. Wang, B. Xing, G. Yi, L. Chen, Y. Wu, Z. Li, *CrystEngComm* **2024**, *26*, 1756–1766.

[43] P. Liang, D. Meng, Y. Liang, Z. Wang, C. Zhang, S. Wang, Z. Zhang, *Chem. Eng. J.* **2021**, *409*, 128196.

[44] Y. Y. Ahn, H. Bae, H. Il Kim, S. H. Kim, J. H. Kim, S. G. Lee, J. Lee, *Appl. Catal. B Environ.* **2019**, *241*, 561–569.

[45] Y. Wu, G. Liang, W. Bin Li, X. F. Zhong, Y. Y. Zhang, J. W. Ye, T. Yang, Z. W. Mo, X. M. Chen, *Chem. Sci.* **2024**, *15*, 9733–9741.

[46] G. Wang, X. Nie, X. Ji, X. Quan, S. Chen, H. Wang, H. Yu, X. Guo, *Environ. Sci. Nano* **2019**, *6*, 399–410.

[47] F. Ghanbari, M. Moradi, *Chem. Eng. J.* **2017**, *310*, 41–62.

[48] X. Chen, W. Wang, H. Xiao, C. Hong, F. Zhu, Y. Yao, Z. Xue, *Chem. Eng. J.* **2012**, *193–194*, 290–295.

[49] L. Hao, J. Zhang, J. Liu, Y. Min, C. Chen, *Chem. Rec.* **2023**, *23*, DOI 10.1002/tcr.202300203.

[50] L. Kong, G. Fang, X. Xi, Y. Wen, Y. Chen, M. Xie, F. Zhu, D. Zhou, J. Zhan, *Chem. Eng. J.* **2021**, *403*, DOI 10.1016/j.cej.2020.126445.

[51] S. Zuo, Z. Guan, D. Xia, F. Yang, H. Xu, M. Huang, D. Li, *Chem. Eng. J.* **2021**, *420*, DOI 10.1016/j.cej.2020.127619.

[52] B. Chen, T. Zhou, C. Zhao, T. Huang, X. Geng, Y. Wang, Y. Zhao, *Environ. Res.* **2024**, *243*, 1–10.

[53] P. T. Huong, K. Jitae, T. M. Al Tahtamouni, N. Le Minh Tri, H. H. Kim, K. H. Cho, C. Lee, *J. Water Process Eng.* **2020**, *33*, 1–7.

[54] S. Wang, J. Wang, *Chem. Eng. J.* **2019**, *356*, 350–358.

[55] B. C. Huang, J. Jiang, G. X. Huang, H. Q. Yu, *J. Mater. Chem. A* **2018**, *6*, 8978–8985.

[56] G. M. Eisenberg, *Ind. Eng. Chem. - Anal. Ed.* **1943**, *15*, 327–328.

[57] W. B. Fortune, M. G. Mellon, *Ind. Eng. Chem. Anal. Ed.* **1938**, *10*, 60–64.

[58] R. E. Ball, J. O. Edwards, M. L. Haggett, P. Jones, *J. Am. Chem. Soc.* **1967**, *89*, 2331–2333.

[59] N. Fessi, M. F. Nsib, L. Cardenas, C. Guillard, F. Dappozze, A. Houas, F. Parrino, L. Palmisano, G. Ledoux, D. Amans, Y. Chevalier, *J. Phys. Chem. C* **2020**, *124*, 11456–11468.

[60] Y. Wang, C. S. Hong, *Water Res.* **1999**, *33*, 2031–2036.

[61] N. San, A. Hatipoğlu, G. Koçtürk, Z. Çinar, *J. Photochem. Photobiol. A Chem.* **2001**, *139*, 225–232.

[62] M. Mrowetz, E. Selli, *Phys. Chem. Chem. Phys.* **2005**, *7*, 1100–1102.

[63] W. Da Oh, J. R. J. Zaeni, G. Lisak, K. Y. A. Lin, K. H. Leong, Z. Y. Choong, *Chemosphere* **2021**, *277*, DOI 10.1016/j.chemosphere.2021.130313.

[64] D. F. Ollis, *Front. Chem.* **2018**, *6*, 1–7.

[65] X. Li, S. Anwer, Q. Guan, B. Li, V. Chan, G. Palmisano, L. Zheng, *Chem. Eng. Sci.* **2024**, *284*, DOI 10.1016/j.ces.2023.119501.

[66] R. R. M. Silva, L. Valenzuela, R. Rosal, L. A. M. Ruotolo, F. G. E. Nogueira, A. Bahamonde, *J. Environ. Chem. Eng.* **2023**, *11*, DOI 10.1016/j.jece.2023.109265.

[67] Y. Wang, L. Zhou, X. Duan, H. Sun, E. L. Tin, W. Jin, S. Wang, *Catal. Today* **2015**, *258*, 576–584.

[68] H. Zhang, L. chao Nengzi, X. Li, Z. Wang, B. Li, L. Liu, X. Cheng, *Chem. Eng. J.* **2020**, *386*, DOI 10.1016/j.cej.2020.124011.

[69] C. A. L. Graça, A. C. de Velosa, A. C. S. C. Teixeira, *Catal. Today* **2017**, *280*, 80–85.

[70] J. Moreno-Andrés, M. Tierno-Galán, L. Romero-Martínez, A. Acevedo-Merino, E. Nebot, *Water Res.* **2023**, *232*, DOI 10.1016/j.watres.2023.119686.

[71] H. Y. Yoo, M. S. Kim, H. Shin, J. Lim, *J. Hazard. Mater.* **2022**, *433*, 1–10.

[72] J. Jia, D. Liu, S. Wang, H. Li, J. Ni, X. Li, J. Tian, Q. Wang, *Sep. Purif. Technol.* **2020**, *253*, 117510.

[73] Y. Jo, C. Kim, G. H. Moon, J. Lee, T. An, W. Choi, *Chem. Eng. J.* **2018**, *346*, 249–257.

[74] Philips Lighting, "Actinic PL-L 24W/10/4P 1CT/25 - leaflet," can be found under https://www.lighting.philips.com/prof/special-lamps/insect-trap/actinic-bl/actinic-bl-pl-s-pl-l/927903221007_EU/product, **2024**.

[75] Y. Zhou, X. Hu, Y. Zhang, X. Chen, H. Zhao, Q. Fu, F. Xu, Y. Gao, *Appl. Surf. Sci.* **2021**, *566*, 150657.

[76] W. Guo, S. Su, C. Yi, Z. Ma, *Environ. Prog. Sustain. Energy* **2013**, *32*, 193–197.

[77] B. Liu, W. Guo, H. Wang, S. Zheng, Q. Si, Q. Zhao, H. Luo, N. Ren, *J. Hazard. Mater.* **2021**, *416*, DOI 10.1016/j.jhazmat.2021.125679.

[78] J. Liu, Z. Zhao, P. Shao, F. Cui, *Chem. Eng. J.* **2015**, *262*, 854–861.

[79] A. Eslami, M. Hashemi, F. Ghanbari, *J. Clean. Prod.* **2018**, *195*, 1389–1397.

[80] Y. Y. and X. Z. Li Chen, Wanyi Fu, Congyu Hou, *Catalysts* **2021**, *11*, 1–18.

[81] F. Hussein, in *Adv. Treat. Text. Effl.*, **2011**, pp. 117–144.

[82] D. F. Ollis, in *Photochem. Convers. Storage Sol. Energy*, **1983**, pp. 593–622.

[83] Y. Feng, W. Sang, Z. Deng, S. Zhang, C. Li, *Sep. Purif. Technol.* **2022**, *280*, DOI 10.1016/j.seppur.2021.119783.

[84] C. Li, Y. Huang, X. Dong, Z. Sun, X. Duan, B. Ren, S. Zheng, D. D. Dionysiou, *Appl. Catal. B Environ.* **2019**, *247*, 10–23.

Chapter 4: Synthesis, characterization and application of TiO_2 NPs on SiO_2-based supports

Chapter 4 is dedicated to the preparation of TiO_2 photocalysts on silica-based materials, such as silica and clays.

First, a brief state-of-the-art regarding the anchoring of TiO_2 NPs on supports is presented, highlighting the advantages of using an adsorbent material as support and describing the structure of the two clays involved in the investigation. The synthesis of two additional SiO_2-based supports is presented, followed by the procedure for depositing TiO_2 NPs on all the supports considered. All the prepared materials will be characterized to define the composition and morphology of the synthetised TiO_2. In addition, preliminary photocatalytic test for the degradation of PC and metal cation adsorption test will be described.

The second part is focused on the application of immobilized TiO_2 NPs in the CO_2 reduction to CH_4 through photothermo catalysis. Two protocols applied for the deposition of Ru NPs on each supported TiO_2 samples is described along with the characterization of the products. Finally, preliminary results in the photothermo catalytic methanation of CO_2 will be presented.

4.1 Synthesis and characterization of TiO_2 NPs on SiO_2-based supports

4.1.1 Introduction to TiO_2 NPs supported on adsorbent materials

The significance of the use of TiO_2 NPs in environmental remediation has been described in Paragraph 1.3.1, as well as some drawbacks due to the nano-dimension, namely the tendency to aggregate due to the high surface energy, decreasing the surface area and the available active sites and the difficulties in separating particles from the slurry.[1] As anticipated, a strategy to overcome both problems is to anchor the photocatalyst to a supporting material to improve and maintain dispersion, but also to facilitate their recovery. In this context, the utilisation of adsorbent supports is a strategic choice[2–4] and various adsorbents have been investigated for the removal of pollutants such as activated carbon[5], zeolite[5] and polymeric adsorbents, like chitosan[5].

It is worth noticing that the application of SiO_2 as an adsorptive supporting material is promising due to its peculiar properties, especially the possibility to tailor its morphology and porosity[6]. A well-known example of the versatility of SiO_2 is represented by MCM-41, a porous silica synthesised through a templated sol-gel procedure. The method proposed by Kumar *et al.*[7] involves a silicon precursor, commonly tetraethylorthosilicate, n-cetyltrimethylammonium bromide and a base as a catalyst.[7] By utilizing a surfactant as a templating agent, the final product is a mesoporous silica with pore size of 2-10 nm organised in a hexagonal ordering.[8]

However, an alternative silica-based material is represented by clays, especially from a sustainable point of view, since they are natural products with high availability and low cost. In addition, depending on the type of clay selected, they have several beneficial properties for an adsorption application like high surface area, remarkable porosity, high mechanical strength and as well as chemical and thermal stability. In particular, porosity and surface area are the most important parameters because they influence the amount of pollutant molecules that come into contact with the photocatalyst active sites.[9] In addition, it's been found that TiO_2/clay nanocomposite can show an improved photoactivity due to lower charge recombination that is tentatively attributed to the presence of interlayer cations in the clay structure which can entrap electrons, making the holes free to start the oxidation process.[10,11]

In this thesis, halloysite (Hall, Figure 4.1a) and sepiolite (Sep, Figure 4.1a) have been chosen as supporting clays for TiO_2 because their structure is significantly different in terms of morphology and porosity.

Hall is a 1:1 dioctahedral clay composed of an octahedral $AlO_2(OH)_4$ alumina sheets and a tetrahedral SiO_4 sheet, which combine to form a unit where Si and Al are joined by sharing oxygen atoms. This results in a sheet-shaped aluminosilicate with general formula $Al_2(OH)_4Si_2O_5 \cdot nH_20$ and the apical oxygens of silica tetrahedrons and alumina tetrahedrons pointing in the two opposite sides of the 2D material. The interesting aspect of Hall is the wrapping of 1:1 mineral multilayers providing the clay with a tubular morphology, kept together by the interposition of a monolayer of water molecules between the overlapping layers.[9,12,13]

On the other hand, Sep is a phyllosilicate consisting of a continuous two-dimensional Si-O tetrahedral sheet and a discontinuous Mg-O octahedral sheet in a 2:1 ribbon structure. The elemental unit of Sep, the ribbon, consists of two inverse-oriented tetrahedral SiO_2 sheets whose apical oxygens point, directed in the same direction, are connected to the octahedral sheet, consisting of Mg. It is also possible that Mg cations can be easily substituted by Al(III) or Fe(III), causing structural defects due to the generation of negative charges. Finally, these ribbons are connected along one axis through the oxygen atoms delimiting their surface, providing sepiolite with a fiber-like structure, with rectangular channels running in the same axis direction.[9,14,15]

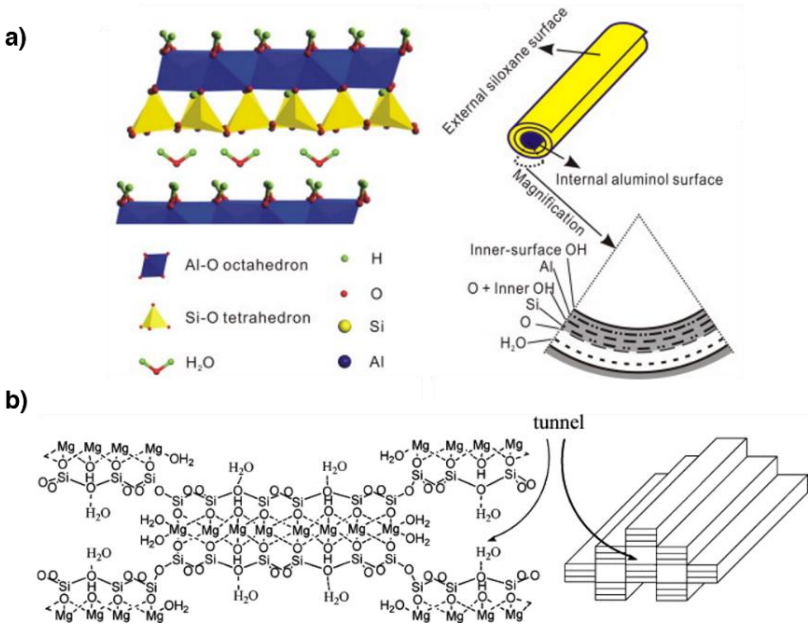

Figure 4.1: representation of the structure of a) Hall and b) Sep. Adapted from [12] and [16]

The application of TiO_2 supported on clays represents a promising strategy to improve the reusability and efficiency of the photocatalyst. Despite the utilization of SiO_2 supports reduces the sustainability of the process, due to the synthetic procedure required, they represent a good reference. At the same time, sustainability is indeed considered even in this approach since the application of clays, which are naturally available and therefore do not require a synthesis procedure, make them green adsorbent materials. To assess the properties of the synthetised materials, preliminary photodegradation tests were conducted using PC as target molecule. Preliminary adsorption tests were performed on a solution of Cu(II), Ni(II) and Y(III). Those metal cations are chosen because Cu and Ni are toxic pollutants commonly discharged from industrial processes like refining or electroplating, while Y is contained in mining wastewater and, being a rare earth, its recovery is economically convenient.

4.1.2 Materials and methods

In this paragraph, the synthetic procedure followed for the preparation of SiO_2 NPs, SiO_2 sheets and the functionalization of all supports with TiO_2 is reported, along with the materials employed. Specifications on the characterization conditions employed and the related sample preparation are reported in Appendix - 2.

4.1.2.1 Materials

Tetraethyl orthosilicate (TEOS) ≥99 %, titanium(IV) isopropoxide (TTIP) ≥97 % ammonia solution (NH_4OH) 25 %, Poly(ethylene glycol)-*block*-poly(propylene glycol)-*block*-poly(ethylene glycol) (Pluronic P123, Mn ~ 5800), sodium chloride (NaCl) >99 %, Hall, $Ni(NO_3)_2 \cdot 3\ H_2O$, $Cu(NO_3)_2 \cdot 6\ H_2O$ and $Y(NO_3)_3 \cdot 6\ H_2O$ were purchased from Sigma-Aldrich and used as received. Sep was purchased from Pangel S9 – Tolsa group. Paracetamol (PC) 98 % was purchased from Thermo Scientific. Hydrochloric acid (HCl) 37 % was purchased from VWR. Ethanol absolute (EtOH) ≥ 99.8 % was purchased from Honeywell. Milli-Q water with a resistivity ρ >18.2 MΩ cm was used.

4.1.2.2 Synthesis of SiO_2 NPs

Silica NPs were synthesised following a modified procedure of the Stöber method

reported by Tripaldi *et al.*[17] Briefly, 50.0 mL of ammonium hydroxide solution (25 wt. % in H_2O) and 1000 mL of EtOH absolute were added to a 2000 mL round-bottom flask, equipped with a reflux condenser. The solution was stirred at 500 rpm and heated at 60 °C. A mixture of 25.0 mL of TEOS and 28.0 mL of EtOH was transferred to a dropping funnel and added dropwise at a rate of ~1 mL min^{-1}. The molar ratio of ammonia, TEOS and water in the final mixture was NH_4OH : TEOS : H_2O = 3 : 1 : 17. The reaction mixture was left at 60 °C for 20 h under magnetic stirring. When the reaction was completed, 25 mL of a 2 mol L^{-1} HCl solution were added to the reaction mixture to favour SiO_2 NPs separation. The product was recovered by centrifugation at 9000 rpm for 30 min and washed three times with EtOH. The collected powder was then dried in an oven overnight at 80 °C. The dried sample, herein labelled SiO_2, was used for the physico-chemical characterization. Scheme 4.1 shows the procedure and mechanism of SiO_2 synthesis.

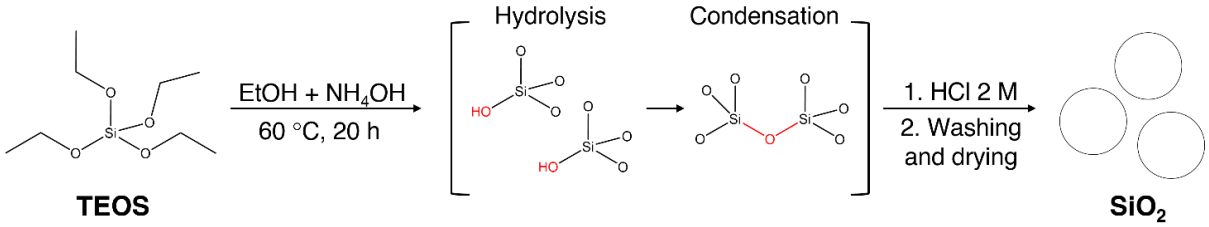

Scheme 4.1: Stöber SiO_2 synthesis via hydrolysis and condensation, starting from TEOS

4.1.2.3 Synthesis of SiO_2 sheets

SiO_2 sheets were synthesized following the procedure described by Okuno *et al.*[18] In a 250 mL round-bottom flask 1.74 g of Pluronic P123 and 2.92 g of NaCl were dissolved in 100 mL of a 1 mol L^{-1} HCl solution. The mixture was stirred at 700 rpm and heated at 35 °C. When the polymer was completely dissolved, 4.17 g of TEOS were added to the mixture and the reaction was left under magnetic stirring, at 35 °C for 24 h. After the reaction was completed, the product was recovered by vacuum filtration and washed at first with distilled water (dH_2O) and then with EtOH. The powder was dried overnight in an oven at 80 °C. In order to efficiently remove the residual Pluronic P123, the powder was calcinated at 550 °C for 3 h. A schematic representation of the synthetic procedure is depicted in Scheme 4.2.

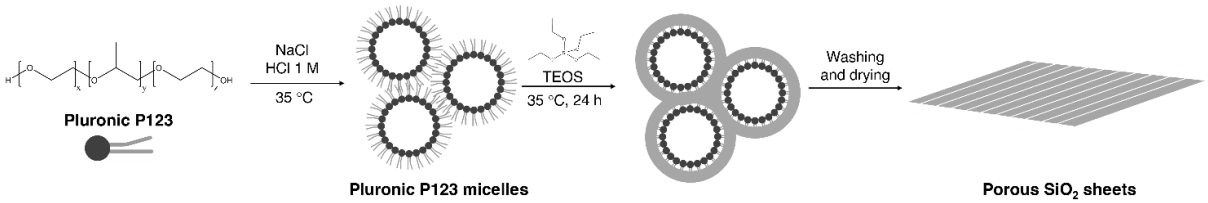

Scheme 4.2: synthetic step for the SiO_2 sheets preparation

4.1.2.4 Synthesis of TiO_2 NPs on SiO_2-based supports

The precursor TiO_2 sol was prepared by mixing TTIP, HCl and EtOH. The TiO_2 sol was prepared by mixing water and TTIP at molar ratio 0.82 and TTIP concentration 0.4 mol L^{-1}. The stock solution was then diluted with EtOH to obtain a TTIP concentration of 0.05 M and a final calculated pH of 2.17.[19] The SiO_2-based support was dispersed in dH_2O (1 wt. %) by 30 min sonication and the TiO_2 sol was dropped to the dispersion, with a dropping funnel, in order to obtain a 50:50 support:TiO_2 weight ratio. The mixture was stirred at RT for 24 h; the product was recovered by centrifugation at 9000 rpm for 30 min followed by washing steps with dH_2O till neutral pH. Before drying the sample, the composite material was dispersed in dH_2O and hydrothermally treated at 180 °C for 5 h in an autoclave. The product, labelled Supp@TiO_2 (Supp = SiO_2, SiO_2 sheets, Hall, Sep) was recovered by centrifugation at 9000 rpm for 30 min and dried overnight in an oven at 80 °C. A scheme of the TiO_2 functionalization procedure is represented in Scheme 4.3.

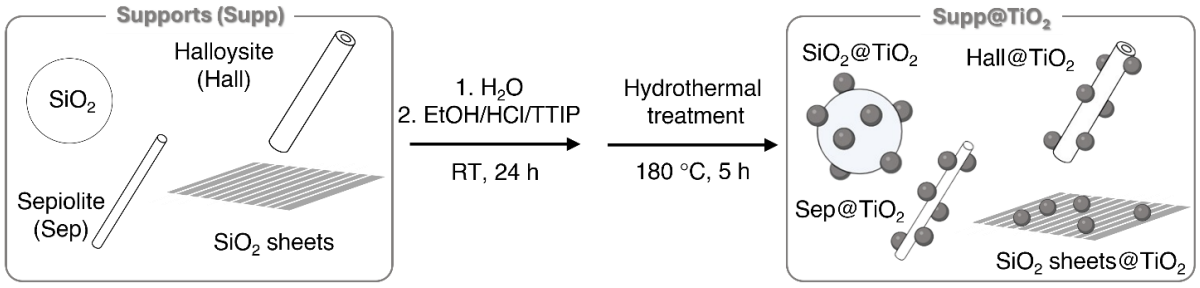

Scheme 4.3: schematic representation of the synthetic procedure of TiO_2 NPs on different SiO_2-based support

4.1.2.5 Photocataytic test procedure

The photocatalytic experiments were performed in the same setup described in Paragraph 3.1.2.2. Briefly, the system consists of a 0.5 L cylindrical pyrex batch

photoreactor equipped with a 125 W medium-pressure Hg lamp (Helios Italquartz, Italy) axially immersed within the photoreactor. The initial PC concentration was 30 ppm, while the amount of catalyst employed was 0.8 g L^{-1} for Supp@TiO_2 samples. After 1 h in the dark, UV lamp was switched on and, at selected times, samples were withdrawn and filtrated through a 0.22 μm hydrophilic PTFE syringe filter (VWR). The quantitative evolution of PC was monitored by measuring its absorption at 243 nm with a UV/Vis spectrophotometer Agilent Cary60 (quartz cuvette, optical path 0.5 cm).

4.1.2.6 Metal cation adsorption test

Preliminary metal cations adsorption test were performed on a mixture of Ni(II), Cu(II) and Y(III). The stock solution of the three metal cations was prepared by dissolving $Ni(NO_3)_2 \cdot 3\ H_2O$, $Cu(NO_3)_2 \cdot 6\ H_2O$ and $Y(NO_3)_3 \cdot 6\ H_2O$ in distilled water and further diluting to obtain the final concentration of 5 ppm for each metal cation. In a typical experiment, 25 ml of metal solutions and 25 mg of adsorbent were mixed in a 50 ml beaker and left under magnetic stirring for 24 h at room temperature. After centrifugation, the concentration of the three metals was determined by ICP-OES. The removal efficiency was calculated according to Eq. 4.1:

$$\eta_c(\%) = \frac{C_i - C_e}{C_i} \qquad 4.1$$

The results presented in this thesis are the average and standard deviation of three separate measurements for each sample.

4.1.3 Results and discussion

This paragraph describes the results of the physico-chemical and morphological characterization of all Supp@TiO_2 samples: SiO_2@TiO_2, SiO_2 sheets@TiO_2, Sep@TiO_2 and Hall@TiO_2. Particular attention will be given to highlight the differences between samples before and after the TiO_2 functionalization.

4.1.3.1 Compositional characterization

At first, the elemental composition of all samples was studied with the XRF

spectroscopy. Despite the samples having a very simple composition, the analysis is useful to detect the eventual contamination occurred during the synthesis and, especially for clays, to define unexpected elements naturally included in their structure

The spectra reported in Figure 4.2 show the normalized XRF spectra obtained for all samples. To simplify, the data for bare SiO_2 sheets are not reported because they are identical to SiO_2 NPs.

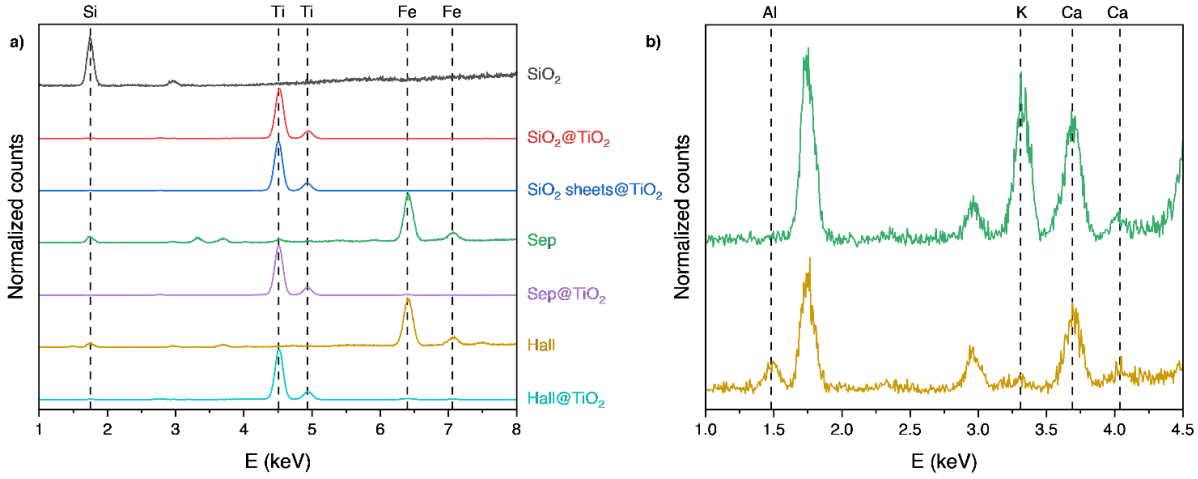

Figure 4.2: a) XRF spectra for SiO_2 (black), SiO_2@TiO_2 (red), SiO_2 sheets@TiO_2 (blue), Sep (green), Sep@TiO_2 (purple), Hall (light brown) and Hall@TiO_2 (light blue). b) highlight of lower XRF intensities signals for Sep and Hall. Dashed lines indicate the position of the XRF signals for the indicated element.

Focusing on the bare supports spectra, all of them show one main peak at 1.74 keV attributed to the Kα1 signal of Si. However, XRF spectroscopy is not the optimal technique to detect light elements like Si. The intensity of the signal is so low that its intensity is comparable to the Bremsstrahlung band and the Kβ1 signal at 1.84 keV, which is the weakest XRF signal for Si, is not detected. In addition, a signal around 3 keV is shown for all bare supports and the only element providing signals at such values is Ar. As Ar can be reasonably considered absent in the samples, the peak is an artefact of the analysis. The two natural clays, Sep and Hall, show additional signals due to the more complex composition. For this reason, in addition to the typical Si signal at 1.74 keV, other naturally occurring elements can be detected: signals attributed to Ca at 3.69 and 4.01 keV and Fe at 6.40 and 7.06 keV (Kα1 and Kβ1, respectively) are observed in both samples, while a peak attributed to K at 3.31 keV (Kα1) is provided by Hall only. Due to the limit of the XRF instrumentation, lighter elements like Al, and especially Mg, which are generally included in clays, cannot be detected efficiently. However, the presence of a weak signal at 1.467 keV, attributed

to Al (Kα1) confirms the aluminosilicate nature of Hall.

By comparing the XRF spectra of each sample before and after the modification with TiO_2, Ti signals at 4.51 and 4.93 keV (Kα1 and Kβ1, respectively) appear for all the investigated supports, indicating that the element is included in all the samples.

Another evidence of the inclusion of Ti is provided by the ATR-FTIR spectra of samples, shown in Figure 4.3.

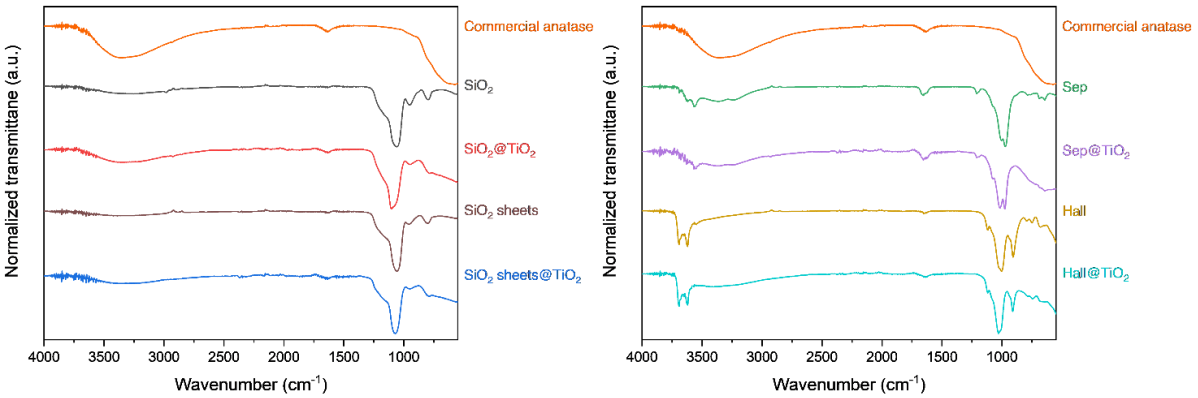

Figure 4.3: ATR-FTIR spectra for commercial anatase (orange), SiO_2 (black), SiO_2@TiO_2 (red), SiO_2 sheets (brown), SiO_2 sheets@TiO_2 (blue), Sep (green), Sep@TiO_2 (purple), Hall (light brown) and Hall@TiO_2 (light blue).

Starting from the bare supports, both SiO_2 and SiO_2 sheets provide the same IR spectra: the main signal centred at 1056 cm^{-1} is attributed to the Si-O-Si bond asymmetric stretching that, along with the peaks at 957 and 789 cm^{-1} due to the Si-OH and Si-O bond stretching, are typical of SiO_2. Finally, the broad band centred at 3200 cm^{-1} is attributed to the O-H groups stretching of both surface silanol groups and adsorbed water.[20,21] Signals associated with -OH groups, hence at 3200 cm^{-1} and 957 cm^{-1}, are less intense for SiO_2 sheets due to the thermal treatment, which causes the condensation and elimination of -OH groups as water molecules.[22] Similar attributions can be observed for both natural clays investigated (Table 4.1). For Sep, peaks at 645, 3568 and 3620 cm^{-1} confirm the presence of Mg in its composition, since they are attributed to the Mg-OH bond stretching.[23,24] Similarly, the Al content in Hall provides the signals at 3691 and 3622 cm^{-1}, attributed to the stretching of the inner hydroxyl groups bonded to Al. The presence of Al is also confirmed by the signal at 908 cm^{-1} and the band rising in the region near 525 cm^{-1}, attributed to the deformation vibration of inner surface hydroxyl groups and Al-O-Si bonds.[25–27]

Table 4.1: attribution of the ATR-FTIR signals for Sep and Hall

Sep		Hall	
Wavenumber (cm^{-1})	**Attribution**	**Wavenumber (cm^{-1})**	**Attribution**
3620, 3568	Mg-OH stretching	3691, 3622	Inner surface Al-OH stretching
3500-3000	O-H stretching	3547, 1647	-OH stretching of inner layer H_2O
1659	-OH bending of water	1118	Si-O in-plane stretching
1210	Si-O-Si stretching	1005	Apical Si-O-Si asymm. stretching
1004	Si-O-Si asymm. stretching	908	Inner-surface -OH stretching
969	Si-O stretching	795, 749, 678	Si-O stretching
688	Si-O out-of-plane stretching	Band at 525	Al-O-Si stretching
645	Mg-OH bending		

Commercial anatase shows a wide band between 3000 and 3500 cm^{-1} attributed to the O-H stretching mode of hydroxyl groups and a signal at 1635 cm^{-1} associated to the O-H bending vibration of water molecules; both these signals are indicative of the presence of hydroxyl groups on the surface of the material and adsorbed water molecules. The band between 900 and 525 cm^{-1} is attributed to the Ti-O-Ti stretching mode, typical of TiO_2.[28,29] Focusing on the Supp@TiO_2 samples, the ATR-FTIR spectra show that supports main signals are not altered by TiO_2 or hydrothermal treatments, suggesting the maintenance of the chemical composition. After the treatment with the TiO_2 sol, an increase in the signal between 900 and 525 cm^{-1} and a loss in the definition of the support peaks in the same region can be observed, indicating the presence of Ti-O bonds in each sample.

4.1.3.2 Structural characterization

Raman spectroscopy was performed to preliminary define the crystalline structure of TiO_2, since anatase and rutile provide distinguishable signals.[30] Raman spectra for all samples are reported in Figure 4.4.

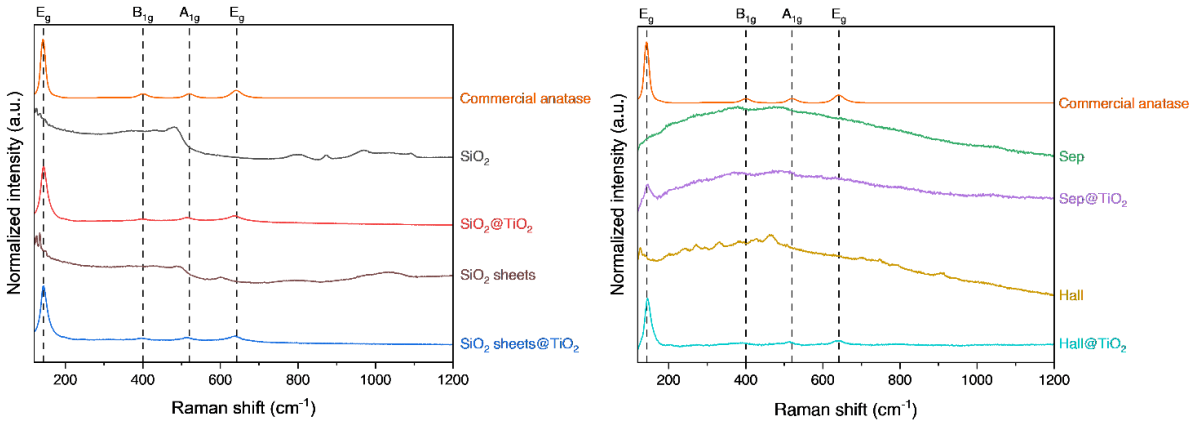

Figure 4.4: Raman spectra for commercial anatase (orange), SiO_2 (black), SiO_2@TiO_2 (red), SiO_2 sheets (brown), SiO_2 sheets@TiO_2 (blue), Sep (green), Sep@TiO_2 (purple), Hall (light brown) and Hall@TiO_2 (light blue).

Starting from the Supp, it's interesting to notice that both SiO_2 samples provide Raman signals: a weak signal around 415 cm^{-1} attributed to the bending mode of oxygen in n-membered rings with n > 4 (R line) and at 490 cm^{-1} due to the breathing mode of 4-membered rings (D_1 line). In addition, the signal at 800 cm^{-1} is the SiO_2 network optical mode, while at 980 cm^{-1} is the vibration of the OH group bonded to Si. Of particular interest is the signal at 602 cm^{-1}, attributed to the breathing mode of 3-membered rings (D2 line), that, along with the D_1 signal, are generally associated to variation in the porosity of silica. While the D_2 signal is absent for SiO_2, it can be seen in the SiO_2 sheets spectra suggesting a remarkable difference in the porous structure of the two materials.[31–33]

Despite Raman spectroscopy does not provide significant information about Sep, Hall spectrum presents many signals[34,35] mainly attributed to the Si-O and Al-O backbone of the clay. Attributions for each signal of Hall are reported in Table 4.2.

By comparing the Raman spectra, before and after the functionalization with TiO_2, four active modes of anatase appear in the spectra at 142, 400, 520 and 640 cm^{-1}, attributed to the symmetries E_g, B_{1g}, A_{1g} and E_g, respectively. [30] While the first signal is clearly discernible for all supports, the other three are less evident due to the weakness of the signal, especially for Sep cause of the high scattering band. However, both the position and the relative intensities confirm the anatase phase of TiO_2.

Additional information about the crystalline phase of each sample and of synthetised TiO_2 are provided by the XRD patterns shown in Figure 4.5

Table 4.2: Attributions of Raman signals for Hall

Raman shift (cm^{-1})	Attribution
135	Si-O bending
158, 162	Al-O symmetric bending
244, 271	O-H-O symm. and asymm. stretching
322, 332, 339	H-bonded H_2O
379 – 385, 396	Si-O deformation
437	Al-O stretch
461, 506	Si-O bending vibrations
701, 747, 779	OH translation
910	Inner Al – OH

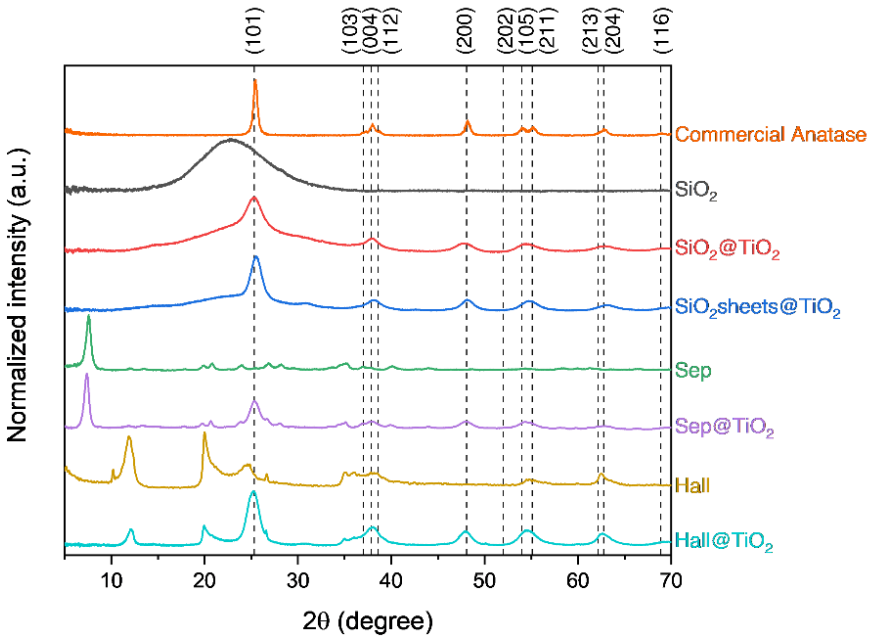

Figure 4.5: XRD patterns for commercial anatase (orange), SiO_2 (black), SiO_2@TiO_2 (red), SiO_2sheets@TiO_2 (blue), Sep (green), Sep@TiO_2 (purple), Hall (light brown) and Hall@TiO_2 (light blue). SiO_2sheets pattern is not reported because identical to SiO_2. Dashed lines highlight of TiO_2 anatase phase reflections and the associated crystallographic plane.

The crystalline structure was studied at first by XRD spectroscopy. The diffractograms of both SiO_2 samples show a single broad band centred at 23°, which is typical of amorphous SiO_2 samples.[36] Focusing on Sep, main signals located at 2θ = 7.58°, 19.8° and 35.0° corresponding, respectively, to (110), (131) and (371) planes are observed. The strong signal at 7.58° proves the bidimensional layered structure of the

mineral: due to its shape, Sep assumes a preferential orientation on the sample holder, selectively exposing a specific crystalline plane; for this reason, the (110) plane is over-expressed in the pattern, compared to other signals.[37,38] The XRD pattern of Hall shows the main signals at 12.0, 20.0, 24.7, 35.0, 54.4 and 62.4° corresponding to the planes (001), (100),(002), (110), (210) and (300), respectively. In addition, the presence of a peak at 26.6° is attributed to quartz residues. Being the main peak at 12.0°, corresponding to a d-spacing of 7.41 Å , the material can be defined as the standard Halloysite-7Å . [39,40]

For all the support materials investigated, the diffractograms show that TiO_2 and hydrothermal treatments do not alter the crystalline structure. In addition, the appearance of TiO_2 anatase signals for all the samples was observed, confirming the anatase crystalline phase as predicted by Raman results.

It must be noted the lack of definition for the multiplet signals of anatase at 37° and 55°, which suggests nanometric dimensions for TiO_2 particles. For this purpose, the crystallite average sizes were estimated by the Scherrer equation applied to the XRD signal at *ca.* 48.2° 2θ (200), since it is the only signal that does not overlap with peaks provided by the supports. The results (Table 4.3) confirm the nanometric dimensions of the TiO_2 particles, which show a similar diameter for all the different supports involved.

Table 4.3: Crystallite diameter calculated by the Scherrer equation, on the XRD signal at 48.2°

Sample	Crystallite diameter (nm)
SiO_2@TiO_2	3.9
SiO_2 sheets@TiO_2	3.9
Sep@TiO_2	4.1
Hall@TiO_2	4.3

Finally, information about the electronic structure, or rather, to determine the band gap energy of the catalyst, the DRS analysis was performed on all samples.

According to the spectra depicted in Figure 4.6a, a decrease in the reflectance in the region around 375 nm can be observed, attributable to the band gap absorption of TiO_2. It is known that anatase has a band-gap energy of 3.2 eV, corresponding to the wavelength of 387 nm.[41] By applying the Kubelka-Munk theory, the band gap of each

sample was calculated and the results, reported in Figure 4.6b, are consistent with the anatase phase.

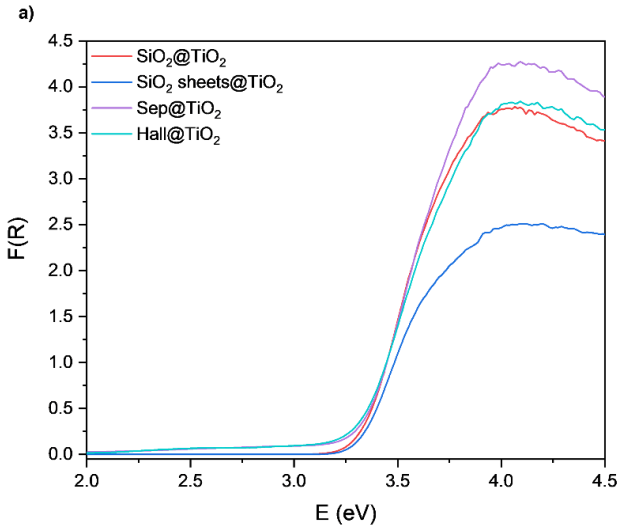

Sample	Band gap (eV)
SiO_2@TiO_2	3.20
SiO_2sheets@TiO_2	3.19
Sep@TiO_2	3.26
Hall@TiO_2	3.25

Figure 4.6: a) DRS results reported after the application of the Kubelka-Munk approximation and b) band gap values calculated for SiO_2@TiO_2 (red), SiO_2 sheets@TiO_2 (blue), Sep@TiO_2 (purple) and Hall@TiO_2 (light blue).

4.1.3.3 Morphological characterization

The morphology of supports and supported TiO_2 samples was investigated by TEM microscopy to assess variation in the support structure and the TiO_2 NPs dimensions

The micrographs in Figure 4.7 top line show that SiO_2 is made of spheric NPs with a mean diameter equal to 35 (±1) nm. Both images and standard deviation value confirm that particles are monodispersed since they have a homogeneous dimension. On the other hand, SiO_2 sheets have a completely different morphology: the images show bidimensional particles with a sheet-like shape, mostly folded on themselves. At a higher magnification (Figure 4.8), these particles show a regular porosity consisting of parallel tubular-shaped pores. A mean value of 2.5 (±0.3) nm was obtained by measuring the pores' diameter, indicating that the material is mesoporous, and a value of 5.6 (±0.4) nm was calculated for the inter-pore walls. These results confirm the difference in the internal structure of the two materials predicted by the D2 band in the Raman spectroscopy. The images obtained for Sep and Hall show a fibrous and tubular morphology, respectively. However, being natural clays, their dimensions are extremely variable in terms of length and width: Sep fibres have a length between 200 and 2000 nm and a width of 10-30 nm, while Hall has a length in the range 200 nm - 1 um, an external diameter of 40-80 nm. While Sep porosity is not visible in TEM

images, Hall shows an inner canal whose diameter was calculated in 13 (± 2) nm.

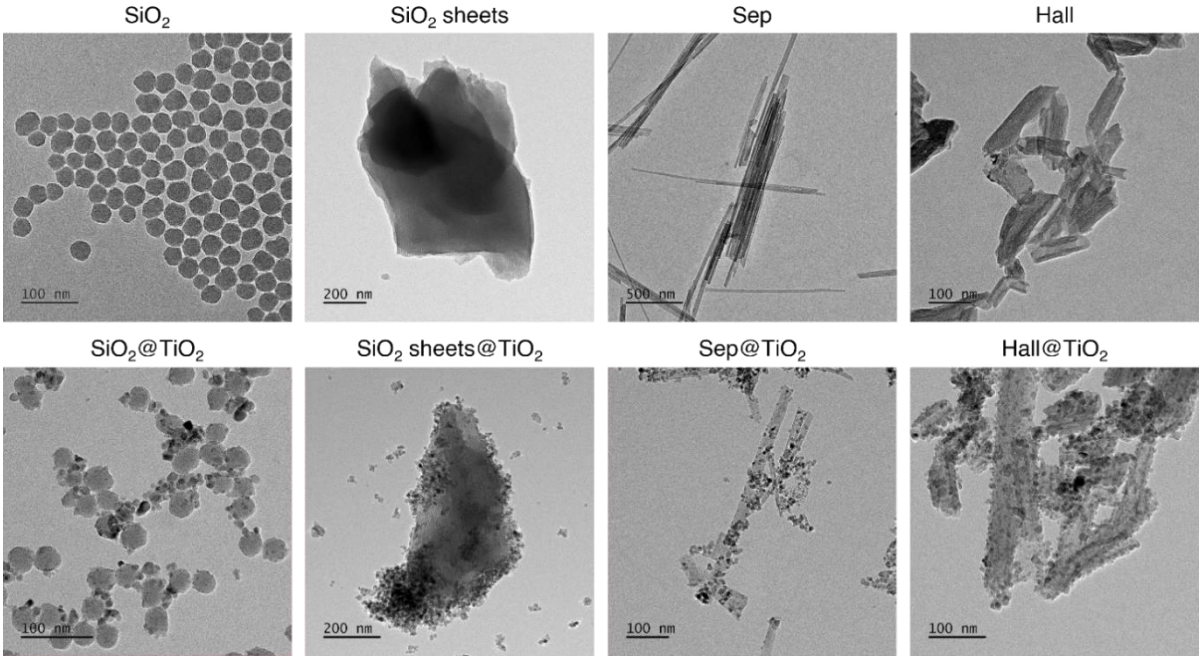

Figure 4.7: TEM micrographs for both bare supports (top line) and Supp@TiO_2 samples (bottom line)

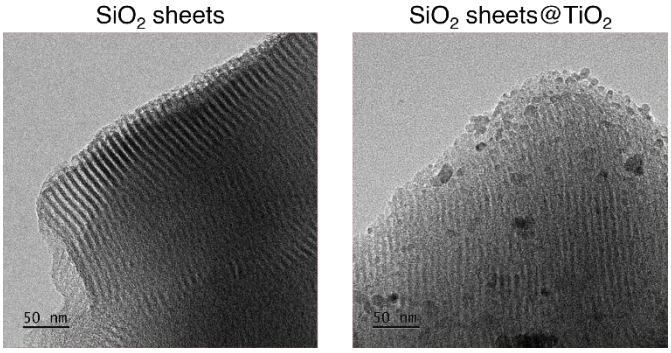

Figure 4.8: magnification of the porosity for SiO_2 sheets and SiO_2 sheets@TiO_2

Finally, the morphology of TiO_2 particles was investigated and the results are depicted in Figure 4.7 bottom line. Firstly, it must be noted that the supports do not show any significant change in their morphology due to the treatments carried out. Furthermore, TiO_2 is efficiently anchored on the surface of each support in the form of monodispersed NPs, with a mean diameter of 7 (± 1) nm for each sample. The dimensions determined by TEM images are consistent with the results obtained by the XRD spectra, considering that the crystallite size obtained with the Scherrer equation is always lower than the exact NP dimension. On the other hand, the TEM analysis shows that TiO_2 NPs are not homogeneously distributed in all areas and aggregation

of multiple NPs can be observed in all samples.

Further investigation of the samples' morphology involved the N_2 physisorption measurement to define both SSA and pore dimensions for all samples. The isotherms are shown coupled according to the support in Figure 4.9a.

Considering the IUPAC classification[42,43], isotherm shapes and hysteresis were attributed. For most of the samples, the presence of a hysteresis at high P/P^0 allows to attribute the isotherm to the type IV with hysteresis resembling a mixture of H1 and H3 type, which is typical of mesoporous materials.

Sep and Sep@TiO_2 represent a first deviation from the previous trend since the first part of the isotherm, namely at lower P/P^0, shows a steep initial adsorption, similar to the type I isotherm. As consequence, both samples have also a remarkable microporosity in their structure, which is consistent with the structure of the supporting clay material.[44] An extremization of this phenomenon is provided by SiO_2 sheets isotherm, whose shape is more similar to a perfect type I than a type IV, indicating a combination of micro and mesopores. Indeed, a small H2 hysteresis is observed at 0.5 P/P^0 due to pore blocking or to cavitation-induced evaporation during the desorption, which causes a rapid decrease in the amount of N_2 desorbed.[45] According to the IUPAC classification, this type of hysteresis is typical of ordered mesoporous materials, which is consistent with the porosity observed in TEM micrographs.

A clear and peculiar deviation from the trend is provided by both SiO_2 and SiO_2 sheets @TiO_2 isotherms. Their isotherms can be classified as type IV, confirming the presence of mesopores, but with a characteristic H5 hysteresis with a double loop. According to literature, this particular shape is ascribed to a porous structure containing both open and partially blocked mesopores.[45] This characteristic can be easily explained considering that both supports show mesopores that are partially blocked, as a consequence of the deposition of TiO_2 NPs.

In Table 4.4, the SSA values calculated by the BET method are reported. The highest areas are provided by SiO_2 sheets and Sep, with SSA values of 367 $m^2\ g^{-1}$ and 302 $m^2\ g^{-1}$, respectively. The high surface area can be ascribable to the high porosity of both materials, especially being the only two supports with a microporosity. In addition, also SiO_2 and Hall provide a surface area of 285 and 57 $m^2\ g^{-1}$ which, as well as for Sep, are in line with previously reported values.[17,45,46]

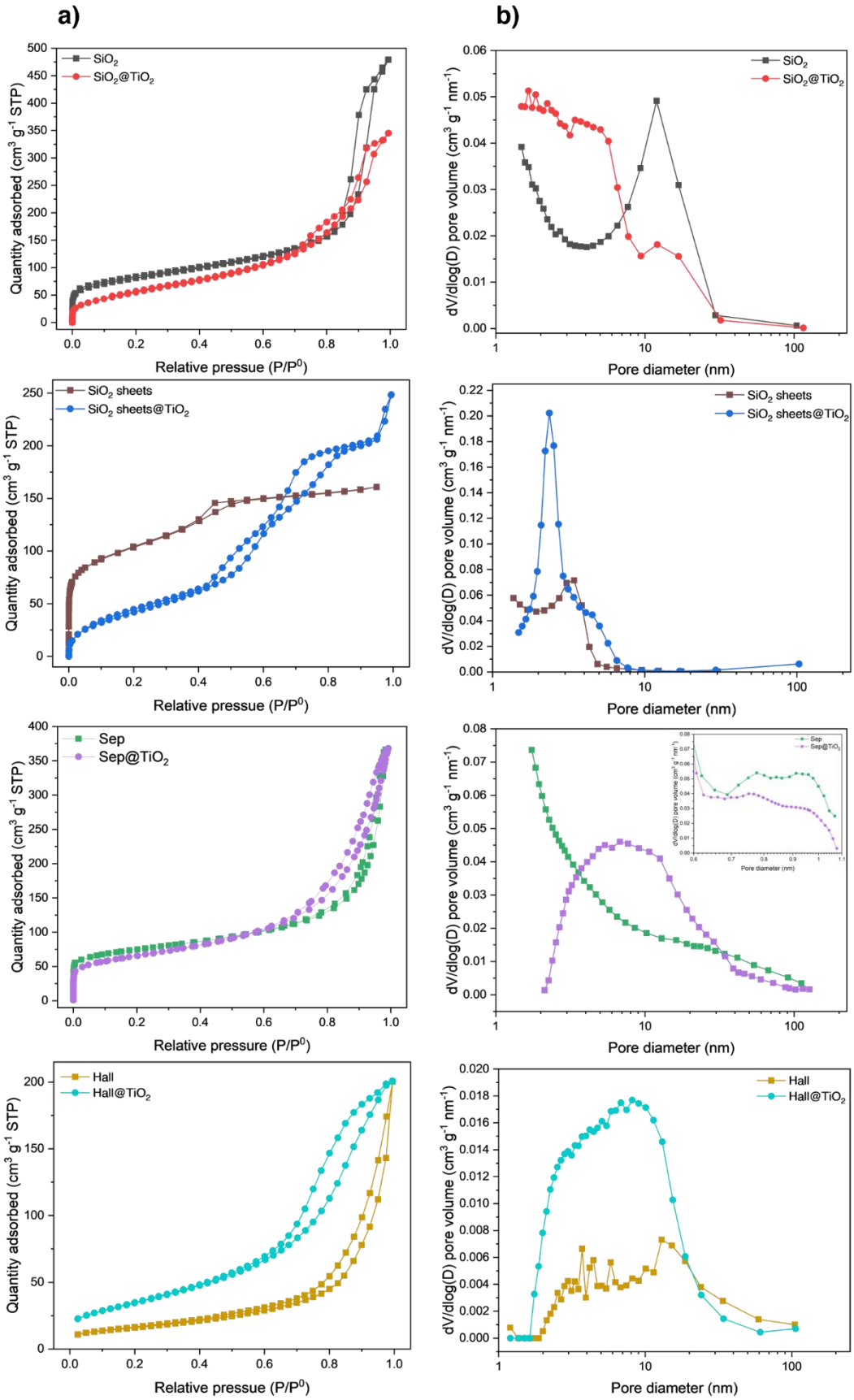

Figure 4.9: a) N_2 adsorption isotherm and b)pore distribution calculated by BJH model for SiO_2 (black), SiO_2@TiO_2 (red), SiO_2 sheets (brown), SiO_2 sheets@TiO_2 (blue), Sep (green), Sep@TiO_2 (purple), Hall (light brown) and Hall@TiO_2 (light blue).For Sep and Sep@TiO_2, the inset shows the micropore size distribution

After the synthesis of TiO_2, both SiO_2 and SiO_2sheets @TiO_2 samples show a decrease in the surface area, which is more significant for the former sample, due to the pores occlusion already deduced by the isotherm. Focusing on clays, for Sep and Hall there is a decrease and an increase, respectively, in the surface area upon TiO_2 functionalization; this phenomenon is perfectly in line with previously reported data.[47]

Table 4.4: specific surface area (SSA), mesopores volume and microporous volume measure by BET, BJH and t-plot method, respectively.

Sample	SSA BET ($m^2\ g^{-1}$)	V $pore_{meso}$ ($cm^3\ g^{-1}$)	V $pore_{micro}$ ($cm^3\ g^{-1}$)
SiO_2	285	0.72	-
SiO_2@TiO_2	215	0.51	-
SiO_2 sheets	367	0.53	0.048
SiO_2 sheets@TiO_2	170	1.1	-
Sep	302	0.53	0.0077
Sep@TiO_2	227	0.56	0.0029
Hall	57	0.53	-
Hall@TiO_2	128	0.57	-

By applying the BJH method to the physisorption results, the mesopore distribution and volume were extrapolated, while for microporous materials the pore volume was calculated by the t-plot. The results are shown in Figure 4.9b and Table 4.4.

SiO_2 NPs show a pore population around 10 nm, persisting in the functionalized sample, that can be ascribed to the interstices between aggregated particles, which is more probable for smaller SiO_2 NPs.[48] However, an increase in the pores population below 10 nm was observed in the treated samples, which could be ascribed to aggregation in the TiO_2 NPs. These phenomena are associated with a decrease in the mesopore volume from 0.72 to 0.51 $cm^3\ g^{-1}$. Focusing on SiO_2 sheets, the pore distribution clearly shows the presence of a main mesopore population centred at 3.34 nm, with a residual microporosity probably due to particle aggregation. After the TiO_2 procedure, the microporosity is completely lost and the pores' dimensions are described by a main peak centred at 2.36 nm with a broad shoulder expanding up to 7 nm. In both cases, the results are not significantly different from the dimensions

calculated by TEM images, where the mean diameter calculated was 2.5 nm. The differences in the porosity, ascribable to both TiO_2 NPs and SiO_2 sheets aggregation, cause a net increase in the pore volume, whose values pass from 0.51 to 1.1 $cm^3\ g^{-1}$. Regarding Sep samples, the TiO_2 functionalization causes the appearance of a new broad pores population between 2 and 40 nm and a decrease in the microporosity volume, probably due to a change in the interparticle aggregation after the hydrothermal treatment. At the same time, the micropore structure does not show any variation in terms of diameter, which shows two main populations at 0.8 and 1 nm, corresponding to the internal pores of sepiolite.[44] In contrast with the previous results, Hall does not show any significant change in its porosity or pore volume due to TiO_2 deposition.[49,50] Indeed, both samples show a pore population that expands from 2 to 100 nm, with the maximum falling in the range 10-15 nm, which is perfectly consistent with the internal diameter calculated by TEM images of 13 nm.

4.1.3.4 Application of Supp@TiO_2 in the PC photodegradation

Photocatalytic tests on the degradation of PC were conducted to assess the photoactivity of all materials. The results for the photodegradation of PC with Supp@TiO_2 samples is reported in Figure 4.10a.

Blank experiments were conducted to evaluate PC photolysis and the effect of photocatalysts under dark conditions: none of these experiments provided a variation in the molecule concentration, therefore the data are not reported. For all experiments, the apparent kinetic constant was calculated according to first kinetic order model: the linear fitting, the apparent kinetic constants and the R-square values for each fitting are reported in Figure 4.10 b,c.

All samples show no adsorption of PC under dark conditions for 1h. On the other hand, all samples proved effective in degrading PC and, considering both the degradation curve and the kinetic constant calculated, the performances of all samples are comparable. Specifically, with a k value of 0.019 min^{-1}, Sep@TiO_2 proved slightly better performances than the other samples, due probably to the higher surface area and porosity. On the contrary, SiO_2 sheets supported samples provided a relatively lower kinetic constant of 0.011 min^{-1}. The IR spectroscopy described in paragraph

showed that the thermal treatment undergone by SiO_2 sheets causes a decrease in the surface -OH groups; as consequence, both the surface adsorption of PC and the aggregation in aqueous media can be both affected.

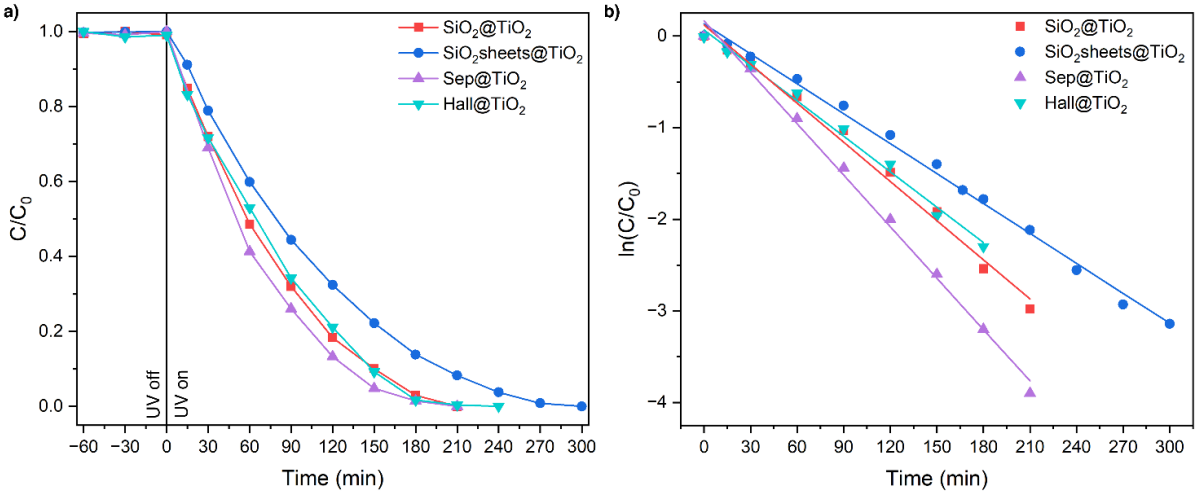

c)

Sample	k (min^{-1})	R-square
SiO_2@TiO_2	0.014	> 0.99
SiO_2sheets@TiO_2	0.011	
Sep@TiO_2	0.019	
Hall@TiO_2	0.013	

Figure 4.10: a) photodegradation curve of PC, (b) linear fitting according to the first order kinetic model and c) apparent kinetic constant and R-square values obtained from the fitting for SiO_2@TiO_2 (red), SiO_2 sheets@TiO_2 (blue), Sep@TiO_2 (purple) and Hall@TiO_2 (light blue)

It is worth noticing that a similar photocatalytic test was performed by Papoulis et al.[47] on both Hall@TiO_2 and Sep@TiO_2 with a 70 % TiO_2 content. The degradation test was performed with the same PC concentration of 30 ppm, with a catalyst concentration of 0.85 g L^{-1} and a 400 W medium pressure Hg lamp as UV source. Unfortunately, the kinetic constants value are not available; however, the degradation efficiencies at 120 min are equal to 83 % and < 93 %[51] for the Hall and Sep supported reference samples, respectively, while our samples provide a degradation of 79 % and 87 %. Therefore, the photodegradation yield is similar, despite the lower TiO_2 content in our samples.

4.1.3.5 Adsorption test on Supp@TiO_2 samples

The results for the adsorption test on a solution containing Cu(II), Ni(II) and Y(III) are

reported in terms of removal efficiency (η_c) in Figure 4.11.

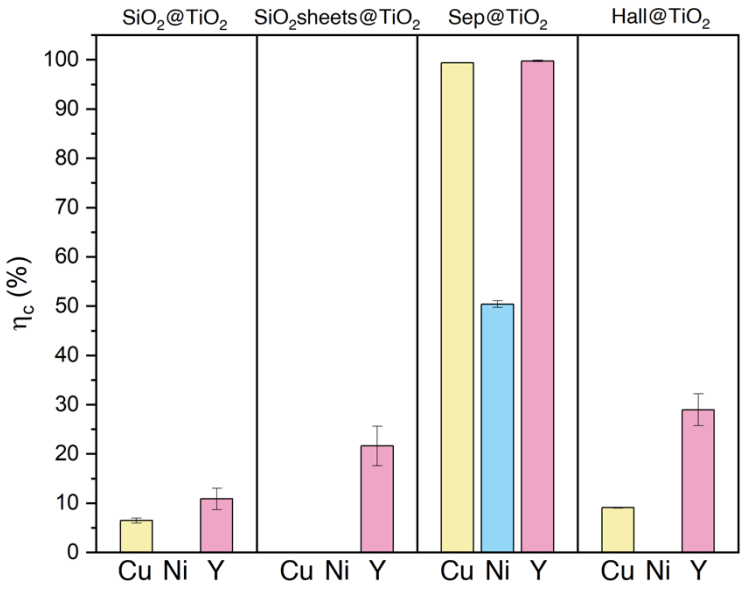

Figure 4.11: removal efficiency of Cu(II),Ni(II) and Y(III) for the Supp@TiO_2 samples. The results are the average of three repetitions of the test

According to the results, except for some particular cases, it can be observed a specific preference in the different cation adsorption: Y is generally captured more efficiently than Cu and even more than Ni. To simplify, the adsorption efficiency can be described as the trend Y>Cu>Ni. This behaviour can be described by the hard-soft classification of elements provided by IUPAC.[52] Specifically, being Y(III) a hard metal, it binds strongly with hard donor ligands like oxygen. Indeed, both supports and TiO_2 are known for their surface hydroxyl groups, which are mainly involved in the adsorption of metal cations. On the other hand, Cu(II) and Ni(II) are classified as borderline elements, meaning that they have an intermediate behaviour and show variable coordination chemistry, hence the exact order of stability with ligands is not known. The preference for Cu(II) may be the results of different physicochemical factors, such as electronegativity, ionic radius, molecular weight and hydration.[53]

Focusing on samples, the results clearly show that Sep@TiO_2 provides the best results in terms of metal cations removal compared to the other samples, since 100 % of Y and Cu and 50 % of Ni are removed from the solution. The optimal results can be attributed to its high surface area and higher porosity, especially in the micropore region, detected by BET analysis. The other samples show a net lower removal efficiency, in the order from best to worst: Hall@TiO_2 > SiO_2 sheets@TiO_2 >

SiO_2@TiO_2. While Hall@TiO_2 behaviour can be ascribed to the lower surface area compared to the other samples, for SiO_2sheets@TiO_2 is reasonable to think that the thermal treatment carried out to remove the templating polymer significantly decreased the amount of surface -OH available for metal adsorption. On the other hand, SiO_2@TiO_2 shows the worst results despite having a remarkable surface area; the reason of this behaviour could be tentatively attributed to the different morphology and porosity of the materials, compared to the others, or to a lower exposition of -OH groups due to the similar dimension between SiO_2 and TiO_2.

4.1.4 Final considerations

With the aim of improving its dispersion, TiO_2 was synthetised on different supporting materials, namely spherical and mesoporous bidimensional synthetic SiO_2 NPs and two natural clays, Sep and Hall. The synthesis was performed by exposing each support to a TiO_2 sol at RT, followed by a crystallization step via hydrothermal treatment. It is worth noticing that the procedure is relatively sustainable since the only reagents involved, except for water, are ethanol, a minimal amount of HCl, and titanium isopropoxide and the maximum temperature reach is 180 °C for the hydrothermal treatment.

By a thorough characterization of all the prepared samples, it was observed that the results obtained are similar, independently from the support employed. Indeed, the procedure led to the deposition of well-dispersed TiO_2 NPs in the anatase phase, with a mean diameter of 7 nm and highly monodispersed. In addition, it was also demonstrated that despite the chemical and hydrothermal treatment, all supports do not show a remarkable change in their morphology and structure.

Preliminary tests on the application of supported-TiO_2 samples for environmental remediation were performed. The photodegradation test on PC demonstrated the efficiency of all samples in degrading the organic pollutant, with slightly better performances observed for the Sep-supported TiO_2. In order to better define the role of adsorption efficiency in photodegradation, a wider selection of pollutants, especially with different functionalities will be investigated. In addition, adsorption test on a model solution of Cu(II), Ni(II) and Y(III) showed a profound difference in the efficiency of the

samples, with Sep@TiO_2 having significantly better adsorption properties, compared to the other samples.

4.2 Photothermo catalytic methanation of CO_2 with supported TiO_2 samples

The Ru deposition and the photothermo catalytic application of Supp@TiO_2 samples was investigated in collaboration with Prof. Nicolas Keller research group at Institut de Chimie et Proceds pour l'Énergie, l'Environnement et la Sant – ICPEES (CNRS\University of Strasbourg). The results presented about this topic are preliminary and further investigations are currently ongoing.

4.2.1 Introduction to the methanation reaction

Photo-thermal catalysis, thanks to the synergic combination of photon and thermal excitation, represents a promising strategy to perform chemical reactions by reducing energy consumption, without detrimental consequences on the efficiency and selectivity of the process. Among the several applications described in Paragraph 1.3.2, the catalytic methanation of CO_2 represents one of the main challenges in the current chemistry research. The conversion of carbon dioxide to methane is known as Sabatier reaction (Eq. 4.2) and it consists of a spontaneous exothermic reaction that involves the hydrogenation of CO_2, mainly by using sustainable H_2 produced through green processes like water electrolysis.[54]

$$CO_2 + 4H_2 \rightarrow CH_4 + 2H_2O \qquad \Delta G^0 = -113 \text{ KJ mol}^{-1} \qquad 4.2$$

The reaction is particularly appreciated mainly for its environmental benefit: the accumulation of CO_2 in the atmosphere is responsible for global warming and climate change and the Sabatier reaction represents a promising strategy to reduce the amount of greenhouse gas, by converting it into a common energy source, namely CH_4. Despite being exothermic, the reaction still requires energy due to its kinetic barriers, mainly dictated by the strong bonds involved in the reagents molecules and, for this reason, the reaction is mostly performed in the presence of a catalyst at a temperature between 200-550 °C and pressure between 1-100 bar.[55][56] Therefore,

the photothermal catalytic strategy represents a feasible way to perform the reaction in milder conditions.

Up to now, the most important metals for methanation catalysis are Ru, Ni, Co, Fe and Mo, but ruthenium proved to be the most active unsupported metal for the reaction[57]. Despite being one of the cheapest noble metals, the main drawback of using Ru-based catalysts as active phase is its high cost and the use of relatively high-loading Ru on the support makes it often unsustainable for economic feasibility. However, Ru-based catalysts show a high CH_4 selectivity and high CO_2 conversion at low temperatures.[58,59]

The combination of Ru and TiO_2 for a photothermal application in the Sabatier reaction has already been investigated in literature. A photo enhancement was observed by Wang *et al.* [60] on 1 wt. % Ru@TiO_2 catalyst under weak sunlight irradiation (1 sun) in the temperature range 150-300 °C. They observed that by operating at 150 °C in the dark, no CH_4 was formed, while under irradiation the phototherm ocatayst provided an increase in CH_4 yield up to 1.7 mmol g^{-1} h^{-1}. The authors suggest that the insufficient driving force for H_2 oxidation could possibly be the reason for the negligible activity observed at RT; however, the authors proposed that the thermal energy introduced by heating increases the kinetic energy of the reactants favouring the overcome of the activation barrier of the reaction and, consequentially, improving CO_2 reduction. This phenomenon explains the higher activity of the catalyst in the range 150-300 °C.

Actually, the contribution to the methanation reaction of Ru-TiO_2 catalyst is more complicated than a simple kinetic effect because several phenomena emerge from the combination of the two materials: i) local heating induced by Ru photothermal effect, ii) charge transfer to adsorbate molecules induced by the excitation of the plasmonic particles and iii) electron-hole charge transfer from TiO_2 to Ru NPs.[61] Additional details on the mechanism are proposed by Zhang *et al.*[62] who investigated the application of Ru@TiO_2 NPs in the methanation reaction with a Ru content ranging from 0.1 to 1.0 wt. % and in the temperature range 25-300 °C. Thanks to DRIFT analysis they demonstrated that CO_2 adsorbs on the catalyst in the form of CO at high temperature, which therefore represents the main intermediates of the methanation reaction. The authors observed that light irradiation causes the transfer of photogenerated electrons in the semiconductor to Ru particles, promoting the electron

back-donation from Ru to CO antibonding orbitals, further destabilizing the molecule and favouring CH_4 production.

In addition, the work of Wang *et al.*[63], Dong *et al.*[64] and Jin et al.[65] demonstrated the remarkable contribution of oxygen vacancies in favouring the photothermo methanation reaction, thanks to their affinity towards CO_2, boosting the adsorption of the molecule and, consequentially, the reaction yield. In the mechanism proposed[63], CO_2 molecules indeed adsorb either on Ru or on the interface Ru-TiO_2 involving the oxygen vacancies (Figure 4.12). Photogenerated electron in the conduction band migrate to Ru decomposing CO_2 to CO and then C. At the same time, as proposed by Ozin *et al.*[66] the photogenerated holes are involved in the activation of H_2, which occurs preferentially on Ru, to form active species which favorably react with C intermediates to form CH_4 as the final product.

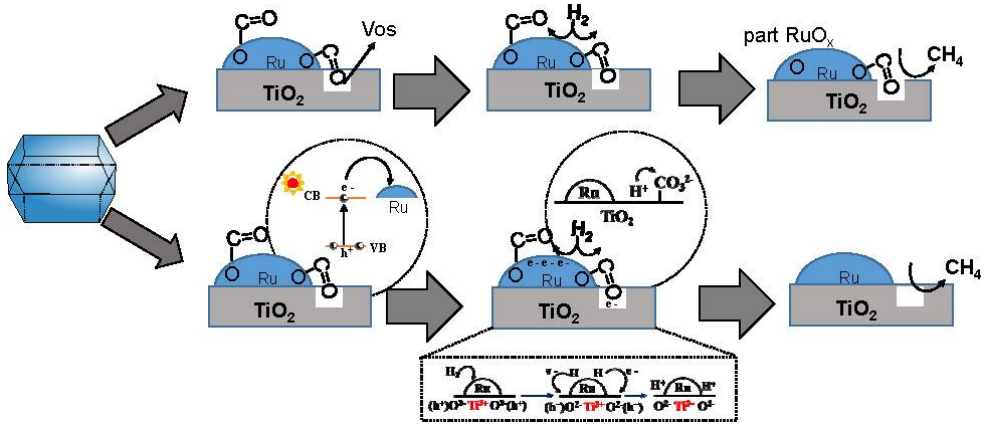

Figure 4.12: schematic representation of the proposed mechanism for CO_2 methanation on TiO_2@Ru, involving oxygen vacancies. Reprinted from [63]

In a system where the adsorption of CO_2 represents a pivotal step in the reaction, the introduction of supported TiO_2 could be beneficial. SiO_2 and clays are known for being able to adsorb CO_2[67–69], which could increase the availability of the reactant near the catalytic component, improving the reaction yield. However, CO_2 adsorption on raw supports is strictly dependent on the temperature, therefore by operating at high temperatures this phenomenon is hindered.[70] However, the advantage described in Paragraph 1.3.1, namely favouring the dispersion of TiO_2 NPs and impeding their aggregation could represent a simple but efficient strategy to improve the exposed surface area and facilitate the interaction between the catalyst and the reagents. In addition, all the supports used show a low thermal conductivity: for SiO_2 bulk is equal

to 1.4 W K^{-1} m^{-1}, for Sep 3.9 W K^{-1} m^{-1} and for Hall 0.65 W K^{-1} m^{-1}.[71–73] Being thermal insulators, they could increase the local temperature generated by the photothermal effect of Ru NPs, by reducing heat dissipation, as already observed in literature.[74,75] For these reasons, the TiO_2-supported materials (Paragraph 4.1) will be investigated for the application in the photo-thermal reduction of CO_2 to CH_4.

4.2.2 Materials and methods

This paragraph will describe the procedures used for the synthesis of the different Ru-based catalysts, based on SiO_2@TiO_2, SiO_2sheets@TiO_2, Sep@TiO_2 and Hall@TiO_2 supports, and on the four bare supports (SiO_2, SiO_2sheets, Sep and Hall). The photocatalytic setup and the reaction conditions used for the methanation of CO_2 are described, as well as the test protocols. The procedure for ICP-OES analysis is described in Appendix – 2.

4.2.2.1 Materials

$RuCl_3 \cdot xH_2O$ 38.0 – 42.0 % Ru basis and Methanol ≥99.9 % (MeOH) were purchased from Sigma-Aldrich. Sodium hydroxide ≥98 % was purchased from VWR. Milli-Q water with a resistivity ρ >18.2 MΩ cm was used.

4.2.2.2 Ru deposition by wet impregnation

The wet impregnation method (Figure 4.13a) was applied for the synthesis of Ru NPs on all the Supp@TiO_2 samples and on the bare supports, with a nominal Ru content of 5 wt. %. Briefly, 250 mg of sample were dispersed in a 5 mL aqueous solution of ruthenium (III) chloride hydrate and left under vigorous stirring (500 rpm) at RT until complete evaporation of the solvent. Following, the collected powder was dried in an oven at 100 °C for 1 h and then transferred in an open crucible to carry out a reductive thermal treatment at 500 °C for 1 h under pure H_2 flux (18 ml min^{-1}), with a temperature ramp of 5 °C min^{-1}. The samples obtained from Supp and Supp@TiO_2 samples were labelled Supp@Ru5% and Supp@TiO_2@Ru5%, respectively.

4.2.2.3 *Ru photo-assisted deposition*

Ru NPs were synthesized at the surface of the Supp@TiO_2 samples with a nominal Ru content of 5 wt. %, by applying a UVA-assisted procedure that allows a fine control of the Ru NPs size distribution (Figure 4.13b).[76]. The synthesis parameters used in that study are derived from previous investigation and optimization on Ru catalysts by the group of N. Keller.[77–80] In particular the role of the pH was highlighted when targeting the synthesis of Ru NPs at high loadings (> 1 wt. %). By operating at pH 8, as described in the procedure, Ru is mostly present in solution in the form of neutral $RuCl_3(H_2O)_3$ or positively-charge $RuCl_2(H_2O)_4^+$ and $RuCl(H_2O)_5^{2+}$. The zero-charge point of the catalyst (i.e. around 6 for TiO_2 anatase) suggests that at pH 8, the surface assumes a negative surface charge and therefore adsorbs more rapidly and efficiently positively-charge Ru species, reducing the processing time. Otherwise, the deposition would require a significantly long time to reach the complete disappearance of Ru^{3+}.[79]

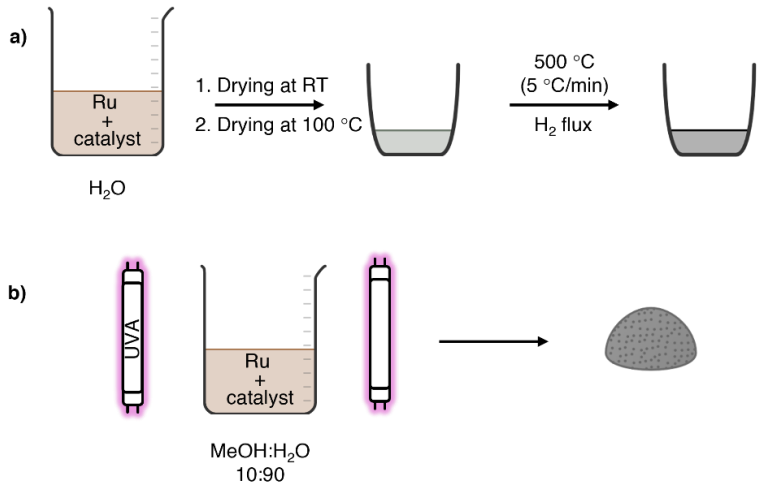

Figure 4.13: scheme of the deposition of Ru on Supp and Supp@TiO_2 by a) impregnation and b) photo-assisted method

In a typical experiment, a proper amount of $RuCl_3 \cdot xH_2O$ was dissolved under stirring in 100 mL of a MeOH and H_2O mixture (10:90, respectively) in a beaker-type glass reactor. Then, 100 mg of sample were dispersed in the solution by sonication and further by magnetic stirring. When a good dispersion was reached, the suspension pH (initially at 4.5) was increased to a value of 8 by using a 5 M NaOH aqueous solution and following the pH variation by a pH-meter (Mettler Toledo). Then, the dispersion was left under stirring at 500 rpm for 0.5 h and then exposed to UVA light with a 57.8 W m^{-2} irradiance within an irradiation chamber composed of 5 UV lamps (λ_{max} = 365

nm, Philips 24 W/10/4P). The decrease in the Ru precursor concentration in the solution was followed by UV-Vis spectrophotometry (VWR UV-3100PC): at selected times, 1.5 mL of samples were taken, filtered (0.20 µm, Aireka Cells) to remove the solid phase and the variation in the absorption peak at λ = 324 nm was monitored. Since the pH change causes the complete adsorption of the Ru precursor on the sample, further disappearance of the absorption peak at λ = 324 nm could not be monitored, and the irradiation time was set at 5 h based on previous studies.[77] At the end, the suspension was vacuum filtered (Nylon membrane filter, 0.22 µ m, Branchia), the collected samples were washed with distilled H_2O and dried in an oven at 100°C overnight. The samples obtained were labelled Supp@TiO_2@Ru5%

4.2.2.4 Photothermo catalytic setup and test

The catalytic tests were performed in a continuous-flow mode in a photothermo reactor consisting in a Harrick Scientific HVC-MRA 5 reaction chamber made from SS-316 alloy material (Figure 4.14) The catalyst was placed in the reactor as a thin layer at a given surface density (depending on the catalyst mass used) on a stainless meshed grid (400x400 mesh, pore size 0.038 mm, 6.3 mm diameter), which was homogeneously heated using an external cartridge heater monitored by a K-type thermocouple (± 1 °C) and using a high flow rate water cooling system to maintain a constant (bulk) temperature. The location of both inlet and outlet flows makes the catalyst operate in a downstream flow-through mode. The catalyst was irradiated via a SiO_2 window (13 x 2 mm) using a Thorlab M365LP1 LED (λ = 365 nm) with tuneable and calibrated irradiance within 0-400 mW cm^{-2} range.

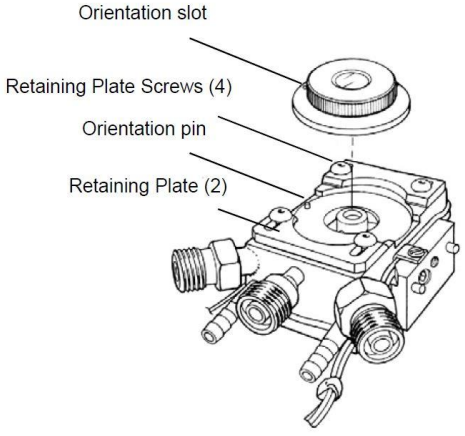

Figure 4.14: scheme of the Harrick Scientific HVC-MRA 5 reaction chamber used as reactor in photothermo catalysis experiments.

In the methanation catalytic tests, gas cylinders of 2 % CO_2 in Ar (Air liquide) and pure H_2 (Air products, 99.995 %) were used. Both flows were mixed following a 12.5:1 flow ratio, resulting in CO_2 and H_2 concentrations of 1.9 % and 7.7 %, respectively, with a total flow of 5.8 mL min^{-1}. Both the pure H_2 and the 2% CO_2/Ar flows were controlled by Brooks 5850 mass flow controllers.

For the methanation tests, 5 mg of catalyst were employed, resulting in a surface density of 16 mg cm^{-2}. The evolution of the reaction was monitored by an on-line quantification of the outlet flow with a R30000A gas micro-chromatography (SRA instruments), equipped with micro-TCDs. The system allows the quantification of CH_4. H_2, O_2, CO, CO_2 and organics on 5A molecular sieve, OV1, PoraPlotQ and Stabilwax columns. A scheme of the system employed for the photothermo catalysis experiments is depicted in Figure 4.15. Prior to the experiments, the reactional flow was stabilized in terms of flow rates and concentrations on a by-pass line, before to be switched towards the photothermo reactor at RT in the dark.

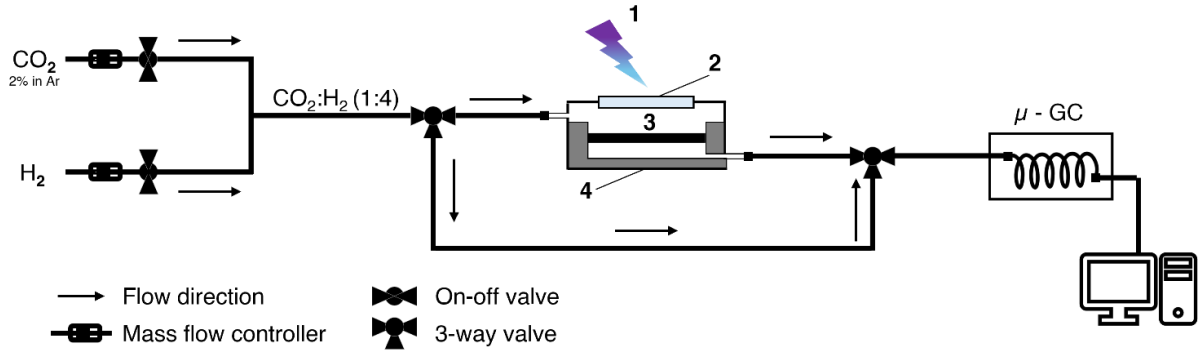

Figure 4.15: scheme of the photothermo catalysis setup employed in the methanation of CO_2. 1) UV-A light, λ = 365 nm, 400 mW cm^{-2}, 2) quartz window, 3) catalyst bed and 4) cartridge heater. The by-pass line for the reactor is also depicted.

The activity of the catalyst was expressed in terms of CH_4 production in mmol g^{-1} h^{-1}, calculated as reported in Eq. 4.3:

$$CH_4 \text{ production } \left(\frac{mmol}{g \cdot h}\right) = \frac{\frac{[CH_4] \cdot \text{flow rate}}{24.4} \cdot 60 \cdot 10^{-6}}{m_{catalyst}} \qquad 4.3$$

The increase in the CH_4 production was calculated according to Eq. 4.4.

$$CH_4 \text{ production increase} = \frac{[CH_4 \text{ production}]_{photothermo}}{[CH_4 \text{production}]_{thermo}} \qquad 4.4$$

where $[CH_4\ production]_{photothermo}$ and $[CH_4 production]_{thermo}$ are the methane production, expressed in mmol g^{-1} h^{-1}, obtained in the photothermo and thermo catalytic tests at the same bulk temperature.

The consumption of CO_2 during the catalytic reaction was expressed in terms of CO_2 conversion %, calculated according to Eq. 4.5.

$$CO_2 \text{ conversion } (\%) = \frac{[CO_2]_{in} - [CO_2]_{out}}{[CO_2]_{in}} \cdot 100 \qquad 4.5$$

where $[CO_2]_{in}$ and $[CO_2]_{out}$ correspond to the inlet and outlet concentration of CO_2, respectively.

Finally, the carbon balance was calculated according to Eq. 4.6.

$$C \text{ balance } (\%) = \frac{[CO_2]_{out} + [CO] + [CH_4]_{out}}{[CO_2]_{in}} \cdot 100 \qquad 4.6$$

where $[CO_2]_{in}$ and $[CO_2]_{out}$ are as previously defined, [CO] and $[CH_4]$ correspond to the concentration of CO and CH_4 in the outlet flow

4.2.3 Results and Discussion

In this chapter, information about the characterization of the samples and preliminary results of the catalytic behavior of the samples in the methanation of CO_2 will be presented and discussed.

4.2.3.1 Supp@TiO₂@Ru5% characterization

The amount of Ru on each sample was quantified with ICP-OES and the results are reported in Table 4.5. According to the results, the Ru wt. % content is lower than the theoretical 5 wt. % value, meaning that part of the Ru was lost during the procedure. For the photo-assisted synthesis method, it has to be considered that TiO_2 is dispersed on different supports. By evaluating the zero-charge points: for SiO_2 is generally < 3, Sep provides a value between 3-3.7 and Hall a value of 3.[81,82] Consequentially, at the

operative condition of pH 8, the supports provide a negatively-charged surface and Ru species can adsorb on them, without being reduced. On the other hand, for the impregnation method, the pH was not adjusted, and the procedure was performed at pH 4.5. In this condition, Ru-chloro complexes species deposition on the positively charged surface of TiO_2 is hindered by electrostatic repulsion.[79] In addition, being the pH so close to the zero-charge point of all the supports, the negative charge on their surface was limited, compared to pH 8. As consequence, the less favourable interaction between Ru species and catalysts could be responsible for the loss of Ru in the impregnation procedure.

Table 4.5: Ru wt. % obtained by ICP-OES

Sample	Impregnation	Photo-assisted
SiO_2@TiO_2@Ru5%	3.4	4.4
SiO_2 sheets@TiO_2@Ru5%	3.0	3.3
Sep@TiO_2@Ru5%	4.4	3.3
Hall@TiO_2@Ru5%	4.3	4.0

Additional information on the potential properties of the samples is provided by the application of the identical Ru deposition procedures on different supports; specifically, the photo-assisted method for TiO_2 P25, TiO_2 UV100, TiO_2 MPT625, TiO_2 P90 and g-C_3N_4 and the impregnation on high surface area SiO_2. The results provided by TEM micrographs shows an average particles dimension of 0.8 (±0.3) and 0.7 (±0.4) nm on P25 and UV100 and slightly higher values equal to 1.0 (±0.3) nm and 1.1 (±0.3) nm for MPT625 and P90, respectively. On the other hand, using different supports like g-C_3N_4 and SiO_2 cause a relative increase in the particles dimensions up to 1.8 (±0.7) and 1.5 (±0.8) nm. The XPS analysis on photo-assisted synthetised samples indeed demonstrated that Ru assumes the metallic state, with evidence of the respective oxides due to surface oxidation by air. The ratio Ru^0:Ru^{n+} observed for TiO_2 samples indeed varied from 64:36 to 38:62[77,83]

4.2.3.2 Photothermo catalysis over impregnated Supp@Ru5%

First photothermo catalytic tests performed on the (metal-free and TiO_2-free) bare

supports demonstrated their complete inactivity in the methanation reaction. Second, the activity of the different catalysts obtained by the decoration of bare supports by Ru via impregnation was investigated, and Figure 4.16 shows the CH_4 production for both thermo and photothermo catalysis. Due to the low activity of the samples, the CO_2 conversion cannot be calculated with accuracy as it remains within the experimental error, therefore the CO_2 consumption graphs will not be shown, and the C balance is not calculated.

Firstly, it must be noted that in all the performed experiments, both in the dark and under UV irradiation, CO was not generated in the process, but only CH_4 was observed as gaseous product. In the pure thermo-catalysis, a low yield to CH_4 < 0.5 mmol g^{-1} h^{-1} was observed at 120 °C, which increased with the increase in temperature, to reach a maximum yield between 0.7 and 1.5 mmol g^{-1} h^{-1} of CH_4 at 200 °C depending on the catalyst. By contrast, a significant enhancement was observed for all samples in photo-thermal conditions, and independently of the test temperature. The CH_4 production rates reached a maximum value of 4.2 and 3.2 mmol g^{-1} h^{-1} for SiO_2sheets@Ru5% and Sep@Ru5% catalysts, respectively, and of 5.0 mmol g^{-1} h^{-1} for both Hall@Ru5% and SiO_2@Ru5% catalysts. It can be seen that the activity ranking under dark and under light conditions was similar. In terms of activity range, it must be said that previous works by J. Ivanez and N. Keller evidenced a production of CH_4 of almost 30 mmol g^{-1} h^{-1} at 200°C and 400 mW cm^{-2} UV-A irradiance under the same experimental condition on a P25@Ru5% catalyst prepared by photo-assisted method.[77] Hence, despite the increase observed under UV illumination in photothermo conditions, the CH_4 yield obtained remained significantly low compared to the reference material. At the same time, synthetic SiO_2 and SiO_2 sheets supported Ru samples provide similar results to previous tests conducted on a commercial high surface area SiO_2 sample decorated with 5 wt. % of Ru with Ru NP size of 1.5 nm, namely 0.7 mmol g^{-1} h^{-1} vs. 3.1 mmol g^{-1} h^{-1} at 200 °C, with and without irradiation respectively.[77]

The low activity of the material was also demonstrated by Peng *et al*.[84] on 3 wt. % Ru loaded Hall, by operating at an irradiance of 640 mW cm^{-2}, and on SiO_2@Ru by operating at 2050 mW cm^{-2}. Considering Al_2O_3 as a model support, representing both clays and wide band gap materials like SiO_2, Wang *et al.*[85] tested a sample consisting of Al_2O_3@Ru1% at 1.5 AM sunlight (1 sun) and obtained a CH_4 production around 5

mmol CH_4 g^{-1} h^{-1} at 200°C. Grote *et al.*[86] tested a similar sample consisting of Al_2O_3@Ru5.9% at 210°C and under 6.2 suns obtaining a CH_4 production of 5.09 molCH_4 g_{Ru}^{-1} h^{-1}, considering that the parameter was calculated on the Ru content instead of the whole catalyst mass, the value is similar to the other samples.

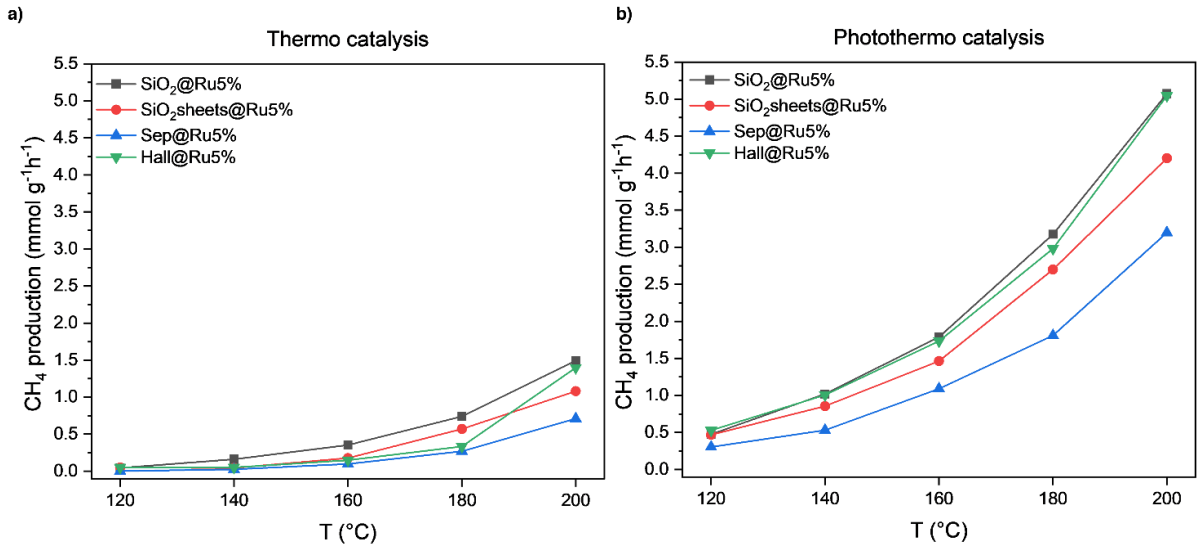

Figure 4.16: methane yield production by CO_2 methanation over the SiO_2@Ru5% (black), SiO_2 sheets@Ru5% (red), Sep@Ru5% (blue) and Hall@Ru5% (green) catalyst under dark (a) and light (b) conditions (I = 400 mW cm^{-2}). Reaction conditions: [CO_2] =2 v/v %, [H_2] =8 v/v %, total flow 5.8 ml min^{-1}, 5.0 mg of catalyst.

Figure 4.17 shows the CH_4 production enhancement induced by UV-A light. A higher enhancement is obtained at low temperatures, while at higher values the conditions are already in favour of the reaction and the effect is less pronounced. Due to the low CH_4 production in both dark and light conditions at 120°C, the calculation of the increase factor would be subjected to a low accuracy and, therefore, it is not reported.

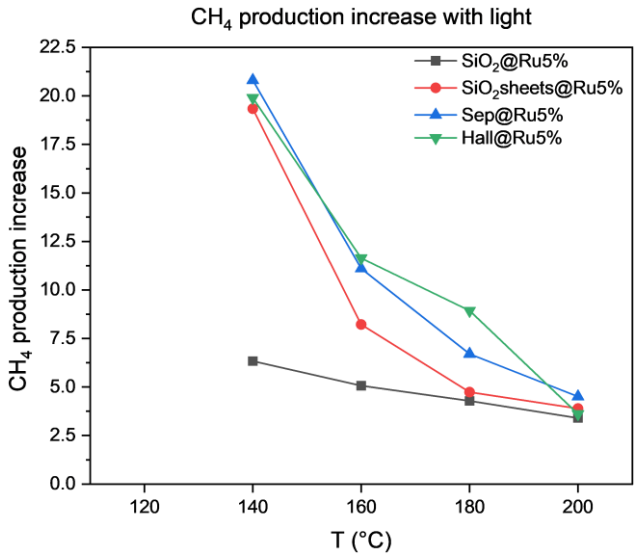

Figure 4.17: increase in the CH_4 production induced by irradiation at different experimental temperatures for SiO_2@Ru5% (black), SiO_2 sheets@Ru5% (red), Sep@Ru5% and Hall@Ru5% (green)

The methane yields obtained at different temperatures were used for deriving the Arrhenius plots, reported in Figure S2 in Appendix - 1. By the linear fitting, the apparent activation energy (E_a) was calculated, and the calculated values are reported in Table 4.6.

Table 4.6: apparent activation energy values calculated by the Arrhenius plot for both thermo and photothermo catalysis for the Supp@Ru5% samples

Sample	$E_{a\ thermo}$ (kJ mol^{-1})	$E_{a\ photothermo}$ (kJ mol^{-1})
SiO_2@Ru5%	66.4	45.5
SiO_2 sheets@Ru5%	57.0	42.8
Sep@Ru5%	89.4	45.9
Hall@Ru5%	87.1	43.3

Ru catalysts based on SiO_2 and SiO_2 sheets show very similar E_a values for both the thermo and photothermo conditions, with an average decrease of 27 % induced by UV light. The values obtained are also consistent with previous experiments on the commercial high surface area SiO_2 sample decorated with 5 wt. % of Ru, which provided an E_a value of 63.0 and 41.9 kJ mol^{-1} for thermo and photothermo catalysis, respectively.[77] In contrast, the Ru catalysts based on clays show a higher activation energy in the thermo-catalysis conditions, with a value of approximately 88 kJ mol^{-1}. However, under light irradiation, the activation energies of both samples assume a value similar to the SiO_2-base samples.

4.2.3.3 Photothermo catalysis over impregnated Supp@TiO_2@Ru5%

In Figure 4.18 the results of thermo and photothermo catalysis are shown for samples obtained by the impregnation method. Even for impregnated samples including TiO_2, the only gaseous product detected during the reaction is CH_4 for all the tests conducted, while CO was not detected.

The results demonstrate that under thermal catalysis, a yield < 0.35 mmol g^{-1} h^{-1} is obtained for all samples by operating at 120°C. By increasing the temperature, the parameter values improved up to 6.9 mmol g^{-1} h^{-1} for SiO_2@TiO_2@Ru5%, 4.5 mmol g^{-1} h^{-1} for SiO_2 sheets@TiO_2@Ru5% and 5.1 mmol g^{-1} h^{-1} for Hall@TiO_2@Ru5% while

Sep@TiO_2 provide a lower value of 1.7 mmol g^{-1} h^{-1}. The combination of photonic and thermal excitation strongly enhanced both CO_2 conversion and methane yield for all the tested samples.

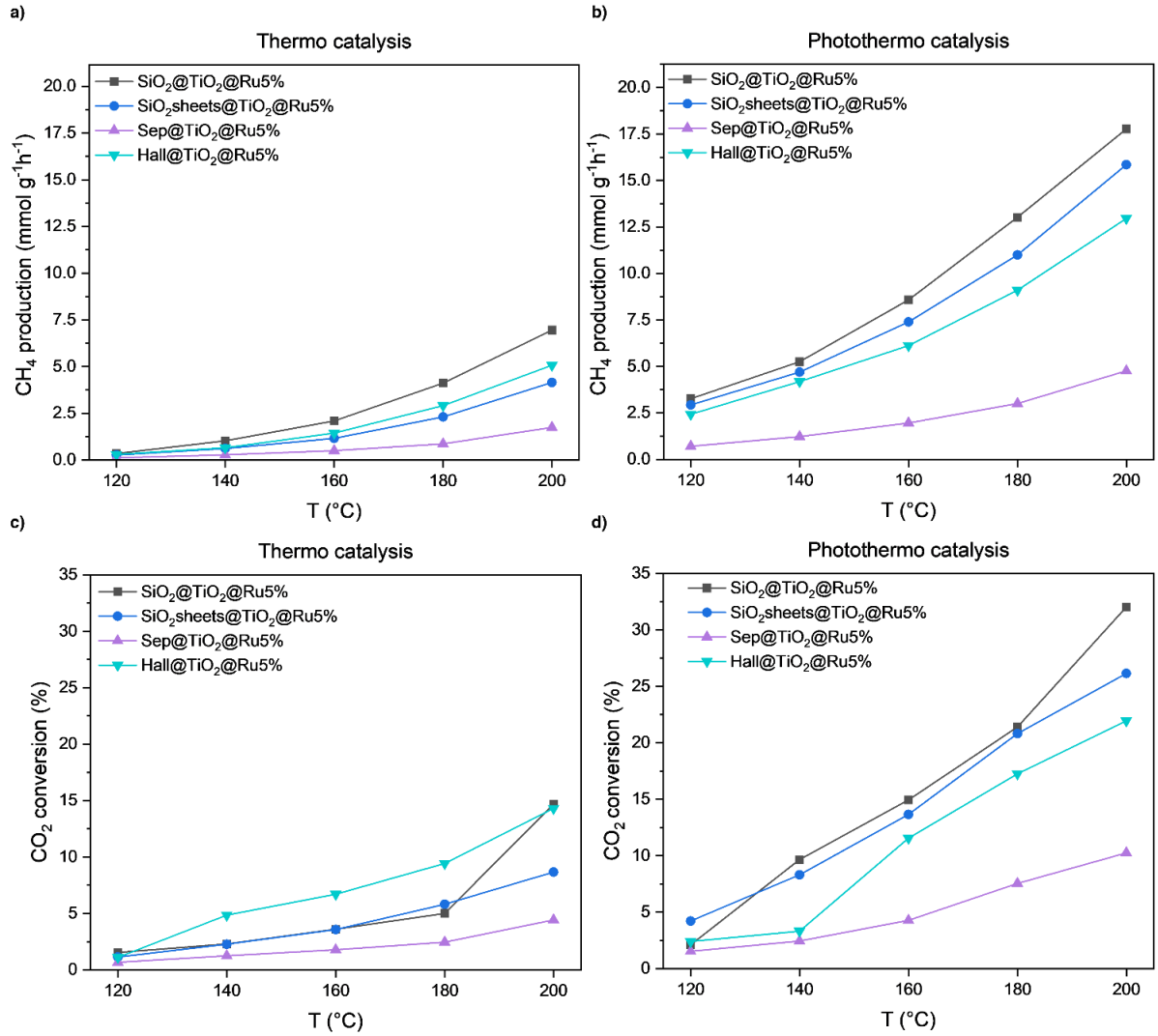

Figure 4.18: methane yield production and CO_2 conversion over the impregnated SiO_2@TiO_2@Ru5% (black), SiO_2 sheets@TiO_2@Ru5% (blue), Sep@TiO_2@Ru5% (purple) and Hall@TiO_2@Ru5% (light blue) catalyst under dark (a,c) and light (b,d) conditions (I = 400 mW cm^{-2}). Reaction conditions: [CO_2] =2 v/v %, [H_2] =8 v/v %, total flow 5.8 ml min^{-1}, 5.0 mg of catalyst.

The comparison with the Supp@Ru5% results described in the previous paragraph further corroborates this synergistic effect. In the absence of TiO_2, the best results were obtained in the photothermo conditions, with a CH_4 production between 3 and 5 mmol g^{-1} h^{-1}. By adding TiO_2 to the samples, such low values are observed in the pure thermo-catalysis, where the synergic effect is not activated. By adding UV light irradiation, the methane production was significantly enhanced and the parameter reaches the maximum value of almost 17.5 mmol g^{-1} h^{-1} at 200 °C. The CO_2 conversion shows an identical trend to the CH_4 production: the higher the CO_2 consumption, the

higher the product yield. This is also corroborated by the C balance value, which ranges from 97 to 101 % for all the tests performed. For the thermos catalysis experiment, the lower efficiency of the reaction and the consequential low variations in the CO_2 concentration, make the parameter more influenced by the instrumental error, therefore it is less precise.

Among the samples tested, while the two SiO_2-supported samples provide similar results, Sep@TiO_2@Ru5% shows the worst performance, with only 5 mmol g^{-1} h^{-1} of CH_4 production at 200 °C under UV light irradiation. This phenomenon cannot be attributed to the Ru content, since the sample shows the highest wt. % value compared to the other samples (4.4 wt. %), according to ICP-OES results. It's interesting to notice that the differences in efficiency could be associated with the porosity. The main limit of the impregnation procedure is that Ru can deposit on the whole samples, not exclusively on TiO_2 and, as demonstrated, when the metal anchors on the SiO_2-based support, its contribution to the CO_2 methanation was negligible. Considering the BET results, shown in Paragraph 4.1.3.3, Sep@TiO_2 is the material with the highest surface area, compared to the other TiO_2 functionalized samples, meaning that the probability that Ru anchors on the support is higher. In addition, the thermal treatment at 500 °C during the Ru wet impregnation procedure causes the crystals folding of sepiolite, due to the removal of internal zeolitic water.[87,88] As consequence, part of the porosity is lost, especially in the micropore range.[89] On the other hand, similar considerations can be made for Hall@TiO_2@Ru5%, since its Ru content is equal to 4.3 wt. %, but the sample shows a lower activity compared to the two SiO_2-supported ones. It is reported also for Hall that a thermal treatment above 450 °C causes the complete removal of interlayer water molecules in the clay structure, resulting in important changes in its structure and morphology. Indeed, the water removal induces the separation of the connected rolled layers forming halloysite, forming new mesopores and deforming the inner cavity.[90–92] Therefore, it is reasonable to hypothesize that Ru deposited on those two clays was less accessible after the thermal reduction treatments, explaining the lower yield compared to other samples observed for both Hall@TiO_2@Ru5% and Sep@TiO_2@Ru5%.

The unique behaviour of Sep@TiO_2@Ru5% is also highlighted by the light-induced enhancement in the CH_4 production, shown in Figure 4.19.

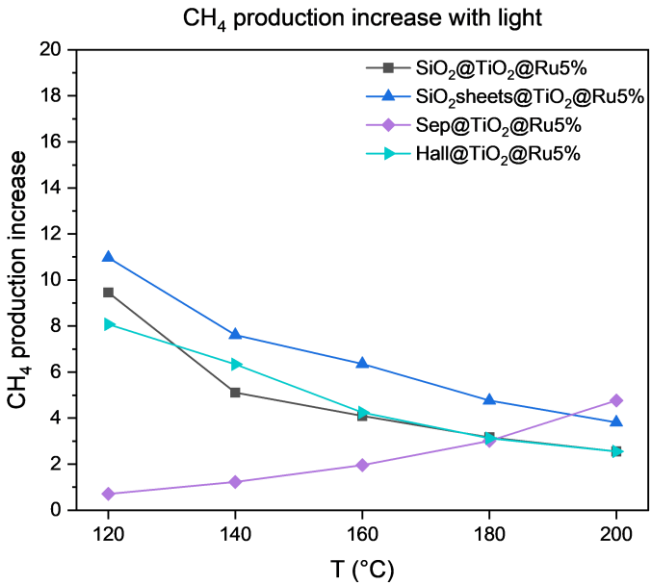

Figure 4.19: increase in the CH_4 production induced by irradiation at different experimental temperature for impregnated SiO_2@TiO_2@Ru5% (black), SiO_2 sheets@TiO2@Ru5% (blue), Sep@TiO_2@Ru5% (purple) and Hall@TiO_2@Ru5% (light blue)

Even for this class of samples, the enhancement was remarkably pronounced at low temperatures, for which the yield of methane was very low at dark conditions. At higher temperatures, for which the conversion was already important, the enhancement was in consequence less pronounced. Sep-supported TiO_2 is the only sample showing an opposite trend, with the major enhancement observed at higher temperatures.

The methane yields obtained at different temperatures were used for deriving the Arrhenius plots, reported in Figure S3 in Appendix – 1. The apparent activation energy values calculated are reported in Table 4.7.

Table 4.7: apparent activation energy values calculated by the Arrhenius plot for both thermos and photothermo catalysis for the Supp@TiO_2@Ru5% samples

Sample	$E_{a\ thermo}$ (kJ mol^{-1})	$E_{a\ photothermo}$ (kJ mol^{-1})
SiO_2@TiO_2@Ru5%	57.5	33.3
SiO_2 sheets@TiO_2@Ru5%	52.6	32.7
Sep@TiO_2@Ru5%	50.3	36.4
Hall@TiO_2@Ru5%	55.2	32.0

All the tested samples show similarities in terms of the influence of light illumination on the apparent activation energy. The activation energy values assume similar values for all samples and a decrease in their values under illumination is clear. By calculating

the average values, an activation energy reduction from 53.9 kJ mol^{-1} to 33.6 kJ mol^{-1} is observed, corresponding to a 37.7 % decrease. By comparing the values with the Supp@Ru5% ones, a decrease in the activation energy under UV irradiation of more than 10 kJ mol^{-1} can be observed by introducing TiO_2 in the samples.

4.2.3.4 Photothermo catalysis on photo-assisted Supp@TiO_2@Ru5%

Photothermo catalytic tests were also conducted on samples obtained by the photo-assisted preparation method. Since the synthesis was driven by the TiO_2-mediated reduction of Ru^{3+} to metallic Ru, reference samples with only the supports (without TiO_2) couldn't be prepared. Figure 4.20 shows the CH_4 production and CO_2 conversion for the four tested samples.

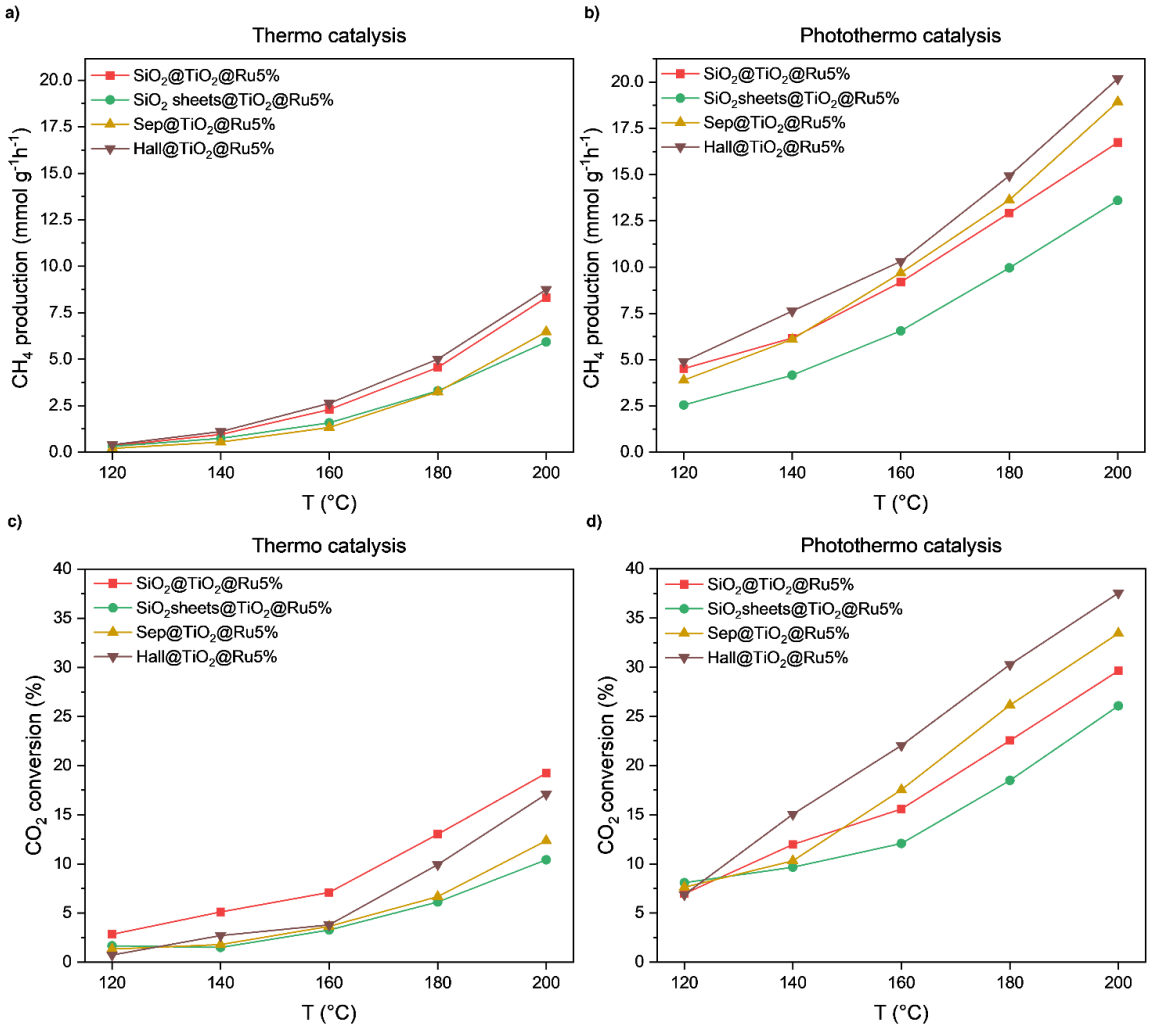

Figure 4.20: CH_4 yield production and CO_2 conversion over SiO_2@TiO_2@Ru5% (black), SiO_2 sheets@TiO_2@Ru5% (blue), Sep@TiO_2@Ru5% (purple) and Hall@TiO_2@Ru5% (light blue) catalysts prepared by the photo-assisted synthesis method, under dark (a,c) and light (b,d) conditions (I = 400 mW cm^{-2}). Reaction conditions: [CO_2] = 2 v/v %, [H_2] = 8 v/v %, total flow 5.8 ml min^{-1}, 5.0 mg of catalyst.

The application of photo-assisted deposited Ru samples demonstrated to be fully selective towards methane production, since CO was not detected during the test. In addition, the C balance ranges from 98 % to 101 % for all the tested samples.

In dark conditions, a CH_4 production < 0.4 mmol g^{-1} h^{-1} and a CO_2 conversion < 2.83 % were obtained for all samples, by operating at 120 °C. By increasing the temperature up to 200 °C, a limited efficiency in converting CO_2 to CH_4 was observed with a CH_4 yield between 5 and 7.5 mmol g^{-1} h^{-1} and a CO_2 conversion in the range of 10 and 17.5 %. However, both CH_4 production and CO_2 conversion clearly show the beneficial photothermal effect originated by the combination of both photonic and thermal excitation, independently from the sample's nature and the reaction temperature.

Specifically, both parameters investigated show an increase of 2 to 3 times in their values: CH_4 production reaches a range value of 15-20 mmol g^{-1} h^{-1}, while the CO_2 conversion percentages range between 30 % and 37.5 %. It is worth noticing the lower results provided by SiO_2 sheets@TiO_2@Ru5% compared to the other samples. Due to lack of information about Ru oxidation state and NPs dimensions is not clear the reason of this behaviour, however part of the explanation could be to the lower Ru, measured by ICP-OES (3.3 wt. %). To further highlight the role played by light irradiation, the increase in CH_4 production was calculated.

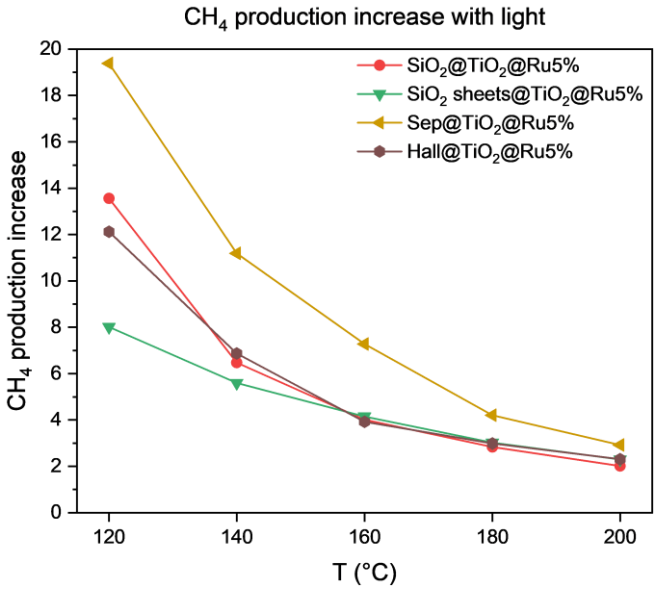

Figure 4.21: increase in the CH_4 production induced by irradiation at different experimental temperature for SiO_2@TiO_2@Ru5% (black), SiO_2 sheets@TiO_2@Ru5% (blue), Sep@TiO_2@Ru5% (purple) and Hall@TiO_2@Ru5% (light blue) synthetised with a photo-assisted method

Figure 4.21 shows the increment in CH_4 production induced by light. As already observed for the samples obtained by impregnation, the enhancement is more pronounced at lower temperature, where the value reaches the maximum of 20, compared to lower temperatures. It is worth noting that Sep@TiO_2@Ru5% sample shows the highest increase in CH_4 production when irradiation with UV light. On the other hand, SiO_2 sheet@TiO_2@Ru5% sample provides a slightly lower CH_4 yield and enhancement under UV irradiation, compared to the other samples.

During the tests, a particular phenomenon was noticed for samples prepared with photo-assisted method: by heating the samples a slight decrease in the [CH_4] detected by μ -GC over time is observed. The phenomenon was observed for all samples, with and without light irradiation; an example of this behaviour is reported as depicted in Figure 4.22 for SiO_2@TiO_2@Ru5%.

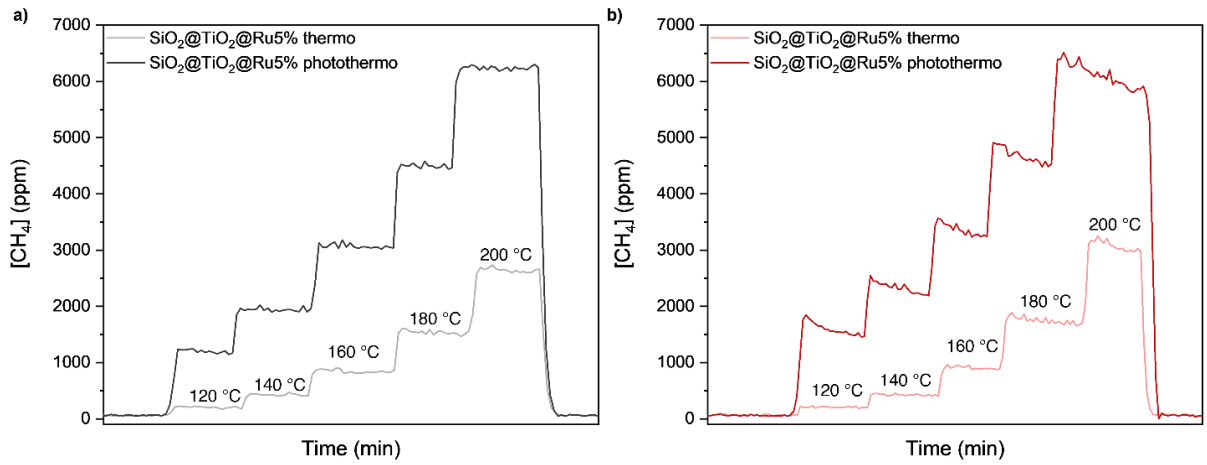

Figure 4.22: [CH_4] evolution during the thermo (light red and grey) and photothermo (dark red and black) catalytic methanation of CO_2 on the SiO_2@TiO_2@Ru5% catalyst prepared by a) impregnation and b) photo-assisted synthesis. The analysis temperatures are reported in figure.

Both physical and chemical deactivation mechanisms have been reported for CO_2 methanation. Among them, the most probable are two: (i) the sintering of the catalyst, due to Ostwald ripening or particle coalescence, causes metal agglomeration, decreasing the number of surface-active sites available or (ii) the physical deposition of carbon on the catalyst, blocking the active sites accessibility. Both phenomena are favoured by high temperatures and could be further enhanced by the exothermic reaction involved.[93–96]

It must be said that this behaviour was not observed for impregnated samples; in

addition, the C balance calculations provide a value of 100 % for all the tests performed, meaning that all consumed CO_2 is converted in CH_4. Therefore, it is possible to exclude the carbon fouling phenomenon.[97] At the same time, the thermal treatment at 500 °C undergone by impregnated samples already stimulates the Ostwald ripening for Ru NPs, therefore the phenomenon is not observed in the photocatalytic test temperature range. Therefore, this result suggests that samples prepared by photo-assisted method are not stable at a temperature higher than 120 °C. On the other hand, the variation in the [CH_4] over time for the photo-assisted synthesised samples limited and it does not significantly alter the final results.

Starting from the Arrhenius plot (see Figure S3 in Appendix – 1), the activation energies were calculated for each sample. The results are summed up in Table 4.8.

Table 4.8: apparent activation energy values calculated by the Arrhenius plot for both thermo and photothermo catalysis for the Supp@TiO_2@Ru5% samples synthetized with photo-assisted method

Sample	$E_{a\ thermo}$ (kJ mol^{-1})	$E_{a\ photothermo}$ (kJ mol^{-1})
SiO_2@TiO_2@Ru5%	62.1	26.0
SiO_2 sheets@TiO_2@Ru5%	56.8	32.7
Sep@TiO_2@Ru5%	67.6	30.7
Hall@TiO_2@Ru5%	59.5	27.1

All the samples show a similar E_a value for both thermo and photothermo conditions. The results clearly show a decrease in the E_a values: from an average value of 61.5 kJ mol^{-1} to 29.1 kJ mol^{-1}, corresponding to a 47.4 % decrease. Considering P25 as the reference model, previous works in the same research group[77] demonstrated that, under the same experimental condition, the activation energy decreased from 84 kJ mol^{-1} to 27.3 kJ mol^{-1} under illumination, corresponding to a 67.5 % reduction. The decrease in the E_a observed for the reference sample is higher than the supported samples. However, considering the absolute values, the supported TiO_2 samples provide a lower activation energy in the dark compared to P25@Ru5%. At the same time, under UV irradiation, E_a values provided by supported samples are comparable to the P25@Ru5%.

4.2.3.5 Considerations on the mechanism

Despite the limited data available, it is possible to make some considerations about the mechanism involved. We described in Chapter 1.3.2 that the photothermo effect is the result of the combination of both photochemical and thermochemical contributions. The thermo effect rises from the conversion of the photon flux into an energy source through non-radiative relaxation processes after light adsorption. As a result, a local temperature increase is established close to the catalyst surface which, consequentially operates as a thermal catalyst. On the other hand, the photochemical effect is associated with the hot charge carriers generated by the decay of LSPR and their promotion to antibonding orbitals of adsorbed molecules or to the conduction band of a supporting semiconductor.[98]

Since the two mechanisms coexist simultaneously, defining which contributes predominantly to the system is not an easy task. However, the E_a can provide meaningful information about both the catalytic performance of the material and the mechanism pathway followed during the reaction.

In the case the combined photon-thermal excitations are favouring the electron-drive mechanism, the reaction would proceed through a transition state with lower energy; in other words, this would lead to a decrease in the apparent E_a.[83,99,100]
The results obtained for both Supp@Ru5% and Supp@TiO_2@Ru5%, either with the impregnation or photo-assisted procedures, show a net decrease in the apparent E_a value when operating under light irradiation, compared to the experiment in the dark. Indeed, the apparent E_a decreases from an average value of 61.7 kJ mol^{-1} for SiO_2@ and SiO_2sheets@ Ru5% and 88.25 kJ mol^{-1} for clays-supported Ru to 44.4 kJ mol^{-1} under light irradiation. Similarly, for samples containing TiO_2 the E_a decreases from an average value of 53.9 kJ mol^{-1} to 33.6 kJ mol^{-1} for impregnated samples and from 61.5 kJ mol^{-1} to 29.1 kJ mol^{-1} for photo-assisted synthesised samples.

On the other hand, the effect of localized heating through non-radiative relaxation does not alter the apparent E_a because the reaction proceeds through a similar mechanism, but at a higher temperature than the bulk. Since the implication of a thermal contribution cannot be excluded, the findings suggest that under dual photon and thermal excitation the CO_2 methanation proceeds through a different mechanism, so the electron-driven effect is prevailing.

Once define the mechanism, it is worth highlighting the central role played by TiO_2 in enhancing the CH_4 yield in the impregnated samples. Indeed, Supp@Ru5% demonstrated to have a prevailing electron-driven mechanism which, considering that the high band gap of all supports, can be tentatively associated to the hot-electron transfer from Ru to adsorbed CO_2/H_2. On the other hand, the presence of TiO_2 allows either an increase in the electron density on Ru or the transfer of hot electron in the conduction band, in both cases favouring the amount of electron available and, consequentially, the reaction.

4.2.4 Final considerations

The application of TiO_2 supported on different SiO_2-based materials and functionalized with Ru NPs were investigated for the photothermal conversion of CO_2 into CH_4. The results confirm the efficiency of Ru in the hydrogenation of CO_2, providing a 100% selectivity for CH_4 production.

By testing Ru functionalized bare supports, a small enhancement provided by both thermal and photon excitation was observed, but the amount of methane produced was extremely low compared to the samples containing TiO_2.

Indeed, TiO_2-containing samples showed a remarkable enhancement in the CH_4 production under UV irradiation. However, some differences were observed depending on the Ru deposition method employed. Specifically, the thermal treatment required for the impregnation deposition is known to modify the morphology and porosity of the two clays, Hall and Sep, leading to a potential decrease in the exposure of deposited Ru and a consequential decrease in the performances of both samples. On the other hand, the photodeposition method avoids this structural rearrangement and less pronounced differences were observed in the CH_4 yield.

The most important result is that the synergic photon and thermal excitation cause a more important enhancement in the CH_4 production at lower temperatures. Indeed, for most samples, the CH_4 yield obtained at the highest temperature (200 °C) in the dark can be achieved at a lower temperature under combined photonic-thermal excitations. From a sustainable point of view, this represents a significant improvement. Operating at lower temperatures reduces the overall energy demand of the process and,

indirectly, lowers the carbon footprint of the process, minimizing the reliance on fossil fuels for heat generation. Overall, the enhancement in CH_4 production through this innovative approach aligns well with global efforts to improve energy efficiency and reduce environmental impacts in chemical manufacturing.

As mentioned at the beginning of the paragraph, these data are the results of a preliminary study. Indeed, further investigations are ongoing to complete the data set and have a more in-depth knowledge of the topic and a clearer vision of the potentiality of the results. In this regard, a deeper characterization of all the samples will be performed, including XPS analysis to define the oxidation state of Ru and TEM microscopy to determine the Ru NPs dimensions. At the same time, additional studies are ongoing to determine the effective role of photogenerated charge carriers in the reaction mechanism.

4.3 Bibliography

[1] C. Li, N. Zhu, S. Yang, X. He, S. Zheng, Z. Sun, D. D. Dionysiou, *Chemosphere* **2021**, *273*, DOI 10.1016/j.chemosphere.2021.129723.

[2] N. Yahya, F. Aziz, N. A. Jamaludin, M. A. Mutalib, A. F. Ismail, W. N. Salleh, J. Jaafar, N. Yusof, N. A. Ludin, *J. Environ. Chem. Eng.* **2018**, *6*, 7411–7425.

[3] E. Jimenez-Relinque, S. F. Lee, L. Plaza, M. Castellote, *Environ. Sci. Pollut. Res.* **2022**, *29*, 39712–39722.

[4] S. S. Alias, Z. Harun, F. H. Azhar, S. A. Ibrahim, B. Johar, *J. Clean. Prod.* **2020**, *251*, DOI 10.1016/j.jclepro.2019.119448.

[5] D. Huang, Y. Miyamoto, J. Ding, J. Gu, S. Zhu, Q. Liu, T. Fan, Q. Guo, D. Zhang, *Mater. Lett.* **2011**, *65*, 326–328.

[6] G. Martínez-Edo, A. Balmori, I. Pontón, A. M. Del Rio, D. Sánchez-García, *Catalysts* **2018**, *8*, DOI 10.3390/catal8120617.

[7] D. Kumar, K. Schumacher, C. Du Fresne von Hohenesche, M. Grün, K. K. Unger, *Colloids Surfaces A Physicochem. Eng. Asp.* **2001**, *187–188*, 109–116.

[8] S. Bhattacharyya, G. Lelong, M. L. Saboungi, *J. Exp. Nanosci.* **2006**, *1*, 375–395.

[9] M. F. Brigatti, E. Galán, B. K. G. Theng, *Structure and Mineralogy of Clay Minerals*, **2013**.

[10] M. Tahir, N. A. S. Amin, *Appl. Catal. B Environ.* **2013**, *142–143*, 512–522.

[11] H. H. Mohamed, G. Wazan, D. H. A. Besisa, *Mater. Sci. Eng. B* **2022**, *286*, DOI 10.1016/j.mseb.2022.116077.

[12] P. Yuan, D. Tan, F. Annabi-Bergaya, *Appl. Clay Sci.* **2015**, *112–113*, 75–93.

[13] H. H. Murray, in *Appl. Clay Mineral. Occur. Process. Appl. Kaolins, Bentonites, Palygorskite-Sepiolite Common Clays*, **2006**, pp. 7–31.

[14] A. I. Ruiz, C. Ruiz-García, E. Ruiz-Hitzky, *Appl. Clay Sci.* **2023**, *235*, DOI 10.1016/j.clay.2023.106874.

[15] G. Tian, G. Han, F. Wang, J. Liang, *Sepiolite Nanomaterials: Structure, Properties and Functional Applications*, **2019**.

[16] H. Chen, M. Zheng, H. Sun, Q. Jia, *Mater. Sci. Eng. A* **2007**, *445–446*, 725–730.

[17] L. Tripaldi, E. Callone, M. D'Arienzo, S. Dirè, L. Giannini, S. Mascotto, A. Meyer, R. Scotti, L. Tadiello, B. Di Credico, *Soft Matter* **2021**, *17*, 9434–9446.

[18] T. Okuno, G. Kawamura, H. Muto, A. Matsuda, *J. Solid State Chem.* **2016**, *235*, 132–138.

[19] M. Langlet, M. Burgos, C. Coutier, C. Jimenez, C. Morant, M. Manso, *J. Sol-Gel Sci. Technol.* **2001**, *22*, 139–150.

[20] B. Shi, L. Xie, B. Ma, Z. Zhou, B. Xu, L. Qu, *Gels* **2022**, *8*, 1–13.

[21] T. N. Tran, T. V. A. Pham, M. L. P. Le, T. P. T. Nguyen, V. M. Tran, *Adv. Nat. Sci. Nanosci. Nanotechnol.* **2013**, *4*, DOI 10.1088/2043-6262/4/4/045007.

[22] R. R. Madathingal, S. L. Wunder, *Thermochim. Acta* **2011**, *526*, 83–89.

[23] D. Jia, J. Q. Liu, X. F. Yao, Y. L. Wang, *J. Wuhan Univ. Technol. Mater. Sci. Ed.* **2004**, *19*, 44–47.

[24] S. Hojati, H. Khademi, *J. Sci. Islam. Repub. Iran* **2013**, *24*, 129–134.

[25] P. Luo, Y. Zhao, B. Zhang, J. Liu, Y. Yang, J. Liu, *Water Res.* **2010**, *44*, 1489–1497.

[26] H. Wei, H. Wang, H. Chu, J. Li, *Int. J. Biol. Macromol.* **2019**, *133*, 1210–1218.

[27] A. P. Nambiar, R. Pillai, M. Sanyal, Y. Vadikkeettil, P. S. Shrivastav, *Environ. Sci. Adv.* **2023**, *2*, 861–876.

[28] P. Praveen, G. Viruthagiri, S. Mugundan, N. Shanmugam, *Spectrochim. Acta - Part A Mol. Biomol. Spectrosc.* **2014**, *117*, 622–629.

[29] R. Poliah, S. Sreekantan, *J. Nanomater.* **2011**, *2011*, DOI 10.1155/2011/239289.

[30] S. Challagulla, K. Tarafder, R. Ganesan, S. Roy, *Sci. Rep.* **2017**, *7*, 1–11.

[31] C. Kinowski, M. Bouazaoui, R. Bechara, L. L. Hench, J. M. Nedelec, S. Turrell, *J. Non. Cryst. Solids* **2001**, *291*, 143–152.

[32] H. Ikeda, S. Fujino, *J. Miner. Mater. Charact. Eng.* **2017**, *05*, 107–117.

[33] L. Spallino, L. Vaccaro, L. Sciortino, S. Agnello, G. Buscarino, M. Cannas, F. M. Gelardi, *Phys. Chem. Chem. Phys.* **2014**, *16*, 22028–22034.

[34] R. L. Frost, H. F. Shurvell, *Clays Clay Miner.* **1997**, *45*, 68–72.

[35] J. T. Kloprogge, in *Dev. Clay Sci.* (Eds.: P. Yuan, A. Thill, F.B.T.-D. in C.S. Bergaya), Elsevier, **2016**, pp. 115–136.

[36] M. Munasir, N. Hidayat, D. H. Kusumawati, N. P. Putri, A. Taufiq, S. Sunaryono, *AIP Conf. Proc.* **2020**, *2251*, DOI 10.1063/5.0015673.

[37] E. Ruiz-Hitzky, C. Ruiz-García, F. M. Fernandes, G. Lo Dico, L. Lisuzzo, V. Prevot, M. Darder, P. Aranda, *Front. Chem.* **2021**, *9*, 1–17.

[38] Q. Tang, F. Wang, M. Tang, J. Liang, C. Ren, *J. Nanomater.* **2012**, *2012*, DOI 10.1155/2012/382603.

[39] M. A. Barakat, R. Kumar, M. Balkhyour, M. A. Taleb, *RSC Adv.* **2019**, *9*, 13916–13926.

[40] I. Daou, G. L. Lecomte-Nana, N. Tessier-Doyen, C. Peyratout, M. F. Gonon, R. Guinebretiere, *Minerals* **2020**, *10*, DOI 10.3390/min10050480.

[41] Y. Mi, Y. Weng, *Sci. Rep.* **2015**, *5*, 1–10.

[42] K. S. W. Sing, **1985**, *57*, 603–619.

[43] M. Thommes, K. Kaneko, A. V. Neimark, J. P. Olivier, F. Rodriguez-Reinoso, J. Rouquerol, K. S. W. Sing, *Pure Appl. Chem.* **2015**, *87*, 1051–1069.

[44] A. I. Ruiz, C. Ruiz-García, E. Ruiz-Hitzky, *Appl. Clay Sci.* **2023**, *235*, DOI 10.1016/j.clay.2023.106874.

[45] V. G. Baldovino-Medrano, V. Niño-Celis, R. Isaacs Giraldo, *J. Chem. Eng. Data* **2023**, *68*, 2512–2528.

[46] M. Suárez, E. García-Romero, *Appl. Clay Sci.* **2012**, *67–68*, 72–82.

[47] D. Papoulis, D. Panagiotaras, P. Tsigrou, K. C. Christoforidis, C. Petit, A. Apostolopoulou, E. Stathatos, S. Komarneni, I. Koukouvelas, *Mater. Sci. Semicond. Process.* **2018**, *85*, 1–8.

[48] N. Plumeré, A. Ruff, B. Speiser, V. Feldmann, H. A. Mayer, *J. Colloid Interface Sci.* **2012**, *368*, 208–219.

[49] D. Papoulis, S. Komarneni, D. Panagiotaras, E. Stathatos, D. Toli, K. C. Christoforidis, M. Fernández-García, H. Li, S. Yin, T. Sato, H. Katsuki, *Appl. Catal. B Environ.* **2013**, *132–133*, 416–422.

[50] D. Papoulis, S. Komarneni, A. Nikolopoulou, P. Tsolis-Katagas, D. Panagiotaras, H. G. Kacandes, P. Zhang, S. Yin, T. Sato, H. Katsuki, *Appl. Clay Sci.* **2010**, *50*, 118–124.

[51] E. Brillas, J. Manuel Peralta-Hernández, *Sep. Purif. Technol.* **2023**, *309*, DOI

10.1016/j.seppur.2022.122982.

[52] J. H. Duffus, *Pure Appl. Chem.* **2002**, *74*, 793–807.

[53] E. Svobodová, Z. Tišler, K. Peroutková, K. Strejcová, J. Abrham, J. Šimek, Z. Gholami, M. Vakili, *Molecules* **2024**, *29*, DOI 10.3390/molecules29102357.

[54] M. Tommasi, S. N. Degerli, G. Ramis, I. Rossetti, *Chem. Eng. Res. Des.* **2024**, *201*, 457–482.

[55] A. Tripodi, F. Conte, I. Rossetti, *Energy and Fuels* **2020**, *34*, 7242–7256.

[56] M. A. A. Aziz, A. A. Jalil, S. Triwahyono, A. Ahmad, *Green Chem.* **2015**, *17*, 2647–2663.

[57] S. Rönsch, J. Schneider, S. Matthischke, M. Schlüter, M. Götz, J. Lefebvre, P. Prabhakaran, S. Bajohr, *Fuel* **2016**, *166*, 276–296.

[58] X. Meng, T. Wang, L. Liu, S. Ouyang, P. Li, H. Hu, T. Kako, H. Iwai, A. Tanaka, J. Ye, *Angew. Chemie - Int. Ed.* **2014**, *53*, 11478–11482.

[59] J. Ren, S. Ouyang, H. Xu, X. Meng, T. Wang, D. Wang, J. Ye, *Adv. Energy Mater.* **2017**, *7*, DOI 10.1002/aenm.201601657.

[60] C. Wang, S. Fang, S. Xie, Y. Zheng, Y. H. Hu, *J. Mater. Chem. A* **2020**, *8*, 7390–7394.

[61] M. Novoa-Cid, H. G. Baldovi, *Nanomaterials* **2020**, *10*, 1–14.

[62] H. Zhang, M. Chen, W. Qian, J. Zhang, X. Chen, J. Fang, C. Wang, C. Zhang, *J. Environ. Sci.* **2024**.

[63] K. Wang, S. He, Y. Lin, X. Chen, W. Dai, X. Fu, *Chinese J. Catal.* **2022**, *43*, 391–402.

[64] T. Dong, X. Liu, Z. Tang, H. Yuan, D. Jiang, Y. Wang, Z. Liu, X. Zhang, S. Huang, H. Liu, L. Zhao, W. Zhou, *Appl. Catal. B Environ.* **2023**, *326*, DOI 10.1016/j.apcatb.2022.122176.

[65] B. Jin, X. Ye, H. Zhong, F. Jin, Y. H. Hu, *Chinese Chem. Lett.* **2022**, *33*, 812–816.

[66] P. G. O'Brien, A. Sandhel, T. E. Wood, F. M. Ali, L. B. Hoch, D. D. Perovic, C. A. Mims, G. A. Ozin, *Adv. Sci.* **2014**, *1*, 1–7.

[67] S. Loganathan, M. Tikmani, S. Edubilli, A. Mishra, A. K. Ghoshal, *Chem. Eng. J.* **2014**, *256*, 1–8.

[68] J. A. Cecilia, E. Vilarrasa-García, C. L. Cavalcante, D. C. S. Azevedo, F. Franco, E. Rodríguez-Castellón, *J. Environ. Chem. Eng.* **2018**, *6*, 4573–4587.

[69] K. Ramadass, G. Singh, K. Singh, M. R. Benzigar, J. Yang, S. Kim, A. Mohammed, T. Belperio, A. Vinu, *Microporous Mesoporous Mater.* **2019**, *277*, 229–236.

[70] N. Chouikhi, J. A. Cecilia, E. Vilarrasa-García, S. Besghaier, M. Chlendi, F. I. F. Duro, E. R. Castellon, M. Bagane, *Minerals* **2019**, *9*, 1–22.

[71] H. Mo, K. Yang, S. Li, P. Jiang, *RSC Adv.* **2016**, *6*, 69569–69579.

[72] H. R. Taghiyari, A. Soltani, A. Esmailpour, V. Hassani, H. Gholipour, A. N. Papadopoulos, *Nanomaterials* **2020**, *10*, 1–15.

[73] T. Gao, B. P. Jelle, *J. Nanoparticle Res.* **2019**, *21*, DOI 10.1007/s11051-019-4556-8.

[74] M. J. Cai, C. R. Li, L. He, *Rare Met.* **2020**, *39*, 881–886.

[75] W. Zhang, L. Wang, K. Wang, M. U. Khan, M. Wang, H. Li, J. Zeng, *Small* **2017**, *13*, 1–5.

[76] J. Wojciechowska, M. Jędrzejczyk, J. Grams, N. Keller, A. M. Ruppert, *ChemSusChem* **2019**, *12*, 639–650.

[77] F. J. Ivanez Castellano, Ru Based Photothermal Catalysts for Formic Acid Dehydrogenation and CO2 Methanation, Université de Srasbourg, **2022**.

[78] J. Wojciechowska, E. Gitzhofer, J. Grams, A. M. Ruppert, N. Keller, *Catal. Today* **2019**, *326*, 8–14.

[79] J. Wojciechowska, E. Gitzhofer, J. Grams, A. M. Ruppert, N. Keller, *Materials (Basel).* **2018**, *11*, 1–14.

[80] A. M. Ruppert, M. Brzezińska, N. Keller, *Catal. Today* **2024**, *433*, DOI 10.1016/j.cattod.2024.114651.

[81] M. Kosmulski, *Adv. Colloid Interface Sci.* **2021**, *296*, DOI 10.1016/j.cis.2023.102973.

[82] M. Kosmulski, *Adv. Colloid Interface Sci.* **2023**, *319*, DOI 10.1016/j.cis.2023.102973.

[83] J. Ivanez, P. Garcia-Munoz, A. M. Ruppert, N. Keller, *Catal. Today* **2021**, *380*, 138–146.

[84] K. Peng, J. Ye, H. Wang, H. Song, B. Deng, S. Song, Y. Wang, L. Zuo, J. Ye, *Appl. Catal. B Environ.* **2023**, *324*, DOI 10.1016/j.apcatb.2022.122262.

[85] C. Wang, S. Fang, S. Xie, Y. Zheng, Y. H. Hu, *J. Mater. Chem. A* **2020**, *8*, 7390–7394.

[86] R. Grote, R. Habets, J. Rohlfs, F. Sastre, N. Meulendijks, M. Xu, M. A. Verheijen, K. Elen, A. Hardy, M. K. Van Bael, T. den Hartog, P. Buskens, *ChemCatChem* **2020**, *12*, 5618–5622.

[87] C. Serna, J. L. Ahlrichs, J. M. Serratosa, *Clays Clay Miner.* **1975**, *23*, 452–457.

[88] S. Balci, *J. Chem. Technol. Biotechnol.* **1996**, *66*, 72–78.

[89] R. Ruiz, J. C. Del Moral, C. Pesquera, I. Benito, F. González, *Thermochim. Acta* **1996**, *279*, 103–110.

[90] P. Yuan, in *Nanosized Tubul. Clay Miner.* (Eds.: P. Yuan, A. Thill, F.B.T.-D. in C.S. Bergaya), Elsevier, **2016**, pp. 137–166.

[91] N. Kohyama, K. Fukushima, A. Fukami, *Clays Clay Miner.* **1978**, *26*, 25–40.

[92] E. Joussein, S. Petit, C. I. Fialips, P. Vieillard, D. Righi, *Clays Clay Miner.* **2006**, *54*, 473–484.

[93] J. Gao, Q. Liu, F. Gu, B. Liu, Z. Zhong, F. Su, *RSC Adv.* **2015**, *5*, 22759–22776.

[94] A. H. Hatta, A. A. Jalil, N. S. Hassan, M. Y. S. Hamid, M. B. Bahari, M. A. Aziz, M. Alhassan, N. Ibrahim, N. W. C. Jusoh, N. H. H. Hairom, *Mater. Today Chem.* **2023**, *33*, DOI 10.1016/j.mtchem.2023.101743.

[95] B. Miao, S. S. K. Ma, X. Wang, H. Su, S. H. Chan, *Catal. Sci. Technol.* **2016**, *6*, 4048–4058.

[96] P. Strucks, L. Failing, S. Kaluza, *Chemie-Ingenieur-Technik* **2021**, *93*, 1526–1536.

[97] A. M. Abdel-Mageed, D. Widmann, S. E. Olesen, I. Chorkendorff, R. J. Behm, *ACS Catal.* **2018**, *8*, 5399–5414.

[98] D. Mateo, J. L. Cerrillo, S. Durini, J. Gascon, *Chem. Soc. Rev.* **2021**, *50*, 2173–2210.

[99] X. Zhang, X. Li, D. Zhang, N. Q. Su, W. Yang, H. O. Everitt, J. Liu, *Nat. Commun.* **2017**, *8*, 1–9.

[100] H. Song, X. Meng, Z. J. Wang, Z. Wang, H. Chen, Y. Weng, F. Ichihara, M. Oshikiri, T. Kako, J. Ye, *ACS Catal.* **2018**, *8*, 7556–7565.

Concluding remarks

The aim of this PhD thesis was to investigate the implementation of the sustainability of TiO_2 in both the origin of the material and the application for environmental decontamination, through the evaluation of a new TiO_2-rich waste material, known as tionite, and the preparation of TiO_2 supported on different adsorbent materials for their utilisation in the more sustainable photothermo catalytic methanation of CO_2.

In order to evaluate the potential application of tionite, at first its composition and morphology were investigated. A very in-depth characterisation of the raw material provided by the company demonstrated a very complex composition with TiO_2 being the majoritarian component, but with nanometric dimension. Once the composition was defined, it was possible to select specific chemical treatments in order to simplify the matrix of the material and potentially improve the catalytic application of the TiO_2 content. The procedures were designed by a step-by-step evaluation of the photocatalytic performance in the degradation of PC and always keeping sustainability in mind, so by considering treatments that require fewer chemicals and lower temperatures. The characterization of all the produced samples confirmed the success of the new procedures and the simplification of the material composition.

Despite the material improvements, the application of both treated and untreated tionite samples in the degradation of organic pollutants demonstrated its scarce efficiency in classical photocatalytic and photo-Fenton processes. On the other hand, the limited photoactivity of the materials proved efficient in the partial oxidation of ferulic acid to vanillin. All the samples demonstrated an increasing selectivity for vanillin over time, with samples providing better results than the classic P25. It is important to underline that the acidic treated sample shows the best performances due to the specific interaction between the organic substrate and the catalyst.

A different photocatalytic application was also explored, through a PMS-assisted strategy. Once the amount of catalyst and PMS were optimised for the reaction, tionite samples were tested for the degradation of 4-CP under UV light. All samples proved efficient, but the interesting result is that better performances were observed for the untreated samples. This represents a pivotal step towards sustainability since the utilization of untreated samples, namely without the consumption of any additional

energy or chemicals, provided better results than the treated ones. By studying the reaction at different irradiation values, a linear relationship between the apparent kinetic constant and the number of photons was also demonstrated. Contrary to classical TiO_2 photocatalysis, where the kinetic constant reaches a plateau value by increasing the photon flux, for PMS-mediated tests the degradation rate continuously increases with the number of photons. Consequentially, the same yield of degradation was obtained in a shorter time, by simply increasing the number of lamps. In addition, tests performed under visible light demonstrated the ability of one of the untreated samples to activate PMS, which is indeed another step towards a more sustainable application of the material because the reaction could be performed under solar irradiation. Despite the remarkable efficiency of tionite samples in PMS-assisted degradation of 4-CP, the mechanism involved in the PMS activation for tionite still remains unknown. This information would be useful to further tailor tionite composition and improve its performance in this photodegradation strategy.

At the same time, a different approach towards a sustainable application of TiO_2 was investigated. TiO_2 NPs were efficiently synthesized on different adsorbent supporting materials, namely spherical and bidimensional SiO_2 NPs and two clays, Sep and Hall, in order to improve their dispersion and exploit the adsorption properties of the supports to facilitate the accumulation of pollutants molecule near the catalyst surface. Photocatalytic tests were conducted on PC, with all materials proving effective in degrading the pollutant, while adsorption tests for a mixture of metal cations demonstrated the superiority of Sep in their removal.

After the deposition of Ru NPs, the samples were tested in the photothermo methanation of CO_2. According to preliminary results, Supp@TiO_2@Ru5% samples demonstrated a significant efficacy in catalyzing the reaction under dual-excitation. By evaluating the increase in the CH_4 production, induced by combined stimulus, it was observed that the enhancement at lower temperatures (120 °C) was more consistent than at higher temperatures (200 °C). Indeed, the same CH_4 yield obtained in the dark was achieved at a lower temperature, when irradiated with UV light.

It is evident that the application of waste materials as primary resources represents a feasible pathway to reduce the environmental impact of more established processes. Despite the difficulties related to the complex composition, it was demonstrated that

using mild chemical processes is an efficient strategy to improve its composition and applicability. On the other hand, photothermo catalysis represents a possible solution to reduce the temperature and improve the efficiency of well-established catalytic processes.

Appendix – 1
Additional images

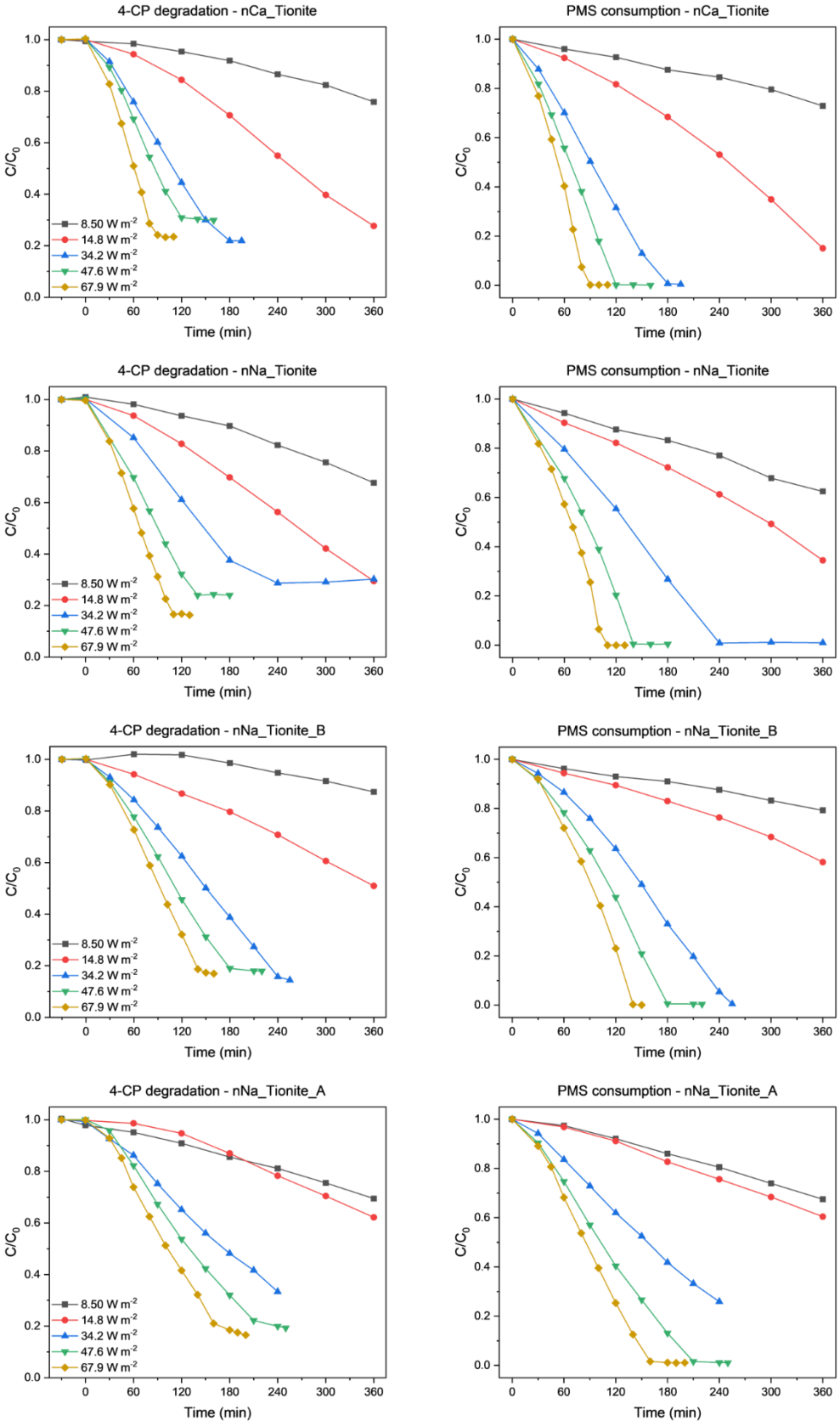

Figure S1: 4-CP degradation and PMS consumption for nCa_Tionite, nNa_Tionite, nNa_Tionite_B and nNa_Tionite A at irradiances value of 8.50 W m^{-2} (black), 14.8 W m^{-2} (red), 34.3 W m^{-2} (blue), 47.6 W m^{-2} (green) and 67.9 W m^{-2} (brown).

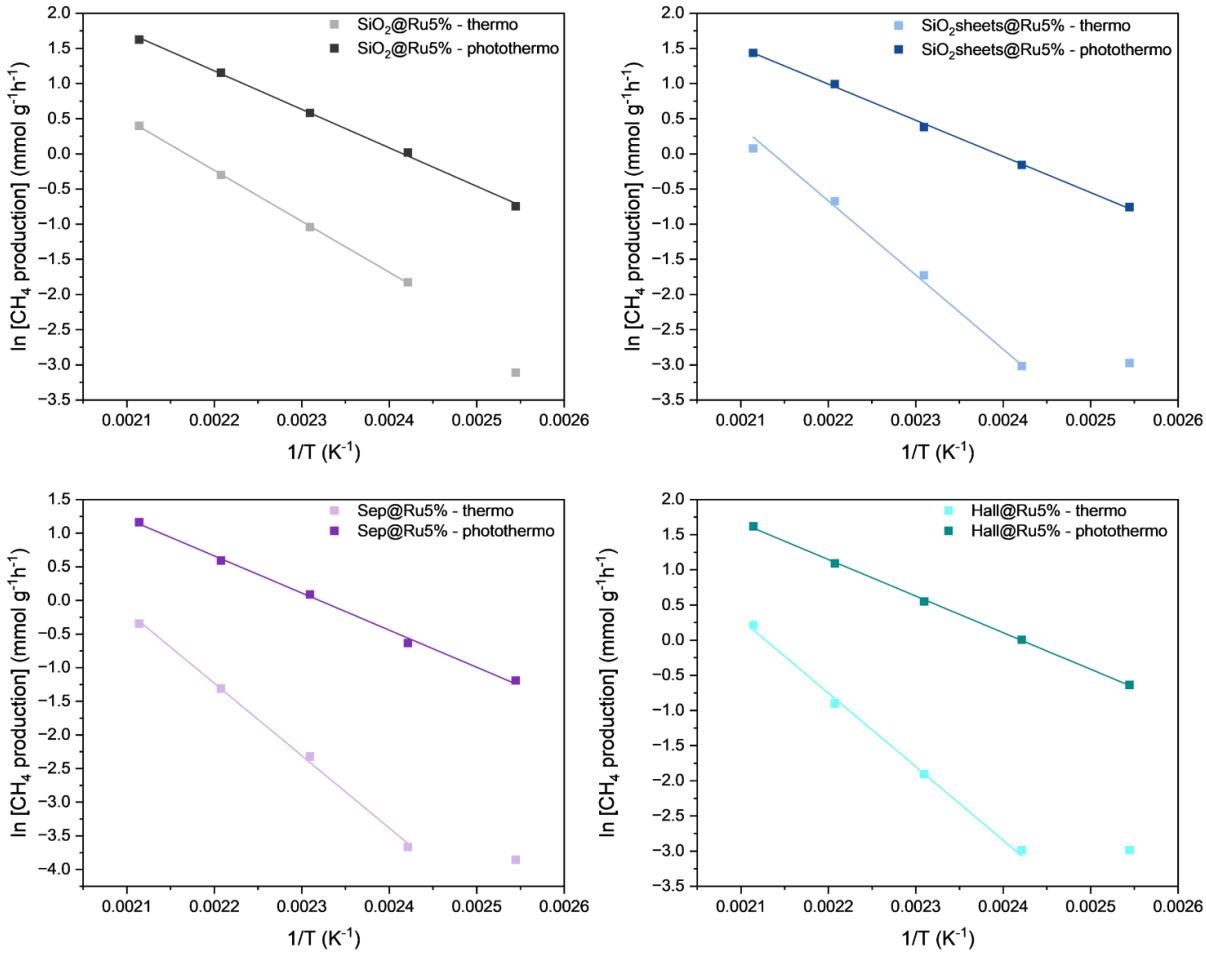

Figure S2: linear fitting of the Arrhenius plot for the calculation of the apparent activation energy (E_a) for all Supp@Ru5% obtained by impregnation method. In each graph, photo and photothermal results are identified by a lighter and darker colour, respectively. For each fitting, R-square > 0.99

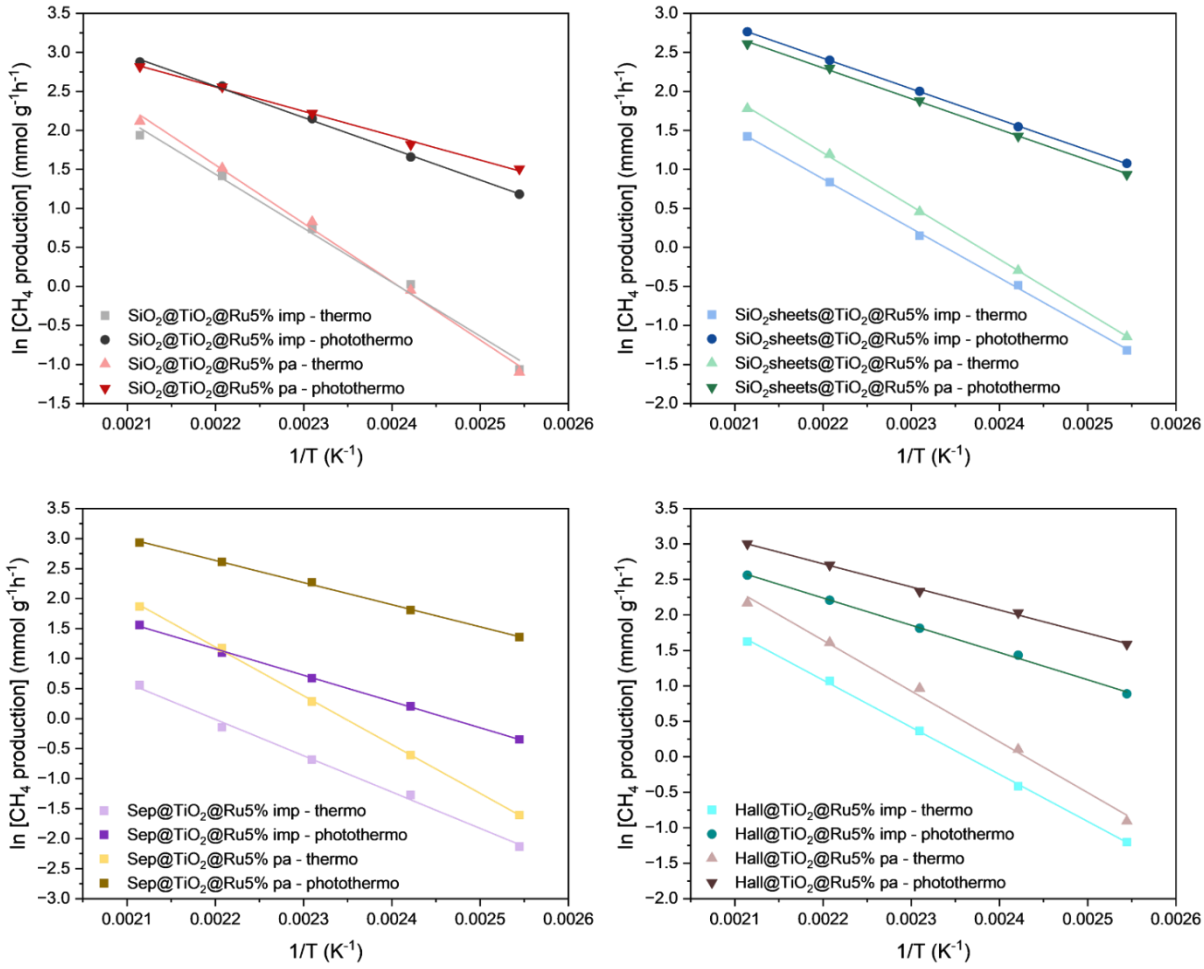

Figure S3: linear fitting of the Arrhenius plot for the calculation of the apparent activation energy (E_a) for all Supp@TiO_2@Ru5% obtained by impregnation (imp) and photo-assisted (pa) method. In each graph, photo and photothermal results are identified by a lighter and darker colour, respectively. For each fitting, R-square > 0.99

Appendix – 2
Characterization methods

A1. Fourier Transformed Infrared Spectroscopy (FTIR)

To study the composition of samples, the analyses were performed with an Attenuated Total Reflectance (ATR) setup on a ThermoFisher Nicolet iS20, acquiring the spectra in the range 4000-550 cm^{-1} with a spectral resolution of 4 cm^{-1}. The spectra presented in this thesis are the result of 128 scans, followed by further refinement of the transmittance signal through baseline correction and normalization in the range 0-100. The analysis was employed to: i) to study the composition of tionite samples and its changes after the chemical treatments and ii) characterize the inorganic SiO_2-based supports before and after the functionalization with TiO_2 NPs.

A3. Elemental analysis (CHNS)

Elemental analysis (CHNS) was performed with an Elemental VarioMICRO analyser, setting the temperature of the combustion and reduction columns at 1150 °C and 850 °C respectively. The technique, typically used for organic materials, thermally converts the main elements of organic molecules (carbon, hydrogen, nitrogen and sulfur) into volatile molecules, which are separated by gas-chromatography, identified and quantified. The measurement was used to quantify and evaluate the change in the amount of the four elements in the two untreated samples of tionite, nCa_Tionite and nNa_Tionite.

A2. Thermogravimetric analysis (TGA)

TGA thermograms were collected by using a Mettler Toledo TGA/DSC1 STARe System at constant air flux (50 cm^3 min^{-1}). The samples holder used was an alumina crucible with 75 µl volume, filled at least until half of its capacity and used without the pan. The measurements were performed in the range between 30 and 1000 °C, at the heating rate 10 °C min^{-1}, with a 15 min isotherm at 150 °C, to remove humidity, and a second one of 5 min at 1000°C. The analysis allowed the investigation of the weight loss percentage of the sample at increasing temperature due to thermal decomposition or oxidation, as well as desorption and vaporization phenomenon. The isotherms aimed to stabilise the sample composition at 150 and 1000 °C and highlight the thermal phenomena which take place in that temperature range, generally attributed to the decomposition of organic compounds or the release of highly bonded water

molecules. The TGA analysis was performed to investigate the thermal phenomena and to quantifiy the carbon compounds for tionite samples.

The TGA instrument was also connected to the FTIR spectroscope in order to study the composition of the gas generated during the thermal treatment. Since the analysis was carried out in an air atmosphere, only the oxidized compound of the elements can be detected, so the decomposed carbon will form CO_2. The analysis was fundamental to define the nature of the thermally degraded compounds of tionite samples.

A4. X-Ray Diffraction (XRD)

Powder X-ray diffraction (XRD) patterns were collected at room temperature with a Rigaku MiniFlex 600 diffractometer, operating with a Bragg-Bentan geometry. In this setup, a Cu Kα radiation X-ray source (λ_1=1.5406 Å, λ_2= 1.5443 Å) was used and the X-ray generated are collimated by slits before reaching the sample. The sample was located in an amorphous holder and with crystallites placed in a random orientation, in order to avoid systematic errors in the diffractogram. The X-rays coming from the sample pass through the receiving slits and reach the detector. The diffractograms shown in the thesis were performed in the 2θ range of 5-90° for tionite samples and 5-70° for supported TiO_2 samples, with a 2θ step 0.02° and 1° min^{-1} scan rate. The analysis was employed to define whether supported TiO_2 NPs form an amorphous or crystalline structure, to define TiO_2 crystalline phase and to investigate the crystalline composition of tionite samples.

A5. Diffusive Reflectance Spectroscopy (DRS)

Reflectance UV-Visible analysis was performed with a UV Lambda 900 Perkin Elmer spectrometer on powder samples, in the range 800-200 nm, with an accuracy of 0.08 nm. The sample is irradiated with a beam generated by a double source, composed of a deuterium lamp and a halogen lamp. After the emission from the source, the beam is reflected by a series of mirrors and monochromators to reach the sample. A typical quartz window was used as a sample holder, where the incident beam collides and is then reflected to the detector. The signal is consequently converted to a current signal by the photomoltiplicator. This analysis was used for the characterization of supported

TiO_2 samples, to determine the band gap energy, and on tionite samples. The calculation of the band gaps was done using the Kubelka-Munk treatment[1], exploiting the following equation

$$F_R = \frac{(1-R)^2}{2R}$$

where R is the measured reflectance and F_R is the absorption coefficient.

A6. X-Ray Fluorescence (XRF)

X-ray Fluorescence Spectroscopy was performed using a micro-XRF spectrometer Bruker ARTAX 200 equipped with a Mo anode X-ray tube, collimated down to 0.65 mm in diameter (excited sample area of 0.33 mm^2). XRF is used to determine the elemental composition of materials through the irradiation with high-energy X-rays and the analysis of the emitted secondary (fluorescent) X-rays at specific energies, characteristic of the elements included.

The spectra were obtained by operating at 20 kV and 1.0 mA and with an acquisition time of 300 s. The attributions of each signal were performed by using the XRF software. The analysis was fundamental to define the composition of all tionite samples, to evaluate the variations caused by the chemical treatments and for confirming the presence of Ti in the TiO_2 functionalized samples.

A7. Nitrogen physisorption

N_2 physisorption isotherms on tionite samples were recorded at 77 K in a liquid N_2 bath by a Micromeritics ASAP 2420 apparatus. Prior to analysis, all materials were degassed for 3 h at 150 °C under vacuum. The specific surface area (SSA) was calculated according to the Brunauer–Emmett– Teller (BET) method,[2] using adsorption data in the 0.07 – 0.25 relative pressure range. Pore size distributions in the mesopore range were determined through the Barrett-Joyner-Halenda (BJH) method[3] with Harkins-Jura curve between 2 and 100 nm. Mesopore volumes were estimated from the volume of N_2 adsorbed at P/P^0 = 0.99. For micropores, the pore volume was estimated by the t-plot, while the pore distribution was determined through the Horvath-Kawazoe method[3]. The analysis was performed to assess the SSA and porosity of all tionite samples and the TiO_2 supported samples. In addition, the

influence of TiO_2 functionalization on the support properties were investigated.

A8. Contact angle

Contact angle measurements provide information about a sample hydrophobicity or hydrophilicity. The static drop method was used, namely a droplet of water was placed on the sample surface and the angle formed by the droplet itself is measured. Contact angles > 90° indicates poor wetting, typical of hydropobic surfaces, while the opposite conditions is achieved at contact angle < 90°. The contact angle analysis was performed using an in-house contact angle setup, consisting of a camera (Fastcam Nova S6, Photron) with Tokina AT-X PRO D (100 mm F2.8 MACRO) as optical lens and backlight illumination. The static contact angle was measured with a drop volume of 6 μ l. The data reported are the average and standard deviation of three measurements. The analysis was performed to assess the variations in tionite surface hydrophilicity after the different treatments. For this purpose, the sample was analyzed in the form of a tab.

A9. X-Ray Photoelectron Spectroscopy (XPS)

XPS analysis a surface analysis used to determine the elemental composition, chemical state and electronic structure of materials. By measuring the kinetic energy of electrons emitted from the sample upon X-ray irradiation, XPS allows the identification of the elements and their oxidation states.Tha characterization was performed on a ThermoVG Multilab ESCA 3000 spectrometer (Al Kα anode ay hλ = 1486.6 eV). The Energy shift due to electrostatic charging was corrected using the adventitious sp2 carbon C 1s band at 284.5 eV. Donich-Sunjic shape and an S-shaped Shirley type background were used for the peak fitting. The surface atomic concentrations were determined by using peak area and sensitivity factor.[4] Briefly, the number of atoms of the element per cm^3 related to a spectra peak is calculates as follows:

$$n = \frac{I}{f\sigma\theta y\lambda AT}$$

Where I is the number of photoelectrons per second of a specific peak, f is the x-ray flux, σ the photoelectric cross-section for the atomic orbital of interest, θ is an

instrumental angular efficiency factor, y is the efficiency in the formation of photoelectrons of the normal photoelectron energy, λ is the mean free path of the photoelectrons in the sample, A is the samples area from which photoelectrons are detected and T is the detection efficiency for the photoelectrons.

The denominator of the equation is defined as the atomic sensitivity factor, whose values are tabulated.[5] To determine the atom fraction of an element x, the following equation is applied:

$$C_x = \frac{n_x}{\sum n_i}$$

The analysis was applied to investigate the surface composition of tionite and the variations induced by the chemical treatments.

A10. Scanning electron microscopy (SEM)

SEM exploit a focused beam of high-energy electrons to produce detailed, high-resolution images of the surface of a specimen. In SEM, electrons interact with the atoms of the sample, generating various signals that reveal information about the sample's topography and composition. By coupling the microscope with the Energy Dispersive X-ray Spectroscopy (EDX) the X-rays emitted from the sample during the electron-beam interaction are used to define the elemental composition and distribution on the sample surface.

SEM images were collected with a Zeiss Gemini 500 microscope in a high-vacuum configuration equipped with the Bruker Quantax detector for EDX. The electron beam excitation was 30 kV at a beam current of 25 pA, and the working distance was 12 mm. In this configuration, the beam spot was 38 nm. The samples were dispersed in EtOH, deposited onto an aluminium substrate by drop-casting and sputtered with gold. SEM analysis was used to study the morphology and, in combination with EDX, to study the composition of tionite and the variations induced by the different treatments applied.

A11. Transmission electron microscopy (TEM)

TEM microscopy uses a beam of electrons transmitted through a thin sample to produce high-resolution images of its structure. Unlike SEM, which scans the surface,

TEM provides detailed images of the morphology, with a resolution of up to a few nanometers.

TEM was performed with a JEOL JEM-2100Plus transmission electron microscopy, operating at an acceleration voltage of 200 kV and equipped with an 8-megapixel Gatan Rio complementary metal-oxide-semiconductor camera and an Oxford EDX detector. Samples dispersed in EtOH were deposited on carbon-coated Cu TEM mesh grids by drop-casting.

TEM micrographs were collected to study more in-depth tionites morphology and composition and to investigate the shape and dimension of the synthetised TiO_2 NPs on each support, ss well as the composition of sheet-shaped particles in Tionite-Na

A12. Raman Spectroscopy

Raman spectroscopy is used to study molecular vibrations and materials compositions and structures by analysing the inelastically scatter light, known as Raman scattering, generated by focusing a laser on the sample. Raman spectra were obtained with a Jasco Ventuno μ-Raman instrument with a Peltier-cooled charge-coupled device (CCD) camera (operating temperature: −50°C) and a He−Ne laser (wavelength, 632.8 nm; power density, 6 kW cm^{-2}).

Raman spectroscopy was used along with XRD to define the crystalline structures included in both tionite and the synthesised TiO_2 NPs.

A13. Inductively Coupled Plasma Optical Emission Spectrometry (ICP-OES)

ICP-OES is used to determine the elemental composition of a solution. It involves a high-temperature plasma to excite atoms and ions in the sample, causing them to emit light at characteristic wavelengths. The emitted light is analyzed by an optical spectrometer to identify and quantify the elements included in the sample.

ICP-OES was performed with a PerkinElmer OPTIMA7000 DV spectrophotometer with a constant flux of Ar of 20 L min^{-1} to transport the vaporized sample.

The analysis was used in the adsorption tests to quantify Cu, Ni and Y in the remaining solution after the reach of the adsorption-desorption equilibrium. The analysis was also performed to quantify Ru deposited on the supported-TiO_2 samples. For this purpose,

the sample was dissolved through a microwave-assisted acidic dissolution with a mixture of HNO_3, HCl and HF at 185 °C under autogenic pressure.

A14. Total organic carbon (TOC)

TOC is a measure of the total amount of carbon included in organic compounds in an aqueous system. The measurement is not direct: total carbon (TC) is measured through the combustion catalytic oxidation and, on a different sample aliquot, the inorganic carbon (IC) is quantified by acidification. The TOC is then calculated according to the following equation:

$$TOC = TC - IC$$

TOC measurements were performed using a Shimadzu TOC-L analyser to determine the organic carbon load of the aqueous suspensions as a function of treatment time.

A15. Granulometry

Granulometry provides information about the texture and composition of the material based on the size, shape, and distribution of its grains or particles. The method employed in this thesis is the sieve analysis: the sample is passed through a stack of sieves with progressively smaller mesh sizes and the material retained on each sieve is weighed. The instrument used is a Malvern Morphologi 4 optical granulometer (Malvern Panalytical, Malvern, UK). The analysis was used to study the granulometry of nCa_Tionite.

Bibliography

[1] S. Landi, I. R. Segundo, E. Freitas, M. Vasilevskiy, J. Carneiro, C. J. Tavares, *Solid State Commun.* **2022**, *341*, 1–7.

[2] S. Brunauer, P. H. Emmett, E. Teller, *J. Am.Chem.Soc.* **1938**, *60*, 309–319.

[3] C. M. Lastoskie, *Stud. Surf. Sci. Catal.* **2000**, *128*, 475–484.

[4] J. F. Moulder, W. F. Stickle, W. M. Sobol, K. D. Bomben, **1992**.

[5] J. E. Castle, *Surf. Interface Anal.* **1984**, *6*, 302.